UNIVERSITY OF OKLAHOMA

GRADUATE COLLEGE

CHARACTERISTICS OF TROPICAL CYCLONES IN THE NORTH ATLANTIC AND EAST PACIFIC

A DISSERTATION

SUBMITTED TO THE GRADUATE FACULTY

in partial fulfillment of the requirements for the

Degree of

DOCTOR OF PHILOSOPHY

By

BRADFORD SCOTT BARRETT
Norman, Oklahoma
2007

UMI Number: 3291242

CHARACTERISTICS OF TROPICAL CYCLONES IN THE
NORTH ATLANTIC AND EAST PACIFIC

A DISSERTATION APPROVED FOR THE
SCHOOL OF METEOROLOGY

BY

____
Lance M. Leslie

____
Evgeni Fedorovich

____
J. Scott Greene

____
Susan Postawko

____
David Stensrud

Acknowledgements

This work was funded through multiple sources that I would like to acknowledge: the U.S. Office of Naval Research, the U.S. Department of State, the University of Oklahoma Lowry Endowed Chair, the University of Oklahoma Graduate College, the University of Graz Wegener Center for Climate Change, and the University of Oklahoma School of Meteorology. Each source of funding allowed me the flexibility to choose a research topic of my interest, and I am thankful for their generosity in providing me the many opportunities I have had as a graduate student. My path to a ph.d. was perhaps atypical for this department: I spent eighteen of my seventy-four months as a graduate student overseas. I was awarded the J. William Fulbright Fellowship to study at the Caribbean Institute for Meteorology and Hydrology in Barbados from August 2005 to June 2006, and I was also awarded a visiting lectureship at the University of Graz from September 2006 to March 2007.

I first thank my advisor and committee chair, Dr. Lance Leslie, for all of his support and encouragement of my studies. Without his blessing (and many letters of recommendation), I would not have been awarded those two prizes, nor would I have had the amazing experiences that came with each opportunity. Lance, thank you! I also thank my officemates, Andy Taylor and Kevin Goebbert, for their friendship, encouragements, jokes, and camaraderie. I consider myself blessed to share our office space after our move to the National Weather Center building. I thank them also for each editing a chapter of this dissertation. I thank the ever friendly and cheerful office staff of the School of Meteorology: Marcia, Celia, Nancy, Kristyn (and Laura, and Lauren). Thanks for brightening our days and handling our never-ending stream of

administrative requests! My fellow graduate students (and frequent chase partners), including Dan, Robin, Mike, Jen, Kodi, Hamish, Jose, John, Alex, Ashton, Elaine, Chris, Gabe, and others, thanks for a great six years! To my "Frisbee Friday" guys, thanks for reminding me to get out, run around, and toss a disc. To the occupants of the offices below me in SEC and the NWC, thanks for enduring the sound of my stress-relief "bouncy ball" pounding into your ceiling. I thank my mentor from the Department of Economics, Bob Reed, for his personal encouragements and wise advice.

I thank my family, and particularly my parents, for truly letting go of the parental strings and allowing me to explore the world, beginning with Greenville and Chapel Hill, continuing to Oklahoma, Barbados and Austria, and now onward to Chile. Life outside of Greenville was new and scary, but it has been well worth the adventure. I love you guys and am ever grateful to you!

As my graduate studies have come to a close, I have concluded that life is far more than sitting in front of a machine from 8-5, worrying about my next paycheck or fretting about deadlines. Life is a gift, every minute to be soaked up and enjoyed. Pour into relationships; I have found that they are sources of great joy. Join a bible study, for in the scriptures lie eternal truths of faith. One of my absolute favorite passages comes from the prophet Isaiah: in a vision, Isaiah sees God seated on a throne in power, and realizes his sin and cries out. An angel comes to him and beautifully forgives, and Isaiah, hearing God ask aloud for ambassadors, proudly responds, "Here I am. Send me." I love the imagery, the emotional swings of Isaiah from utter desolation to triumphant purpose, and I long to have the same courage to continue that response! It is my hope that all people, regardless of background or intellect or spirit, will experience and center their lives around the true Living God, who from Abraham and Isaac, Isaiah and David, to Peter and Matthew and Paul, has sought the world, even giving Jesus, his son, to reconcile all men. So I conclude with a doxology, a hymn of praise, which conveys the attitude of my heart and the hope upon which my life is based. After I, and this research, have long ago passed into dust, He will remain, eternal and everlasting.

33 *Oh, the depth of the riches of the wisdom and knowledge of God!*
How unsearchable his judgments,
and his paths beyond tracing out!
34 *"Who has known the mind of the Lord?*
Or who has been his counselor?"
35 *"Who has ever given to God,*
that God should repay him?"
36 *For from him and through him and to him are all things.*
To him be the glory forever! Amen.

-Paul, Romans 11:33-36

Table of Contents

Chapter 1. Introduction

Tropical cyclones (TCs), known variously as hurricanes, typhoons, or cyclones, are among the most extreme geophysical phenomena on the surface of the planet: wind speeds can surpass 90 m s^{-1}; rainfall rates approach or exceed 100 mm hr^{-1}; and ocean waves are churned up to 35 m. At landfall, death and destruction are spread across wide areas without respect for geopolitical boundaries. Coastal buildings are flooded by the ocean surge; inland waterways overflow their banks and claim homes and businesses; tornadoes chart narrow but unpredictable paths in the outer bands and eyewall; and both coastal and inland structures are damaged and destroyed after prolonged battering by wind and wind-driven projectiles. Although the recent U.S. impacts of Hurricanes Katrina, Rita, and Wilma, 2005; and Hurricanes Charley, Frances, Ivan, and Jeanne, 2004 (which combined for over $150 billion in damage and 2,000 fatalities) are fresh in our minds, it is important to remember that the toll can be much greater. A single, poorly-forecasted cyclone made landfall in Bangladesh in 1970 and killed upwards of half a million people, almost double the widely publicized and catastrophic toll of the December 2005 Indian Ocean tsunami disaster.

While often the focus of news media and emergency management, landfalling TC impacts are not restricted to the dramatic or cataclysmic. They provide beneficial rainfall over many tropical and middle-latitude land areas, and their recurring floods rinse toxins from hydrologic ecosystems. Greatly contrasting with the general quiescence of the tropical atmosphere, they have been the subject of intense inquiry for centuries, but only in the recent sixty years has substantive scientific progress been achieved in understanding their genesis, structure, motion, and connection to the earth-atmosphere system around them.

Because TCs are such significant geophysical hazards, it is essential that this substantive work be extended. Very recent advances in technological capacities, including high-resolution NWP models, advanced computing capabilities, improved instrumentation used to gather in situ observational data, and enhanced satellite and radar remote-sensing techniques, have enabled the expansion of our observational and theoretical understanding of TC structure and motion. New and more accurate historical datasets are now available that span thirty or more years, providing for the first time the ability to define climatological norms and anomalies. Combining these technological advances with the continued annual extension of climatic datasets, TC research is now more feasible than ever before. However, we need only look to the very recent cases of Hurricane Felix and Hurricane Humberto (2007) to demonstrate that additional studies are needed to expand our understanding and ability to predict TC genesis, structure, and organization. Felix, whose genesis east of Barbados was not predicted by either man or machine, underwent very rapid, and very poorly forecasted, intensification; the 1500 UTC 01 September 36 hr intensity error was 75 kt! Humberto formed and strengthened into hurricane, with sustained winds of 75 kt, in only 18 hr, and similar to Felix, was not forecasted to do so. Thus, it is necessary to improve our understanding of TC genesis, intensification, track, and frequency on timescales ranging from weeks to decades. The goal of this research is to provide greater understanding of the complex interaction between the TC and its surrounding larger-scale environment.

In this dissertation, I present a series of investigations intended to expand our understanding of TCs in the East Pacific and North Atlantic basins. First, I developed and applied a climatological tool that quickly and succinctly displays the spread of historical TC tracks for any point in the North Atlantic basin. This tool is useful in all parts of a basin because it is derived from prior storm motion trajectories and summarily captures the historical synoptic and mesoscale steering patterns. It displays the strength of the climatological signal and allow for rapid qualitative comparison between historical TC tracks and NWP models. Second, I have used a robust statistical technique to quantify the relationships between fifteen different metrics of TC activity in nine ocean basins (see Figs. 1.1-1.2 and Table 1.1) and twelve climate indices of the leading modes of atmospheric and oceanic variability. In a thorough, encyclopedic manner, over 12,000 Spearman rank correlation coefficients were calculated and examined to identify relationships between TCs and their environment. This investigation was not limited to the East Pacific or North Atlantic, and new climatic associations were found between seasonal levels of TC activity and the major climate indices across the nine basins. This information is critical to forecasters, economists, actuaries, energy traders, and societal planners who apply knowledge of levels of TC activity on intraseasonal to interdecadal timescales. The statistics are also valuable to climatologists seeking to understand how regional TC frequency will change as the global climate warms. Third, I have examined the leading intraseasonal mode of atmospheric and oceanic variability, the Madden-Julian Oscillation (MJO), and discovered statistically significant relationships with the frequency of TC genesis, intensification, and landfall over the nine basins. Like the significance of the longer-period oscillations to the frequency of TC activity on intraseasonal and longer timescales, these results are highly relevant to the problem of short-term (one- to two-week) predictability of TC activity. These three investigations demonstrate the utility of historical datasets across a wide range of applications, from short-term forecasting to climate studies. In this way, the results highlighted in this dissertation represent a significant and positive contribution to meteorology. Collectively, they reveal multiple characteristics of TCs in the East Pacific and North Atlantic and provide greater understanding of the complex interactions between TCs and their surrounding larger-scale environment.

This dissertation is organized into five parts. This introductory chapter has presented the problem investigated by the dissertation research. It continues with a definition of the TC as a geophysical phenomenon and an examination of the conditions for development; an evaluation of the behavior, structure, and substructure of TCs; an analysis of the physical processes fundamental to the TC, especially focusing on the boundary layer parameterization of the drag coefficient in mesoscale meteorological models; and a description of the theories and methods used in forecasting forecast TC track and intensity, with a specific emphasis on the role of terrain in influencing TC evolution. Questions regarding the drag coefficient and terrain were previously posed in the dissertation prospectus, and although they are not investigated in this dissertation, they remain significant questions and thus are still reported in Chapter 1. Chapter 2 focuses on the climatological track forecasting tool, highlighting the work presented in Barrett et al. (2006). Chapter 3 presents the relationships between TCs and the leading modes of atmospheric and oceanic variability and presents results quantifying the important associations. Chapter 4 details the modulation of TC activity by the leading mode of intraseasonal atmospheric variability, the MJO (Barrett 2007). Chapter 5 summarizes the important findings of the dissertation research and provides several suggestions for future studies which stem from this research. The dissertation concludes with a bibliography and the tables and figures referenced in the text.

1.1. Definition and historical observations

The term "tropical cyclone" (TC) is a general term for a cyclone originating over the tropical oceans (Glickman 2000) that is "driven principally by heat transfer with the ocean" (Emanuel 2003b). TCs with wind speeds of at least 39 mph but not more than 73 mph are known as tropical storms. TCs with wind speeds at or over 74 mph (64 kts, or 33 m s^{-1}) are known as hurricanes in the North Atlantic and eastern North Pacific Oceans, typhoons in the Northwest Pacific Ocean, severe tropical cyclones in the Southwest Pacific and Southeast Indian oceans, and severe cyclonic storms in the North Indian Ocean (Neumann 1993). The term "hurricane" was derived from the various West Indian words for "monstrous gods" (Dunn and Miller 1960). Many early American records include references to hurricanes, and in 1847 the first known warning system was established by the Lt. Col. William Reed of England while stationed in Barbados (Sheets 1990). By 1860, the typical surface wind and sea level pressure patterns were well-known: a surface observer, during a TC passage, would record gradually lowering pressures and increasing cyclonic winds, and then a sudden drop in pressure and change to near-calm winds in the eye, followed by an equally dramatic increase in winds and pressure as the eye passed. The U.S. civilian service, through the Weather Bureau and now the National Weather Service and National Hurricane Center, was tasked with monitoring, forecasting, and warning for hurricanes since the public outcry following the 16 September 1875 hurricane that completely destroyed Indianola, Texas with no advance warning (Dunn 1971). From the late 1800s through the early 1900s, meteorological observing stations were established at coastal sites in the U.S. and at ports in the Caribbean (Sheets 1990). Until satellite coverage began in the 1960s, these coastal observing stations provided the only accurate confirmation of TC landfall. Funding for improvements in TC forecasts was spurred by public outcry from several tragic forecast "misses" (e.g., Galveston 1900 and Miami 1926). Forecast responsibility for the North Atlantic basin was consolidated in Miami in 1943 (Burpee 1988). Since 1944, that office has maintained the "best track" historical record of all TCs in the Atlantic basin and has extended the dataset back to 1851 (Jarvenien et al. 1984).

1.2. TC genesis and development

1.2.1. Conditions for development

Coincident with the placement of coastal observing stations and the establishment of a consolidated forecasting center in Miami was the development of several TC research programs. These programs and their early scientific staff subsequently began to document the conditions that led to the genesis and development of TCs. Dunn (1940) and Riehl (1948) noted that TCs tend to form from a westward-progressing wave embedded in the easterly trade winds moving beneath a region of upper-tropospheric divergence. Yanai (1964) and Fett (1966) advanced the theory to include broad-scale deep vorticity convergence along the wave axis. Sadler (1976) and Tanabe (1963) looked for development from an existing vortex along the surface equatorial trough. Ramage (1959) noticed that development tended to occur downstream of a mid-oceanic upper trough that provided the necessary "energy dispersion" mechanism. Gray (1968) hypothesized that even though initial mechanisms for genesis varied from basin to basin, the process by which TCs developed and intensified should be similar globally. His necessary, but not sufficient, conditions for TC development are now regarded as classical:

(1) strong moisture convergence into the vortex caused by frictionally-forced low level convergence (i.e., Ekman turning),
(2) accompanying upper tropospheric divergence that leads to deep cumulus convection,
(3) slightly more net divergence than convergence in the vortex column,
(4) horizontal wind shear present in the lower troposphere but minimal vertical shear,
(5) sea-surface and deeper ocean temperatures at or exceeding 26.5 °C,
(6) poleward latitude of at least 5 degrees to invoke Coriolis turning, and
(7) a pre-existing low-level vorticity disturbance.

1.2.2. TC genesis

A great deal of complexity, associated with interactions on a variety of time and space scales, surrounds the accurate identification of tropical cyclone genesis. The AMS defines a TC as a disturbance of low pressure that originates over the tropical oceans, encompassing depressions, tropical storms, typhoons, and hurricanes (Glickman 2000). Gray (1968) further defines a tropical storm as a "warm-core cyclonically rotating wind system in which the maximum sustained winds are 17 m s^{-1} (35 kt, 40 mph) or greater." Between seventy-five and ninety such systems are classified globally each year, although there is a high degree of intraannual, interannual, and basin-to-basin variability (Webster et al. 2005). The definition of what constitutes a TC remains vague, and while forecasters are able to easily identify a mature TC, they are routinely faced with the ambiguities of specifying the point when a tropical disturbance should be classified as a TC. The latest advances in observing technologies have only served to complicate the problem, as evidenced by the heated debate over whether the low that came ashore in southeastern Brazil in January 2003 was a TC or not.

In the 1980s, due to the differential evolution of TC classification schemes by various national weather bureau units, it was realized that consensus definitions were necessary to standardize the classification across basins (McBride 1981). A "cloud cluster", the typical tropical weather system, was defined as "a loosely organized collection of deep convective clouds covered in the upper levels by a thick cirrus shield" (McBride 1981). The cloud cluster has a residence time of 1-3 days and a horizontal scale of 500-800 km. The "tropical depression" was defined as the least-organized type of TC. It required an unambiguous closed surface circulation, defined as one or more closed surface isobars, and its highest sustained surface wind speeds (over 1 min or longer) could not exceed 33 kts (17.5 m s^{-1}). The "tropical storm" was defined as the next-organized type of TC, with the same definition as a tropical depression but with highest sustained surface wind speeds between 34 and 63 kt, inclusive. The “hurricane” (or “typhoon” west of 180°) was defined as a TC with highest sustained surface winds greater than 63 kt (McBride 1981).

1.2.3. Climatological observations of TC genesis

Gray (1968) identified eight global ocean basins where TCs tended to develop: NE Pacific, NW Pacific, Bay of Bengal, Arabian Sea, Southwest Indian Ocean, Southeast Indian Ocean (off NW Australian coast), South Pacific (off NE Australian coast), and NW Atlantic (including Caribbean Sea and Gulf of Mexico). Identification and classification of TCs has evolved based on differing regional considerations and forecaster biases, which include various formative mechanisms and observing capabilities. The majority of the world’s TCs form equatorward of 20° on the poleward side of an equatorial doldrums trough (Gray 1968). For example, Dunn (1940) and Riehl (1948) observed that North Atlantic TCs tended to form from westward-moving isallobaric waves in the easterly trades. Consistent with this theory, it is estimated that, on average, 63% of the tropical cyclones in the Atlantic basin form from tropical waves (Avila et al. 2000).

Yanai (1964) focused on broad-scale deep vorticity convergence as a primary formative mechanism in the northwest Pacific. Many early studies such as these concentrated on the pre-existing disturbance as a prelude to TC genesis. Palmén (1948) isolated the location of the 26.5°C sea surface temperature (SST) isotherm as critical for development. To physically explain the preferred geographical areas of TC genesis, Gray (1968) observed that the geographical variation of potential buoyancy, defined as the difference between equivalent potential temperature at the surface and 500 hPa, was not of primary importance. He did, however, find a strong association between the regions of August and January storm formation and climatological minima in zonal tropospheric vertical wind shear (defined as the difference between zonal 200 hPa and 850 hPa winds). Gray (1968) thus proposed that the high degree of inter-annual and seasonal variability in TC occurrence can be partially explained by "departures of these circulation features from their climatological values".

1.2.4. Theoretical genesis and energetics

Charney and Eliassen (1964) noted that hurricanes develop from pre-existing tropical depressions that exhibit a warm core and circular symmetry. They also noted that these disturbances are rare with respect to the seemingly favored small scale cumulus convection. They suggested viewing the cumulus cell as not competing for the same energy as the pre-hurricane depression, but rather supplying it by producing low-level convergence of moisture. They demonstrated that surface friction was an energy creating mechanism, and also noted that the individual cumulus cells cooperatively interacted with the large-scale motion to lead to upscale amplification of the disturbance. They treated the hurricane as a forced circulation, driven by heat released through organized cumulus convection, rather than a free circulation driven by an imbalance in buoyancy. The term "conditional instability of the second kind" (CISK) was given to describe this energy cycle. Emanuel (1986) proposed that tropical cyclones begin as finite-amplitude instabilities that involve feedback between the wind-induced evaporation and the cyclone. He noted that TCs do not develop spontaneously but invariably arise out of “preexisting disturbances of presumably independent dynamic origin” (see section 1.4 for a more thorough discussion of TC energetics).

1.3. TC structure and governing equations

TCs have been observed with many different platforms that have changed as the technology has advanced. Early mariners and coastal settlers relied on basic instruments, such as barometers and cup anemometers, which they combined with post-storm damage assessments to gauge storm intensity. In 1944, routine aircraft reconnaissance began in the Atlantic basin, and for the first time, accurate wind and barometric pressure measurements could be taken in storms before they approached land. The advent of weather radar in the early 1950s provided even more insight into storm structure. With the launch of polar-orbiting and geostationary satellites in the 1960s, a detailed conceptual model of the mature TC emerged that remains largely unchanged today.

1.3.1. Structural observations

Much of what we know of the dynamical and thermodynamical structure of a mature TC has come through increasingly advanced observing technologies and has been refined primarily over the past sixty years. The first airborne attempt to obtain a position fix of a TC that was approaching land occurred on 27 July 1943, as Major Joe Duckworth flew into the core of a tropical storm (Markus et al. 1987). Routine aircraft reconnaissance, begun in the Atlantic in 1944, gave the first composite view of radial and azimuthal variations of temperature, moisture, and wind. Ground-based radiosondes, aircraft-deployed dropwindsondes, and ground-based and airborne Doppler radar added additional detail and led to the widely accepted three-dimensional picture of the approximately axisymmetric and steady TC vortex. More recently, high-resolution microwave satellite sensors have provided a composite understanding of upper-level and near-surface airflow in and surrounding the TC (Hawkins et al. 2001). Today most of the world's open-ocean TC intensity measurements are made from analysis of satellite imagery (Kossin and Velden 2004).

1.3.2. Life cycle and parts of a mature TC

TCs have three classical stages in their life cycle. In the genesis stage, disorganized arrays of squalls and clouds are associated with a perturbation in tropical easterly flow. In the mature stage, a strongly rotational circulation and cloud pattern is well-organized around an axisymmetric low pressure center. Finally, in the dissipation stage, the circulation weakens and elongates asymmetrically from the center.

To a first approximation, the mature TC is a symmetric vortex circulation (Ooyama 1982; Moller and Montgomery 1999). The wind stress over the open ocean generates surface waves and drives upper-ocean circulations. Maynard (1945) and Wexler (1947) documented the spiral nature of the outer rain bands and noticed distinct cellular convective elements. These outer bands have been approximated as breaking Rossby waves (Montgomery 1997; Moller and Montgomery 1999). Bergeron (1954), using a series of measurements taken by Deppermann (1947) as a typhoon crossed the Philippines, was the first to document the inner core structure. He noticed a distinct outward slope (with height) of the radii of maximum winds and rainfall. A mature TC has an rain-free “eye” at its center and an eyewall, defined historically as a “ring” (Willoughby et al. 1982) of intense convective activity, surrounding the rain-free eye (Palmén and Newton 1969).

TCs are typically considered to straddle the border between meso- and synoptic-scales (Bluestein 1992; Holton 2004). However, the TC substructure is considered to be composed of mesoscale or convective-scale entities. The eye, eyewall, and spiral rain bands are all considered mesoscale features (Jorgensen 1984) with a typical horizontal scale less than 100km. The eyewall and spiral rain bands, however, have been found through extensive radar observations to contain cellular convective elements with typical horizontal scales of 10 to 20 km.

1.3.3. TC as a modified-Rankine vortex

Winds through most of the depth of the TC core flow cyclonically (in the same sense as the local vertical component of earth’s rotation), increasing toward the center. Although “no two hurricanes are exactly alike” (Anthes 1982), the inner-core flow of the vortex is in approximately solid-body rotation, with calm winds in the center increasing (sometimes quite dramatically in intense eyewall convection) outward radially to a “radius of maximum winds” (RMW). The remainder of the vortex flow is effectively irrotational, with winds gradually decreasing radially outward from the RMW, eventually becoming indistinguishable from the ambient environmental flow. This type of modified-Rankine vortex was first applied to the hurricane vortex by Deppermann (1947), who noted that outside the RMW,

$$Vr^{-1} = C \tag{1.1}$$

where V is gradient wind, r is the distance from storm center, and C is a constant. Inside the RMW,

$$Vr = C \tag{1.2}$$

describes the flow, which is in effective solid-body rotation (and C is a different constant). Due to frictional dissipation of cyclonic angular momentum (see [1.14] below) as air converges inward in the boundary layer, (1.2) was modified to

$$Vr^x = C \tag{1.3}$$

by Gray and Shea (1973). They determined x empirically from wind observations to lie between 0.4 and 0.6. Using an empirical, parametric fit and the gradient wind relationship, Holland (1980) developed relationships for RMW (R_w) and maximum wind (V_m),

$$R_w = A^{\frac{1}{B}}, \text{ and} \tag{1.4}$$

$$V_m = \left(\frac{B}{\rho \times e}\right)^{\frac{1}{2}} \left(p_n - p_c\right)^{\frac{1}{2}}, \tag{1.5}$$

where A and B are climatological scaling parameters based on maximum wind, p_n is an ambient pressure value (in practice taken as the value of the first anticyclonically curved isobar), p_c is the central pressure of the vortex, ρ is the air density (assumed to be 1.15 kg m^{-3}), and e is the base of natural logarithms. The formulation for R_w is advantageous because it does not depend on ambient or central pressure values. Holland (1980) fit these equations to data observed in severe cyclone Tracy (1974) and noted that, while sensitive to the choice of A and B (Holland chose $A = 23$ and $B = 1.5$), radial values of both pressure and wind could be accurately estimated. This study was the first of many subsequent attempts to empirically calculate radially-varying parameters in the TC vortex (e.g., Large and Pond 1982; Emanuel 1986; Emanuel 1995; Andreas and Emanuel 2001; Emanuel 2003a; Makin 2005).

1.3.4. TC primitive equations

It is useful to define a set of equations, in cylindrical coordinates (r, λ, z) whose origin is the center of a stationary TC, that govern the flow and energetics of a mature TC. We start first with the r and λ components of the equations of motion,

$$\frac{\partial v}{\partial t}+u\frac{\partial v}{\partial r}+v\frac{\partial v}{\partial \lambda}+w\frac{\partial v}{\partial z}+fu+\frac{uv}{r}=-\frac{1}{\rho r}\frac{\partial p}{\partial \lambda}+\frac{1}{\rho}\frac{\partial \tau_{z\lambda}}{\partial z}+F_{H\lambda} \tag{1.6}$$

$$\frac{\partial u}{\partial t}+u\frac{\partial u}{\partial r}+v\frac{\partial u}{\partial \lambda}+w\frac{\partial u}{\partial z}-fv-\frac{v^2}{r}=-\frac{1}{\rho r}\frac{\partial p}{\partial \lambda}+\frac{1}{\rho}\frac{\partial \tau_{zr}}{\partial z}+F_{Hr}\,, \tag{1.7}$$

Here u is the radial velocity component dr / dt , v is the tangential velocity component $r\, d\lambda / dt$, w is the vertical velocity component, f is the Coriolis parameter, ρ is the air density, $\tau_{z\lambda}$ and τ_{zr} are the tangential and radial stresses due to small-scale vertical momentum mixing, and $F_{H\lambda}$ and F_{Hr} are the tangential and radial components of horizontal mixing. The vertical component (w) of the equation of motion can be expressed as

$$\frac{dw}{dt}=-\frac{1}{\rho}\frac{\partial p}{\partial z}-g+F_z \tag{1.8}$$

Where p is the air pressure, g the acceleration due to gravity, and F_z is a summary term representing forces associated with precipitation particle drag and turbulent mixing and terms involving the vertical Coriolis component have been omitted. Because dw / dt, F_z, and the Coriolis terms (not shown) are typically three to four orders of magnitude less than the vertical pressure gradient force, it is possible to approximate (1.8) hydrostatically, as

$$\frac{\partial p}{\partial z} = -\rho g \,, \tag{1.9}$$

while noting that vertical motions in hurricanes are produced by imbalances between the right-hand terms in (1.8). To complete the system, we add the full continuity equation,

$$\frac{\partial \rho}{\partial t} + \frac{\partial \rho r u}{r \partial r} + \frac{\partial \rho v}{r \partial \lambda} + \frac{\partial \rho w}{\partial z} = 0 \,, \tag{1.10}$$

where the changes of density of dry air are related to horizontal and vertical advection; the first law of thermodynamics expressed in terms of temperature (*T*),

$$\frac{\partial T}{\partial t} = -u\frac{\partial T}{\partial r} - \frac{v}{r}\frac{\partial T}{\partial \lambda} - w\frac{\partial T}{\partial z} - \frac{\omega}{\rho c_p} + \frac{Q}{c_p} - \frac{1}{\rho c_p}\frac{\partial H_s}{\partial z} + F_{HT} \;, \tag{1.11}$$

where $\omega = dp \,/\, dt$, Q is the diabatic heating rate, H_s the vertical heat flux due to turbulent eddies, c_p is the specific heat capacity at constant pressure, and F_{HT} represents horizontal mixing due to turbulence; and the continuity equation for water vapor,

$$\frac{\partial q}{\partial t} = -u\frac{\partial q}{\partial r} - \frac{v}{r}\frac{\partial q}{\partial \lambda} - w\frac{\partial q}{\partial z} - C - \frac{1}{\rho}\frac{\partial H_q}{\partial z} + F_{Hq} \,, \tag{1.12}$$

where q is the specific humidity, C the condensation (evaporation) rate, H_q the vertical flux of water vapor, and F_{Hq} the effect of horizontal mixing of water vapor. These equations, along with the equation of state for dry air (where R is the universal gas constant),

$$p = \rho R T \;, \tag{1.13}$$

complete a system of primitive equations that adequately describes the essential dynamical and moist thermodynamical processes of the TC (Anthes 1982). It is also helpful to define two conserved quantities: absolute angular momentum, M, and specific entropy, s. Angular momentum is conserved following axisymmetric displacement of air parcels and is defined as

$$M = rV + \frac{1}{2} fr^2 \tag{1.14}$$

where r is radial distance from center, V tangential velocity, and f the Coriolis parameter. In strong TCs, M decreases inward and upward and has very strong eyewall gradients. Entropy, which reaches its maximum value at the radius of maximum wind in the eyewall, is defined as

$$s \approx c_p \ln(T) - R_d \ln(p) + \frac{L_v q}{T} - qR_v \ln(H)\,, \tag{1.15}$$

where R_d and R_v are the gas constants for dry air and water vapor, H is the relative humidity, L_v is the latent heat of vaporization, and q the concentration of water vapor.

1.4. TC boundary layer

Only since 1997, after the installation of global positioning systems (GPS) technology on dropsondes released from Atlantic hurricane reconnaissance, has a complete and accurate picture of the TC boundary layer been possible (Powell et al. 2003). Earlier studies, such as the one reported by Large and Pond (1981), were performed in low-wind environments, and earlier non-GPS-equipped dropsonde measurements from Atlantic hurricane reconnaissance were unreliable in the lowest 500 m.

The momentum transfer coefficient, C_D, has been theorized to depend on sea-surface roughness length, surface wind speed, and wave spectral properties such as age, steepness, and directional component (Charnock 1955). From 1997-1999, in the CBLAST ocean-atmosphere experiment, 331 wind profiles were measured in hurricane eyewalls in the North Atlantic and central and eastern North Pacific basins. Typical dropsonde fall speeds ranged from 10-15 m s^{-1}, and measurements were taken every 0.5 s (for vertical resolution between 20 and 30 m). Wind speed accuracies are typically within 0.5-2.0 m s^{-1}, with a height accuracy of 2 m. The drag coefficients C_D and C_K were computed from (1.24) and (1.25) after roughness height, z_0, and friction velocity, u_*, were determined by fitting a least-squares line to determine the logarithmic slope and intercept. The data revealed that u_* increases with U_{10} up to 40 m s^{-1}, then levels off, while z_0 and C_D increases as U_{10} approaches hurricane force (33 m s^{-1}). For U_{10} less than 40 m s^{-1}, the surface parameters behave very similar to that described by Large and Pond (1981). The most remarkable result was a large decrease in both z_0 and C_D when U_{10} greater than 40 m s^{-1}. None of the previous investigations had indicated that type of response in the high wind environment (Powell et al. 2003).

1.4.1. Boundary layer energetics

Early theoretical and numerical studies of TC energetics (e.g., Charney and Eliassen 1964; Ooyama 1969; Carrier et al. 1971; Anthes 1972) relied heavily on pre-existing environmental instability (with respect to saturated vertical perturbations of surface parcels) to provide buoyancy and energy for the developing tropical disturbance. Charney and Eliassen (1964) term this energy source “conditional instability of the second kind” (CISK), given to denote the perceived synergistic cooperation between the cumulus convective processes and the larger-scale tropical circulation. Unsatisfied with this theory of TC energy production (and coincident with Rosenthal's [1978] successful numerical simulation of a mature, intense TC while accidentally forgetting to turn on the cumulus parameterization), Emanuel (1986) and Rotunno and Emanuel (1987) re-examined the energetics of tropical cyclones. They questioned whether the ascending boundary layer air in a numerical model is able to sufficiently penetrate to altitudes observed in TCs in presence of dry entrainment. Following the hypothesis of Riehl (1954), Emanuel (1986) and Rotunno and Emanuel (1987) proposed that the flux of latent heat from the sea surface, not the presence of ambient environmental instability, was essential to TC intensification. They also noted that the CISK mechanism of Charney and Eliassen (1964) is a linear instability: moisture convergence in the boundary layer of a balanced vortex supports cumulus convection. They questioned the existence of this type of linear instability in nature, noting that while some convective available potential energy (CAPE) certainly exists for saturated tropical parcel ascent, the ability to realize this potential energy is uncertain. They theorized that if CISK was truly the favored energetic mechanism in the tropics, then weak cyclones should be "ubiquitous" and "not confined to maritime environment" (Emanuel 1986). Emanuel (1986) proposes a new type of "air-sea instability", whereby TCs are "developed and maintained against dissipation *entirely* [his emphasis] by self-induced anomalous fluxes of moist enthalpy from the sea surface with virtually no contribution from preexisting CAPE." This requires a pre-existing finite amplitude disturbance, which is in agreement with the observational findings of Gray (1968) and Riehl (1954). This newly described instability requires on three gradients: the temperature gradients that drive the circulation, the radial gradients of sea-air transfer of heat, and the gradients of surface wind speed. Heat acquired from the sea surface is redistributed vertically by cumulus convection in a manner that maintains the neutrally stable environment (with respect to slantwise moist convection) and is consistent with the hypothesis of quasi-equilibrium of Arakawa and Schubert (1974). Thus, the ambient tropical environment can be taken to be convectively neutral, and therefore, kinetic energy is generated from in situ CAPE generation rather than from ambient CAPE.

1.4.2. TC as a Carnot engine

Heat transfer from the ocean is the basic source of energy for the tropical cyclone (Riehl 1950; Kleinschmidt 1951). The mature, steady TC can be considered as a simple Carnot heat engine, where axisymmetric inflow air in the boundary layer acquires moist entropy from the sea surface, rises, and releases latent heat at the much lower temperature of the upper troposphere (Emanuel 1986; Lighthill 1998). This net heating is used to do work against frictional dissipation, and also to change the angular momentum back to its ambient value at large outflow radii. As air spirals inward toward the low pressure center, its pressure drops and its entropy, s, increases due to both frictional dissipation of kinetic energy and evaporative enthalpy transfer from the ocean surface. This frictional kinetic energy destruction is the most important sink of momentum in the TC (Emanuel 2003a). The inward, convergent leg is approximately isothermal. Once parcels reach the eyewall, they rise adiabatically, following surfaces of constant angular momentum and entropy. The upper-level outflow then releases entropy by radiating to space during the isothermal compression leg of the cycle. The

Carnot engine is closed as air on the perimeter of the TC descends and warms adiabatically (Bister and Emanuel 1998). This cycle explains why the TC is a tropical phenomenon: energy production is dependent on the concentration of water vapor under saturated conditions, which increases exponentially with temperature, but there is no temperature dependence in the energy dissipation rate (Lighthill 1998).

1.4.3. Boundary layer structure

Emanuel (1986) divides the tropical cyclone boundary into three regions: the innermost region that extends from the storm center out to the inner side of the eye wall; the middle region that extends from the inner eye wall out to the radius of maximum winds; and an outer region that extends from the radius of maximum winds out to an outer radius (typically the outermost closed isobar). In the innermost region, the air is unsaturated and mechanically maintained by inflow outside the eye. The middle region is saturated and is the only region with significant cyclone-scale vertical velocity, and saturation is maintained by lack of entrainment of low equivalent potential temperature (θ_e) air from aloft. The outer region has little Ekman (frictional) turning, and thus its mean vertical velocity is small. This is the region that is characterized by vigorous turbulent exchange of θ_e through the top of the boundary layer by entrainment and unsaturated downdrafts. The total energy flux through the sea surface (sensible and latent) is offset mostly by these turbulent θ_e exchanges rather than by horizontal advection. Thus, the TC boundary-layer energetics can be effectively summarized in a three-part process (Lighthill 1998):

(a) transfer of water vapor from ocean to atmosphere, allowing for saturated deep convection in the eyewall and energy transport to the upper troposphere,

(b) sensible heat transfer from ocean to atmosphere that keeps their temperatures remarkably equivalent, and

(c) transfer of mechanical momentum from air to ocean (associated with frictional resistance to surface winds).

1.4.4. Boundary layer equations

The cycle of heat energy input and kinetic energy dissipation in the TC is known as air-sea transfer (Emanuel 1986; Andreas and Emanuel 2001; Emanuel 2003a). A droplet of seawater lofted into sea spray by surface wind stress need only lose 1% of its mass to evaporation to drop its temperature back to the wet bulb temperature. When it returns to the sea surface (cooler than when it left), it has effectively transferred enthalpy from the sea to the atmosphere. As surface wind speeds increase, the quantity of re-entrant sea spray also increases, thus giving rise to a positive feedback whereby stronger surface winds increase enthalpy transfer. It is convenient to define bulk transfer formulae for momentum (F_m) and enthalpy (F_k),

$$F_m = -C_D \rho |V| V \tag{1.16}$$

$$F_k = C_K \rho |V| \left(k_0^* - k\right), \tag{1.17}$$

where V is the near-surface wind, ρ is the air density, k is the specific enthalpy of air just above the surface, k_0^* is the enthalpy of air in contact with the ocean (which is assumed to take the same temperature as the ocean and be saturated with water vapor), and C_D and C_K are the dimensionless transfer coefficients of momentum and enthalpy discussed earlier.

Using these basic definitions, a fundamental and highly important relationship between the transfer coefficients and maximum surface wind can now be developed (see Bister and Emanuel 1998). By taking the vertically-integrated net dissipative heating, D, of the boundary layer,

$$D = 2\pi \int_a^b C_K \rho |\mathbf{V}|^3 r dr, \tag{1.18}$$

where $\mathbf{V}$ is the velocity vector, a and b represent the bottom and top of the boundary layer, respectively, and equating it to the net production of mechanical energy, P, from the ascending Carnot leg,

$$P = 2\pi \frac{T_S - T_0}{T_S} \int_a^b \left[C_K \rho |\mathbf{V}| \left(k_0^* - k \right) + C_D \rho |\mathbf{V}|^3 \right] r dr, \tag{1.19}$$

where T_s is the SST and T_0 is the mean temperature of the upper-level outflow, we can arrive at an approximate expression for maximum surface wind speed, $V_{\max}$ (Bister and Emanuel 1998),

$$|V_{\max}|^2 \approx \frac{C_K}{C_D} \frac{T_S - T_0}{T_0} \left(k_0^* - k \right). \tag{1.20}$$

The first term is the ratio of transfer coefficients, which Bister and Emanuel (1998) and Emanuel (2003a) assumed to be unity "for lack of better information." The middle thermodynamic efficiency term has outflow temperature as the denominator (instead of inflow temperature), which reflects the additional contribution from dissipative heating. The final term represents a measure of thermodynamic disequilibrium between the ocean and atmosphere, which allows for convective heat transfer to occur. If $|\mathbf{V}|$ is approximated as V, (1.20) represents a system where enthalpy is added to the system at the high temperature of the ocean surface and removed at the low temperature of the outflow at the tropopause (Emanuel 2004).

Powell et al. (2003) reported, for the first time, accurate measurements of the lowest 10 -200 m of the hurricane boundary layer (see Fig. 1.3). They found that the wind speed u increases logarithmically with height z, and concluded the "log-wind profile" was appropriate in the lowest levels, where u at height z is given by

$$u_z = \frac{u_*}{\kappa} \ln \frac{z}{z_0}, \tag{1.21}$$

where u_* is the friction velocity (defined as the square root of the horizontal stress τ divided by the air density ρ), κ is the von Karman constant (typically of value 0.4), and z_0 is the roughness parameter, defined by Charnock (1955) as

$$z_0 = z_* \frac{u_*^2}{g}, \tag{1.22}$$

where z_* is the Charnock constant (approximately 0.07 over the open ocean; Smith 1980) and g is the acceleration due to gravity. In the near-surface region of the atmospheric boundary layer, the distribution of stress, τ, does not vary with height and is equivalent to the friction velocity squared,

$$\tau \equiv -\rho_a \overline{u'w'} = u_*^2, \tag{1.23}$$

where $-\overline{u'w'}$ is the turbulent flux of momentum. The 10 m drag coefficient can then be represented, under neutral stability conditions, as

$$C_{D_{10}} = \frac{\tau_S}{\rho_a U_{10}^2} = \left(\frac{u_*}{U_{10}} \right)^2, \tag{1.24}$$

where u_* is the friction velocity and U_{10} is the 10 m wind speed that would be observed with neutral stratification.

1.4.5. Drag coefficient parameterization

Many different parameterizations for the drag coefficient, C_D, have been developed over the past fifty years. Fig. 1.4 shows the variation of C_D with 10 m wind speed for seven previous studies: Palmen and Riehl (1954), Miller (1965), Hawkins and Rubsam (1968), Amorocho and Devries (1980), Large and Pond (1981), Shay (1999), and Makin (2005). While each study, except Amorocho and Devries (1980), shows at least some monotonic increase in C_D with increasing velocity, only one study, Makin (2005), which is based upon the Powell et al. (2003) observational data, has an inflection point and subsequent decrease of C_D with increasing velocity (see Fig. 1.4). The most commonly-used parameterization of C_D was developed by Large and Pond (1981):

$$10^3 C_{D_{10}} = \begin{cases} 1.2 & \text{for } 4 \le U_{10} \le 11 \text{ m s}^{-1} \\ 0.49 + 0.065 U_{10} & \text{for } 11 \text{m s}^{-1} \le U_{10} \end{cases} \tag{1.25}$$

Several hundred over-land and over-water observations, taken from the Bedford Tower experiment and the CCGS *Quadra* and reported by Pond and Large (1978) and Large (1979), were used to arrive at this formulation. It is valid for neutral stability conditions, which are typical of the high-wind environment of the hurricane boundary layer (Andreas 1998).

1.4.6. Resistance law for the sea surface

A possible explanation for the somewhat surprising reduction of z_0 and C_D for U_{10} greater than 40 m s^{-1} (Fig. 1.5) is the generation of large patches of sea foam generated as steep wind-waves break and are sheared off in the high-wind environment of the TC eyewall (Emanuel 2004; Powell et al. 2003). This foam acts as an emulsion layer, creating a slip surface at the air-sea interface. Using the observational evidence reported in Powell et al. (2003), the wind profile in the suspension layer (Makin 2005) can be represented as (1.21), where the roughness length, z_0, is given by

$$z_0 = c_l^{(1-1/\omega)} c_{z_0}^{1/\omega} \frac{u_*^2}{g}, \tag{1.26}$$

where c_l is a constant (of whose value, 10, z_0 is not overly sensitive to), c_{z_0} is the Charnock constant (0.01), g is the gravitational acceleration 10 m s^{-1}, and ω is a positive relation defined as

$$\omega = \min\left(1, \frac{a_{\mathrm{cr}}}{\kappa u_*}\right), \tag{1.27}$$

where a_{cr} is the critical terminal droplet fall speed, calculated to be 0.64 m s^{-1}. This speed corresponds to a droplet radius of about 80 μm (Makin 2005). Using (1.24), (1.26), and (1.27), the resistance law at hurricane wind speeds for the sea surface at saturation can be written as

$$C_{D_z} = \frac{u_*^2}{u_z^2} = \kappa^2 \left[\ln \frac{z}{z_0}\right]^{-2}. \tag{1.28}$$

This resistance law provides a reasonable fit to the observational data analyzed by Powell et al. (2003) (see Fig. 1.5).

1.4.7. Numerical simulations with varying drag coefficients

While Atlantic basin track forecasts have shown steady annual improvements since the 1950s, hurricane intensity forecasts have been much more problematic, showing little significant improvement over the past 15 years (Krishnamurti et al. 2005) even as numerical models and observational techniques and spatial coverage have continued to rapidly advance (Aberson 2001). Several numerical simulations (e.g., Bao et al. 2000; Wang et al. 2000; Andreas and Emanuel 2001) found that hurricane simulations are very sensitive to the parameterization of air-sea fluxes at high wind speeds. They also found that simulated TCs depended on the ratio of the transfer coefficients, and that a ratio higher than unity yielded a more intense TC. However, the formulation and treatment of transfer coefficients for heat and momentum at high wind speeds remains highly uncertain (Chen and Surgi 2002). Thus, the question remains to investigate numerical model sensitivity to the observationally-representative drag coefficient formulation of Makin (2005).

1.5. Summary of current TC track forecasting methods

1.5.1. Trends in TC track forecasting in the Atlantic

Tropical cyclone (TC) track forecasts in the Atlantic basin have steadily improved over the last 30 years. Franklin et al. (2003), updating the work of McAdie and Lawrence (2000), found that position errors in the National Hurricane Center's (NHC) official track forecasts for the Atlantic basin decreased at an average annual rate of 1.3%, 1.9%, and 2.0% at 24, 48, and 72 h, respectively, from 1970 to 2001. However, in contrast to the basin-wide track forecast improvements, forecasts of landfall location for TCs approaching the U.S. coastline have not improved significantly since 1976 (Powell and Aberson 2001). Powell and Aberson (2001) attribute this lack of significant improvement in part to a "conservative, least-regret" forecast philosophy.

Over this same period, global and regional numerical weather prediction (NWP) models have become much more skillful (Shuman 1989; Kalnay et al. 1990; Caplan et al. 1997; Bender and Ginis 2000; Aberson 2001), and several NWP models designed specifically for TC prediction have been introduced, including the NOAA GFDL model (Kurihara et al. 1993, 1995, 1998; Bender et al. 1993) and the Florida State University "multimodel superensemble" (Krishnamurti et al. 1999; 2000a,b; 2001). Recently developed statistical techniques, such as the Self-Adapting Analog Ensemble prediction method (Sievers et al. 2000; Fraedrich et al. 2003) and the simple consensus forecasts and ensemble averages determined from multiple NWP models (Goerss 2000; Goerss et al. 2004) also have produced TC track forecasts superior to the individual model components. Because track forecasts from global and regional NWP models have improved so much in the last decade (Weber 2003), they now are used operationally by forecasters at the Tropical Prediction Center (TPC) in Miami and the Joint Typhoon Warning Center (JTWC) in Pearl Harbor (Goerss 2000). Much of the steady reduction in TC official track errors therefore appears to have resulted from an increased reliance upon improved NWP model forecasts (Sheets 1990; McAdie and Lawrence 2000).

1.5.2. Continued role of climatology in TC track forecasting

One of the consequences of the rapid advance of dynamical models has been a relative decline in the improvement, development, and operational use of statistical-climatological prediction schemes (Bessafi et al. 2002). However, it will be argued here that these climatology-based models still have and should continue to have a role to play in TC track prediction. For example, they can be used to: (1) provide a convenient reference from which to assess the performance of NWP model predictions (Neumann and Pelissier 1981a; Aberson 2001); (2) evaluate forecast difficulty of particular storms and TC basins (Franklin et al. 2003; Goerss et al. 2004); (3) conveniently generate bogus TC tracks (Bessafi et al. 2002); (4) provide very early TC track, speed, and heading forecasts in all localities of a basin (Neumann and Pelissier 1981b); and (5) provide an accurate forecast when departures from climatology and persistence are minor (Neumann and Hope 1972). Such statistical methods remain capable of providing rapid and valuable guidance with wide-ranging functionality. Therefore, one of the three major components of this dissertation research is to demonstrate the utility of a qualitative, climatology-based forecasting tool in predicting Hurricane Ivan's (2004) track through the southern Windward Islands.

1.5.3. Hurricane analog technique

The HURRAN (HURRicane ANlog) technique was developed by Charles J. Neumann and John R. Hope (1970) at the National Hurricane Center in 1969 in an attempt to take maximum advantage of past tracks of Atlantic hurricanes and tropical storms since 1886. It searched the climatology database, which contained tracks of all Atlantic tropical storms and hurricanes, to find storms with similar location, speed, and direction that occurred in a similar time of the year. The criteria used to select analog storms, specifically listed in Table 1.2, include geographical (2½-degree latitude circle around current storm), temporal (current storm within 15 days), and storm-motion-specific factors (direction within 15° and speed within 5 kt).

Once the analog storms were chosen, their tracks were re-centered to pass through the location of the current storm, and then probability ellipses were calculated based on the tracks of these analog storms. HURRAN often yielded accurate predictions for storms tracking south of 25°N (i.e., when the storm was located in a region of persistent synoptic steering), but because it included no information about the surrounding synoptic environment, HURRAN did not perform well in predicting the tracks of storms when recurvature was either imminent or occurring. If fewer than five storms existed in the historical record for a specific region in the basin, HURRAN would be unable to produce an analog forecast in real-time. To improve the technique, the authors proposed adding current synoptic information, either summarily through a previous motion vector or through raw observational data. HURRAN is not presently operational at the National Hurricane Center.

1.5.4. Climatology and persistence

CLIPER (CLImatology and PERsistence, Neumann 1972, Neumann and Leftwich 1977) is a substantial improvement over HURRAN because it combines current synoptic information with historical climatology data. It is composed of a set of regression equations that predict future east-west (zonal) and north-south (meridional) movements of a tropical cyclone at intervals out to 120 hours. The predictors include current and 12-h previous storm motion, current and 12-h previous storm position, surface wind speed, and day of the year. The most important predictor in CLIPER is persistence, which is contained in the initial motion of the storm. The equations were developed from a training data set of historical storm track data for all storms in the Atlantic basin from 1931 – 1970 that persisted for at least five days.

One of the most important present-day uses for CLIPER is to assess the skill of both operational forecasts and forecasts produced by more complex numerical models.

Forecasts whose errors are lower than CLIPER are said to show skill relative to CLIPER. Additionally, comparing CLIPER errors from year to year is a way to diagnose the difficulty of a particular season. A season with high CLIPER errors is considered a difficult forecast season.

McAdie and Lawrence (2000) used CLIPER in their inter-annual comparison of operational forecast errors from 1970 to 1998. Because the data from that 29-year period is inhomogeneous (i.e., it contains both “easy” and “difficult” forecast seasons), it needs to be standardized; otherwise, possible improvement trends may either be exaggerated or dampened. A group of relatively “easy” forecasts with many storms occurring in regions of the ocean with lower average errors (equatorward of 20°N) near the end of a period might incorrectly imply that forecast skill has increased. Thus, errors should be adjusted for yearly bias by subtracting the actual official forecast errors from forecast errors predicted from a linear regression using CLIPER as the sole predictor. The resulting adjusted errors can then be plotted with respect to time to determine any trends in forecast skill.

Because CLIPER is still used as a historical benchmark, its training data set has not been updated operationally beyond the original years used by Neumann (1931 – 1970). Aberson (1998) updated the CLIPER prognostic equations using a more recent 40-year data set (1956-1995). He found that the absolute errors of the updated version were less than 2% smaller than the old version and that the difference was not statistically different at a 90% confidence interval. The updated version of CLIPER did remove much of the bias found in the previous version: the 84-h bias of the updated version was comparable to the 24-h bias in the previous version. Regardless of which time period is used, however, conclusions based on this dataset are problematic because the historical record does not appear to be stationary (Barrett and Leslie 2005). Aberson (2001) noted this problem, but nonetheless concluded that the need for datasets large enough to develop a sufficient historical record necessitates using the available data.

1.5.5. Statistical-synoptic models

An inherent weakness with CLIPER and other purely statistical forecasting methods is the inability to forecast anomalous motion characteristics. Therefore, beginning with NHC73 and continuing into the present, the National Hurricane Center has used statistical-synoptic models to predict tropical cyclone tracks. Neumann and Lawrence (1975) found that most of a statistical tropical cyclone prediction model's variance reduction comes from three sources: (1) climatology and persistence, (2) steering of some type, and (3) intensity and position of the surrounding synoptic-scale features. Appropriately, these models combine climatology and persistence with weighted current and 24-h-old synoptic data, including 1000, 700, and 500-hPa height and wind analyses. The most recent statistical-synoptic model, NHC90, takes 24-, 36-, 48-, 72-, and 120-h forecast deep-layer-mean height analyses from the current NCEP global model and uses them as predictors to modify the CLIPER forecast.

1.5.6. Barotropic models

The science of forecasting tropical cyclone tracks changed dramatically in 1970 with the introduction of the Sanders barotropic (SANBAR, Sanders and Burpee 1968) model, the first operational primitive equation NWP track prediction model used by forecasters at the National Hurricane Center. The model used a very deep (1000–100 hPa flow) steering layer, and the motion of a synthetic vortex was forecast using the barotropic vorticity equation. The Moveable Fine Mesh model (MFM) further advanced the science of forecasting, using 10 vertical layers and employing a grid with 60-km horizontal spacing that moved with the storm. The Quasi-Lagrangian Model (QLM) was the first multi-nested high-resolution hurricane model with a semi-Lagrangian scheme. It employed more vertical levels (18), used a tighter horizontal grid resolution (40 km), and merged an idealized synthetic vortex in gradient balance with the large-scale analysis. The Beta and Advection (BAM) models (Holland 1983) incorporated the Global Spectral Model (GSM)'s wind forecast for a specific layer at the storm's location and constantly corrected the 1-h advection periods to account for Beta drift. The VICBAR (DeMaria et al. 1992) model forecasted the 850-200-hPa deep-layer-mean flow with the boundary conditions from the NCEP GSM. This model merged a synthetic vortex that included the current motion vector with the environmental flow, unlike previous models that used synthetic voriticies without current motion vector information. The LBAR (Limited-area BARotropic, Horsfall et al. 1997) model is very similar to the VICBAR model, except that it is a spectral (sine transform) barotropic model whereas VICBAR is a cubic b-spline spectral nested barotropic model.

1.5.7. Optimal linear combination technique

Leslie and Fraedrich (1990), building on the work of Thompson (1977) and Fraedrich and Leslie (1987), predicted the horizontal (meridional and zonal) displacement components of a tropical cyclone center by linearly combining two forecast displacements: the Australian NWP Model and CLIPER scheme. The coefficients of the predictor equations were obtained by applying standard multiple linear regression techniques to over 50 tropical cyclone "best" tracks observed from the 1979/80 to the 1983/84 seasons. The authors found that the combination method had lower mean errors at each forecast lead-time (12, 24, 36, and 48 hours) than any other available stand-alone method.

1.5.8. Self-adapting analog ensemble predictions

Sievers et al. (2000) created an analog forecast scheme that is self-adapting. They extended the approach of Fraedrich and Ruckert (1998), who "developed a method that iteratively reduces a user-defined forecast error by suitably fitting metric weights for the components of the reconstructed states entering the analog scheme". This analog scheme adapts itself to minimize error (i.e., it achieves an optimal prediction) in the dependent dataset. First, they reconstructed the state space and defined the error measure to use. Second, they evaluated the analog forecast scheme by defining a metric of observed minus analog which, together with the first step, forms the basis for the analog forecast. Third, they improved the scheme by using a learning rule that optimizes the weights for each component of the metric. Finally, they iterated the learning rule 400 times and chose the weights which optimized the metric. After the model-building process, independent ensemble mean forecasts (of *N* members) were made and compared with the best adapted analog (*N* =1) and the CLIPER reference model. The optimal ensemble size, reached "when the corresponding self-adapting scheme achieves the best performance within the verification dataset" (Sievers et al. 2000), was *N* = 18 for the Atlantic and *N* = 22 for the east Pacific. They used twenty phase-space components for the analog model: latitude and longitude at 0 hours and the previous four 6-h forecasts (time = -6, -12, -18, and -24 hours), 6-h change in latitude and longitude between each dimension (time = -6 to 0 hours, -12 to -6 hours, etc.), Julian date, and maximum sustained surface wind speed.

1.5.9. Global and mesoscale general circulation models

The NOAA/National Centers for Environmental Prediction (NCEP) Global Forecast System (GFS) model (Lord 1993), the Geophysical Fluid Dynamics Laboratory (GFDL) model (Bender et al. 1993) which replaced the QLM as the operational baroclinic dynamic hurricane model, the United Kingdom Meteorological Office (UKMet) model (Radford 1994), the Navy Operational Global Atmospheric Prediction System (NOGAPS) model (Hogan and Rosmond 1991), and the European Centre for Medium-Range Weather Forecasts (ECMWF) model are widely used by forecasters to examine the evolving mass fields to produce long-range forecasts. These purely dynamical models range from mesoscale to global in coverage and are run operationally at various national centers. Their handling of the synthetic vortex varies. The European Centre for Medium-Range Weather Forecasts (ECMWF) model does not presently use synthetic data to represent the tropical cyclone vortex, while other national centers initialize the vortex with synthetic observations. These models have provided great advances in the science of tropical cyclone track forecasting. Besides the ability to combine the individual forecasts into an ensemble as shown by Goerss (2000), forecasters are able to observe the evolution of the height and mass fields with time.

1.5.10. Dynamical ensemble techniques

Building upon the work of Leslie and Fraedrich (1990), Goerss (2000) demonstrated that a joint ensemble of independent tropical cyclone track forecasts were more accurate, on average, than the individual model forecasts. The ensemble technique was tested on tropical cyclones in the Atlantic basin in 1995-1996; improvements were, with respect to the best individual model, 16% at 24 hours, 20% at 48 hours, and 23% at 72 hours. Furthermore, the standard deviation of the forecast error was reduced by the joint ensemble. Finally, Goerss noted that the spread of the ensemble forecast was useful to forecasters as a benchmark to improve confidence in the forecast.

1.6. TC circulation interaction with island terrain

TC behavior – structural change, intensification, and direction of motion – is directly affected by the surrounding environment. One of the most important interactions between the TC and its environment occurs at the interface between the TC vortex and any landmasses. As the TC approaches land, the underlying topography transforms from a mostly homogeneous water surface to a complex, varying, and sometimes quite mountainous land surface. The interaction between the TC vortex and the terrain is important because it impacts the future TC track, intensity, and rainfall distribution. The interaction also contributes to structural changes (Bender et al. 1987), including introducing asymmetries in the pattern of convection. In the case where the landmass is large or the TC is slow-moving, rapid weakening and transition from a tropical to an extratropical cyclone occurs.

The earth's topography, whether a small hill or large mountain, influences atmospheric motion. The case where the TC circulation interacts with mountainous island topography is particularly interesting. Such TCs have been observed to increase forward translation speed (Kintanar et al. 1974), deflect northward upon approach (Brand and Blelloch 1973 and Herbert 1980), rapidly decay (Hawkins 1983), and generate copious rainfall along windward slopes (Brunt 1968; Hope 1975). The TC vortex has even been observed to "jump" across an island, as lee-cyclogenesis associated with cross-mountain flow deepens a hydrostatic, secondary surface low center which then connects with the mid- and upper-level circulation to become the primary circulation (Chang 1982). Despite the observational records, "the interaction of a landfalling tropical cyclone (TC) with mesoscale topographic features is not well understood. Significant variations in wind, pressure, and precipitation distribution in TC's have been observed over mountainous regions" (Cangialosi and Chen 2005). This lack of understanding is highly problematic for small island nations, such as those in the southern Windward Islands in the eastern Caribbean Sea, as a track deflection of only tens of kilometers can mean the difference between tremendous destruction and only slight damage.

Previous numerical studies of the interaction between TCs and island orography have tended to cluster in several key areas: the Greater Antilles (Cuba, Hispaniola, Puerto Rico, and Jamaica), the Philippines, Taiwan, and Japan. TC genesis studies have examined the role of Papua New Guinea in the Gulf of Carpentaria and the East Coral Sea, and TC decay studies have examined the Sierra Madre and coastal Mexican mountain ranges. However, no recent studies using a high-resolution mesoscale model to simulate the orographic effects of the southern Windward Islands in the eastern Caribbean Sea on the TC circulation have been undertaken.

1.6.1. Early idealized simulations

One of the earliest idealized numerical studies of the interaction between a TC vortex and a hypothetical tropical mountain range was performed by Bender et al. (1985). They constructed a large (2000-km long) north-south coastal range with peak elevation of 1000 m and embedded a TC vortex in uniform 10 m s^{-1} easterly flow. The numerical simulations were multiply-nested, with a highest horizontal resolution of 20 km, and each model domain used a terrain-following σ-coordinate with 11 half-σ levels. As the TC approached the coast from the east, it deflected 50 km south (to the left) in its track and intensified 10 mb more than the control (no mountain) simulation. The coastal range was found to have induced a slight northerly flow component at mid- and upper-levels east of the mountain range, and this anomalous flow component is suspected to have caused the southward track deflection. The coastal range was also shown to reduce the low-level zonal easterly flow starting several hundred kilometers upstream. This reduction led to moisture convergence and increased environmental mixing ratios as the TC vortex approached, thus causing the 10 mb intensification prior to landfall.

1.6.2. Case study simulations

To try to relate their work to more realistic scenarios, Bender et al. (1987) built on their earlier (1985) theoretical simulations to instead include terrain forms that were semi-representative of three major tropical island groups: Taiwan, Luzon (in the Philippines), and the islands of Hispaniola, Puerto Rico, and Cuba. Those three island groups were chosen for several reasons: 1) they are annually threatened by landfalling TCs; 2) they are relatively large (and thus their mountain ranges were able to be relatively well-represented in the 20 km horizontal grid); and 3) they are mountainous. The Central Mountain Range (CMR) of Taiwan is aligned north-northeast to south-southwest, spans the length of the island, and is almost 4000 m at several locations in the north-central part of the island. Hispaniola and Puerto Rico each have peaks that exceed 1000 m, and Luzon's central mountains are over 1500 m at their highest point. Instead of developing an idealized TC vortex and embedding it in uniform zonal flow (as in the 1985 experiments), Bender et al. (1987) initialized historical cases of TCs that traversed the various island groups. In all cases, they found that the TCs' forward translational speeds increased as the TCs approached the mountainous islands (accelerated when compared to the no-terrain control simulations). For the case of Taiwan, whose orography resembles the earlier (1985) idealized simulations, the authors found a northward deflection in TC track, which agrees well with the earlier observational studies (Brand and Blelloch 1974 and Herbert 1980). They also found a southward deflection as TCs approached Luzon and Hispaniola, which matches well with the Bender et al. (1985) theoretical simulations.

1.6.3. TC interaction with Taiwan

Yeh and Elsberry (1993a,b) continued to examine the interaction between the TC vortex circulation and the orography of Taiwan. They examined 53 tracks of historical westward-moving TC approaches to Taiwan, and found that – in all cases – the TCs experienced an upstream acceleration prior to landfall on Taiwan, with along-track translational speed increases averaging 4.5 m s^{-1} (Yeh and Elsberry 1993a). However, they also conclude that this translational speed increase is more likely related to synoptic steering currents than to mesoscale effects from flow blockage due to the CMR. This became evident when they stratified the 53 TCs by intensity. The weaker storms (maximum rotational velocities less than 33 m s^{-1}) slowed upon approach, but the stronger storms continued to accelerate. They attributed this acceleration/deceleration pattern to the ability of stronger vorticies' ability to "resist development of asymmetric (secondary) circulations more so than the weak vortex" (Yeh and Elsberry 1993b).

Super Typhoon Herb's (1996) landfall in northern Taiwan and subsequent direct passage over the newly-installed WSR-88D (Weather Surveillance Radar 88-Doppler) radar in Ryukyu provided the most comprehensive assessment of the terrain-TC vortex interaction. Wang (1997) found Herb was "greatly modified" by the central mountain range (CMR) of Taiwan. As Herb approached the NE coast of Taiwan, a classical "trough-ridge-trough" pressure pattern developed across the island. Northwesterly flow passing through the Taiwan straight and impinging on the western coastline was gradually orographically lifted, resulting in a hydrostatically-induced trough on the windward slope. As flow encountered the steep CMR, a dynamically-induced ridge developed along the center mountains. Finally, as the flow quickly descended the leeward (eastward) side of the CMR, it turned almost at a right angle to the mountain and converged into Herb's center (with a very pronounced cross-isobaric component). This flow pattern resulted in both a hydrostatically-induced and a dynamically-induced lee-side trough (lower pressure as the descending air compressed and warmed and increased vorticity as the column deepened and stretched). As expected for this pattern, potential temperatures were observed to increase from 301 K in northwestern Taiwan to 318 K at the peak of the CMR to 304 K on the eastern side, indicative of moist ascent west of the CMR and dry descent to the east.

This classical "trough-ridge-trough" pattern (see Fig. 1.6) was well-simulated by Peng and Chang (2002) using a three-domain mesoscale model with 81, 27, and 9 km horizontal resolution, 30 vertical levels, and 1 km model terrain resolution. The complex sea level pressure and wind patterns they observed at 9 km reveals the high degree of spatial variability of a landfalling TC. Several observing station in the northern part of the island received very strong (greater than 50 m s^{-1}) winds, while other close by stations experienced much weaker flow. The rainfall pattern was equally complex, both in observations (Wang 1997) and simulations (Peng and Chang 2002). The windward slope – in this case the west- and northwest-facing CMR slopes, due to Herb's approach to the northern end of the island – received over 1000 mm of rainfall. Peng and Chang (2002) note that only the highest-resolution (9 km) simulated TC made landfall in northern Taiwan. This high degree of spatial complexity in the sea-level pressure, surface wind, and rainfall distribution patterns demonstrates the necessity of capturing the mesoscale effects to produce an accurate TC forecast.

1.6.4. Identifying patterns of TC interaction with island terrain

To summarize, mountainous island terrain was found to have the following mesoscale impacts on an approaching TC vortex: the generation of heavy orographic rainfall, an along-track acceleration and deflection of the TC vortex, and a modification of the TC intensity (stronger before landfall, weaker after landfall due to the stronger cross-isobaric [energy dissipating] flow). As demonstrated in several studies over the last 25 years, not all TCs experience all of these impacts. Shallow (scale height less than 6 km) and weak (maximum tangential wind less than 50 m s^{-1}) typhoons tend to follow "discontinuous tracks," where the vortex "jumps" across the island in response to secondary low formation on the lee (typically western) side. However, strong (maximum tangential wind greater than 50 m s^{-1}) and deep (scale height greater than 10 km) TCs tend to cross over the island and maintain a more continuous track becausethe main surface circulation is not blocked by the mountain.

1.6.5. Orographic parameters

Lin et al. (2002) developed and applied ten systematic "orographic parameters" to attempt to identify which TCs would experience track deflections and intensification. They found three such control parameters to be positively correlated with TC vortex continuity and along-track, pre-landfall deflection: (1) the vortex Froude number, V_{Fn},

$$V_{Fn} = \frac{V_{\max}}{Nh}, \tag{1.29}$$

where $V_{\max}$ is the maximum tangential wind velocity, N is the Brunt-Väisälä frequency, and h is the mountain height; (2) the ratio of vortex Froude number to the basic-flow Froude number (U / Nh), $R_{V_{Fn}/U_{Fn}}$,

$$R_{V_{Fn}/U_{Fn}} = \frac{V_{\max}}{U}, \tag{1.30}$$

where U is the background zonal flow (assumed to be perpendicular to the island terrain, and can be approximated by the westward vortex translational speed); and (3) the measure of inertial stability, I_{stab},

$$I_{\text{stab}} = \frac{V_{\max}}{Rf}, \tag{1.31}$$

where R is the radius of maximum tangential wind velocity and f is the Coriolis parameter. The inertial stability parameter can be considered as a pseudo-Rossby number ($Ro = U / fL$), where the horizontal length scale L of the disturbance is approximated by the radius of maximum winds R of the TC. Lin et al. (2002) found that when all three parameters were large (greater than 1.6, 7.0, and 4.0, respectively), the TC vortex tended to maintain continuity, i.e., pass over the mountain range without experiencing any "jumps" from primary to secondary low centers. Physically, this means that when control parameters are large in value, air flow is able to go over the obstacle instead of being blocked and forced to go around. Also, when the vortex Froude number is larger than 1.6, the kinetic (rotational) energy associated with the impinging vortex is sufficient to lift the stratified flow up and over the orographic (potential energy) barrier. For pre-landfall, along-track TC track deflection, a large vortex Froude number implies that air parcels in the northwestern outer circulation (for a TC moving westward toward an island mountain) are able to pass more easily over the obstacle, which results in a northward deflection as the TC crosses the topography. When the vortex Froude number is small, more air parcels are blocked by the terrain (sometimes resulting in the development of a coastal barrier jet), which results in a southward track deflection (Lin et al. 2002).

1.6.6. Importance of investigating terrain-TC interactions

The peaks of southern Windward Islands are the first land obstacles to low-latitude, westward-moving Atlantic TCs. Averaging between 350 m and 1500 m high, these islands are prone to periodic TC passages (about every 5 yrs). According to the Liu et al. (2002) orographic parameters, TCs crossing these islands should maintain a continuous track (not experience any low pressure center "jumps") and should experience a slight northward track deflection upon approach. Using values for V_{max}, N, h, U, R, and f characteristic of Hurricane Ivan (50 m s^{-1}, .01 s^{-1}, 1000 m, 7 m s^{-1}, 150 km, and 5.5 x 10^{-5} s^{-1}, respectively), the vortex Froude number is 5.0, the ratio of vortex Froude number to the basic-flow Froude number is 7.1, and the inertial stability number is 6.0. However, the interaction between a passing TC circulation and the island topography has yet to be studied using a high-resolution numerical model, and the Lin et al. (2002) hypothesis needs to be tested for this region of the southern Caribbean. This dissertation does not continue researching the question posed above; it is left as an interesting exercise for the future.

Chapter 2. Climatological forecasting tool

For part one of this dissertation research, I have developed and employed a climatological tool that quickly and succinctly displays the spread of historical TC tracks for any point in the Atlantic Ocean basin. This investigation has two main objectives. First is to illustrate the continued operational usefulness, and therefore necessity, of statistical methods that rely largely or entirely upon the archived TC climate record. I show that large along-track trajectory (speed and direction) errors can be reduced when there is a strong climatological signal that has a small spread and is based on a large number of archived cases. Hurricane Ivan, which occurred during the 2004 Atlantic season, is an excellent recent example. Ivan was a classical long-lived, long-track major hurricane that was responsible for twenty-five deaths and over $14 billion in U.S. losses (Stewart 2005). It afforded the NWP models many opportunities to predict its track. However, trajectory forecasts from statistical methods based upon the climate record were significantly more accurate, over an eight-day period, than the tracks predicted by the NWP models. Ivan is an example that demonstrates powerfully that the NWP and official forecasts can have large trajectory errors when their predictions are significantly different from the tracks suggested by the climatological scheme used in this study

Second, this investigation reminds TC forecasters and other users of climate data of the continued utility of climatological data, especially when it provides an early means of alerting TC forecasters to NWP predictions that have potentially large track errors. This study and its conclusions are based on a wide range of input data. Over 500 forecasts from fourteen different operational NWP models and statistical prediction methods were examined, and over 400 historical Atlantic TC records were used to compute the climatological signal most relevant to Ivan. This climatological tool is useful in all parts of the basin because it is derived from prior storm motion trajectories and summarily captures information about the historical synoptic and mesoscale steering patterns. It will also display the strength of the climatological signal and allow for rapid qualitative comparison between the historical tracks and the more robust NWP models, thus demonstrating the continued utility of climatology in predicting TC tracks.

2.1. TC motion climatology

Associated with every geographical location in the North Atlantic basin is a TC "motion climatology" derived from the historical movement characteristics of all TCs that passed near it. A technique was developed for this study to calculate and display graphically the TC motion climatology. In brief, the Atlantic TC data set is used to compute motion tendencies (speeds and directions) of past TCs at or near a specified geographical point (Barrett et al. 2006). The focus here is on the 24-h motion climatology because this time period is critical for operational warning decisions (Sheets 1990). Other historical analog techniques, such as the hurricane analog (HURRAN) method of Hope and Neumann (1970) and the self-adapting ensembles of Sievers et al. (2000) and Fraedrich et al. (2003), generate forecasts by adapting entire tracks of any storm in the historical database. In contrast, my climatological technique focuses on individual motion characteristics of storms located within a specified geographical radius of influence (as defined below). Furthermore, unlike the widely used operational climatology and persistence model, known as CLIPER (Neumann 1972; Neumann et al. 1981b; Leslie et al. 1990), my system generates and displays probabilistic estimates of future 24-h TC trajectories rather than the single point forecasts produced by CLIPER. A short description of the dataset used to calculate the motion climatology is given in Section 2.2. The computational aspects of the motion climatology are discussed in Section 2.3.

2.2 Best track dataset

The so-called "best track" Atlantic hurricane dataset, described by Jarvinen et al. (1984) and updated annually by the NOAA Tropical Prediction Center, was used to compute the motion climatology statistics used in this study. The dataset uses all available surface, satellite, and aircraft reconnaissance observations – including those not accessible in real-time – to revise and refine the official post-storm estimates of TC position and intensity (Neumann and Pelissier 1981b). This dataset is a record of all TC activity in the Atlantic basin dating back to 1851. For this study, only the most recent (1970–2003) records are used in an attempt to maximize the stationarity of the dataset and minimize any discontinuities due to secular improvements in observing technology or changes in operational classification schemes (Landsea 1993; Landsea et al. 1996; Buckley et al. 2003; Barrett and Leslie 2005). The 1970-2003 period of the dataset provide three pieces of information critical to any TC climatology study: geographical location (latitude and longitude); temporal location (month, day, and year); and intensity (maximum sustained 1-min surface winds and minimum sea level pressure). These data are available four times daily (0000, 0600, 1200, and 1800 UTC) over the life of each TC. For a much more thorough discussion of the uses and limitations of best track datasets, refer to section 3.1.

2.3. The TC motion climatology prediction scheme

The motion climatology for a specified geographical point is calculated by first searching the best track dataset to find all TC records located within a prescribed distance, or "radius of influence" of that point (Barrett et al. 2004). The speed and direction vector components are computed directly from the great-circle distance (GCD) traveled by the TC in the 24-h period, that is,

$$\mathrm{GCD} = 111\cos^{-1}[\sin(\varphi_1)\sin(\varphi_2)+\cos(\varphi_1)\cos(\varphi_2)\cos(\lambda_2 - \lambda_1)] \tag{2.1}$$

where ($\varphi_{1,}\lambda_1$) and ($\varphi_{2,}\lambda_2$) are the initial and final latitudes and longitudes of the center of the TC.

Because each motion vector contains both a speed and a directional component, it is possible to divide the vectors into convenient radial "bins" of direction (in degrees) and speed (in knots). For this study, we divided the vector space into 180 bins: thirty-six radial categories, each ten degrees in azimuth, and five translational speed categories, each five knots in range. Each historical TC record can then be sorted into its corresponding radial sector and speed bins. These bin totals are converted into relative frequencies and displayed graphically in a format analogous to a probabilistic "wind rose". These relative frequencies, which range from 0.00 to 1.00, represent the historical mean 24-h trajectories for that specific geographical point. The calculations and graphics are computationally negligible, requiring about 2 seconds on a desktop PC. With just one program command, the climatological mean TC speed and heading information is available for any point in the Atlantic basin. Furthermore, because the technique is initialized using just the TC initial position, the prediction is available at the beginning of the forecast period, as there is no need to wait several hours for a numerical analysis.

2.4. Motion climatology interpretation

Hurricane Ivan was chosen from the 2004 TC season as a case study that clearly illustrated the potential errors in NWP model track forecasts when they differ repeatedly from the strong climatological signal calculated using the climatological scheme developed for this study. Ivan formed in the eastern tropical North Atlantic basin on September 3 and traveled west-northwest through the southern Windward Islands into the Caribbean Sea and Gulf of Mexico, eventually making landfall near Gulf Shores, Alabama on 16 September (Fig. 2.1) (Stewart 2005). From 0000 UTC on 5 September through 1200 UTC on 13 September, Ivan moved from the south-central Tropical North Atlantic Ocean, through the southern Windward Islands, to the western tip of Jamaica, reaching Category 5 (Simpson 1974) at its peak intensity. This eight-day period is of most interest to us for four reasons: (1) Ivan remained a well-organized, long-track hurricane (intense hurricane) for thirty (twenty-five) of the thirty-five forecast periods; (2) over 500 forecasts were generated by fourteen different operational prediction methods; (3) Ivan's westward motion was repeatedly, and consistently, under-forecast by almost every operational NWP model; and (4) the climatological signal in this part of the tropical Atlantic basin clearly indicated a preference for a continuing westward motion. In Fig. 2.2, the length of each radial sector corresponds to the probabilistic 24-h trajectory preferences of all TCs located within a radius of influence of the chosen location. The longer radial sectors denote preferred TC trajectories. In Fig. 2.2a-b, it is easily seen that approximately 80 percent of TCs comprising the climatology (the numbers of cases are 102 and 114, respectively) have directional headings in a small range between 270° and 295°. For comparison, the observed motion vector for Hurricane Ivan is superimposed onto the historical motion climatology. Note the remarkable agreement between Ivan and climatology in Fig. 2.2b, where the climatological signal is strong and has a narrow spread.

This type of climatological product has several key features. First, as discussed already, it quickly and simply displays the climate information relevant to each TC track. Second, it gives an indication of the variability of the synoptic steering flow. A strong, unimodal preference for westerly directional headings with average speeds of 11 to 20 kts is apparent in Figs. 2.2a-b. However, a more evenly distributed synoptic signal with westerly through northeasterly directional headings is present in Fig. 2.2c. Third, unlike many statistical methods such as CLP5 and A98E (see Table 2.1 for a complete description of each prediction method), this product does not specify a point forecast, but instead displays the spread of past TC trajectories.

As a consequence, the climatological scheme adds considerable value to a real-time forecasting setting. Because "tropical cyclone tracks tend to be repetitive and are associated with likewise repetitive synoptic patterns" (Bessafi et al. 2002), these climatological relative frequencies convey highly valuable probabilistic information to forecasters, especially so in the deep tropics where synoptic steering patterns tend to be more repetitive than in the subtropics and in basins where TC tracks are not as erratic (Pike and Neumann 1987).

2.5. NWP forecasts of Ivan

To assess Ivan's predictability, the performances of fourteen operational prediction methods initialized between 0000 UTC 4 September through 1200 UTC 12 September were evaluated: two statistical-climatological schemes, six NWP models, four limited-area barotropic models, and three ensembles of NWP models (see Table 2.1 for a summary of each prediction method). In addition, the TPC official ("OFCL") forecast was included. All the TC track forecasts were provided by the Hurricane Research Division (HRD) in Miami, FL and the Naval Research Laboratory (NRL) in Monterey, CA.

The 24-h forecast positions for each of the twelve non-statistical prediction methods were found to be consistently to the right (poleward) of Ivan's actual track (as indicated by positive trajectory errors in Table 2.2). The largest trajectory errors were associated with the dynamical models, namely the GFDL, UKMET, AVNO, and NOGAPS, and their ensemble forms (CONU, GUNS, and GUNA). During the eight-day period in early September, thirty-five forecasts were generated by each of the GFDL, AVNO and NOGAPS models, while sixteen forecasts were made by the UKMET model (see Fig. 2.3 for a representative sample of NWP track forecasts). The 24-hour mean trajectory errors from these models ranged from +4.0 to +6.3 degrees (positive values indicate poleward track biases). Each trajectory error was tested for statistical significance using a two-tailed student's t-test. Three null hypotheses, comparing the NWP forecasts to zero (no error), CLP5, and OFCL, were considered. A summary of the statistical *p* values is presented in Table 2.3. The null hypothesis required *p* values to be less than 0.005 to be rejected at the 99% confidence level. It was found that all of the dynamical model forecasts (GFDL, UKMET, AVNO, and NOGAPS) and their ensembles (CONU, GUNS, and GUNA) had a statistically significant right-of-track-bias (at the 99% confidence level). Furthermore, the OFCL forecast was also found to have a statistically significant right-of-track bias (also at the 99% confidence level).

In marked contrast, the two statistical-climatological methods examined in this study, A98E and CLP5, had much smaller mean trajectory errors than the dynamical models (Table 2.3), and the errors were *not* significant at the 99% confidence level. The error verifications revealed that these methods captured Ivan's preference for continued westward motion far better than the global and regional models. Moreover, the OFCL forecasts were found to be statistically different from both A98E and CLP5 (at a 99% confidence level), but not from AVNO, GFDL, NOGAPS, or UKMET models, or the three consensus models CONU, GUNA, and GUNS. This finding agrees well with Stewart (2005), who suggested that the OFCL forecasts relied heavily on the dynamical model forecasts rather than the climatological models.

2.6. Steering flow for IVAN

Stewart (2005) concluded that the right-of-track bias in the NWP models can be attributed largely to the models' premature erosion of the strong subtropical ridge in the mid-Atlantic. To examine the synoptic currents in the vicinity of Ivan, we calculated a deep-layer mean steering flow from the NCEP Reanalysis 2 dataset using a 7x7 box averaged over 850mb-200mb. The deep layer mean was used as it has been suggested that the deep layer mean is the most appropriate choice for the strongest storms (see, for example, Velden and Leslie 1991). This computation applied the trapezoidal rule to the 6-hourly values at 200, 250, 300, 400, 500, 600, 700, and 850 hPa. The resulting track forecast, which we refer to hereafter as "FLOW", is indicated in Fig. 2.3 by an open diamond. When Ivan was south of Hispaniola, the steering flow-based trajectory was more accurate than most NWP and consensus models. Unlike these models, FLOW did not exhibit a statistically significant right-of-track bias. However, its mean square trajectory errors were comparable to the NWP models, and it can be seen in Fig. 2.3 that the FLOW trajectory forecast was often left-of-track. This equatorward pattern of errors in the FLOW trajectory forecast reveals the strength of the synoptic scale ridge centered north of Ivan. Thus, the official forecast for Ivan, which relied heavily upon the NWP models instead of the statistical and climatological models, had significant right-of-track errors.

In addition to the above treatment of Ivan, we examined the steering flow for TC Lili, from the 2002 Atlantic season, in the same manner. Lili formed and tracked over a similar path to Ivan and also reached hurricane intensity. However, the NWP models did not exhibit the same right-of-track bias as for Ivan. With Lili, the GUNA dynamical ensemble and the official forecast both had smaller 24-h position errors (49 and 54 km, respectively) than the climatology model CLP5 (87 km; Lawrence 2002; Pasch et al. 2004). These findings, which are in contrast with those for Ivan, provide further support our advocating a return to weighting more heavily the predictions available from statistical and climatological methods, particularly when the climatological scheme consistently has a strong track prediction signal that differs from the NWP models and the number of cases making up the climatology is large.

2.7. Climatological tool conclusions

A consequence of the rapid advance of dynamical models has been a move away from the operational use of TC prediction schemes based on climatology and statistical methods. In this study, I showed that neglecting these methods is a strategy that is easily remedied. I devised a simple climatological scheme that provides graphical displays of climatological TC motion data in a quick and timely manner. When the climatological signal from the scheme is strong and has a small spread, deviations from the climatologically derived synoptic direction predictions, while still possible, are expected to be minimal. Conversely, when the signal is weak and has a large spread, the climatological scheme is not expected to be of much value, other than to suggest that additional care should be taken to examine the various components that comprise the resultant steering of the TC.

This case study examined here was TC Ivan, which reached hurricane intensity during the 2004 Atlantic season and caused significant loss of life and property in the southeast U.S. My focus here is on an earlier period when, as a consequence of the sustained poleward track errors from the NWP models and the official forecast, evacuation orders were issued for the Florida Keys at 1200 UTC on September 9. However, Ivan passed more than 450 km to the west of Key West, in the open Gulf of Mexico waters. The evacuation was initiated because twelve different NWP models consistently, and incorrectly, predicted a poleward motion component which was not observed as the TC traversed the tropical North Atlantic as far as western Cuba. This poleward bias was shown to be statistically significant for all of the dynamical models and for the official forecast at the 99% confidence level. These forecast errors contrast with the contradictory strong climatological signal that correctly indicated a more westward motion. The forecast errors in the NWP models have since been attributed to the premature erosion of the mid-Atlantic subtropical ridge by the NWP models. The official forecast exhibited the same right-of-track bias due to its very heavy reliance on the (inaccurate in this case) NWP model predictions. Not all the operational forecast systems had poleward biases, however. The climatology and persistence model, the statistical–dynamical model, and the deep-layer mean steering flow forecast did not exhibit significant poleward biases, and were found to have no directional bias at the 99% confidence level.

Hurricane Ivan is an example that shows how NWP and official forecasts can have large position errors when they are significantly different from the tracks produced by the climatological scheme used in this study. The best track historical record contains many other recent TCs in which the statistical-climatological methods outperform the NWP models for at least some part of the forecast period. Table 2.4 summarizes the error statistics for these TCs from the 2004 Atlantic season. Hurricane Emily of the 2005 Atlantic season was also examined, and she was found to be remarkably similar to Ivan in several aspects. In mid-July, Emily tracked across the eastern North Atlantic and into the southeastern Caribbean Sea. While Emily was east of the Windward Islands, from 10 July to 13 July, the suite of operational NWP track guidance models consistently predicted a northward motion component that did not develop. As with Ivan, the climatological signal for Emily indicated a strong preference for westward motion component, and it is noteworthy that again the TC followed the strong climatological signal and did not develop the northward motion component forecasted by the NWP guidance models.

In summary, TC Ivan has demonstrated that a greater role should be accorded to the statistical-climatological methods when a strong climatological signal conflicts with the NWP or other deterministic predictions. The simple tool used here provides a means of identifying TCs that are potentially difficult to forecast by the NWP models. If the computed climatological signal is persistent, has a small spread, and is supported by a large number of archived cases, then our study demonstrates that the operational statistical-climatological schemes are potentially at least as accurate as the dynamical methods.

Chapter 3. TC activity and geophysical variability

For the second part of this dissertation, I investigated the relationships between TC activity and several leading modes of atmospheric and oceanic variability. The primary objective of this section is to demonstrate understanding of the role of TCs in the earth-atmosphere system on multiple spatial and temporal scales. To accomplish this goal, I examined the relationships between the number, periodicity, and frequency of seasonal TC activity and monthly, seasonal, annual, interannual, and decadal climatic indices. TCs are fundamentally connected to both the atmospheric and oceanic general circulation (Chan 2005), and thus it is reasonable to expect the dominant modes of tropical and extratropical atmospheric and oceanic variability to have detectable effects on TC activity. Therefore, one of the major goals of this dissertation is to research and systematically quantify the relationships between TC activity and the dominant modes of climatic variability.

TCs affect the livelihoods of billions of people and trillions of dollars in economic activity. Because they are essentially unpredictable on timescales beyond a few days, there is great interest in developing knowledge of the climate factors which control interseasonal, interannual, and interdecadal fluctuations in TC activity (Bell and Chelliah 2006). The "dominant modes of atmospheric and oceanic variability," which will be defined extensively in section 3.5, are determined through several methods. Some modes represent the first principal components of analyses of SST, geopotential height, or sea level pressure. Others are identified as peaks in the power spectra of wavelet analyses of the same variables. Regardless of how the modes are determined, however, it is well known that their impacts are not limited regionally and span timescales from several months to several decades (Li et al. 2007). Through teleconnections with Rossby, Kelvin, and gravity waves, these modes reach into every hemisphere, continent, and ocean, and they impact temperature, precipitation, pressure, and circulation (Johansson 2007; Alford and Zhao 2007).

Atmospheric datasets, including the NCEP/NCAR global reanalysis (Kalnay et al. 1996) and TC best track records, although not without flaw, have recently reached sufficient length (30+ years) in the satellite era (from 1970 to present) to aid in developing a comprehensive picture of the global interconnectivity between ocean and atmosphere. The tropical cyclone is a critical component of this interface, and these datasets, although not without unanswered questions regarding their quality, enable quantitative analysis of the links between TCs and their larger-scale environment. As meteorology advances its understanding of the geophysical planet, we are able to not only pose questions such as "What are the connections between equatorial SSTs, stratospheric winds, midlatitude geopotential height, or polar sea level pressure, and different measures of TC activity? Do these connections depend on time? Space? Are they restricted to the in situ or are they teleconnected? And have they been stationary in time and space?", but we are able to use our new knowledge, applied to newly available datasets, and actually answer the questions. Furthermore, the answers to these questions are immediately applicable to the presently highly-charged debate over the role of anthropogenic climate change (e.g., Landsea 2007; Holland and Webster 2007; Trenberth and Shea 2006; Mann and Emanuel 2006; Shriver and Huber 2006).

The annual mean number of TCs is 90 globally, with a standard deviation of 10, and although these numbers are disputed (Frank and Young 2007), to date, no evidence exists of a long-term trend in either the global frequency or variability (Kossin et al. 2007; Webster et al. 2005; Emanuel 2005). There is evidence, however, of regional control of TC activity, with variability in tropical SSTs and deep tropospheric wind shear correlated with trends in TC intensity and duration (Emanuel 2006; Frank and Young 2007). It is this regional control of TC activity that is the focus of the research in this chapter, regional not in the sense of the climate system (which, as mentioned above, is on the hemispheric to planetary scale), but regional in the sense of the impacts on specific TC basins and subbasins. This research uses statistical techniques that leverage multiple metrics of TC activity, which are new in definition or dataset length (or both) and provide thorough and encyclopedic answers to the questions posed in the introduction.

3.1. Best track datasets: uses and limitations

All of the measures of TC activity used in this study are based on data contained in the North Atlantic and East Pacific best track datasets. The best track datasets are a postseason construction of a TC's actual position and intensity (Jarvinen et al. 1984). The analyses are performed after the TC's dissipation, giving sufficient time to receive and archive data that were not available in the real-time forecast setting. The best track intensity estimations are based most heavily on satellite intensity estimates from the Dvorak (1975, 1984) technique (Kossin and Velden 2004). When TCs threaten land, aircraft reconnaissance flight-level, dropsonde, and onboard Doppler and microwave data, and ocean- and ground-based in situ instrumentation are also available. The utility of the best track process is to combine the often-differing estimates of intensity and location into a consensus. However, each of the measurement tools has limitations, and thus the best track datasets are essentially best estimates of position and intensity derived from the most current theory using all available observations.

The best track datasets used in this study estimate maximum sustained 1 min surface (10 m) wind speed to the nearest 5 kt, minimum sea level pressure to the nearest mb, and latitude and longitude positions which are precise to the nearest 0.1°, or to within about 10 km horizontal accuracy. These data are reported every six hours for the life of the TC, and in some cases, data points are recorded even when the system is classified as a non-TC (an extratropical cyclone, subtropical cyclone, or tropical wave) to provide continuity over the life cycle of the disturbance. Those non-TCs are excluded from this study, as are any TCs with maximum sustained 1 min surface winds below 35 kt (the threshold of a tropical storm; McBride [1981]).

As mentioned above, the best track datasets do not contain perfect information, nor are they without flaw. Considerable care must be taken with their use. One author declared these archives "places where even angels fear to tread" (Frank and Young 2007). Before the launch of geostationary satellites in the late 1960s and 1970s, TCs that did not encounter land, plane, or ship were simply not included in the historical record. Once satellites were launched, the Dvorak (1975, 1984) technique of estimating intensity from cloud features (cloud banding, coverage, and brightness temperature) was introduced to standardize the determination of TC intensity. While limited by its reliance on a regression curve fit to a cloud of wind-pressure relationships, the Dvorak technique does provide a measure of intensity for TCs far from land and in the absence of aircraft reconnaissance. In the East Pacific, satellite intensity estimates from the

Dvorak technique are used by forecasters to estimate the intensity of nearly every TC, and in the North Atlantic, they are used exclusively for roughly half of the TCs that form (primarily those TCs east of 50°W; DeMaria and Kaplan 1999).

Despite providing a great benefit to forecasters – namely, the ability to achieve an estimate of TC intensity in locations unsampled by aircraft, ship, or buoy – reliance on satellite estimates introduces further uncertainty in the intensity estimates recorded in the historical databases. For example, for the East Pacific and North Atlantic basins, Dvorak intensity estimations are available four times daily from three satellite-interpretation groups: the U.S. Air Force Global Weather Center (AFGWC), the NOAA Satellite Applications Branch (SAB), and the NOAA/NCEP Tropical Analysis and Forecasting Branch (TAFB). However, the three agency intensity estimates are not only frequently dissimilar by 5 to 10 kt (Kossin and Velden 2004), they are also systematically biased to over (under) estimate minimum sea level pressure in high (low) latitude TCs (Kossin and Velden 2004). This bias presents a substantial limitation when using the best track datasets to investigate climatological relationships (Kossin et al. 2007; Olander and Velden 2007). Furthermore, ground-based anemometer, Doppler radar, and aircraft reconnaissance dropsonde measurements are often different from the Dvorak satellite estimates. Comparisons between aircraft reconnaissance and satellite intensity estimates have found an average error in the mimimum central pressure of 10 mb (Olander and Velden 1997), corresponding to a wind error of 10-15 kt (DeMaria and Kaplan 1999). It is possible, although not likely, that through an entire season these "noisy" differences will cancel each other out; but regardless, the error potential remains.

Routine aircraft reconnaissance began in the North Atlantic basin in 1944 (Sheets 1990). For the first ten years of aircraft reconnaissance, surface winds were estimated by visual inspection of the sea. Radar altimeters were installed onboard in the early 1950s, which provided an accurate determination of the aircraft altitude. Combining altitude with pressure measurements at flight-level, estimates of the flight-level geopotential height were made, and the surface pressure was estimated from empirical relationships using the flight-level geopotential height. This technique was used without material modification from the 1950s until accurate dropsonde technology came online in the late 1980s (Emanuel 2005). The aircraft reconnaissance minimum pressure estimates were converted to maximum sustained surface winds using "semi-empirical wind-pressure relations that did evolve with time" (Emanuel 2005).

Only since 1997, after the installation of global positioning systems (GPS) technology on dropsondes released during North Atlantic Air Force reconnaissance flights, has a complete and accurate picture of the TC boundary layer been possible (Powell et al. 2003). Before 1997, the operational practice was to estimate maximum sustained 10 m 1-min surface winds at 80% of the mean flight-level (700 hPa) wind. From 1997-1999, in the CBLAST ocean-atmosphere experiment, 331 wind profiles were measured in hurricane eyewalls in the Atlantic, Central, and Eastern Pacific basins. Typical dropsonde fall speeds ranged from 10-15 m s^{-1}, and measurements were taken every 0.5 s (for vertical resolution between 20 and 30 m). Wind speed accuracies were typically within 0.5-2.0 m s^{-1}, with a height accuracy of 2 m; however, the dropsonde was only a point measurement and it is difficult to ascertain whether the sonde penetrated the region of maximum winds during its descent. For example, one dropsonde released in the southwest quadrant of Hurricane Felix (2007) during its rapid intensification actually splashed down in the northeast quadrant, over 100 km away from its release point.

Although it has been argued that "tropical cyclone detection rates have been close to 100% globally since 1970, when global satellite coverage became nearly complete" (Holland 1981; Emanuel 2005), recent technology improvements have been shown to aid in detection and classification of multiple TCs across several basins (Buckley et al. 2003), including the North Atlantic. For example, current passive-microwave satellite technology from NASA, the Quick Scatterometer called "QuikSCAT", available since June 1999 (Hoffman and Leidner 2005), has facilitated detection of closed wind circulations at the surface (and a closed circulation is the requirement of McBride [1981] for a tropical cloud cluster to be classified as a tropical depression). The QuikSCAT system was designed to allow ocean surface wind retrieval in multiple surface conditions except moderate to heavy rain, and it is useful qualitatively even in the observations of the extreme winds of a hurricane (Hoffman and Leidner 2005). Using an algorithm that combines positive vorticity with a measure of the extent of horizontal winds, the QuikSCAT platform has been shown to correctly identify and classify TCs an average of 20 h before operational classification (Sharp et al. 2002).

One of the most difficult problems for operational TC forecasters – and by association, the best track datasets – is the estimation of the TC's maximum sustained surface wind. When aircraft reconnaissance data are provided, they are typically obtained from 10,000 ft (700 hPa) flight-level, and forecasters are forced to both determine the surface wind speeds that correspond to those flight-level winds and also reconcile that determination with any other available data, including satellite intensity estimates, ship reports, and buoy observations. Powell and Black (1990) determined that a ratio of 63% to 73% was an acceptable range of flight-level-to-surface reduction (thus providing that a flight-level wind measurement of 100 kt corresponds to 63 to 73 kt 1-min maximum sustained 10 m winds). However, operational practice at the NHC, while varying over time, typically used an 80% to 90% reduction factor from the 1960s through the 1990s for East Pacific and North Atlantic TCs. Furthermore, based upon dropsonde data collected during the 1997-1999 CBLAST field project in the North Atlantic, Franklin et al. (2003) reached two conclusions that have dramatically altered the practice of flight-level-to-surface wind reductions in the North Atlantic. First, they found a broad wind maximum centered 500 m above the surface, with wind speeds decreasing with altitude above this level due to the warm core of the cyclone. The 500 m winds were found to be approximately 20% greater than the 700 hPa wind speeds. Below 500 m, winds were found to decrease due to the frictional boundary layer, decaying nearly linearly with the logarithm of the altitude. The 10 m wind was found to be approximately 75% of the peak 500 m wind. Thus, the surface winds were found to be approximately 90% of the 700 hPa winds. This conclusion has the potential to profoundly impact the maximum winds recorded in the best-track historical dataset, as many of these data points are based almost exclusively on reports from aircraft reconnaissance that used a reduction factor other than 90%.

To illustrate the potential errors contained in the historical record, we turn to the highly-publicized alteration of the best-track dataset for the case of Hurricane Andrew

(1992). At the time, it was reported that Andrew made landfall at Homestead Air Force Base, Florida, at 0905 UTC on 24 August 1992 with a minimum pressure of 922 mb and maximum sustained winds of 125 kt (Rappaport 1993). This information was recorded in the best track data in early 1993. It remained there until 2004, when a review panel at the NHC determined that the maximum sustained winds were not 125 kt at landfall, but instead 145 kt. This 20 kt upward adjustment was based primarily on a new dropsonde-derived flight-level-to-surface wind reduction factor (Landsea et al. 2004), and illustrates that the best track data are essentially only best estimates from the observations and theory available at the time. While a reanalysis project is being discussed at the NHC, no other adjustments have been made to TCs from the same time period as Andrew whose intensities were derived using the same potentially flawed methods.

Another important example of the potential errors contained in the historical record, this one highlighting the inability to determine TC intensity to within even two Saffir-Simpson hurricane categories (±15 kt), comes from Super Typhoon Saomai, which formed in the western North Pacific on 04 August 2006 and made landfall in mainland China on 10 August 2006. Before making landfall in China, Saomai was not investigated by aircraft reconnaissance, and it did not pass directly overhead of any surface observation instruments (such as drifting or fixed buoys). The World Meteorological Organization (WMO) Regional Specialized Meteorological Center (RSMC) in Tokyo, Japan, is tasked with keeping the best track historical records for the western North Pacific basin. RSMC Tokyo determined that Saomai's standard (10 m) 10 min sustained wind intensities were 95, 100, 105, and 100 kt for the period from 0000 UTC to 1800 UTC on 09 August 2006, respectively, and it assigned minimum sea level pressures of 935, 930, 925, and 930 mb at the corresponding synoptic times. According to Powell et al. (1996), a rough conversion factor from 10 min to 1 min sustained winds is 112:100, meaning the 1 min sustained winds will be 12% faster than the 10 min sustained winds. Applying this conversion factor, Saomai's 1 min sustained winds were approximately 106.4, 112, 117.6, and 112 kt, respectively, from 0000 UTC to 1800 UTC on 09 August 2006. Because of its military interests in the region, the U.S. Navy, through the Joint Typhoon Warning Center (JTWC), has maintained separate best track datasets for the western North Pacific since 1945. Using the same satellite data, JTWC determined that the 1 min sustained winds of Super Typhoon Saomai were 105, 125, 140, and 140 kt, respectively, from 0000 UTC to 1800 UTC on 09 August 2006, and that the minimum sea level pressures were 938, 916, 898, and 898 mb. The large differences in intensity, ranging from 10 to 25 kt, are primarily due to differential applications of the Dvorak technique and varying interpretations of the climatological wind-pressure relationships in the western North Pacific. Thus, even with all of the technology available to forecasters in 2006, it was still not possible to conclude the current intensity of a typhoon to within 25 kt.

Limitations in the best-track datasets, such as those highlighted by Hurricane Andrew (1992) and Typhoon Saomai (2006), make accurate determinations of seasonal levels of TC activity and trends in TC activity very difficult. Reanalysis can overcome some of these limitations (e.g. Landsea et al. 2004; Kossin et al. 2007); however, the brevity of the records (with the satellite era only beginning in 1970), as well as shifts in technology (satellite horizontal and vertical resolutions have improved since 1970), remain problematic. One method used to extend the meteorological record back in time is paleotempestology, which relies on geological and biological proxies of TC activity to sample very rare, catastrophic events that have long recurrence intervals (hundreds to thousands of years; Frappier et al. 2007). The paleotempestology study of Liu (2007) documented a period of "hyperactive" landfalls along the U.S. Gulf Coast about 3800 to 1000 years ago, in which strong hurricanes made landfall at a rate 3 to 5 times greater than the most recent millennium. While paleotempestology data attempt to provide a connection between climate and TC activity, it alone is unlikely to provide an accurate estimate of the future return period of extreme events. This dissertation, completed in 2007, uses the satellite-era best track data from 1970-2006, acknowledging its flaws but recognizing that it is the best that is presently available. Satellite coverage of the North Atlantic and East Pacific basins had begun by 1970 (Barrett and Leslie 2005; Webster et al. 2005); thus this study focuses on TC activity from 1970-2006.

3.2. Metrics of TC activity

Because of the limitations and uncertainty contained in the historical record, this study uses fifteen different methods to quantify "TC activity." When more than one metric exhibits similar correlations with the climate indices, it is possible to give greater confidence to the relationship. Just as in the previous sections, a "TC" is defined in this chapter as any warm core circulation classified by the NHC and determined to have maximum sustained surface winds of at least tropical storm force (35 kt). One obvious method to measure TC activity is to count the number of TCs, hurricanes, and intense hurricanes, respectively, which occur each season in each basin. This method has the advantage of simplicity because it is not sensitive to knowledge of the actual intensity of a TC. With the cases of Andrew and Saomai, both would have been included in counts of TCs, hurricanes, and intense hurricanes. While simple, however, this method is remains sensitive to errors that compound during the long time series of TC activity. First, observational technology and operational practice do not remain stationary over any period of record longer than several years (Buckley et al. 2003). Geostationary and polar-orbiting satellites, ground and aircraft-based radar, dropsonde technology, and aircraft reconnaissance have been introduced (beginning in 1944 with routine aircraft reconnaissance in the North Atlantic) in the past several decades. These different observing platforms are not available across all basins, and in the case of polar-orbiting satellites, which were first launched in the late 1950s, their coverage does not always extend to each TC. Second, the best-track historical datasets round TC intensity estimates to the nearest 5 kt. Thus, any TC, hurricane, or intense hurricane whose intensity hovers near a break-point (35, 65, or 100 kt, respectively) will potentially skew the counts, depending on which observational platform(s) were used to sample it and how the the data were interpreted for the best track analysis. Third, the Dvorak and flight level-to-surface wind reduction techniques have not been applied equally since 1970. It is these collective discrepancies that I hope to mitigate by using fifteen different metrics of TC activity.

To try to account for the difficulties posed by binning TCs around firm breakpoints in the intensity data, a metric was developed to quantify TC activity using continuous data. The accumulated cyclone energy (ACE; Bell et al. 2000) is a quantity that accounts for frequency, intensity, and longevity of TCs in a basin. Seasonal ACE is defined as the sum of the squares of the 6-hourly-maximum sustained surface wind speed (either knots^2 or m^2 s^{-2}) for all TCs in a basin or subbasin having at least a minimum-specified intensity (usually taken to be tropical storm intensity, although because the wind speeds are squared, the 25- and 30-kt depressions are not weighted heavily and become almost irrelevant against a long-lived 130 kt Category 5 hurricane). The ACE has several advantages as an index of TC activity. First, it is useful for correlating and regressing against other climate variables of interest because it is a continuous variable. Thus, it does not suffer from the limits of counts of TCs, hurricanes, or intense hurricanes, which are quantized into discrete integer bins. Furthermore, because it is an integrated quantity, it incorporates information about storm intensity and longevity that TC counts do not. For instance, despite reaching similar maximum intensities (160 kt for Wilma; 150 kt for Katrina), Hurricane Wilma (2005) achieved an ACE of 404,750 kt^2, while Hurricane Katrina (2005) had an ACE of only 206,075 kt^2. The substantial difference between ACE values can be explained by combining both the intensity and longevity differences between the two storms: Wilma maintained at least major (100 kt) intensity for 19 synoptic 6-hr periods and hurricane (64 kt) intensity for 30 6-hr periods; however, Katrina was at major hurricane intensity for only 9 6-hr periods and hurricane intensity for 16 6-hr periods. This example illustrates the strength of the ACE activity index, namely that it is an effective combination of both intensity and longevity and facilitates easy comparison between seasons. The example also, however, illustrates the primary weakness in the ACE activity index, namely that one or two long-lived major hurricanes dominate the seasonally integrated quantity and can mask other levels of activity. For example, the

2004 and 2005 North Atlantic hurricane seasons had ACE values of 2247 x 10^3 kt^2 and 2480 x 10^3 kt^2, respectively. Using ACE as a metric, the two seasons had relatively similar levels of activity (the 2004 season had 90% of the activity of the 2005 season). However, the 2005 season was incredibly active with 27 TCs, 15 hurricanes, and 7 intense hurricanes; the 2004 season had only 14 TCs, 9 hurricanes, and 6 intense hurricanes. The similarity in ACE value (due to the similarity in the number and longevity of the intense hurricanes in each season) obscures the fact that the 2005 North Atlantic season was the most active, as measured by TC counts, on record.

Another measure of TC activity is a simplified power dissipation index, PDI (Emanuel 2005). The PDI is derived from the equation for power dissipation, PD, which is given by

$$\mathrm{PD} = 2\pi\int_0^{\tau}\int_0^{r_0} C_{\mathrm{D}}\rho\left|\mathrm{V}\right|^3 r\,\mathrm{d}r\,\mathrm{d}t \qquad (3.1)$$

where C_D is the surface drag coefficient, ρ is the surface air density, $|\mathbf{V}|$ is the magnitude of the 10 m surface wind, and the equation is integrated from an outer radius, r_0, to the center, and over the storm lifetime τ. The power dissipation has units of energy and provides the total power dissipated by a storm during its life. The area integral in (3.1) is difficult to evaluate from historical datasets (which seldom include information on storm size), however, radial profiles of wind speed are generally similar geometrically and the maximum wind speed shows no correlation with measures of storm size. Thus the random errors introduced in equation (3.1) would tend to cancel out, and because surface air density varies over 15% and the drag coefficient varies roughly as a factor of two (Emanuel 2005), the integral will be dominated by high wind speeds. By assuming that the product $C_D\rho$ is a constant, the PDI can be defined as

$$\mathrm{PDI} \equiv \int_0^{\tau} V^3_{\max} \mathrm{d}t \tag{3.2}$$

where $V_{\max}$ is the maximum sustained 1-min wind speed at the conventional altitude of 10 m. Because of these assumptions, particularly the assumption that $C_D\rho$ is a constant (C_D is known to vary inversely with wind speed; Makin 2005), the PDI is not a perfect mathematical measure of power dissipation. However, "this index is a better indicator of tropical cyclone threat than storm frequency or intensity alone" (Emanuel 2005). Because it is similar to ACE, the PDI has similar advantages and disadvantages. Even more than ACE, PDI is highly sensitive to very high wind speeds. Thus one long-lived Category 4 or 5 hurricane will mask variability in weaker TC activity.

To attempt to minimize problems with the quality of the best track datasets and to broadly define TC activity, fifteen different metrics are used in this study to quantify seasonal TC activity. Each metric is computed for each season from 1970-2006 for each basin, except for the landfall metrics (10)-(15), which are computed only for the EPAC and NATL and only from 1976-2006.

(1)	TCC	number of TCs
(2)	HC	number of hurricanes
(3)	IHC	number of intense hurricanes
(4)	ACE	total ACE
(5)	PDI	total PDI
(6)	STCD	scaled TC days
(7)	SSD	season start day
(8)	SMD	season mean day
(9)	SED	season end day

(10) TCLC number of TC landfalls

(11) USLC number of TC landfalls in the U.S.

(12) USLHC number of H landfalls in the U.S.

(13) TCLP proportion of TCs which make landfall

(14) USLP proportion of TCs which make landfall in the U.S.

(15) USLHP proportion of Hs which make landfall in the U.S.

The definition, strengths, and weaknesses of metrics (1)-(5) are discussed above. The "scaled TC day" metric (6) is simply a weighted count of numbers and longevity of TCs, hurricanes, and intense hurricanes. It attempts to take into account the monthly impact of a TC on the low-frequency tropical general circulation (Fiorino 2007, personal communication). An intense hurricane of 130 kt, for instance, is theorized to have only twice the impact of a hurricane of 65 kt, verses four times the impact in ACE or eight times the impact in PDI. For each best track data point, the scaled TC day count is calculated as follows:

$$sTCd = \begin{cases} 0.5/4 & 34\text{kt} \le V_{\max} \le 63\text{kt} \\ 1.0/4 \;, & 64\text{kt} \le V_{\max} \le 95\text{kt} \\ 2.0/4 & 96\text{kt} \le V_{\max} \end{cases} \tag{3.3}$$

where $sTCd$ is the fractional-day contribution to scaled TC day and $V_{\max}$ is the maximum sustained wind speed. Thus a short-lived TC that has sustained winds of 40 kt at 00 UTC, 70 kt at 06 UTC, and 20 kt at 12 UTC has a $sTCd$ of 0.375. The $sTCd$ quantity behaves similarly to ACE and PDI in its accounting for both intensity and longevity of TCs, but unlike ACE and especially PDI, it is not as sensitive to long-lived intense hurricanes.

The season start day (7) is given as the Julian date that each season reaches 10% of its total ACE value for that season. The season end day (9) is given as the Julian date that each season reaches 90% of its total ACE value for that season. Seasonal ACE values are chosen because they are a continuous distribution and represent an integrative measure of total TC activity. In addition to quantifying early-starting and late-ending TC activity, these two metrics are able to account for late-starting but still active seasons and early-starting but relatively inactive seasons. In the case of late-starting seasons with large (small) ACE values, the 10% day is shifted earlier (later) relative to that season's mean day. In the case of early-ending seasons with small (large) ACE values, the 90% day is shifted later (earlier) relative to that season's mean day. The metrics are limited by seasons whose actual ACE is low but evenly distributed throughout the season, and also by seasons where ACE is dominated by one or two very intense or long-lived TCs.

The season mean day (8) is calculated as the expected value of a Gaussian distribution and is given by

$$Mean_{jday} = \sum_{jday=1}^{jday=365} \frac{ACE_{jday}}{TotalACE} \times jday \tag{3.4}$$

where the mean Julian day of each season is a summation over the entire year of the contributions of the daily value ACE (ACE_{jday}) divided by the total ACE that season (metric (4), *TotalACE*) multiplied by that Julian date.

The number of TC landfalls (10) is a simple count of the number of TCs that make landfall anywhere in the basin. The number of U.S. TC (11) and H (12) landfalls are similarly computed, except restricted to the mainland U.S. (excluding Puerto Rico and the U.S. Virgin Islands). The landfall metrics include TCs whose center passed within 60 nm of land and those TCs that caused greater than $1 million USD in damage as reported in the post-season tropical cyclone reports produced by the Tropical Prediction Center. The proportion of TC (13), U.S. TC (14), and U.S. H landfalls (15) per season are simple ratios of the number of TC landfalls (10), number of U.S. TC landfalls (11), and number of U.S. hurricane landfalls (12) to the TC count (1), the TC count (1), and the H count (2), respectively. As mentioned above, the six landfalling metrics are calculated for only the East Pacific and North Atlantic basins.

3.3. Early studies of periodic variability in North Atlantic TC activity

The first known study which attempted to connect interannual variability of North Atlantic TC activity with regularly-measured atmospheric variables was undertaken by Brennan (1935), who examined rainfall, wind speed at 1 km above ground level, and barometric pressure data at Kingston, Jamaica, from May to July (MJJ), 1903-1934. Brennan (1935) found that above (below) normal MJJ rainfall, below (above) normal wind speed, and below (above) normal barometric pressure were all associated with above (below) normal August-September hurricane activity in the Caribbean. Five decades later, seasonal prediction of TC activity was pioneered by Dr. William Gray of the Tropical Meteorology Project at Colorado State University (CSU). The theoretical hypothesis used by Gray (1984) was that Atlantic hurricane activity did not occur in isolation and thus it should be related to other atmospheric variables. Gray (1984) began his work by noticing that during periods of warm (cool) SSTs, Atlantic hurricane activity was suppressed (enhanced) compared to the seasonal mean. A similar relationship held for the east (west) phase of the equatorial stratospheric quasi-biennial oscillation (QBO), that Atlantic hurricane activity was suppressed (enhanced) compared to the seasonal mean. At the time, it was surprising that the atmosphere-ocean system had a long-period "memory" which enabled skillful prediction of events such as TCs several months in advance (Klotzback 2007).

There is also evidence of the influence of TC activity on the larger-scale environment in the West Pacific (e.g., Sobel and Camargo 2005). In time series of outgoing longwave radiation, relative vorticity, SSTs, and column water vapor, TC impacts were found at multiple timescales. The TCs themselves were found to modulate each variable over one- to two-week time periods (e.g., cooler SSTs for several days following the passage of a TC), and at several months, a slowly evolving signal indicative of the El Niño-Southern Oscillation (ENSO; Trenberth 1997) phenomenon was seen in each of the variables (Sobel and Camargo 2005). Regionally varying impacts on the large-scale environment by TCs is examined briefly in this dissertation and is left for an interesting future study.

3.3.1. Relationships between large-scale climate and TC activity

Since the work of Gray (1984), there have been many observational and theoretical studies which examined the relationships between interannual TC activity and various atmospheric variables, beginning with the North Atlantic and continuing into other global basins. Professor Johnny Chan and the City University of Hong Kong began issuing seasonal forecasts of TC activity over the western North Pacific basin and also the South China Sea in 1998 (Chan et al. (1998). They used two monthly indices as predictors representing (a) the ENSO phenomenon and (b) East Asian and western

North Pacific environmental conditions from April of the previous year to March of the current year. Carmago and Sobel (2005) re-examined the relationship between western North Pacific typhoon activity and ENSO, and they found that during El Niño years, there is a tendency for both more intense and longer-lived TCs in the western North Pacific. Kim et al. (2005) quantified the relationship between anomalous midtropospheric flows between Japan and Korea and East Asian TC activity and found that enhanced cyclonic (anticyclonic) circulation around Japan was correlated with low (high) typhoon frequency south of Korea. Chu and Wang (1997) and Clark and Chu (2002) examined the relationship between central North Pacific TC activity and ENSO, and both studies found that the mean number of TCs that approach Hawaii during El Niño years is significantly higher than during non-El Niño years. Ho et al. (2006) also examined the relationship between ENSO and TC activity, this time in the South Indian Ocean. They found that during warm ENSO years, TC activity was enhanced west of 75°E and reduced east of 75°E, and that this shift was due in part to a westward shift in tropical convection.

The early North Atlantic studies of Gray (1984), hypothesizing that TCs were connected to the larger earth-atmosphere system, investigated the connections between North Atlantic hurricane activity and ENSO and the equatorial stratospheric (QBO). Hurricane activity in the western Atlantic was found to reduce (increase) during the season following the onset of the warm-phase (cold-phase) ENSO (El Niño; La Niña) event. Specifically, the mean number of Atlantic hurricanes per season from 1900-1982 during El Niño years was 3.0, and during non-El Niño years the mean was 5.4. The mean numbers of Atlantic TCs per season from 1900-1982 during El Niño years was

5.3, and during non-El Niño years the mean was 9.0. For the period 1950-2001, Larson et al. (2005) found a mean of 6.9 (9.3) Atlantic TCs in August, September, and October (ASO) during El Niño (La Nina) years. Gray (1984) calculated that the ratio of Category 4 and 5 (Simpson 1974) hurricanes striking the U.S. to those remaining at sea was 0.25 during El Niño years but 0.75 during non-El Niño years, a ratio of three-to-one. Larson et al. (2005) calculated that the rate of landfalling Atlantic hurricanes in ASO was 0.6 (1.92) during El Niño (La Nina) years, also a ratio of three-to-one.

The CSU Tropical Meteorology Project's statistical predictions of levels of TC activity have generally proven skillful against climatology (see Table 3.1), but only when considering the June and August forecasts for same-season activity. The December and April forecasts, issued for the coming season, are not statistically superior to climatology. The recent 2006 North Atlantic predictions illustrate the difficulty of seasonal prediction of levels of TC activity. The team from CSU, in their June forecast (issued 31 May 2006), predicted 17 TCs, 9 hurricanes, and 5 intense hurricanes. However, only 9 TCs, 5 hurricanes, and 2 intense hurricanes formed, resulting in skill (measured by mean absolute error) much below the climatological of 10.3, 6.2, and 2.7 TCs, hurricanes, and intense hurricanes, respectively, per season in the North Atlantic.

As of 2007, seasonal levels of TC activity have been predicted using both statistical and dynamical models, although the dynamical models have yet to document skill at levels comparable to statistical ones (Vitart and Stockdale 2001; Klotzbach 2007). The statistical techniques most often use multiple linear regression, and they have been developed and honed over the past two decades to examine multiple atmospheric variables, including SST, tropospheric and stratospheric wind, sea level pressure, and precipitation, as well as their composites (e.g., Gray et al. 1992, 1993, 1994; Elsner and Schmertmann 1993, 1994; Klotzbach and Gray 2003; Owens and Landsea 2003; Blake and Gray 2004; Klotzbach 2007). Most recently, several studies have used statistical techniques to begin forecasting landfall activity (e.g., Gray et al. 1998, Klotzbach and Gray 2004; Saunders and Lea 2005; Lea and Saunders 2006; Jagger and Elsner 2006), although the level of peer-reviewed literature on verification and methods is not comparable to the extensive literature describing algorithms to forecast basin-wide activity (Elsner and Jagger 2006).

In addition to the Tropical Meteorology Project forecasts of Atlantic basin seasonal TC activity, NOAA (begun in 1998), Tropical Storm Risk (TSR, begun in 1999), and the Cuban Institute of Meteorology (begun in 1999) also issue annual forecasts of TC activity levels. NOAA bases its forecasts primarily on two primary and two secondary predictors. The primary predictors are the observed state of the Atlantic multidecadal oscillation (AMO) and the forecast state of ENSO from the Climate Prediction Center (CPC), and the secondary predictors are the forecast August-October Atlantic basin SST anomalies and the forecast August-October Atlantic basin vertical wind shear (Klotzbach 2007). TSR, a private consortium based in the United Kingdom, relies on predicted August-September trade wind speeds in the Caribbean and tropical North Atlantic, as well as predicted August-September SSTs in the tropical North Atlantic (Lea and Saunders 2006). The Cuban Institute of Meteorology uses multiple linear regression with sea level pressure, tropical North Atlantic SSTs, and the observed and predicted ENSO state as predictors. The Cuban Institute of Meteorology is the only known office that issues subbasin forecasts of activity (they issue for the Caribbean; Klotzbach 2007).

3.3.2. Relationships between East Pacific TCs and climate

For multiple reasons, climate-TC relationships in the East Pacific basin have not received the same extensive attention in the peer-reviewed literature as have the relationships in the North Atlantic and the western North Pacific basins. This lack of attention is perhaps due to the fact that relatively few East Pacific TCs make landfall, as most East Pacific TCs form equatorward of 20°N where the climatological steering flow is predominately westward away from land. Since 1976, only 15% of East Pacific TCs have made landfall, compared with 45% of North Atlantic TCs (two-thirds of the North Atlantic landfalls occur in the U.S., or 30% of all TCs in the basin). Another reason that the East Pacific may have received relatively less attention is that its “coefficient of variation,” a measure of the ratio of the seasonal mean to the seasonal standard deviation of TC activity (see Table 3.2), is lower (0.28) than the North Atlantic (0.42), and thus it is considered more stable. However, when examining the East Pacific subbasins, the coefficients of variation are much higher, ranging from 0.63 in the east and west East Pacific to 0.34 in the central East Pacific. These coefficients of variation are much higher than the entire North Atlantic basin and on par with the Gulf of Mexico and Atlantic main development region. Whatever the reason for the lack of peer-reviewed studies, a substantial portion of this dissertation research is devoted to the East Pacific basin and its subbasins (defined earlier as the eastern East Pacific, central East Pacific, western East Pacific, and the Central Pacific), as they are fundamentally important to understanding the relationships between climate-scale oscillations and TC activity.

3.4. Vertical wind shear and TCs

The connection between environmental winds and TC intensity change has been investigated for almost 90 years (e.g., Weightman 1919). Numerous studies have noted the negative effects of vertical shear on genesis and intensification (e.g., Ramage 1959; Gray 1968; Merrill 1988; Herbert 1978; Dvorak 1984; DeMaria and Kaplan 1994; DeMaria 1996; Zehr 2003; Patterson et al. 2005; Heymsfield et al. 2006). For this study, the term "vertical shear" refers to the change in wind (both speed and direction) with height of the environmental wind, typically taken as a vector difference between 850 hPa and 200 hPa (e.g., DeMaria 1996). This definition is given to differentiate from a point value of vertical wind shear, which will be sensitive to the circulation of the TC. The approximately axisymmetric TC circulation will tend to average out over the environment, leaving the environmental wind profile. The deep-layer (850 hPa to 200 hPa) mean of this wind has also been referred to the "steering flow" (Chan 2005), and it is well correlated to TC motion.

Vertical wind shear over the TC vortex is produced by many different atmospheric features, and these features are manifested on multiple spatial scales, from the mesoscale to the planetary scale. A weak and shallow TC vortex (one extending up into the troposphere less than 5 km) that is embedded in easterly trades of 10 m s^{-1} or greater will commonly experience net vertical shear because the upper-tropospheric flow is usually weaker than 10 m s^{-1}. As TCs emerge from the deep tropics into the midlatitudes, they interact with traveling Rossby waves and their associated trough systems. Strong - and increasing with height – westward and poleward midtropospheric wind components ahead of these traveling waves produce vertical wind shear over the TC vortex. It is important to note, however, that not every interaction between a TC and a midlatitude trough is detrimental to the TC. Occasionally the TC-trough interaction will produce favorable upper-tropospheric "ventilation", aiding the outflow and thus the thermodynamic efficiency of the inner-core air-sea interaction (Emanuel 1996). Typically, vertical wind shear of 10 m s^{-1} is the break-point between intensification and dissipation (Paterson et al. 2005). When vertical wind shear is between 2 m s^{-1} and 4 m s^{-1}, rapid intensification is favored, and vertical wind shear above 12 m s^{-1} favors rapid dissipation. Paterson et al. (2005) found a time lag of 12 to 36 h between the onset of increased vertical shear and the onset of weakening.

During the warm ENSO event, anomalous deep cumulus convection in the eastern Pacific enhances anomalous westerly upper-tropospheric wind patterns over the equatorial Atlantic and Caribbean basin (Gray 1984). The typical June to November lower-tropospheric flow in this region is northeasterly; thus, enhanced upper-tropospheric westerly flow leads to anomalous and broad regions of enhanced vertical wind shear. Gray (1984) examined composite rawinsonde data from seven stations across the Caribbean: Swan Island (17° 23'N, 83° 55'W); Grand Cayman Island (19° 16'N, 81° 22'W); Kingston (17° 55'N, 76° 47'W); Curaçao (12° 12'N, 68° 58'W); San Juan (18° 26' N, 66° 01'W); St. Maarten (18° 03'N, 63° 07'W), and Barbados (13° 04'N, 59°29'W). The difference between Aug-Sept mean 200 hPa winds at these seven stations was between 1.3 and 5.8 m s^{-1}, with the positive anomaly corresponding to stronger westerly winds. Gray (1984) also examined teleconnections between ENSO and six other global basins (North Indian, Northwest Pacific, Northeast Pacific, South Indian, Australia, and Southwest Pacific), but found no significant modulation of TC activity in any of those basins.

When the upper-tropospheric wind differs from the lower-tropospheric wind, the potential vorticity associated with the vortex circulation is tilted in the vertical (DeMaria 1996). To maintain a balanced mass field when the vortex is tilted, a positive, midlevel temperature perturbation must develop over the vortex center and, correspondingly, a negative temperature perturbation must develop in the downshear direction (DeMaria 1996). These temperature perturbations act to stabilize the environment above the vortex and thus reduce the already-limited environmental instability available to air rising in the vortex center (Emanuel 2003). The result is a marked asymmetry in the inner-core vertical motion with ascent to the downshear left of the shear vector and descent to the upshear right of the shear vector (Kepert 2006). The coupled pattern of midlevel warming and cooling also acts to disrupt the convective symmetry of the circulation, leading to a broadening of the latent heating that drives the surface cyclone. In a vertically-sheared TC, deep convective clouds are located on the downshear side and shallow, low-level clouds will be exposed on the upshear side (Zehr 2003). This vortex-disrupting process is most pronounced at lower latitudes, where the relatively lower vorticity contribution from the Coriolis parameter – and the relatively larger Rossby radius of deformation – act to require relatively greater vertical coherence to maintain the cyclonic circulation (DeMaria 1996).

From a climate standpoint, vertical shear prediction is critical to interannual-to-seasonal prediction of TC activity. The inverse relationship that exists in the temporal scale of an individual TC also exists between large-scale values of vertical wind shear and tropical cyclogenesis on the seasonal and longer timescales. The North Atlantic and East Pacific basins seem to be particularly affected by large-scale shifts in the magnitude and extent of favorable conditions for cyclogenesis (as evidenced by their coefficients of variation), and vertical wind shear is one such important factor. As mentioned above, the coefficient of variation is one measure of the variance from basin to basin. From 1986 to 2005, the coefficients of variation in the North Atlantic and East Pacific are much larger other basins including the West Pacific and North Indian Ocean. For example, in 1983, the North Atlantic had only 4 named storms, while in 2005, it had 27. The North Atlantic coefficient of variation is 0.42; the East Pacific coefficient of variation is 0.28; and the West Pacific coefficient of variation is only 0.15. Table 3.2 summarizes the coefficients of variation for each basin and subbasin in the East Pacific and North Atlantic.

Variations in East Pacific and North Atlantic TC frequency significantly affect human activities and thus impact the global economy. Landfalling TCs bring threats of storm surge, violent surface winds, and tremendous precipitation. TCs at sea disrupt shipping and aviation patterns and their wave energy erodes coastlines and creates rip currents. Understanding the interannual climatology and the teleconnections to the leading modes of interannual variability is thus critically important (Larson et al. 2005). As long-range climate predictions from dynamical models become more accurate, understanding the relationships between the leading atmospheric modes of variability and TC activity will aid seasonal long-lead forecasts (Klotzbach 2007).

3.5. The climate indices

In this investigation, I examined the relationships between twelve leading climate indices and fifteen metrics of TC activity. In section 3.5, each climate index is briefly defined, with relevant citations from earlier studies, and the physical implications of each index are discussed. The climate indices are all reported as monthly values, from Jan 1970 to Feb 2007. A three-month unweighted moving average was used to smooth the data into seasonal values (e.g., Anderson 2007), so the Jan-Mar data are simply an average of the Jan, Feb, and Mar indices. This smoothing technique does remove some of the variability on monthly timescales; however, in this chapter, I am interested in examining the variability of seasonal TC activity with climate indices whose periodicities range from seasonal to interdecadal. Furthermore, sensitivity tests between unsmoothed (monthly) and smoothed (three-month average) indices revealed that most of the correlation coefficients differed by less than 0.10. Finally, I use Spearman rank correlations which do not depend directly on the index values themselves, but rather on the relative ranks of the index values. Thus, the climate indices are smoothed into three-month averages.

In section 3.7, significant associations between the climate indices and TC activity are highlighted (with a complete display of all 12,816 correlations in Figs. 3.3-3.37). The following list identifies the twelve climate indices, and the next sections identify the acronyms and summarize how they are calculated.

(1) NINO1.2

(2) NINO3

(3) NINO4

(4) NINO3.4

(5) NASST

(6) QBO

(7) PDO

(8) SOI

(9) NOI

(10) NAO

(11) PNA

(12) AO

3.5.1. The El Niño-Southern Oscillation (ENSO)

Perhaps the most studied of all the modes of climatic variability is ENSO, the leading pattern of two- to eight-year global climatic variability (Nicholls 1988). A quick non-scientific query of the publications of the American Meteorological Society reveals that 133 peer-reviewed articles containing "ENSO" in the abstract were published between Jan. 2006 and Aug. 2007, a rate of over 7 articles per month! Thus this sectional summary concerning ENSO will be brief; refer to Trenberth (1997) for a thorough description of ENSO.

Combining the seesaw pattern of sea level pressure between Darwin and Tahiti (the Southern Oscillation; see discussion below) and the occasional warming of the equatorial eastern Pacific (the El Niño), ENSO accounts for a greater proportion of oceanic and atmospheric variability on timescales from one to ten years than any other single phenomenon, except the tilt of the earth (Wright 1985). ENSO-related fluctuations impact the oceanography, meteorology, biology, ecology, economy, and sociology of huge regions of the earth. Because of its interseasonal timescale and quasi-annual warm (or cold) phase duration, most of the studies examining the predictability of TC activity at the seasonal level have focused primarily on ENSO. The long life cycle of ENSO (primarily from two to seven years; Rasmusson and Carpenter 1982) and its dominance of that mode of atmospheric and oceanic variability, allow for its predictability. Relying on lag relations with ENSO, civil planners, social scientists, and biologists can infer the likely near- and short-term impacts from the phenomenon and recommend action to take advantage of the knowledge (Nicholls 1988). However, predictability studies of TC activity are limited by the low skill in forecasting ENSO before the March-April barrier (Lloyd-Huges et al. 2004). The business cycle of insurance industry rate negotiations occurs in the winter prior to each hurricane season, and billions of dollars of cost (to home- and business owners) and revenue (for insurance companies) are at stake in each season's rate negotiations. The current seasonal forecasts of TC activity remain unreliable at the skill level needed for profitability in this industry (Lonfat et al. 2007), as evidenced in the seasonal forecasts for 2006 that predicted more than two major hurricane landfalls (nearly 300% above the thirty-year baseline) when zero landfalls occurred.

The ENSO SST indices used in this study were calculated by the NOAA CPC for four ENSO regions, NINO1.2 (0-10°S, 80-90°W), NINO3 (5°N-5°S, 90-150°W), NINO3.4 (5°N-5°S, 120-170°W), and NINO4 (5°N-5°S, 150°W-160°E), using the optimum interpolation technique of Reynolds et al. (2002). SST data from the NCEP/NCAR Reanalysis (Kalnay et al. 1996) over the specified regions are used to compute the indices. The four monthly ENSO indices may be accessed online at <http://www.cpc.noaa.gov/data/indices/sstoi.indices>. Unlike other studies (e.g., Larson et al. 2005) which use rigid "yes/no" classifications of El Niño, this study correlates monthly SST anomalies in the four NINO regions with measures of TC activity. Positive (negative) ENSO index values indicate warm (cool) SST anomalies in the respective NINO indices.

It is interesting to note that the NINO3.4 region was added in April 1996 to allow a better understanding of SST changes in the critical space between the NINO3 and NINO4 regions. This change highlights one of the objectives of the research of this chapter, namely to illustrate the need to examine both basins and subbasins when determining physical associations between TC activity and the large-scale environment.

3.5.2. North Atlantic SSTs (NASST)

When SSTs in the tropical and North Atlantic are anomalously warm, TC activity is higher (Dunn 1940; Gray 1968; Shapiro and Goldenberg 1998; Goldenberg et al. 2001). The November 2006 World Meteorological Organization (WMO) statement on tropical cyclones and climate change (WMO 2006), which resulted from the consensus discussions of over 100 scientists and forecasters, acknowledged that, for the North Atlantic, "it is well established that SST is one of the factors impacting the number and severity of (tropical) cyclones" (WMO 2006). The WMO statement also acknowledged that no other such in situ relationships have been established for other ocean basins.

The SST index for the North Atlantic (NATL) uses the weekly 1° spatial resolution optimal interpolation (OI) analysis of Reynolds et al (2002). Monthly averages are calculated from the weekly OI analyses, and anomalies are calculated using a 1971-2000 base period. The NATL region is bounded by 5-20°N and 60-30°W, and the raw SST data are taken from the NCEP/NCAR Reanalysis (Kalnay et al. 1996). Positive (negative) NASST values represent anomalously warm (cool) SSTs over the domain. The monthly NATL indices may be accessed online at <http://www.cpc.noaa.gov/data/ indices/sstoi.atl.indices>.

3.5.3. QBO

The QBO index used in this study is calculated by the NOAA CPC as the monthly average of the 30 hPa zonal wind at the equator. The positive (negative) QBO index corresponds to easterly (westerly) zonal wind at 30 hPa. Monthly QBO index values are taken from the NCEP/NCAR Reanalysis (Kalnay et al. 1996) and can be accessed at <http://www.cdc.noaa.gov/Correlation/qbo.data>.

The QBO is an east-west oscillation in the stratospheric winds above the equator. It is a "spectacular demonstration of the role of wave, mean-flow interactions in the fluid dynamics of a rotating atmosphere" (Baldwin et al. 2001). The QBO is clearly evident in time series data of monthly-mean zonal wind component. Gray et al. (2001) reexamined stratospheric wind direction from radiosonde data (up to 31 km above ground level) from Canton Island (2.8°N), Gan Island (0.7°S), and Singapore

(1.4°N), and rocketsonde data (from 31 to 60 km above ground level) from Kwajalein (8.7°N) and Ascension (8.0°S) islands, beginning in 1964 and continuing to 1990. They verified that the QBO is continuous and that it has a period ranging between 22 and 32 months (e.g., Reed 1961).

The atmospheric forcing for the QBO remains uncertain, although it is believed to be driven by a combination of vertically-propagating Kelvin, Rossby-gravity, inertia-gravity, and gravity waves excited by tropical convection (Baldwin et al. 2001). The QBO phase is defined by the equatorial wind direction at 40 hPa, the east-west pattern of winds propagates downward from the upper stratosphere to near the tropopause, and the transition between east and west phases of the QBO tends to occur in boreal summer in the upper stratosphere and reach the tropopause near boreal autumn (Murnane 2004). Gray (1984) found that westerly QBO events were associated with 50-100% more hurricane activity than easterly QBO events, and he attributed this difference to reductions in vertical wind shear between the upper troposphere and lower stratosphere. Another possible connection exists between the QBO phase and the location of enhanced tropical convection. During the west (east) phase of the QBO, convection is enhanced poleward (equatorward) of 5°, which is a favorable (unfavorable) environment for future development of African easterly waves into hurricanes (Gray et al. 1992; Knaff 1993). However, the physical connection between Atlantic hurricane activity and the QBO is not obvious (Baldwin et al. 2001), and the connection between the QBO and TC activity in other basins has yet to be explored. Using accurate QBO forecasts to predict TC activity in the near-future is extremely valuable to the reinsurance industry, whose business cycle is timed so that it also makes critical hedging decisions on an annual basis (Murname 2004). Thus, relationships between the QBO and nine basins will be examined in this chapter.

In addition to its effects in the tropics, the QBO affects variability in the extratropics by modulating the effects of extratropical waves. For example, during the easterly phase of the QBO, Rossby waves tend to be confined to higher latitudes. This modification of the mean Northern Hemisphere wave train will potentially impact the AO and NAO. Furthermore, because the QBO modulates the height of the equatorial tropopause, it could influence the MJO (Murname 2004), and because the primary tropical atmosphere modulation of the MJO is to shift the location of deep convection, the MJO is likely to impact the QBO.

3.5.4. Pacific Decadal Oscillation (PDO)

Walker and Bliss (1932) discovered evidence of a Pacific analog to the NAO, with a similar north-south seesaw in sea level pressure from the high latitudes (extending from eastern Siberia to western Canada) to the lower latitudes (poleward to about 40°N). They termed it the PDO, although it is known by other names, including the North Pacific Oscillation (NPO) and the Interdecadal Pacific Oscillation (IPO). Regardless of its name, the PDO is a leading index used widely to characterize decadal variability of Northern Hemisphere climate (Mantua et al. 1997). The oscillation varies on interannual to decadal timescales, and several pronounced pattern shifts have been observed (Schneider and Cornuelle 2005). The 1976/77 shift has been studied extensively (Schneider and Cornuelle 2005). It manifested itself through 2 mb lower November-March surface pressures throughout the North Pacific (averaged every five degrees from 27.5°N to 72.5°N, 147.5°E to 122.5°W) from 1977-1988 when compared with the period 1946-1976 (Trenberth 1990). After the shift in sea level pressures, western and central North Pacific SSTs became cooler and equatorial and eastern North Pacific SSTs became warmer (Dawe and Thompson 2007). The PDO is significantly correlated with many other climate indices and proxies, including precipitation (e.g., Chan and Zhou 2005), fishery populations (Chavez et al. 2003), and tree ring climatologies (Biondi et al. 2001).

The spatial pattern of PDO impacts resembles a horseshoe, with SST anomalies in the Alaska gyre, off California, and toward the tropics surrounded by anomalies of the opposite sign in the central North Pacific (Schneider and Cornuelle 2005). Warm and cold phases of the PDO have been found to last up to thirty years. The oscillation in SST anomalies impact in situ sea level pressure, surface temperature anomalies in northeastern Asia (Minobe 2000), the onset and intensity of the Asian monsoon (Krishnan and Sugi 2003), and precipitation, streamflow, and surface temperature anomalies across North America (Mantua and Hare 2002). Positive (negative) PDO indices indicate warm (cool) SSTs along west coasts of the Americas, cool (warm) SSTs in the central North Pacific, low (high) sea level pressures over the North Pacific and high (low) sea level pressures over the subtropical Pacific and western North America.

Because its variability is on the interannual to decadal timescales, the PDO modulates ENSO teleconnections. This modulation is evident in precipitation and temperature anomalies over North America. A deeper Aleutian low (a positive PDO index) sends the mean extratropical storm track southward, and during the warm ENSO phase, enhanced tropical moisture is available for these storms to tap. Alternatively, when a weaker Aleutian low (a negative PDO index) is paired with the cold ENSO phase, the mean extratropical storm track is farther north and thus precipitation is enhanced in the Northwest U.S. and British Columbia and suppressed in the Southwest U.S. (Gershunov and Barnett 1998; Goodrich 2007). In addition to modulating ENSO, the PDO also is modulated by ENSO through the poleward propagation of oceanic Kelvin waves along the Pacific coasts of the Americas.

The PDO warm-cold pattern is consistent with atmospheric forcing similar to the NAO pattern. A deepened Aleutian low in the central North Pacific decreases SSTs by advecting cool, dry air from the north and increasing westerly winds and turbulent heat fluxes from the ocean to the atmosphere. The opposite occurs in the eastern Pacific and Gulf of Alaska, as a deep Aleutian low enhances poleward transport of heat and moisture and results in anomalously warm SSTs.

The PDO index used in this study is defined as the leading empirical orthogonal function of monthly SST anomalies in the Pacific Ocean poleward of 20°N (Mantua et al. 1997). The monthly PDO index data may be accessed online at <http://jisao.washington. edu/pdo/PDO.latest>

3.5.5 Northern Oscillation Index (NOI)

The Northern Oscillation Index (NOI) was introduced by Schwing et al. (2002) to complement the SOI as a new index of climate variability based on sea level pressure anomalies in the North and South Pacific. The Northern Oscillation Index (NOI) is computed from the NCEP/NCAR Reanalysis sea level pressure anomalies (the monthly sea level pressure minus the climatological monthly sea level pressure from 1948-1997) of the North Pacific high (NPH; 35°N, 130°W) and Darwin (10°S, 130°E). The index is given as

$$\mathrm{NOI} = NPH_{slpa} - Darwin_{slpa} \tag{3.5}$$

where NPH_{slpa} and $Darwin_{slpa}$ are the sea level pressure anomalies of the North Pacific high and Darwin, respectively. Those two locations were chosen because of their connection to the North Pacific Hadley-Walker atmospheric circulation and their direct linkage with the atmospheric wave train between southeast Asia and northwest North America. The NOI captures a wide range of both tropical and extratropical climate and varies on intraseasonal, interannual, and decadal timescales. The primary oscillatory period of the NOI is on the interannual timescale, reflecting its strong association with the phase of ENSO, and it is no surprise that the NOI is highly correlated with the SOI (Schwing et al. 2002). Decadal periods of oscillation are also found in the NOI time series, peaking at 14 years. A positive (negative) NOI value corresponds to northeasterly (southwesterly) surface winds in response to the anomalous pressure gradient between Darwin and the North Pacific. The NOI values in this study are positively correlated with SOI values (r of +0.60) and negatively correlated with ENSO (r of -0.56 to -0.70).

The sea level pressure data were taken from the NCEP/NCAR Reanalysis (Kalnay et al. 1996) and may be accessed online at <http://www.pfeg.noaa.gov/products/PFEL/modeled/indices/NOIx/noix.html>.

3.5.6 Southern Oscillation Index (SOI)

The Southern Oscillation Index (SOI) is classically defined as a standardization of Tahiti sea level pressure minus Darwin sea level pressure. The index values are calculated as follows:

$$\mathrm{SOI} = \frac{\left(Tahiti_{std} - Darwin_{std}\right)}{MSD} \tag{3.6}$$

where $Tahiti_{sdt}$ is the standardized sea level pressure at Tahiti, $Darwin_{std}$ is the standardized sea level pressure at Darwin, and *MSD* is the monthly standard deviation. $Tahiti_{std}$, $Darwin_{std}$, and *MSD* are given by

$$Tahiti_{std} = \frac{\left(Actual\_Tahiti(slp) - Mean\_Tahiti(slp)\right)}{Tahiti\_stdev}, \tag{3.7}$$

$$Darwin_{std} = \frac{\left(Actual\_Darwin(slp) - Mean\_Darwin(slp)\right)}{Darwin\_stdev}, \text{ and} \tag{3.8}$$

$$MSD = \sqrt{\sum_{i=1}^{n} \frac{\left(Tahiti_{std} - Darwin_{std}\right)^2}{n}}, \tag{3.9}$$

where *Actual_Tahiti*(*slp*) and *Actual_Darwin*(*slp*) are the monthly mean sea level pressures at Tahiti and Darwin, respectively, *Tahiti_stdev* and *Darwin_stdev* are the monthly standard deviations of sea level pressure at Tahiti and Darwin (calculated separately for each month for the base period 1951-1980), and *n* is the total number of months. A positive (negative) value of the SOI index corresponds to higher (lower) mean sea level pressures anomalies at Tahiti than Darwin. The positive (negative) SOI phase results in easterly (westerly) surface stress anomalies and warm (cool) SST conditions in the west Pacific. The SOI is strongly negatively correlated with the

ENSO indices (see 3.5.1.), with Pearson product-moment correlation coefficients ranging from -0.63 to -0.73 for the January SOI and ENSO indices used for this study. Monthly SOI data are archived by the NOAA CPC and may be accessed online at <ftp://ftp.cpc.ncep.noaa.gov/ wd52dg/data/indices/soi>.

3.5.7 North Atlantic Oscillation (NAO)

The North Atlantic Oscillation (NAO) has been identified as a major source of interannual variability in the northern hemispheric atmospheric circulation (Hurrell 1995). The oscillation has been defined differently by several authors (Ambaum et al. 2001), but it has always been associated with a north-south dipole structure in mean sea level pressure over the Atlantic Ocean (e.g. Walker and Bliss 1932; Wallace and Gutzler 1981; Hurrell 1995; Ambaum et al. 2001). As an index, the NAO is defined by only two points, unlike another major mode of northern hemispheric variability, the Arctic Oscillation (AO), which is derived from hundreds of data points across the entire northern hemisphere. A common way to calculate the NAO is to subtract the standardized (by standard deviation) mean sea level pressure anomaly at Stykkisholmur, Iceland from the standardized mean sea level pressure anomaly at Lisbon, Portugal (Hurrell 1995). This method is in line with the usual definitions of the NAO which examine the gradient in sea level pressure from the Azores high and the Icelandic low (Broccoli et al. 2001). Positive (negative) NAO index values correspond to a stronger (weaker) than usual Azores high and deeper (lower) than usual Icelandic low. In the positive (negative) NAO index, increased (decreased) pressure gradient results in more (less) frequent and stronger (weaker) extratropical cyclones crossing the North Atlantic on a more meridional (zonal) storm track.

When the Azores high pressure cell is stronger than average in March, April, and May, it feeds back in a self-enhancing loop that increases surface trade winds and thus surface evaporation in the eastern Atlantic. The increased evaporative cooling leads to cooler SSTs and higher surface pressures. The mean strength of this subtropical ridge in the Atlantic is negatively correlated with pressure anomalies in the Caribbean during the summer (Knaff 1998). Caribbean sea level pressure during the peak of the Atlantic hurricane season was one of the earliest known predictors of TC activity (e.g., Gray 1984), explaining 31% of the interannual variance in hurricane activity and 29% of the interannual variance in intense hurricane activity during the 1950-1995 period.

The NAO overlaps with the AO in the North Atlantic, and thus time series of the two patterns are highly correlated (the AO and NAO monthly values used in this study have linear correlation coefficients as large as 0.81), although the AO covers more of the Arctic and thus has a more zonally symmetric appearance (Thompson and Wallace 1998). Because the two indices are so related, there is some debate as to whether they are actually different indices for the same phenomenon (Wallace 2000), or if the NAO and Pacific-North American (PNA; see section 3.5.8) pattern together comprise the AO. Regardless, all three oscillations' phenotypical expressions are linked, and thus it is not surprising that the indices and spatial patterns are similar. The NAO exhibits both interannual and interseasonal variability, and consecutive months where the index is in one phase, followed immediately by consecutive months in the opposite phase, are common (Hurrell 1995).

3.5.8. Pacific-North American (PNA) pattern

The Pacific-North American (PNA) pattern is one of the two most important modes of variability (along with the NAO) in the northern hemisphere teleconnections patterns (Johansson 2007). Synopticians have routinely noticed persistent configurations of midtropospheric geopotential height in boreal winter extending from the middle Pacific Ocean to eastern North America (Wallace and Gutzler 1981). Above normal geopotential height over western North America tends to be accompanied by strongly negative height anomalies in the middle Pacific, near 45°N, and over the southeastern U.S. Specifically, strong positive correlations were noticed between 700 mb heights in the North Pacific (40°N, 150°W) and Cape Hatteras (35°N, 75°W; Namias 1951), and troughs over the eastern U.S. were often accompanied by ridges over the western U.S. on the mean monthly composite maps (Klein 1952). Dickson and Namias (1976) were the first to document the Pacific/North American teleconnections pattern. Wallace and Gutzler (1981) computed an index based on the linear combination of normalized (by standard deviation) 500 hPa geopotential height anomalies near Hawaii (20°N, 160°W), the North Pacific ocean (45°N, 165°W), Alberta (55°N, 115°W), and the U.S. Gulf coast region (30°N, 85°W). Specifically, the Wallace and Gutzler (1981) PNA pattern is given by

$$\begin{gathered}\mathrm{PNA}=\frac{1}{4}[z^*(20^\circ\mathrm{N},160^\circ\mathrm{W})-z^*(45^\circ\mathrm{N},165^\circ\mathrm{W})\\+z^*(55^\circ\mathrm{N},115^\circ\mathrm{W})-z^*(30^\circ\mathrm{N},85^\circ\mathrm{W})]\end{gathered} \tag{3.10}$$

where z^* (X,Y) denotes the monthly mean 500 hPa geopotential height anomaly at latitude X and longitude Y obtained by subtracting the monthly value from the mean monthly value over the 1950-2000 base period. The positive (negative) phase of the PNA index corresponds with above (below) average 500 hPa geopotential heights over Hawaii and southwestern North America and below (above) average 500 hPa geopotential heights south of the Aleutian Islands and in the southeastern U.S. The positive phase brings an enhanced East Asian jet stream and an eastward shift in the climatological position of the East Asian jet exit region. The negative PNA phase typically brings blocking (quasi-stationary regions of high geopotential heights) over the North Pacific and a strong split-flow jet stream configuration over the central North Pacific.

To determine skill in predicting the PNA and the NAO, 6 h forecasts from the operational uncoupled NCEP and ECMWF global models were examined out to seven days (168 h) for the period 22 January 2000 to 24 March 2005 (Johansson 2007). Skill was quantified by calculating a correlation coefficient between observed and forecast indices. The predictability of both the PNA and the NAO indices was found to be higher than that for the climatological Northern Hemisphere midlatitude flow. The PNA was found to have greater forecast skill than the NAO, although the physical reasoning remains unclear (Johansson 2007). Perhaps the five-year study was too short to fully capture the variance of the oscillations, which vary on interannual to decadal timescales.

The physical mechanisms that force the PNA and NAO are not very well understood (Johansson 2007). However, the two oscillations are thought to be internal to the atmosphere, primarily contained in the extratropical troposphere, and not directly coupled to the oceans (Hurrell et al. 2003; Straus and Shukla 2002). The extratropical oceans do indirectly modulate feedbacks to the atmosphere, as SSTs modulate sea level pressure and precipitable water content (e.g., Mosedale et al. 2006), and the tropical oceans, particularly the ENSO phenomenon, “probably” influence the PNA (Johansson 2007).

3.5.9. Alternative method for calculating NAO and PNA

Following the procedure outlined by the Climate Prediction Center (available online at <http://www.cpc.noaa.gov/data/teledoc/teleindcalc.shtml>), Northern Hemisphere teleconnections indices can be calculated using the Rotated Principal Component Analysis (RPCA) of Barnston and Livezey (1987). The CPC applied the RPCA technique to monthly mean 500 hPa height anomalies, standardized by the 1950-2000 base period, over the region 20°N-90°N. The data were provided by the CPC climate data assimilation system, CDAS, which is also the system used in the NCEP/NCAR Reanalysis (Kalnay et al. 1996). The CPC calculation proceeds as follows. For each calendar month, the ten leading unrotated empirical orthogonal functions (EOFs) are determined from the standardized monthly height anomalies over the three-month period centered on that month (centered using a simple arithmetic mean). A Varimax (Barnston and Livezey 1987) rotation is then applied to the ten leading un-rotated modes. This rotation yields ten time series for that calendar month, and the ten leading rotated modes are therefore based on 153 (51 years x 3 months) monthly standardized anomalies. During the Varimax rotation technique, the actual monthly indices are calculated using a least squares solution. The primary teleconnections patterns for all months are isolated and time series of each pattern are constructed. Of the twelve sets of rotated modes, ten are found to be the dominant teleconnections patterns. They are referred to as the North Atlantic Oscillation (NAO), the Pacific/North American (PNA) teleconnections pattern, the East Atlantic pattern, the West Pacific pattern, the East Pacific-North Pacific pattern, the East Atlantic/Western Russia pattern, the Tropical/Northern Hemisphere pattern, the Polar-Eurasian pattern, the Scandinavia pattern, and the Pacific Transition pattern. The monthly standardized northern hemisphere teleconnections indices may be accessed online at <ftp://ftp.cpc.ncep.noaa.gov/wd52dg/data/indices/tele_index.nh>.

3.5.10. The Arctic Oscillation (AO)

The Arctic Oscillation (AO) is defined as the first EOF of Northern Hemisphere mean sea level pressure. It is the dominant mode of variability of the extratropical Northern Hemisphere circulation (Zhou and Miller 2005), explaining 25% of the variance of the first EOF (Ambaum et al. 2001). It appears in EOF analysis of mean sea level pressure on a very broad time spectrum ranging from weeks to decades, and it exists in any season. The AO is maintained by midlatitude planetary Rossby waves, both stationary and transient, which interact with the mean zonal flow by their poleward transport of latent heat. The most pronounced feature of the AO pattern is the two same-signed correlation centers over the North Pacific and North Atlantic Oceans. Thus positive (negative) sea level pressures in the North Pacific correspond with positive (negative) sea level pressures over the North Atlantic.

The AO has been primarily linked with atmospheric variability during the cold season, when the oscillation is most pronounced. However the AO also contributes to a significant portion of the atmospheric circulation's total variance during the warm season, and the AO is evident in the troposphere throughout the year (Murname 2004). Positive (negative) AO index values are associated with higher (lower) sea level pressures at low latitudes, and positive (negative) values are also associated with stronger (weaker) westerly winds at mid- and high-latitudes.

The monthly AO index used in this study is constructed by the NOAA National Centers for Environmental Prediction (NCEP) Climate Prediction Center (CPC). It is calculated by first projecting daily 1000 hPa geopotential height anomalies poleward of 20°N onto the leading EOF of mean 1000 hPa geopotential heights and then averaging the daily values for each month. The geopotential height data are archived in the NCAR/NCEP Reanalysis (Kalnay et al. 1996) data, and the first EOF was derived from the mean 1000 hPa geopotential height during the 1979-2000 period following the methodology of Thompson and Wallace (1998). Monthly values of the index were then created from the mean of the daily values. The monthly AO index used in this study may be accessed online at <http://www.cpc.ncep.noaa.gov/products/precip/CWlink/daily_ao_index/monthly.ao.index.b50.current.ascii.table>.

3.5.11 Different datasets yield different correlation patterns

The NAO and PNA patterns have been studied extensively by climate scientists since their identification by Wallace and Gutzer (1981). A series of sensitivity tests conducted using two different datasets for both the NAO and the PNA show that the correlations between the climate indices and different measures of TC activity are dependent on the dataset chosen. The NAO and PNA indices first considered for this study were derived by the NOAA CPC using the method of rotated empirical orthogonal functions (Barnston and Livezey 1987) discussed above. The NAO index is a least-squares regression of monthly data onto the first rotated EOF; the PNA is a least-squares regression of monthly data onto the fifth rotated EOF. The second NAO index considered for this study is calculated from the method of Jones et al. (1997), Osborn (2004), and Osborn (2006), using a simple subtraction of the normalized sea level pressure at Reykjavik from the normalized sea level pressure at Gibraltar. The monthly NAO index is given by

$$\mathrm{NAO}_i = \frac{slp_{\mathrm{GIB},i}}{\sigma_i} - \frac{slp_{\mathrm{REY},i}}{\sigma_i} \tag{3.11}$$

where i represents the month and σ_i is the standard deviation of sea level pressure for month i. The normalization procedure divides the monthly pressure values by their standard deviations over the period 1951-1980 and removes the NAO bias toward Iceland (whose standard deviation is at least twice, and in some seasons four times, the standard deviations at Gibraltar).

The second PNA index considered for this study is calculated by the NOAA CPC using the modified pointwise method of Wallace and Gutzer (1981),

$$\begin{aligned}\mathrm{PNA}_{\mathrm{modified}} = \frac{1}{4}[&z*(15\text{-}25^\circ\mathrm{N},180\text{-}140^\circ\mathrm{W}) - z*(40\text{-}50^\circ\mathrm{N},180\text{-}140^\circ\mathrm{W}) \\ &+ z*(45\text{-}60^\circ\mathrm{N},125\text{-}105^\circ\mathrm{W}) - z*(25\text{-}35^\circ\mathrm{N},90\text{-}70^\circ\mathrm{W})]\end{aligned} \tag{3.12}$$

where z^* (X,Y) denotes the monthly mean 500 hPa geopotential height anomaly at latitude X and longitude Y obtained by subtracting the monthly value from the mean monthly value over the 1950-2000 base period.

Absolute differences between correlation coefficients using the methods described in 3.5.9 and the methods described in 3.5.11 were often 0.3 or greater. Furthermore, the NAO and PNA indices described in 3.5.9 were rarely statistically significantly correlated with TC activity. Therefore, because they provide stronger correlations with several metrics of TC activity, the Jones et al. (1997) monthly NAO indices and the modified Wallace and Gutzer (1981) PNA indices were used for this study. The NAO indices may be accessed online at <http://www.cru.uea.ac.uk /~timo/projpages/nao_update.htm>, and the monthly PNA indices may be accessed online at <http://www.cpc.noaa.gov/products/precip/CWlink/pna/norm.mon.pna.wg. jan1950-current.ascii.table>.

3.6 Quantifying relationship between TC activity and climate indices

To explain patterns of atmospheric and oceanographic variability, meteorologists frequently examine the temporal and spatial relationships between atmospheric variables and climatic indices. The most commonly employed statistical method to determine the relationship between two different variables is the test of linear correlation (e.g., Maloney and Esbensen 2007; Zheng and Frederiksen 2007; McGregor et al. 2007; Mandal et al. 2007; Chu and Zhao 2007; Grantz et al. 2007). Linear correlation is a robust statistical measure that quantifies the degree of monotonic association between two variables (Wilks 1995; Pires and Perdigão 2007). The Pearson product-moment correlation coefficient is one such measure of linear relationship between two variables. The correlation coefficient is given by

$$r = \frac{S_{xy}}{\sqrt{S_{xx}S_{yy}}}, \tag{3.13}$$

where S_{xy} is the covariance between variables x and y, S_{xx} is the variance of variable x, and S_{yy} is the variance of variable y. The covariance is given by

$$S_{xy} = \sum_{i=1}^{N} \frac{\left(x_i - \bar{x}\right)\left(y_i - \bar{y}\right)}{N}, \tag{3.14}$$

where $\bar{x}$ is the arithmetic mean of variable x, $\bar{y}$ is the arithmetic mean of variable y, and N is the number of observations. The Pearson product-moment correlation coefficient is useful because it does not depend on the units of x or y. It is also commutative, in that the correlation between variables x and y is the same as the correlation between variables y and x. Coefficients r vary between $-1.00 \leq r \leq 1.00$, where positive r corresponds to a positive linear relationship and negative r a negative linear relationship. Pearson's correlation is limited by its inability to resolve nonlinear relationships, an underlying assumption that the population is normally distributed, and by its sensitivity to outliers (Wilks 1995).

An alternative statistical test that does not require the population be normally distributed (only Gaussian) and is resistant to outliers is given by Spearman (Grantz et al. 2007). The Spearman rank correlation coefficient does not compute the correlation on the actual data, but rather from the ranks of the actual data. The smallest x (y) is assigned a rank of 1 (*1*) and the largest x (y) is assigned a rank of n. Spearman's rank correlation coefficient is given by

$$r = 1 - \frac{6\sum_{i=1}^{n} d_i^2}{n\left(n^2 - 1\right)}, \tag{3.15}$$

where d_i is the difference between the ranks of pair x_i and y_i and n is the number of paired values. Like the Pearson correlation, the Spearman correlation is sensitive to the data at the start and end of the record (Grantz et al. 2007). However, the correlation analysis uses ranks instead of actual data, thus decreasing its sensitivity to outliers, in this case very active or inactive TC seasons.

Both the Pearson and Spearman correlation coefficients rely on the assumption that the samples being tested have a Gaussian shape. Histogram plots of the datasets used in this study are have a Gaussian shape (e.g., see Fig. 3.1), but is this assumption valid for the correlation tests used in this section? Fortunately the answer to this question is found in the central limit theorem, which states for datasets of noninfinite variance and sufficiently large sample size, their sum will have a Gaussian distribution (LaCasce 2005). The datasets, both TC activity and climate indices, have noninfinite variance, and their sample sizes are larger than n=30. Thus the datasets are assumed Gaussian.

However, in addition to the Gaussian shape assumption, a Pearson correlation assumes that a sample is also normally distributed (Wilks 1995). To determine whether the TC activity metrics and climate indices are normally-distributed, the Anderson-Darling (Anderson and Darling 1952) empirical distribution function test of normality is used. The Anderson-Darling test is useful for several reasons: first, it only requires knowledge of a sample's mean and variance; second, it is robust and not sensitive to U-shaped or peaked rank historgrams; and third, it converges rapidly and thus retains considerable power even for small sample sizes (Elmore 2005). The relevant test statistic A^2 is given by

$$A^2 = \left(1 + \frac{0.75}{n} + \frac{2.25}{n^2}\right)\left[-n - \frac{1}{n}\sum_{i=1}^{n}(2i-1)\left(\ln\Phi(Y_i) + \ln\left(1-\Phi(Y_{n+1-i})\right)\right)\right], \quad (3.16)$$

where $\Phi(Y_i)$ returns the standard normal cumulative distribution function of Y_i, n is the number of observations (for this study, n is typically 37, from 1970-2006), and i is the summation index. The function Y_i returns the standardized value of each index x_i and is given by

$$Y_i = \frac{x_i - \bar{x}}{s}, \quad (3.17)$$

where $\bar{x}$ is the mean and s the standard deviation of the index. A null hypothesis H_0 stating that a sample is not significantly different from the standard normal distribution can be rejected, with 95% confidence, in favor of an alternative hypothesis H_A stating that the sample is significantly different from the standard normal distribution, whenever critical A^2 values do not exceed 0.721 (Stephens 1974).

Anderson-Darling test statistics were computed for each of the fifteen metrics of TC activity for each relevant basin (the landfalling TC metrics are only generated for the EPAC and NATL basins). Test statistics were also computed for each of the twelve climate indices for all twelve three-month periods. Tables 3.3-3.4 report the values of A^2 for each dataset. One hundred and three (71%) of the 144 climate indices are normally-distributed, but only 28 (31%) of the 89 TC activity metrics are normally-distributed. Therefore, because the Pearson product-moment correlation assumes that a sample is normally-distributed, this study will use the Spearman rank correlation to test the relationship between TC activity and climate indices. The Spearman correlation also has the advantage of being resistant to outliers.

To calculate Spearman correlation coefficients used in this study, each of the fifteen metrics of TC activity from each of the nine basins were ranked, with the year having the lowest level of activity ranked as "1" and the year having the highest level of activity ranked as "37". The corresponding climate indices were also ranked in the same manner. Then the ranks were used in (3.15) to generate correlation coefficients *r*. Similar to the Pearson coefficient discussed above, the Spearman coefficients *r* vary between $-1.00 \le r \le 1.00$, where positive *r* corresponds to a positive linear relationship and negative *r* a negative linear relationship. When *r* is unity, the relationship is perfectly one-to-one. The significance of the correlation coefficient is given by

$$t_{crit} = \frac{r}{\sqrt{\left(1-r^2\right)\left(n-2\right)}}, \tag{3.18}$$

where *r* is the Spearman rank correlation coefficient and *n* is the sample size (Press 1992). For *n*-2 degrees of freedom, the critical *t* for 95% confidence is 2.032. This *t* corresponds to a correlation coefficient of ± 0.329. Thus, correlation coefficients that are greater than 0.329 or less than -0.329 are, with 95% confidence, statistically significantly different from 0.0.

3.7 Relationships and associations between TC activity and climate indices

The previous discussion detailed several reasons to examine the relationships between TC activity and various atmospheric variables. Up to the present day, no encyclopedic quantification of the relationship between the nine basins and the twelve climate indices has been undertaken. Now that the climatic records – both of TC activity and modes of atmospheric variability – are sufficiently long, such a record must be presented. The twelve climatic indices are divided into twelve 3-month periods, and nine ocean basins with fifteen TC activity metrics are examined. In total, 12,816 rank correlation coefficients were calculated and scrutinized to determine the relationships between the atmosphere, the oceans, and TC activity.

Two themes are prevalent throughout the correlation data, and these themes are highlighted in the sections below. The first major theme is the strength of the SST signal in each of the other modes of oscillation. In a wavelet analysis of 1970-2006 monthly NINO3 SSTs, following the method of Torrence and Compo (1998) that is available online at <http://atoc.colorado.edu/research/wavelets/software.html>, peaks in the power spectra occur at the timescales of the PNA and the MJO (intraseasonal oscillations), ENSO, NAO, QBO, SOI, and NOI (interannual oscillations), and AO and PDO (decadal to interdecadal oscillations) (Fig. 3.33). The modes are also visible in wavelet analyses at peaks in the power spectra corresponding to the timescales of the leading modes (see Figs. 3.34-3.38). The second major theme is the out-of-phase relationships between the East Pacific and North Atlantic (and subbasins). TC activity between each basin is negatively correlated, and coefficients *r* are routinely statistically significant (Table 3.5). The correlations reveal that active (inactive) EPAC seasons tend to be paired with inactive (active) NATL seasons. These correlations are repeatedly substantiated by the out-of-phase correlations between EPAC and NATL TC activity and the climate indices. When the out-of-phase relationships were first noticed, it was not clear why they appeared so frequently between multiple metrics of TC activity. However, they were suggestive of teleconnections with larger-scale atmospheric and oceanic modes of variability, and it was this out-of-phase relationship which spurred much of the investigation presented in Chapter 3. Specifically, I wanted to test the hypothesis that large-scale patterns which favored TC activity in some basins would also limit TC activity in other basins.

Fig. 3.2 shows the spatial distribution of the correlations between IHC and Jul-Sep climate indices. Notice that NINO1.2, NINO3, NINO3.4, NINO4, SOI, and NOI correlations switch signs from the NATL, CARIB, and GOM to the EPAC, EEPAC, WEPAC, and CPAC, corroborating the see-saw patterns of TC activity between the EPAC and NATL. Notice also the relative importance of NINO4 to the WEPAC and CPAC, and NASST to the NATL, CARIB, and AMDR. These two (NINO4 and NASST) are approximately in situ measures of SST in those basins. Finally, notice the high correlations between the PNA and the WEPAC and CPAC; for those basins, the PNA is also an approximately in situ measure of midtropospheric geopotential height.

These associations are a preview of the many relationships found within and across the nine basins. In the next nine subsections, relationships between subbasin TC activity and the climate indices will be discussed in context of the dominant themes outlined above. The utility of the fifteen metrics of TC activity will also be demonstrated with foci on the advantages and disadvantages of each metric and which method(s) are the best for quantifying TC activity. Beginning with the EPAC and concluding with the AMDR, Figs. 3.3 – 3.32 display each of the correlation coefficients between each metric and climate index.

3.7.1 EPAC

The EPAC, as with most of the subbasins, exhibits mostly statistically insignificant correlations ($-0.329 \leq r \leq +0.329$) in the months before the start of the season (on 15 May). However, for every three-month period, at least two statistically significant correlations, one positive and one negative, exist. The Jan-Mar AO and NAO are positively correlated with ACE and PDI, indicating that the AO and NAO are possible predictors of seasonal values of ACE and PDI. However, the Jan-Mar AO and NAO are not significantly correlated with TCC, HC, or IHC. The largest EPAC correlations are found in Jun-Aug, Jul-Sep, Aug-Oct, and Sept-Nov, and are between the four NINO indices and SMD. This result is indicative of the prominence of the association between SSTs (the first theme discussed above) and TC activity. Although correlation coefficients only reveal relation, not causation, in this case the causation is straightforward. When the NINO indices are positive during the summer months, warm SSTs favor TCs forming later in the season, and thus SMD is later. The same signal is also seen in the correlations between ENSO and SED: warm Jun-Nov SSTs favor for late-forming TCs. The strongest negative correlations in the EPAC are found between ACE, PDI, SMD, and SED and the SOI and NOI. These signals are not surprising considering the strong ($|r| \geq 0.7$) correlations of SOI and NOI with ENSO. Negative SOI and NOI values occur when the tropical Pacific easterlies are anomalously weak, and these weak trade winds are associated with warm SSTs in the ENSO regions. Warm SSTs are favorable for TC genesis. Finally, illustrating both the first and second themes, the NASST index is significantly negatively correlated with EPAC TCC, HC, IHC, and ACE, beginning in Aug-Oct and continuing through Dec-Feb. Warmer North

Atlantic SSTs are related to lower EPAC activity levels, although the causation remains unclear. Thus to summarize: the AO and NAO indices are significant during boreal winter, and the NINO1.2, NINO3, NINO3.4, NINO4 , NOI, SOI, and NASST indices are significant during boreal summer and early autumn months.

3.7.2 NATL

Like the EPAC, the most frequently significant correlations with TC activity in the NATL are the indices closely tied to SST: NINO1.2, NINO3, NINO3.4, NINO4, NASST, NOI, and SOI. From May-Jul to Dec-Feb, these SST-based indices indicate not only a statistically significant relationship with TCC, HC, IHC, ACE, SMD, SED, TCLC, and TCLP, but often a strong relationship with $|r|$ exceeding 0.6. The correlations reveal an inverse association between warmer (cooler) equatorial Pacific SSTs and fewer (more) NATL TCs, hurricanes, and intense hurricanes. They also reveal that warm equatorial Pacific SSTs occur during NATL seasons with early SMD and SED. Interestingly, the only SST-based index that maintains a strong correlation with PDI is the NASST, indicating that in situ SSTs are important for long-lived (but not necessarily intense; see below) TCs. It is not surprising that the NINO-based indices are also related to TC landfall: fewer (more) NATL TCs make landfall when the NINO indices are positive (negative), and not only do fewer (more) TCs make landfall, but also a smaller (larger) proportion of TCs make landfall when the NINO indices are positive (negative).

These relationships (except the NASST) are all part of the established teleconnection between ENSO, vertical shear, and NATL TC activity. Earlier studies found an inverse relationship between ENSO and NATL hurricane activity, but this dissertation is unique in its approach to separating the different ENSO regions and testing their relationships to TC activity across ocean basins and subbasins. There have been many recent studies that examined the relationship between one combined ENSO index and NATL TC activity (e.g., Smith et al. 2007; Elsner et al. 2006; Jagger and Elsner 2006; Bell and Chelliah 2006; Xie et al. 2005; Larson et al. 2005; and Lyons 2004); however, few studies separate the individual NINO regions (e.g., Klotzbach and Gray 2004), and to the author's knowledge, no studies examine the relationship between individual NINO regions and the nine basins selected for this investigation. The four NINO regions are strongly positively correlated with one another ($r \approx 0.70$), however, they are not equal, and different ENSO events have had differing impacts on regional SSTs (e.g., Trenberth and Smith 2006). Thus there is value in treating each NINO index separately.

The approximately in situ NASST is significantly positively correlated, beginning in May-Jul and continuing to Dec-Feb, with NATL TC, HC, ACE, and PDI. NASST shows weaker positive correlations with IHC, which is surprising given the ongoing (as of September 2007) heated discussion of the impacts of changing global temperature on intense hurricanes. The lack of relationship between NASST and IHC is also surprising given its strong correlation with ACE and PDI. Recall that ACE, and especially PDI, are very sensitive to extreme wind speeds, but that they are also integrated quantities that are also sensitive to longevity. Thus warm North Atlantic SSTs (positive NASST index) indicate a preference for not only more frequent but also longer-lived TCs, and this result is verified by the strong positive correlations between

NASST and STCD (a measure of longevity of TCs). The weaker, but still positive, correlation between NASST and IHC indicates that perhaps the most intense hurricanes are not limited by SST but instead by another atmospheric variable.

It is also interesting that the Pacific SST correlation patterns align in an east-to-west direction, whereby the region closest to the NATL, NINO1.2, has the highest correlations, and the region farthest from the NATL, NINO4, has the lowest correlations. For IHC, the NINO1.2 correlations between Jul-Sep and Sep-Nov are almost twice as negative as the NINO4 correlations. The strongest negative correlations for the four NINO regions (reflected by the strongest positive NOI and SOI correlations) are with the IHC metric. Given that the warm ENSO phase is associated with anomalously high vertical wind shear over the NATL, it is interesting to see the ENSO phase most strongly associated with NATL IHC (instead of TCC or HC). This relationship matches well with the discussion above regarding the insensitivity of NATL IHC to NASST. Specifically, the two relationships provide evidence that intense hurricanes are perhaps not limited by the warmth of the sea surface beneath them but instead by the vertical wind shear of their environment. This hypothesis deserves future investigation as it has significant implications in the debate over the impacts of global temperature change on regional TC activity.

Interestingly – and significantly – absent from the NATL correlations is the QBO. This is in direct contrast with the early studies of Gray (1984) and Gray et al. (1993), which reported an association between QBO phase and NATL hurricane activity. The only statistically significant relationships (but only moderately strong, $|r| \leq 0.4$) are found between the Oct-Dec and Nov-Jan QBO and IHC and also between the

Jan-Mar QBO and TCLP. The lack of association is perhaps linked to differences between measurement of QBO, although both Gray (1984) and the QBO index of this study use the zonal wind measured at 30 hPa to determine the phase. This study has the advantage of 24 additional years of data, but Gray (1984) used actual rawinsonde data whereas this study uses Reanalysis data. Instead of measurement differences, however, it is perhaps more likely that the QBO does not impact tropical cyclogenesis outside of the deep tropics (poleward of 20°). The NATL index covers the entire North Atlantic basin, including deep tropics, subtropics (between 20° and 35°), and midlatitudes (poleward of 35°). Thus it will be resistant to impacts from the QBO. The true impacts of the QBO can be seen by its strong correlations (*r* approaching -0.70) with CARIB and AMDR, subbasins which are almost entirely within the deep tropics. This relationship is in agreement with Gray (1984), where positive QBO (easterly zonal winds) results in fewer intense hurricanes in the deep tropics. Thus, the importance in relating climate indices to basin activity is demonstrated: in the full NATL basin, TC activity has no significant relationship to QBO phase, but in the deep tropics, it has a moderate to strong relationship. Without examining basins smaller than the NATL, this relationship would remain obscured.

The PDO and PNA have some statistically significant correlation with TC activity. The Jul-Sep to Nov-Jan PDO is significantly negatively correlated with IHC, and to a lesser extent, TCC and HC, but it is not significantly correlated with ACE, PDI, or STCD. This relationship indicates that positive PDO phase (warm SST anomalies and positive sea level pressure anomalies in the northeast Pacific) is associated with reduced NATL TC activity, which is not surprising given the tendency for the PDO to couple in-phase with ENSO (Goodrich 2007). The most significant PNA correlations occur in the mid-season Jul-Sep, Aug-Oct, and Sep-Nov periods. It is positively correlated with PDI and STCD (but not significantly related to TCC, HC, IHC, or ACE). As discussed above, STCD and PDI are sensitive to longevity, and thus the positive PNA index, which brings positive 500 hPa height anomalies over the southeast U.S. and into the western North Atlantic, is associated with long-lived TCs. The PNA-to-TC-longevity relationship is physically reasonable, as a pronounced 500 hPa anticyclone over the western North Atlantic steers any TCs that form westward, preventing recurvature and the decay that comes with cooler SSTs and greater wind shear in the midlatitudes. Thus, forecasts of TC activity on a weekly timescale should account for the current phase of the PNA. The PNA index does not correlate with TC genesis, but it does correlate with longevity.

Finally, the AO and NAO show some significant, but moderate ($|r| \leq 0.6$), negative correlations at the important lead times of Jan-Mar, Feb-Apr, and Mar-May for TCC, HC, and IHC. (Winter months with statistically significant correlations are important because their indices allow for seasonal predictions of TC activity from observational, rather than model, data.) These relationships indicate that weaker and more zonal middle and high latitude winds, characteristic of the weak Azores-Iceland gradient (the NAO signal) and negative sea level pressure anomalies in the low latitudes (the AO signal), are associated with more NATL TC activity. Because the dominant the NASST index is most correlated with NATL TC activity, the question remains whether the NAO and AO are related to, or perhaps even force, North Atlantic SSTs. However, the Feb NAO and AO are not correlated with Feb or Sep NASST ($|r| \leq 0.20$), implying that the NASST signal is independent of the NAO and AO signals. Thus the pre-season values of AO and NAO have important relationships to NATL TC activity.

3.7.3 CARIB and GOM

Because the CARIB and GOM are adjacent subbasins of the NATL, the three have several similar correlation patterns. Like the NATL, the CARIB May-Jul to Dec-Feb NOI and SOI are significantly positively correlated with TCC, HC, ACE, and STCD, and NINO1.2, NINO3, NINO3.4, and NINO4 are negatively correlated with TCC, HC, ACE, and STCD. Spatially, the correlations are strongest in the easternmost tropical Pacific (NINO1.2 region) and diminish westward (to the NINO4 region). The corresponding GOM correlations are not as strong but have the same statistical pattern as the CARIB. The physical implications remain the same for both subbasins: warm ENSO waters are associated with lower CARIB and GOM genesis (TCC), intensification (HC and ACE), and longevity (STCD) because the relevant ENSO teleconnection is to modulate vertical wind shear over the NATL, CARIB, and GOM. The ENSO-related indices are also significantly correlated with CARIB SED, and these correlations are significant from Jan-Mar through the season. As with the NATL, the physical interpretation is that warm ENSO waters enhance vertical wind shear over the CARIB (and, to a lesser extent, the GOM), but the strongest vertical shear anomalies arrive at the end of the season.

NASST is moderately, and occasionally strongly, positively correlated with CARIB ACE, PDI, and STCD, and its correlations are statistically significant at all time periods. The preseason (Jan to Jun) NASST correlations are especially interesting because their signal can be used as a preseason predictor. Like its parent basin the NATL, the CARIB NASST index is not strongly correlated with the counted metrics of TC activity (TCC, HC, or IHC), indicating that warm water in the North Atlantic during winter and spring is associated not with more TCs, hurricanes, or intense hurricanes, but rather with longer-track TCs of varying intensities. As discussed for the NATL, a statistically significant negative correlation exists between QBO and IHC. However, this relationship is only found between the QBO and CARIB intense hurricanes, not GOM intense hurricanes, thus providing further evidence that the QBO is restricted to the tropics equatorward of 20°.

The AO and NAO are both significantly negatively correlated with CARIB and GOM HC and IHC from Jan-Mar to Apr-Jun, and the AO is strongly correlated with CARIB and GOM IHC. Physically, a negative AO index corresponds to low sea level pressures in the tropical North Atlantic and weaker westerly winds in the mid- and high-latitude North Atlantic; a negative NAO index corresponds to a weak pressure gradient between the Azores high and the Icelandic low, leading to weaker midlatitude winds and more zonal extratropical storm track across the North Atlantic. The connection to CARIB and GOM intense hurricanes is not very straightforward: when the AO and NAO are negative from Jan to Jun, zonal flow prevails across the central and northern North Atlantic, preventing midlatitude extratropical systems from reaching deep into the tropics. The lack of extratropical systems extending into the deep tropics keeps SSTs warmer during the winter and spring and translates into favorable conditions for CARIB and GOM intense hurricanes. The teleconnection between winter-spring AO and NAO and September NASST was examined in the last section and no correlation was found. However, this pattern is potentially useful as a predictor, and thus future study examining the physical relationship is suggested.

Like the full NATL basin, CARIB and GOM TCC and HC are negatively correlated with late spring (Apr-Jun) PNA and early autumn (Sep-Nov and Oct-Dec) PDO. Negative PNA corresponds physically with 500 hPa ridging over the southeast U.S. and western North Atlantic, and positive PDO corresponds to warm SSTs along the U.S. west coast and high sea level pressures in the subtropical north Pacific. Physically, the midtropospheric ridging associated with the negative PNA sets up favorable conditions for early-season TCs to develop (TCC) and intensify (HC). The PDO is known to enhance ENSO when the two are in the same phase; thus, positive PDO will enhance the effects of the positive ENSO phase and reduce TCC, HC, and IHC over the CARIB and GOM.

3.7.4 AMDR

The AMDR is essentially an eastward extension of the CARIB subbasin, extending along roughly the same latitude zone from West Africa to Central America. It includes most of the CARIB basin; however, because it is farther east than the CARIB and occupies the southernmost portion of the NATL, it is a unique subbasin. For example, the ENSO signal, which is prominent for the NATL, CARIB, and GOM, is only weakly statistically significant in the AMDR, indicating that the teleconnection between warm equatorial Pacific waters and enhanced tropical Atlantic vertical wind shear is not as strong across the hemisphere. NASST remains moderately to strongly positively correlated with TCC, HC, IHC, ACE, and PDI, but it is no longer the source of the largest correlations. AMDR IHC is strongly associated with QBO, AO, and NAO. In particular, the Jan-Mar to Apr-Jun AO is very strongly negatively correlated with IHC, with $r \approx -0.9$. Following linear correlation theory, the AO thus explains over 80% of the variance (r^2) in AMDR intense hurricane activity. However, by Aug-Oct, the AO is no longer statistically significant, complicating the question of its association to IHC. In a similar fashion, the NAO is strongly negatively correlated with IHC in winter and spring, but by the peak of the season, it is not statistically different from zero correlation. Thus, in addition to the spatial teleconnection between AO and NAO and the AMDR, the temporal teleconnection between Mar-May AO and NAO and Aug-Oct intense hurricane activity is very important. The physical reasoning for these connections, however, remains unclear.

Like the CARIB, GOM, and NATL, the PDO and PNA are mostly insignificant for the AMDR subbasin. However, they are negatively correlated with TCC and HC, with the PNA signal appearing early in the season and the PDO signal appearing late in the season. The physical reasoning behind these associations is similar to the reasoning for the CARIB and GOM subbasins.

3.7.5 EEPAC and CEPAC

The eastern subbasins of the EPAC are spatially adjacent and thus they have similar correlation patterns. Surprisingly, though, neither subbasin has much association between the ENSO indices and TC activity. Only NINO1.2 is statistically significantly correlated with EEPAC and CEPAC PDI, and the general pattern is for the rest of the correlations to be weak ($|r| \leq 0.3$). The only consistent pattern of correlation with the ENSO indices is found with SMD, where the Jul-Sep to Dec-Feb ENSO indices are mostly statistically significant. Physically, this association implies that warm ENSO waters do not cause more TC activity, but rather cause the season to peak at a later date. This shift is found only in the mean day, not the start or end day, implying the season is not longer but more active later. For populations along the west coast of Mexico, where almost every landfalling TC has its origins in either the EEPAC or CEPAC, and the North American monsoon region of northwest Mexico and the southwest U.S., this relationship implies that the sensible weather brought by EEPAC and CEPAC TCs will occur later in the year.

The QBO is significantly negatively correlated with EEPAC, but not CEPAC, hurricane activity (HC), reinforcing the conclusion that the QBO's effects are contained in low latitudes (the EEPAC is mostly equatorward of 20°N, while the CEPAC extends poleward of 20°N). The PDO, PNA, NAO, and AO are all negatively correlated with EEPAC HC, indicating that low sea level pressures in the subtropical Pacific (negative PDO), low 500 hPa heights along the U.S. west coast (negative PNA), weak pressure gradient across the North Atlantic (negative NAO), and low sea level pressures across the tropical North Atlantic (negative AO) are all associated with more hurricanes in the EEPAC. In the CEPAC, negative Aug-Oct PNA and positive Aug-Oct NAO are both statistically significantly correlated to TCC. Finally, it is important to note that only one intense hurricane formed in the EEPAC from 1970-2006 (and therefore correlations between that activity metric and the climate indices are not available).

3.7.6 WEPAC and CPAC

Like the EEPAC and CEPAC, the WEPAC and CPAC show less sensitivity to NINO1.2, NINO3, NINO3.4, and NINO4 than their Atlantic subbasin counterparts. Unlike the eastern EPAC subbasins, though, the most significant correlations are found between the PNA and SOI and IHC, with several three-month periods approaching $r \geq -0.8$. Similar but weaker correlations are found between PNA and WEPAC TCC and HC, and similarly strong correlations are found between the SOI and CPAC TC and HC. The physical relationship behind these strong associations is clear: both the PNA and the SOI are based in the central Pacific Ocean, and thus their teleconnections to the atmosphere and oceans are nearly in situ. Negative PNA corresponds to low 500 hPa height anomalies over Hawaii, and negative SOI corresponds to warm SST in the central tropical Pacific. Both physical responses are associated with favorable conditions for TC genesis (TCC) and intensification (HC and IHC). They do not, however, favor TC longevity, as the correlations between PNA and SOI and ACE, PDI, and STCD are much lower. The in-season (May-Jul to Oct-Dec) AO and NAO are moderately negatively correlated with CPAC IHC, indicating that the teleconnections between the North Atlantic extend halfway around the globe. Finally, the QBO is strongly ($r \leq -0.6$) negatively correlated with CPAC IHC, and because almost all CPAC intense hurricanes form equatorward of 20°N, this relationship provides yet another confirmation of the importance of the QBO in the intensification of TCs in the deep tropics.

3.8 Conclusions and future work

The goals of this investigation were to (1) show that TC activity is related to the leading modes of atmospheric and oceanic variability; (2) quantify the association using robust statistical techniques; (3) demonstrate that the relationships are not static but vary across subbasins and TC activity metrics; and (4) infer physical relationships, where possible, that connect TC activity to the atmosphere and oceans. I used TC best track data, along with time series of twelve climate indices, to document accomplish these goals. I found that SSTs dominate the frequency, intensity, duration, and seasonality of TC activity. These patterns of variation – particularly the detailed linkages between the four NINO regions, the Northern and Southern oscillations, and North Atlantic SSTs and the nine basins – are one of the major contributions of this investigation. I add value to earlier studies of the relationships between TC activity and ENSO which did not examine the NINO regions separately or correlate them over different basins or metrics of TC activity. I also found that the QBO is very relevant, particularly to intense hurricane activity, at low latitudes, equatorward of 20°N, but that its importance rapidly diminishes beyond the deep tropics. Finally, I found significant relationships between TC frequency, intensity, and seasonality and the PNA, NAO, AO, and PDO, and that these associations are spread throughout the nine basins. These relationships are vital to users across the disciplines of meteorology, economics, business, and sociology who wish to understand seasonal variability in TC activity. The most natural next step for this research is to apply it to predict TC activity in the forecasting arena on intraseasonal to seasonal timescales and in the climate arena on interannual to interdecadal timescales.

Chapter 4: Modulation of TC activity by the Madden-Julian Oscillation

For the final section of this dissertation, I investigated the relationships between TC activity and the leading intraseasonal mode of atmospheric and oceanic variability, the Madden-Julian Oscillation. Initialization errors and chaotic atmospheric variability lead to diminishing atmospheric predictability from dynamical numerical weather prediction beyond about seven days (Leslie et al. 1989). However, accurate guidance of TC activity on one- to two-week timescales would be highly useful (Hall et al. 2001) to many users, including forecasters, energy traders, and emergency managers. Thus, the primary objective of this section is to demonstrate modulation of TC activity in nine basins on one- to two-week timescales by the MJO. To accomplish this goal, I examined the relationships between an operational MJO index and North Atlantic and East Pacific TC activity. Like the previous investigation, I define TC activity in several ways, categorizing it by genesis, intensification, and landfall. I quantify the MJO's modulation by contrasting observed TC activity in each basin with expected TC activity during each MJO phase. Statistically significant relationships were found for each basin and across the MJO indices, and these results are presented in this chapter.

Understanding tropical cyclogenesis is fundamental to both short and long term planning decisions. Immediate actions, in response to a possible tropical cyclone threat, need to be taken by multiple levels of societal organization. Satellite rapid-scan operations can be ordered (and the appropriate satellites could be repositioned, if necessary), aircraft reconnaissance and other in situ observation platforms (both operational and research) can gather instrumentation and personnel and pre-deploy, civilian, military, and commercial human forecasting shifts can be scheduled, processor time can be reserved on national supercomputing systems, and emergency management operations can be brought to a higher level of readiness, all with foreknowledge of likely tropical cyclogenesis activity in a specific basin or sub-basin. Organized preparations for landfalling TC impacts lead to dramatic reductions in loss of life and property (Sheets 1990). Thus, the ability to accurately predict these impacts is highly beneficial to society.

Much of recent research has concentrated on two ends of a time spectrum: the near-real-time timescale, forecasting track and intensity of an existing TC out to five days, and the climate timescale, forecasting seasonal and longer trends in TC activity. Advances in near-real-time forecasts have come primarily through improvements in numerical weather prediction, both dynamical and statistical-climatological (Barrett et al. 2006). Beyond this timescale, in the 5- to 20-day window, initialization errors and chaotic atmospheric variability lead to diminishing atmospheric predictability from dynamical numerical weather prediction (Leslie et al. 1989). It is in this window that accurate guidance, particularly in forecasting cyclogenesis, would prove highly useful (Hall et al. 2001). For sub-basins where the life cycle from disturbance to landfall is often only a few days, such as the Gulf of Mexico, Caribbean Sea, and the eastern East Pacific adjacent to Mexico, short-term guidance for expected TC activity is especially needed. Because currently-available dynamical guidance does not provide reliable predictions for TC activity beyond about five days, establishing controlling relationships between predictable long-period oscillations – such as the MJO – and TC activity will provide great benefit in both the short- and long-term planning arenas. It should be noted that for this chapter, the MJO will be presented as a cohesive, planetary-scale oscillation that exists in some form outside the eastern hemisphere tropics. As will be discussed below, there is some debate whether the oscillation can be truly identified in the western hemisphere, as the coupled upper- and lower-tropospheric divergence-convergence couplet is not seen in time series analyses of rawinsonde data in several western hemisphere stations. However, because the upper-tropospheric divergence component of the MJO is still observed in the western hemisphere, for the purposes of this dissertation, the phenomenon will be labeled the MJO.

4.1. The Madden-Julian Oscillation

In a spectral analysis of tropical rawinsonde data from 1959-1967 at Canton Island station (2.8 °S, 171.7 °W) in the South Pacific Ocean, Madden and Julian (1971) noticed distinct spectral peaks (maxima) in the 850 hPa and 150 hPa zonal (*u*) wind component in the 41-53 day range. Specifically, when positive *u*-wind anomalies (weak easterlies, or westerlies) were observed at 850 hPa, negative *u*-wind anomalies (weak westerlies, or easterlies) were observed at 150 hPa. The greatest coherence-squared values between 850 and 150 hPa were observed at a period of 44 days, and the *u*-wind was found to be out of phase by 177 ° (strong easterlies at 850 hPa were accompanied by strong westerlies at 150 hPa; Madden and Julian 1971). No similar oscillations were found in the meridional (*v*) wind component.

To further examine the uniqueness of their observation, Madden and Julian (1972), hereafter MJ72, performed the same spectral analysis on data from several other tropical rawinsonde stations, including Balboa, Panama (9.0 °N, 79.6 °W); Dar es Salaam (0.8 °S, 39.3 °E); Gan Island (0.7 °S, 73.2 °E); Singapore (1.4 °N, 103.9 °E); and Chuuk (7.4 °N, 151.8 °E). The 40- to 50-day kinematic oscillation observed at Canton Island station was also observed at these locations, thus confirming the existence and planetary scope of the oscillation. However, by examining tropical stations in all four hemisphere quadrants, a discontinuity in the spectral data was revealed. The low-tropospheric (850 hPa) disturbance was found confined to the Pacific region, while the upper-tropospheric disturbance was found to affect the entire circumference of the earth. The disturbances were found to have eastward phase angles (and thus motion components). MJ72 also examined station pressure data from 25 sites equally distributed around the tropics, and they carefully selected several of the sites to include very long time series, some originating before 1900. The results of the long spectral analysis allowed MJ72 to conclude that the 40- to 50-day oscillation was not a temporary phenomenon in the equatorial Pacific that occurred only in the late 1950s and 1960s. Rather, it was found frequently throughout the 70-year time series, and as was corroborated by other shorter-period analyses from the stations listed above, the disturbance was not confined to the Pacific basin.

Zonal wind and surface pressure anomalies were seen to progress steadily eastward on time-height figures. Thus, MJ72 separated the disturbance temporally and spatially into eight 5-day categories, labeled A through H, and together the eight "phases" depict the disturbance circumnavigating the tropics in 40 days (Fig. 4.1). The first phase, arbitrarily labeled "F" by MJ72, features a developing area of concentrated convection near the maritime continent (the region including Indonesia, northern

Australia, and surrounding islands), coupled with surface (upper-level) convergence (divergence) and high (low) sea level pressures to the east (west). Halfway through the oscillation, or twenty days beyond phase "F", in phase "B", the region of enhanced convection, along with the surface convergence and upper divergence dipole, is shown to have propagated eastward into the central Pacific. Sea level pressures had risen over the maritime continent and fallen in the central and eastern pacific. The next frames, "C" to "E", show the disturbance propagating back into the eastern hemisphere and completing the circuit to the maritime continent. This eight-phase categorization has since become the classical manner to describe the phenomenon now named the "Madden-Julian Oscillation" (MJO). The oscillation has come to be regarded as one of the primary low-frequency (when compared against the periodicity of other modes of variability, such as ENSO, NAO, AO, or PDO) modes of variability in the tropical atmosphere, and the primary mode of oscillation on intraseasonal timescales (Jones et al. 1998).

4.1.1. Atmospheric physical response to the oscillation

The MJO originates as synoptic-scale circulation cells oriented in the equatorial plane that propagate eastward from the Indian Ocean into the central Pacific Ocean. Although the complete circulation cells do not extend beyond the Pacific, zonal wind and velocity potential anomalies in the upper-troposphere are observed to circumnavigate the globe. A primary phenotypical expression of the oscillation is in the enhancement (or suppression) of convective regions, which are also observed to propagate eastward. It is therefore no surprise that one of the first-analyzed impacts of the MJO was in the Indian-Australian monsoon region. Using space-time spectral analysis of satellite-determined cloud brightness from May to October 1967, a relative maximum in the eastward propagation was found at 60 days (Gruber 1974). This finding is consistent with the observation that during northern summer the maximum convective activity was between 5° and 10°N, and during northern winter it was between the equator and 5°S, thus implying that the maximum 40- to 50-day convective cloud activity was found in the intertropical convergence zone (ITCZ). The MJO is also evident in space-time plots of outgoing longwave radiation (OLR). Lau and Chan (1986) presented observations of a 40-50-day oscillation in May-October OLR over nearly the entire northern Indian Ocean and western Pacific, and the maximum amplitude was found to occur in the eastern hemisphere.

Although the classical reference was to a “40-50-day oscillation” (Madden and Julian 1971), the oscillation is now regarded as a relatively broadband phenomenon, not a highly-tuned periodicity. The 40- to 50-day constraints are only approximate, as other authors (e.g., Krishnamurti and Subrahmanyam 1982 and Weickmann et al. 1985) have preferred to label it as the 30-to 50- or the 30- to 60-day oscillation. These labels are not contradictory to the original finding of MJ72, because while the original spectral analysis peaked from 41-53 days (MJ72), it had long tails. Furthermore, Gray (1988) and Kuhnel (1989) found that during strong warm ENSO periods (especially the 1982/83 event), the oscillation tends to have a higher frequency, although there is no obvious change in the mean period with season (Anderson et al. 1984; Madden and Julian 1994). The oscillation was found to have slight seasonality with its locations of maximum OLR variability, and this variability was found to be connected with annual fluctuations in SSTs (Knutson and Weickmann 1987).

It has been shown that equatorially trapped waves (Kelvin and Rossby waves) are the primary modes of the MJO (Geerts and Wheeler 1998). Specifically, in the eastern hemisphere, the MJO exhibits mixed Kelvin-Rossby wave structure, and it exhibits only a Kelvin wave structure in the western hemisphere. Surface observations taken during the TOGA-COARE experiment reveal local changes in SST in excess of 1°C associated with passage of the MJO (Gutzler et al. 1994; Weller and Anderson 1996). These SST fluctuations resulted primarily from variations in shortwave radiation and the latent heat flux (Hendon 2000) and were associated with the passage of the region of maximum convection. The maximum surface moisture convergence, and hence latent heat flux at the surface, was found to slightly lag the decrease in shortwave radiation during the cloudy phase. Based on the TOGA-COARE observations and with supporting model results, several recent studies have concluded that two-way air-sea interaction is very important to the dynamics of the MJO (e.g., Inness and Slingo 2003; Krishnamurti and Chakraborty 2005). The MJO convection and SST anomalies are connected, as positive SST anomalies lead enhanced convection (positive SST anomalies are found to the east) because evaporation is lower and insolation greater in that phase of the oscillation (Lau and Sui 1997; Jones et al. 1998; Shinoda et al. 1998; see Fig. 4.2). As the oscillation progresses eastward over the positive SST anomalies, convective activity is enhanced causing lower insolation and increased surface winds (Maloney and Kiehl 2002). The MJO signal is visible at peaks in the power spectrum of about 40 days in a wavelet analysis of NINO3 SST data following the method of Torrence and Compo (1998) discussed in chapter 3 (see Fig. 4.18).

The MJO phase speed in the eastern hemisphere is eastward at approximately 5 m s^{-1}, but in the western hemisphere, it is observed to propagate eastward faster, at 10 m s^{-1}. The oscillation influences temperature, moisture, sea level pressure, the divergent and rotational wind components, and deep convection, and these influences can be found in both the tropics and the extratropics (Zhou and Miller 2005). Because of its interaction with deep convection (which has cold cloud tops and thus radiates less in the infrared), the MJO is readily detectable in time series of OLR anomalies. In the Australian and west Pacific basins, the MJO interacts strongly with deep convective thunderstorms, enhancing convection in one phase and suppressing convection in the opposite phase (Hendon and Liebmann 1994). During the active, convection-promoting MJO phase, "superclusters" (SCCs, Nakazawa 1988) of convective clouds, with diameters on the order of 3000 km, have been observed, forming a region of enhanced mesoscale organization. Khalsa and Steiner (1988) reported that high precipitable water contents accompanied the SCCs and noted that almost every occurrence of precipitable water anomalies above 38 mm was accompanied by an anomalous eastward-moving region of upper-tropospheric divergence (as measured by the 200 hPa velocity potential ϕ). This connection between the upper-tropospheric MJO and these tropical SCCs prompted research into multiple areas. One such phenomenon that was probably the first direct connection between the MJO and the earth-atmosphere system is the relationship between the MJO and the timing of the onset of the Asian-Australian summer monsoons (Yasunari 1980; Lau and Chan 1986; Hendon and Liebmann 1990).

It is from regions such as these SCCs that TCs initially form; thus, the MJO's modulation, whether to enhance or suppress tropical convection, depending on the phase, was hypothesized to be an important contributor to tropical cyclogenesis (Nakazawa 1988). Furthermore, as Madden and Julian (1971) observed, the disturbance affects upper-tropospheric flow in all tropical oceans, and the role of these upper-tropospheric teleconnections in modulating TC activity, especially in the western hemisphere, should be tested.

4.1.2. Oceanic physical response to the oscillation

Because the atmospheric component of the MJO extends to the near-surface flow, it affects wind stress variations over the global oceans. Positive wind stress occurs when surface winds are easterly (negative u) and yields transfer of eastward momentum from the earth to the atmosphere. Thus, the oscillation is also manifest in the underlying seas (Lau and Chan 1985, 1986), and a 30- to 60-day oscillation has been detected in time series of SSTs and near-surface ocean currents (see Fig. 4.18). The most prominent of these ocean-atmosphere linkages is the possibility of the MJO causing the onset of the warm ENSO phase (Krishnamurti et al. 1988). Oceanic Kelvin waves are excited west of the date line and propagate eastward, and then poleward along the west coasts of the Americas. The periodicity and phase delay of 43 days corresponds with a propagation velocity of 2.9 m s-1, which suggests that the MJO is a possible factor in encouraging the onset of ENSO.

The MJO interacts with a wide range of atmospheric and oceanic phenomena: the Indian monsoon system (Lau and Chan 1986); the tropical ocean (via strong westerly surface wind bursts); and the extratropics (Jones et al. 2004; Pohl and Chamberlin 2006), through which the MJO may impact weather and climate forecasts on longer timescales. In addition to the kinematic response in the lower- and upper-tropospheric wind fields, other near-surface and upper-ocean parameters also exhibit the MJO 30- to 60-day signature (e.g., Krishnamurti et al. 1988; McPhaden and Hayes 1991; and Jones and Weare 1996). Because the MJO is characterized by timescales long enough to interact with the oceans, the feedback is not limited in the atmosphere-to-ocean direction. SST variations in the Indian and Pacific Oceans, including the annual cycle of SST in the Indian Ocean monsoon region, can be determining factors in the spatial and annual variations of the MJO (Jones et al. 1998). In some cases, following successive eastward MJO passages into the eastern Pacific Ocean, westerly wind bursts that follow the convective anomalies excite Kelvin waves that propagate into the east Pacific. These oceanic waves result in slow eastward movement of higher SSTs and bear some similarities to the onset of the warm ENSO phase (Kessler et al. 1995). However, the knowledge of how these SST variations complement, or even cause, the onset of El Niño is still very incomplete (Jones et al. 1998).

4.1.3. MJO effects in North America

The eastward progression of MJO convective anomalies has been shown to influence the downstream development of a persistent North Pacific lower- and upper-tropospheric circulation anomaly during boreal winter (e.g., Higgins and Schubert 1996; Higgins and Mo 1997; Mo 2000; Hendon et al. 2007). This circulation anomaly – and therefore the MJO – has been connected with rainfall variability along the western

United States, including flash flooding events (Jones 2000; Whitaker and Weickmann 2001; Benedict and Randall 2007). Furthermore, Northern Hemisphere summertime precipitation variability is directly linked with the circulation anomalies over the Pacific-South American sector (e.g. Jones and Schemm 2000; Paegle et al. 2000; Ruane and Roads 2007). The North American monsoon, a seasonal enhancement of convective precipitation from June-September that is driven largely by enhanced solar heating along the Sierra Madre Occidental, is also directly affected by the MJO. When the MJO is active in the Western Hemisphere, there is a 40% increase (over the inactive phase) in the frequency of surges of moisture up the Gulf of California (Higgins and Gochis 2007). Northwest Mexico and Arizona rainfall exhibits significant correlation with MJO phase (Lorenz and Hartmann 2006).

4.1.4. Predicting the MJO

Although observed in multiple time series and studied for over three decades, the causative forcing of the MJO remains uncertain (Jones et al. 1998; Vitart et al. 2007). Several recent studies have demonstrated skillful empirical prediction of the MJO at lead times out to 15-20 days (von Storch and Xu 1990; Waliser et al. 1999; Lo and Hendon 2000; Mo 2001; Wheeler and Weickmann 2001; Jones et al. 2004; Reichler and Roads 2005; Hendon et al. 2007). This skill, while empirical, is demonstrably greater than current and previous NWP models (Waliser et al. 1999; Jones et al. 2000; Hall et al. 2001; Vitart 2003; Vitart et al. 2007). Given the theoretical growth of baroclinic disturbances (e.g., Lorenz 1969, 1982), the theoretical limit of predictability of synoptic-scale systems is on the order of a week or so. However, in the tropics, due to the overwhelming influence of diabatic heating from cumulus convection (Tiedtke et al. 1988) and the difficulty of parameterizing such processes whose timescales are much shorter than one week, NWP models often show skill at only a few days (Hendon et al. 2000). Additionally, NWP models with prescribed (fixed) SSTs have been generally unable to simulate the MJO event, producing a weak MJO that moves eastward too fast and with the wrong seasonality (Zhang 2005). An ensemble of forecasts can improve upon a single model's prediction (Toth and Kalnay 1993), providing a better estimate of weather elements' expected value and dependent probability distribution (Toth et al. 2001). However, beyond the skill barrier, useful extended-range predictions must rely on the exploitation of lower-frequency periodicities which occur in the atmosphere (Wheeler and Weickmann 2001). The MJO is one such intraseasonal oscillation that exists in the tropics and acts to organize convective elements upscale, from the mesoscale into spatial scales much larger than the individual elements themselves, and to temporal scales up to several weeks.

4.2. MJO connection to TC activity

4.2.1. Climatology of tropical cyclogenesis

Environmental conditions necessary for tropical cyclogenesis have been well known for four decades (e.g., Gray 1968; Gray 1979; Briegel and Frank 1997; Webster et al. 2005; Emanuel 2005; Mann et al. 2007): SSTs greater than 26.5 C with a deeply mixed warm ocean layer; a cyclonic low-level vorticity anomaly; weak and preferably easterly vertical shear of the horizontal wind; high values of low and middle atmospheric specific humidity; and a persistent region of organized deep convection.

However, these conditions are not sufficient, as individual tropical cyclones form infrequently and sporadically within large areas of otherwise favorable environmental conditions. Furthermore, Gray (1979) observed that tropical cyclogenesis tends to cluster in time, with a two- to three-week period of multiple instances of TCs, followed by a two- to three-week period of few to no occurrences of cyclogenesis. This temporal periodicity suggests a connection to an intraseasonal mode of variability, such as the MJO. During periods of MJO activity in the tropics, medium-range numerical weather prediction (NWP) models exhibit significantly greater skill if the tropical convection associated with MJO passage is correctly handled (Inness and Slingo 2003).

A climatology of TC occurrence indicates that the entire western Atlantic basin, including the Windward and Leeward Islands, the Greater Antilles, the northern coast of South America, the eastern coasts of Central America, the Gulf of Mexico, and the Atlantic seaboard from Florida to Newfoundland, is at risk for destructive effects from TCs. The East Pacific basin, while experiencing more TC activity each season, is less prone to landfalls due to the lack of continental areas once disturbances move west from the Mexican coast. Nevertheless, East Pacific TCs still affect the west coast of Mexico, and their remnant moisture plumes contribute to frequent flooding events in the North American monsoon region.

To discuss modulation of TC genesis by various-scale atmospheric phenomena, it is important to first begin with a discussion of the basic TC climatology. Specifically important is the geographic and seasonal distribution of TC formation in each basin (see Figs. 1.1-1.2). The North Atlantic hurricane season begins each year on 01 June and continues until 30 November (Sheets 1990). While Atlantic tropical and sub-tropical

(Herbert and Poteat 1975) cyclones have existed in every month of the calendar year, the six-month "season" coincides with the prevalence of the classical TC genesis parameters (Gray 1968). In the East Pacific basin, the hurricane season begins fifteen days earlier, on 15 May, and also continues until 30 November. Although the background environmental conditions are similar between basins and seasons (as has been discussed earlier in this section), TCs have been observed to develop from a diversity of types of disturbances; for example, from trade wind cloud clusters, easterly waves, vorticity centers along the Intertropical Convergence Zone (ITCZ), or from convective clusters persisting over a stalled midlatitude cold front (McBride 1981).

Tropical weather patterns are not as predictable as mid-latitude weather patterns (Geerts and Wheeler 1998). The mid-latitudes are governed by upper-tropospheric Rossby waves, and these interact with surface weather patterns through baroclinic instability. In the tropics, Rossby waves and baroclinic instability are largely absent, and therefore near-term (1-10 day) predictability is less. Until recently the tropical weather patterns on timescales less than one year were believed to be essentially random.

4.2.2. Current understanding of the relationship between the MJO and TC activity

Several studies have examined the connection between tropical cyclone activity and the MJO. Von Storch and Smallegange (1991) focused on the North and South Pacific oceans and found connections between outgoing longwave radiation (OLR) and TC numbers over a 5-year period. Liebmann et al. (1994) attributed changes in west Pacific TC activity with the phase of the MJO and were the first to connect these changes to meso- and synoptic-scale organization of deep convection. Maloney and Hartmann (2000) found a strong connection between eastern North Pacific hurricane activity and the MJO, with hurricanes more than four times more likely to generate during easterly than during westerly wind phases, and they attributed the relationship to the modified low-level 850 hPa anomalies during the passage of the eastward-propagating MJO. Mo (2000), using a very limited dataset (five selected years from 1976-1986), examined OLR anomalies and N. Atlantic tropical storm activity and found that – in the selected years – a relationship exists between positive OLR anomalies (i.e., suppressed convection) in the Indian Ocean and enhanced tropical storm activity in the N. Atlantic. Hall et al. (2001) were the first to quantify the statistical significance of the relationship between the MJO and tropical cyclone activity, and they focused on the Australian region. Separating the MJO into five "phases", and binning TC genesis into each of those "phases", they found that cyclogenesis was especially favored during one phase of the MJO and suppressed during another. They connected this relationship to the MJO's modulation of low-level relative vorticity, finding large regions of anomalous cyclonic vorticity corresponding to the favored cyclogenesis regions for a particular phase of the MJO. Other than Hall et al. (2001) in the Australian region, however, little quantitative research has been undertaken to study the frequency and statistical significance of the relationship in other basins, particularly the East Pacific and North Atlantic.

4.3. MJO modulation of North Atlantic, East Pacific, and sub-basin TC activity

The MJO is poorly simulated by dynamical NWP models, at least partially due to the poor parameterization of tropical cumulus convection (Xue et al. 2002). Ensembles of dynamical NWP models, as well as statistical prediction methods, have shown modest skill for two-week predictions of wintertime precipitation (Whitaker and Weickmann 2001). However, neither statistical nor dynamical prediction models have demonstrated skill in forecasting the MJO beyond week two (Xue et al. 2002). It is hypothesized that the lack of skill of these models, particularly statistical models, is at least partially related to a continued lack of theoretical understanding of the MJO and our inability to accurately identify the circulation in real-time. Thus, efforts continue to improve the monitoring and assessment of the MJO's influence on atmospheric circulation, and this identification is accomplished primarily by developing EOFs (see section 4.3.1) from geophysical data and mapping the MJO through spatial patterns in the principal components.

4.3.1. The method of extended empirical orthogonal functions

For at least four decades, geophysicists, meteorologists and climate dynamicists have observed that geophysical fields are often significantly correlated in both time and space. Empirical orthogonal function (EOF) analysis techniques were developed to enable relatively simple descriptions of complex variations in these geophysical fields using a small number of functions with time coefficients (Kutzbach 1967; Barnett 1977). These derived empirical functions are extremely useful as they often enable insightful physical interpretation of complex variables (Walsh and Richman 1981), including the development of phase propagation vectors and spatial correlations (Richman 1981). Kutzbach (1967) concisely described EOFs as a series of time-independent functions which are derived so that they are, successively, the most correct linear predictors of a geophysical field. An eigenvalue-eigenfunction equation arises when the functions are linear combinations of the data. From this equation's solution, the "principal components" may be derived. Finally, these components together objectively explain a measurable fraction of the total variance in the original field.

Weare and Nasstrom (1982) developed an analysis technique that allowed data set expansion in terms of functions that "best represent" the data set for a time series. They defined functions that not only analyze geophysical fields in space, but also in time, computing the auto- and cross-correlations between these interrelated fields. The advantages to this approach are two-fold: (1) the data fields can often be compacted to be used in regression models; and (2) the dominant functions are able to be interpreted not only in terms of their dominant modes of variability but also in terms of the "dominant modes of space-time sequences of events" (Weare and Nasstrom 1982). Kim and Wu (1999) tested eight different methods of EOF analysis on an idealized geophysical field, including the extended-EOF (EEOF) method of Weare and Nasstrom (1982). They found that the EEOF method correctly identified both the pattern (spatial) and temporal correlations as well as the physical modes. Kim and Wu (1999) concluded that the EEOF technique was a valid method of EOF analysis for periodic datasets, but they cautioned that discretion be used with any EOF technique when applying them to non-stationary datasets.

It is not the goal of this study to develop EOFs from geophysical data and identify the MJO from the principal components. In fact, several recent studies have done just that (Lo and Hendon (2000), Higgins and Shi (2001), Hall et al. (2001), Xue et al. (2002), and Wheeler and Hendon (2004)). The NOAA Climate Prediction Center currently maintains a real-time MJO composite index (Xue et al. 2002), and because this study focuses on the relationships – both statistical and physical - between the MJO and TC activity, this study will use the MJO composite of Xue et al. (2002) rather than redevelop indices that have already been published in multiple studies.

4.3.2. Velocity potential as a measure of divergence

The real-time MJO composite index of Xue et al. (2002) uses the 200 hPa velocity potential to identify the oscillation. It is therefore important to understand the properties of the velocity potential and how it is connected to deep convective activity. The two-dimensional condition of irrotationality is

$$\frac{dv}{dx} - \frac{du}{dy} = 0, \tag{4.1}$$

where u and v are the two-dimensional zonal and meridional components of the three-dimensional wind, and x and y are the spatial derivatives. The condition of irrotationality guarantees the existence of a scalar function ϕ called the *velocity potential*, which provides that the velocity vector **u** can be written as the gradient of a scalar potential ϕ,

$$\mathbf{u} \equiv \nabla \phi. \tag{4.2}$$

This velocity potential is related to the components u and v by

$$u \equiv \frac{d\phi}{dx}\ ;\ v \equiv \frac{d\phi}{dy}\ . \tag{4.3}$$

The velocity potential satisfies the Laplace equation,

$$\nabla^2 \phi = \frac{\partial^2 \phi}{\partial x^2} + \frac{\partial^2 \phi}{\partial y^2}\ . \tag{4.4}$$

Within the tropics, upper and lower-level velocity potential anomalies tend to be 180° out of phase (Knutson and Weickmann 1987). Thus, large-scale convergence, represented by positive velocity potential anomalies at lower-levels, tends to be accompanied by large-scale divergence (negative velocity potential) anomalies at upper levels. This results in large-scale rising motion in the intermediate levels. The divergent wind is therefore directed toward higher values of velocity potential. Negative velocity potential anomalies identify regions of anomalous rising motion, and regions of high (low) height anomalies can be inferred to exist when the velocity potential anomalies are positive (negative). In the tropics, upper-tropospheric divergence (convergence) is strongly associated with the formation of deep cumulus convection (Knutson and Weickmann 1987). MJ72 recognized this connection as well, and the MJO schematic (Fig. 4.1) shows that upper divergence (convergence) tends to be co-located with active (suppressed) regions of cumulus convection.

4.4. Construction of Madden-Julian Oscillation indices

To construct indices of the MJO, Xue et al. (2002) apply extended empirical orthogonal function (EEOF; Weare and Nasstrom 1982) analysis to the bandpass filtered non-overlapping five-day means of velocity potential at 200 hPa derived from the NCEP/NCAR Reanalysis data (Kalnay et al. 1996) during the November to April period from 1979-2000. The bandpass filter eliminates frequencies that are not germane to the MJO, and in this dataset, the band was set to 10-90 days (e.g., Zhou and Miller 2005). The five-day periods will be referred to as pentads, and the boreal winter months are selected for the EEOF analysis because the MJO signal is most pronounced during boreal winter (Madden and Julian 1994). To limit contamination of the signal by ENSO, the dominant interseasonal mode, the EEOF is only calculated from data during neutral and weak ENSO years (as defined by the NOAA Climate Prediction Center, available online at http://www.cpc.nep.noaa.gov/research_papers/ncep_cpc_atlas/8/ensoyrs.txt). This filtering results in 15 of the 22 years in the dataset selected to calculate the EEOF of velocity potential at 200 hPa. The first EEOF is composed of ten time-lagged patterns (i.e., ten modes, or principal components, of variation) and describes an eastward propagation of the MJO with a timescale of about 45 days. The ten time-lagged patterns were found to be centered at ten unevenly spaced longitude locations: 80°E, 100°E, 120°E, 140°E, 160°E, 120°W, 40°W, 10°W, 20°E, and 70°E (see Fig. 4.5).

The CPC archives the ten MJO indices on-line (http://www.cpc.noaa.gov/products/precip/CWlink/daily_mjo_index/proj_norm_order.ascii). A sample of the data for the period 02 June to 29 November 2005 is provided in Table 4.1. Each pentad has ten MJO index values associated with it. The values are the result of regressing the 200 hPa velocity potential anomalies onto the corresponding pattern of the first EEOF and then standardizing each index value by dividing it by its standard deviation.

4.4.1. Physical interpretation of MJO Index values

The MJO phases used in this study are defined as follows: ENH, or "enhanced", is any value equal to or lower than -1.00; NEU, or "neutral", is any value between -1.00 and +1.00, and SUP, or "suppressed", is any value greater than or equal to +1.00. Because velocity potential is physically coupled with convergence, a positive index value implies that upper-tropospheric convergence is favored. A favored region of upper-tropospheric convergence implies that the convectively inactive phase of the MJO is also centered at that index. Upper-tropospheric divergence has been shown to be positively correlated with anomalously low values of outgoing longwave radiation (OLR). OLR is a reasonable approximation for tropical cumulus and cumulonimbus activity because the tops of the very tall ("deep") convective clouds are much colder, and thus do not radiate at the same blackbody temperature as the sea surface. The causal relationships between upper-tropospheric zonal wind and tropical deep convection can be summarized as follows: positive [negative] velocity potential anomalies → upper-tropospheric convergence [divergence] → suppressed [enhanced] deep cumulus convection. Thus, the phases are named "enhanced", "neutral", and "suppressed" because of the connection between the 200-hPa divergence (and, by association, the velocity potential) and deep convection.

The value of MJO Index 1 on 02 June 2005 is calculated by regressing the 200 hPa pentad velocity potential anomaly, taken as a simple mean of the 00 UTC velocity potential anomalies from 31 May to 04 June 2005 at 80° E (computed every five degrees along 80°E from 30°N to 30°S), onto the pattern of the first EEOF at 80°E. The resulting value is then normalized by the standard deviation of the MJO values at Index

1 from 1979-1995. Thus, the 02 June 2005 MJO value for Index 1, +1.13, implies that the 200 hPa velocity potential anomaly centered at 80°E is 1.13 standard deviations above normal. Following from the discussion above, this also implies that above-normal 200 hPa convergence and suppressed convective activity are centered on 80°E.

The entire MJO Index values for the pentad centered on 02 June 2005 are: +1.13, +0.49, -0.23, -1.01, -1.42, -1.00, -0.30, +0.52, +1.29, and +1.24 for Indices 1-10, respectively. Indices 4, 5, and 6 are in “ENH” phase; Indices 2, 3, 7, and 8 are in “NEU” phase; and Indices 1, 9, and 10 are in “SUP” phase. Table 4.2 presents the linear correlations of each index with the other indices from June to November 2005. The global (wavenumber one) spatial distribution of the oscillation is very apparent in the linear correlations between indices: the largest positive correlations occur between adjacent indices (e.g., Index 1 and Index 10, + 0.97; and Index 2 and Index 3, +0.88) and the largest negative correlations occur between indices that are farthest apart (e.g., Index 1 and Index 6, -0.99; and Index 3 and Index 8, -0.98). Thus, the coherence between the adjacent – and the opposing –indices (Fig. 4.6) is not surprising, and the wave number and amplitude of the oscillation is readily apparent in the 02 June time series (Fig. 4.7).

4.4.2. Transforming the indices to normality

After normalizing each index by its standard deviation, the regression results in ten Gaussian indices with mean zero and standard deviation one. A positive (negative) index corresponds to a positive (negative) 200 hPa velocity potential anomaly. The base period for calculating the standard deviation of each index is 1979 to 1995.

However, the tropical cyclone activity occurs only from May (June) to November for the East Pacific (North Atlantic) basin, and therefore we only use a subset of the annual dataset. Because the statistical test (the *z*-test) used below assumes a normally-distributed dataset, it is important to ensure normality of the indices. The seasonal MJO Index values are approximately centered on zero (their central value is zero), but they exhibit long left and right tails (the second, third, and fourth statistical moments, standard deviation, skewness, and kurtosis, are not zero, zero, or three, respectively; see Table 4.3). Therefore, to bring the seasonal subset closer to normality, the Manly (1976) exponential transformation technique was applied (e.g., Delleur and Kavvas 1980). While useful in adjusting the first four moments closer to normality, Delleur and Kavvas (1980) note that for meteorological datasets, it is possible that no exponential transformation can bring the original data to normality (and this was the case with Index 10). Manly's transformation is given as

$$Y = \begin{cases} [\exp(kx)-1]/k & k \neq 0 \\ x & k = 0 \end{cases}, \tag{4.5}$$

where x is the original series and Y is the transformed series. For the MJO seasonal (Jun-Nov) Index values, the optimal k-values are given in Table 4.3 along with the first four untransformed and transformed statistical moments.

4.5. Significance testing TC activity

For this study, "TC activity" is measured using two methods, and each method is tested separately: (1) cyclogenesis and intensification; (2) landfall. To determine TC activity for the first method, every point of tropical cyclogenesis was identified for nine different basins and sub-basins (see Table 1.1 and Figs 1.1-1.2 for basin and sub-basin identification, and see sections 1.1 and 1.2.2 for definitions of a TC, hurricane, and intense hurricane). Tropical cyclogenesis is defined as the first TC point in the best-track historical record with at least 35 kt sustained surface winds. It is important to note that the best track record includes non-tropical systems, but this study excludes these recordings of subtropical cyclones (Herbert and Poteat 1975), tropical waves, tropical depressions (McBride 1981), and extratropical cyclones (e.g., Evans and Hart 2003). Hurricane genesis is defined as the first TC point with at least 65 kt sustained surface winds. Intense hurricane genesis is defined as the first TC point with at least 100 kt sustained surface winds. The location of the TC, hurricane, or intense hurricane genesis point defines the basin to which the TC belongs. Each east Pacific TC can belong to at most two basins: the whole EPAC basin and one sub-basin; each North Atlantic TC can belong to at most three basins: the whole NATL basin and possibly two sub-basins: either the Gulf of Mexico or the Caribbean and/or the "main development region" (Goldenberg and Shapiro 1996), which overlaps with the Caribbean. The Julian date of genesis determines the MJO pentad to which it belongs, and TC genesis events are then binned according to basin, MJO Index phase, and storm type.

To determine TC activity for the second method, only the Julian date of landfall is considered, as it determines to which MJO pentad the landfall point belongs. TC landfalls are only computed for the NATL and EPAC. Landfall points are determined subjectively using several rubrics. First, if the post-storm report includes a landfall coordinate, then this study considers it. However, landfall coordinates are usually given only when the eye of the TC crosses a coastline. This restriction unnecessarily excludes TCs that cause great damage to coastlines as the eyewall passes nearby but does not actually cross the coast. Many of the "landfalls" of the West Indies and Greater Antilles fall into this category, and in general, if the eye of a TC passes within 60 miles, and/or the post-storm report includes mention of high sustained winds with a near-miss, it is recorded as a landfall. Finally, for the EPAC and sub-basins, no detailed landfall database (i.e., one that includes information about the specific landfall, such as date, time, location, and intensity) exists. Instead, the best-track dataset includes only a binary "landfall" discriminator: either the TC made landfall or it did not. This information, while limited, is still useful, and it is therefore included in the "*landfall-genesis*" section below.

4.5.1. Null hypotheses and test statistics

To test the connection between the MJO and TC activity, this study will test a null hypothesis that tropical cyclone events are uniformly distributed across MJO phase. The null and alternative hypotheses are given as

$$\begin{aligned} H_0 &: \hat{p} = p_0 \\ H_{\mathrm{A}} &: \hat{p} \neq p_0 \end{aligned}, \tag{4.6}$$

where the null hypothesis implies that there is no modulation of TC activity by the MJO and the alternative hypothesis implies that TC activity is modulated by the MJO. Coincident with this null hypothesis, the probability of cyclogenesis was assumed to be fixed, thus leading to a binomial distribution (e.g., Hall et al. 2001; Bessafi and Wheeler 2006). The relevant test statistic – which exists for each of the ten MJO indices, and is duplicated for both TC activity methods – is therefore

$$Z_{basin,storm\_type,MJO\_phase} = \frac{\hat{p}_{basin,storm\_type,MJO\_phase} - p_{0_{MJO\_phase}}}{\sqrt{p_{0_{MJO\_phase}}(1 - p_{0_{MJO\_phase}}) / N_{storm\_type}}} \tag{4.7}$$

where $\hat{p}$ and p_0 are the observed and expected fraction of TCs that form in each category and N is the total number of TC events in each category. The indices *basin, storm_type,* and *MJO_phase* are defined as follows:

Index	Description
Basin	Location of the TC event, either EPAC, NATL, CARIB, GOM, EEPAC, CEPAC, WEPAC, CPAC, or AMDR (acronyms defined in Table 1.1)
Storm_type	Type of TC event: tropical storm, hurricane, or intense hurricane
MJO_phase	Phase of the relevant MJO index (1-10): "ENH", "NEU", or "SUP"

For example, Index 1 was in the ENH phase 161 (out of 1066) pentads, or 15.1% of the total seasonal pentads. Index 1 was in the NEU and SUP phases 774 and 131 pentads, or 72.6% and 12.3%, respectively. If the MJO does not modulate TC event activity, then we should expect to find that 15.1% of TC events occur when Index 1 is in the ENH phase and that 72.6% and 12.3% of TC events occur when Index 1 is in the NEU and SUP phases, respectively.

4.5.2. MJO phase definition

As stated above, the MJO phases are defined as follows: ENH is any value equal to or lower than -1.00; NEU is a value between -1.00 and +1.00, and SUP is a value greater than +1.00. The namesake recipient of the expression is the tendency of the 200-hPa velocity potential to act on deep convection. For example, the MJO index values for the pentad centered on August 1, 2005 are: 0.44, -0.55, -1.34, -1.83, -1.41, -0.22, 0.79, 1.58, 1.76, and 0.80, for Indices 1-10, respectively. Indices 3, 4, and 5 are in "ENH" phase; Indices 1, 2, 6, 7, and 10 are in "NEU" phase; and Indices 8 and 9 are in "SUP" phase.

The observed fraction of TCs, $\hat{p}$, is calculated as follows. For each phase (ENH, NEU, SUP) of each MJO Index (1-10), the number of TC events (either genesis or landfall) per basin and storm type are calculated, and this total is divided by the sum of TC events across MJO phase. For example, in the East Pacific basin, 45, 345, and 91 TCs formed when Index 1 was in ENH, NEU, and SUP phase, respectively, resulting in $\hat{p}$ of 0.09, 0.72, and 0.19, respectively, for Index 1. (See Tables 4.5-4.9 for a complete summary of the observed TC fractions). The expected fraction of TCs, p_0, is calculated as follows. The number of pentads of each phase (ENH, NEU, SUP) of each MJO Index is divided by the total number of pentads. For example, Index 1 had 161, 774, and 131 pentads in the ENH, NEU, and SUP phases, respectively, resulting in p_0 of 0.15, 0.73, and 0.12, respectively. (See Table 4.4 for a complete summary of the expected TC fractions). N is the total number of TC events for each basin and storm type, and in the example above, N is 481 total TCs. Therefore, for the example above, the relevant test statistics, Z, are -3.52, -0.43, +4.43, for TC genesis when Index 1 is in the ENH, NEU, or SUP phase, respectively. For a two-tailed test, the corresponding critical values of Z that allow 95% confidence in rejecting the null hypothesis are $\pm$ 1.96. (For reference, the critical Z for 90% confidence is $\pm$ 1.645, and for 99% confidence, the critical Z is $\pm$ 2.575.) Thus, with 95% confidence, we can reject the two null hypotheses that Index 1 ENH and SUP phases are unrelated to TC activity. In the ENH case, TC events are not favored, and in the SUP phase, TC events are favored.

4.6. Interpreting the *Z*-statistics

4.6.1. TC activity as measured by genesis points

Table 4.10 presents a summary of all of the test Z-statistics, sorted by basin, storm type, MJO phase, and MJO Index. The statistics should be interpreted as follows: positive Z-statistics indicate that TC events are favored; and likewise, negative Z-statistics indicate that TC events are not favored. For the example in subsection 4.6.1., it is important to realize that Index 1 of the MJO is centered in the eastern hemisphere at 80°E, thus when Index 1 is in ENH phase, the 200-hPa velocity potential anomalies enhance deep tropical convection at that longitude. The MJO has a zonal wavenumber of one, and 180 degrees east of 80°E is 100°W, which is squarely in the middle of the East Pacific basin. If the MJO velocity potential anomaly centered at 80°E is negative, corresponding to upper-tropospheric divergence and enhanced deep convective activity, then the atmospheric response in the opposite hemisphere will likely be opposite: positive velocity potential anomaly, upper-tropospheric convergence and suppression of deep convective activity. The opposite-hemisphere response is not completely certain because the atmosphere is influenced by many other components of variability besides the MJO. Regardless of the uncertainty, however, the confidence is very high (99%) that TC activity in the East Pacific basin is modulated by the MJO when Index 1 is in either the ENH or the SUP phase. Specifically, Index 1 ENH depresses TC genesis activity, while Index 1 SUP supports genesis activity.

The statistical relationship with the MJO decreases for EPAC hurricane activity, which measures the numbers of already-formed TCs that continue to intensify into hurricanes (with sustained 1-min 10 m winds of 64 kt or greater). Specifically, the test *Z*-statistics are -3.02, +1.22, and +1.63, for Index 1 ENH, NEU, or SUP. These statistics can be interpreted as a strong depression of hurricane genesis when Index 1 is in ENH phase (confident at the 99% level), but essentially neutral modulation of EPAC hurricane genesis when Index 1 is in the NEU or SUP phases. For EPAC intense hurricane genesis, we cannot reject the null hypothesis for any of the three phases of MJO activity, as the test *Z*-statistics lie between -1.00 and +1.00.

4.6.2. Comparing basins and sub-basins

Instead of focusing on one particular basin or MJO Index, it is also possible to interpret the test *Z*-statistics through the lens of determining favorable conditions for TC events. For example, the results can be used to answer the question “When is intense hurricane genesis favored in the North Atlantic Main Development Region (AMDR)?” With 95% confidence, the important answer to that question is “Intense hurricane genesis is favored in the AMDR sub-basin when MJO Indices 5 and 6 are in SUP phase. Additionally, intense hurricane genesis is not favored, or unlikely when MJO Indices 1 and 10 are in SUP phase and when Index 6 is in ENH phase.” The actual data that support that claim are as follows: "A total of thirty-three intense hurricanes formed in the AMDR sub-basin from 1978-2006, and when MJO Index 5 was in SUP phase, 10 intense hurricanes formed (30% of the total that formed). Similarly, 10 intense hurricanes formed when MJO Index 6 was in SUP phase. Zero intense hurricanes formed when MJO Indices 1 and 10 were in ENH phase and when MJO Index 6 was in SUP phase." Thus, the data are very useful in identifying modulation of TC events by the MJO and in quantifying the statistical significance of the modulation.

4.6.3. TC activity measured by landfall

In addition to measuring TC activity by genesis events, activity can also be measured by landfall frequency. Setting aside the scientific questions, this method of quantifying TC activity is arguably more beneficial to society, as landfalling TCs are one of the most damaging geophysical events on the planet's surface. Similar to the method discussed above, landfalling TCs, hurricanes, and intense hurricanes are stratified by the phase of ten MJO indices. As before, the null hypotheses state that the TCs will be distributed with the same frequency as the MJO indices. With the same assumption of a binomial distribution, the relevant *Z*-statistic remains

$$Z_{basin,storm\_type,MJO\_phase} = \frac{\hat{p}_{basin,storm\_type,MJO\_phase} - p_{0_{MJO\_phase}}}{\sqrt{p_{0_{MJO\_phase}}(1 - p_{0_{MJO\_phase}}) / N_{storm\_type}}} \tag{4.8}$$

where the variable definitions are given above. The only difference is that now instead of counting *all* TC genesis events, only TC landfall events are counted. Thus N_{storm_type} is not the total number of TCs but instead the total number of *landfalling* TCs (or hurricanes, or intense hurricanes).

This study uses two methods to stratify landfalling TCs by MJO phase. The first method bins the *future* landfalling TC (or hurricane, or intense hurricane) by the MJO phase *at its genesis*; this method will be referred to as *landfall-genesis*. The second method bins the landfalling TC (or hurricane, or intense hurricane) by the MJO phase *at its landfall*; this method will be referred to as *landfall-actual*. The difference is subtle (and in the case of TCs that form within 5 days of making landfall, irrelevant), but important: the MJO's modulation of TC landfall activity begins at genesis and ends with the actual landfall. Thus both will be examined, although accurate landfall records (which include date, time, and intensity of landfall) back to 1978 were only kept for the North Atlantic. Therefore, only the NATL events will be binned by MJO phase at landfall.

4.6.4. MJO modulation of TC landfall activity

Table 4.11 reports the *Z*-statistics for *landfall-genesis* events, and Table 4.12 reports the *Z*-statistics for *landfall-actual* events. When MJO Index 1 is in the ENH phase, significantly fewer (with 95% confidence) TCs and hurricanes *that go on to make landfall* form in the EPAC (see Table 4.11). However, when Index 1 is in the ENH phase, significantly more (again with 95% confidence) TCs *that go on to make landfall* form in the NATL, CARIB, and AMDR. Furthermore, significantly more hurricanes *actually make landfall* in the NATL (see Table 4.12). Conversely, when MJO Index 1 is in the SUP phase, the EPAC and CPAC both favor TC genesis, and the CPAC favors TC, hurricane, and intense hurricane genesis. The NATL, CARIB, and GOM do not exhibit any statistically significant favor for TC, hurricane, or intense hurricane genesis (see Table 4.11). Furthermore, significantly fewer TCs and intense hurricanes (but curiously not hurricanes) *actually make landfall* in the NATL (see Table 4.12). Finally, when MJO Index 1 is in the NEU phase, significantly fewer hurricanes *actually make landfall* in the NATL.

4.7. Graphical display of modulated TC activity

The Z-statistic data found in Tables 4.10-4.12 are easily interpreted when plotted graphically using the freely available geographic information system (GIS) platform Google Earth (e.g., Smith and Lakshmanan 2006; Lakshmanan et al. 2007). By creating a user-defined "layer", the activity data can be easily combined with a wide range of other "layers", including any type of archived meteorological and oceanographic data (e.g., monthly mean SSTs, mean 500 hPa heights, etc.), current or historical shipping routes, and population density, to name just a few. Of the ten MJO Indices of Xue et al. (2002), Index 6 is centered closest to most of the data points in the nine basins and sub-basins. Thus it is selected as a mini case-study on the utility of graphically displaying the data.

Recall that for each index and basin, the MJO can be sorted into three phases, and the TC events can be stratified by intensity (TC, hurricane, intense hurricane). Including the graphical display of all three phases for each basin, there exist 36 separate plots for TC events, 36 for hurricane events, and 36 for intense hurricane events. Considering that the MJO has ten indices, the number of plots quickly balloons – to 1,080. For this short example, I have chosen to include the 36 figures of Index 6 TC genesis events for each of the nine basins. From the Z-statistics in Table 4.10, it is clear that the relationships between TC genesis and the MJO will manifest themselves in several areas (see Table 4.13 for a summary): activity is favored in the EPAC, CEPAC, WEPAC, and CPAC when Index 6 is in the ENH phase. Activity is favored in the NATL and AMDR when Index 6 is in the SUP phase. Activity is not favored in the EPAC and WEPAC when Index 6 is in the SUP phase, and activity is not favored in the NATL and CARIB when Index 6 is in the ENH phase. When the MJO Index 6 is in the NEU phase, it does not significantly modulate TC activity in any basin, most likely because the indices are often in the NEU phase (over 70% of the pentads), and therefore any MJO modulation signal can be more easily masked by other sources of variability. These NEU phase results are in agreement with the Bessafi and Wheeler (2006) and Hall et al. (2002) studies, which also found no relationship between the NEU phase of the MJO and TC events.

4.8. Quantifying TC modulation by MJO at genesis

Fig. 4.6 displays the location of every EPAC TC genesis point. The points are colored by MJO Index 6 phase: yellow for ENH, cyan for NEU, and red for SUP. This color-coding scheme will be used throughout Figs. 4.6-4.17. The TC genesis points cluster south and southwest of the Mexican Riviera coast and extend westward, trailing off in number, to 180°W. The two genesis points northwest of Hawaii are real and included in the best-track dataset. West of 125°W, only three TCs (out of over 50 total) formed when Index 6 was in SUP phase; therefore it is reinforced that TC genesis is favored in the CEPAC, WEPAC, and CPAC when Index 6 is in the ENH phase and not favored in the WEPAC when Index 6 is in the SUP phase. Figs. 4.7-4.9 plot the TC genesis points for the CEPAC, WEPAC, and CPAC for each MJO Index 6 phase. Fig. 4.10 plots the TC genesis points for the EEPAC, and due to the relatively even distribution, TC genesis is neither favored nor suppressed for any phase of the Index (although at the 90% confidence level, TC genesis is favored in the ENH phase).

Moving eastward, Fig. 4.11 shows the location of every NATL TC genesis point. The TC genesis points are spread throughout the basin, from the west coast of Africa through the West Indies, into the western Caribbean and Gulf of Mexico, and off the southeast U.S. coast into the central North Atlantic. Fig. 4.12 shows the NATL TC genesis points stratified by phase of MJO Index 6. It is clear that far more TCs form when Index 6 is in SUP phase (66 out of 325) than when it is in ENH phase (23 out of 325). This conclusion is supported by the *Z*-statistics in Table 4.10. In the CARIB sub-basin (Fig. 4.13), only 1 TC (out of 54 total) formed when the Index was in ENH phase. In the Gulf of Mexico, while more TCs formed when Index 6 was in the SUP phase (13 out of 65) than in the ENH phase (5 out of 65; see Fig. 4.14), the result is not statistically significant. The AMDR sub-basin, which has favored TC genesis when the Index is in the SUP phase (42 out of 159 verses 11 out of 159 for the SUP and ENH phases, respectively), is shown in Fig. 4.15.

4.9. Quantifying TC modulation by MJO at landfall

As mentioned above, perhaps the most societally important modulation of TC activity by the MJO occurs with landfalling TCs. Fig. 4.16 shows all 238 TCs (not stratified by intensity) that made landfall in the NATL basin between 1978 and 2006. As with the TC genesis display from the NATL, landfall events are clustered around the

Caribbean, Central America, the U.S. Gulf coast and eastern seaboard, even extending to the Canadian Maritimes and the island of Bermuda. Fig. 4.17 shows the stratification of landfall by MJO Index 6 phase. When Index 6 is in the ENH phase, only 13 TCs (out of 238 total) make landfall; while when Index 6 is in the SUP phase, 65 TCs make landfall. As expected, this result is statistically significant (with 95% confidence): namely, that the MJO Index 6, when in the ENH phase, suppresses TC landfall activity in the NATL, and when in the SUP phase, favors hurricane and intense hurricane landfall activity in the NATL.

4.10. Advantages to these methods of quantifying TC activity

Two previous studies, Hall et al. (2001) and Bessafi and Wheeler (2006), developed and applied rigorous statistical hypothesis testing to determine the extent of MJO modulation of TC activity. As previously mentioned, Hall et al. (2001) examined only the Australian region and limited their study to the 20-yr period ending in 1996. Bessafi and Wheeler (2006) examined the Indian Ocean basin. Both of these studies develop only one MJO Index (instead of ten), and partition it into five (seven) different phases. Thus the MJO is always confined to one phase in these two studies. Higgins and Shi (2001) briefly examined the connection between the MJO and hurricane genesis in the Pacific Ocean. They calculated seven MJO Indices from 200 hPa velocity potential, similar to Xue et al (2002). However, they limited their study to a 19-year period and did not complete the analysis, omitting many of the genesis points for the Western North Pacific and nearly all of the points in the East Pacific and North Atlantic during this time. For example, fewer than 20 hurricane genesis points were plotted for the North Atlantic (Higgins and Shi 2001); yet during the period 1979-1997, 103 hurricanes formed.

This study uses the ten-index method of Xue et al. (2002) to quantify the MJO. Unlike Hall et al. (2001) and Bessafi and Wheeler (2006), which force the MJO into only one phase bin at any given time, the method of this study allows the MJO to be binned ten different times at ten different longitudinal locations spread throughout both the eastern and western hemispheres. Like the Xue et al. (2002) method, the Hall et al. (2001) and Bessafi and Wheeler (2006) methods find the MJO in neutral phase more often than in any other phase. Unlike the earlier studies, however, the method in this dissertation produces many "non-neutral" MJO phases. For example, during the tropical season (June to November), the ten individual indices average 770 NEU phases, out of 1066 total (about 72%). However, only 451 pentads (about 42%) have *all* of the ten indices in NEU phase, a gain of about 30%. Hall et al. (2001) examined the sensitivity to changing the definition of the non-neutral phases and found slightly stronger modulation signals when the neutral phase was larger. Thus, this study will keep the relatively high amplitude threshold of -1.00 and +1.00 (Bessafi and Wheeler 2006 used thresholds of ± 0.8).

4.11. Conclusions and connections to future work

This study examined the modulation of TC activity by the MJO. Null hypotheses stating that the MJO had no effect on TC activity were tested, with the assumption that the occurrence of TC events in a non-modulated environment would be distributed evenly and at the same frequency as the various phases of the MJO. TC activity was measured in two methods: genesis and landfall. The Julian day of the corresponding TC event was matched with the corresponding pentad of velocity potential from the real-time MJO composite index produced by the NOAA CPC (Xue et al. 2002). Observed frequencies of TC events for each MJO phase were compared with frequencies of the MJO phases themselves, and a test statistic was computed and compared against a critical score to determine if the null hypothesis could be accepted or rejected. The landfall measure of activity was further divided into two parts, with the first measure using the Julian day of genesis of TCs that went on to later make landfall and the second measure using the Julian day of actual landfall.

The results of the statistical tests are that the MJO does indeed modulate East Pacific and North Atlantic TC, hurricane, and intense hurricane activity. The primary advantage of this study is that it is the first to quantify the modulation by sub-basin and to report different modulations by different MJO Index phases. The modulation was also frequently manifest in the form of a teleconnection, extending from the region of active convective activity a hemisphere away. This study had far more cases of "neutral" MJO phase than either Bessafi and Wheeler (2006) or Hall et al. (2001), which allowed the MJO non-neutral signal to be amplified. Several of the modulation Z-statistics exceed ±3.50, which correspond to greater than 99.9% confidence in a two-sided test!

While connections between the MJO and TC activity have been hypothesized since the MJO was discovered in the 1970s, there have been very few studies to date that actually investigate and quantify the connection. Part of this lack of research has stemmed from the absence, until recently, of a manner to quantify the MJO itself. Thus this study is pioneering in its combination of the MJO Index with the latest best-track TC data. Now that the relationships between the EPAC, NATL, and other basins and the various MJO Indices have been established, it is a natural next step to implement them in a real-time forecasting procedure. This application will prove very useful to society, especially the ability to connect the low-frequency oscillation with both genesis and landfall.

Chapter 5. Conclusions and future work

Tropical cyclones are among the most extreme geophysical phenomena on the surface of the planet. At landfall, death and destruction are spread across wide areas without respect for geopolitical boundaries. Coastal buildings are flooded by the ocean surge; inland waterways overflow their banks and claim homes and businesses; tornadoes chart narrow but unpredictable paths in the outer bands and eyewall; and both coastal and inland structures are damaged and destroyed after prolonged battery by wind and wind-driven projectiles. Besides their peril, TCs also bring beneficial rainfall and hydrologic basin recharge to coastal and inland regions.

Because TCs are such significant geophysical events, it is essential that we understand their connections to the earth-atmosphere system. Very recent advances in technological capacities, including high-resolution NWP models, advanced computing capabilities, improved instrumentation used to gather in situ observational data, and enhanced satellite and radar remote-sensing techniques, have enabled the expansion of our observational and theoretical understanding of TC genesis, structure, intensification, decay, and motion. Historical datasets are now available that span thirty or more years, providing for the first time the ability to define climatological norms and anomalies and test the relationships between historical TC activity and leading modes of climatic variability.

In this dissertation, I presented a series of investigations to expand our understanding of TCs in the East Pacific and North Atlantic basins. First, I developed and applied a climatological tool that quickly and succinctly displays the spread of historical TC tracks for any point in the North Atlantic basin. This tool is useful in the real-time forecast setting because it is derived from prior storm motion trajectories and summarily captures the historical synoptic and mesoscale steering patterns. It displays the strength of the climatological signal and allow for rapid qualitative comparison between historical TC tracks and NWP models. Second, I have quantified the relationships between different metrics of TC activity spanning multiple ocean basins and climate indices of the leading modes of atmospheric and oceanic variability. I found that SSTs dominate the frequency, intensity, duration, and seasonality of TC activity, and that there is a tendency for the strongest correlations to be found where the SST-related indices (ENSO, NOI, SOI, and NASST) are approximately in situ. These patterns of variation – particularly the detailed linkages between the four NINO regions, the Northern and Southern oscillations, and North Atlantic SSTs and the nine basins – are one of the major contributions of this investigation. Earlier studies of the relationship between TC activity and ENSO did not examine the NINO regions separately or correlate them over different basins or metrics of TC activity. I also found that the QBO is very relevant, particularly to intense hurricane activity, at low latitudes, equatorward of 20°N, but that its importance to rapidly diminishes beyond the deep tropics. Finally, I found significant relationships between TC frequency, intensity, and seasonality and the PNA, NAO, AO, and PDO, and that these associations are spread throughout the nine basins. These relationships are vital to users across the disciplines of meteorology, economics, business, and sociology who wish to understand seasonal variability in TC activity. The most natural next step for this research is to apply it in the forecasting arena on intraseasonal to seasonal timescales and in the climate arena on interannual to interdecadal timescales. Third, I have examined the leading intraseasonal mode of atmospheric and oceanic variability, the Madden-Julian Oscillation (MJO), and discovered statistically significant relationships between the MJO and the frequency of TC genesis, intensification, and landfall over the nine basins. I found that during certain phases of the MJO, TC genesis is statistically favored, and during other phases, it is statistically not favored; similar relationships were found for intensification and landfall. By comparing TC activity in nine different basins to a real-time global MJO index, this investigation adds significant value to earlier studies which only examined the MJO at one longitude or computed associations for TC activity over an entire ocean basin. Just as the relationships between TC activity and the intraseasonal to inderdecadal atmospheric modes are valuable to intraseasonal and seasonal predictions of TC activity, the MJO associations are highly relevant to the problem of short-term (one- to two-week) predictability of TC activity. Finally, as perhaps an unintended benefit, through these three investigations I have demonstrated the utility of historical datasets, despite their quality limitations, across a wide range of applications, from short-term forecasting to climate studies.

This research can be extended in a variety of ways. Landfalling TCs are not uniform in their destructive potential, with variations in maximum wind speed, radius of maximum winds, forward speed, angle of approach to the coastline, coastal bathymetry, coastal population density, liquid water content, and local topography all contributing to substantially different landfall impacts from different TCs. It would be therefore useful to combine these parameters into a new metric of TC activity and test this metric for temporal and spatial variability as well as connections to the climate indices. The relationships between different levels of TC activity and climate indices can be combined into predictive equations, in the form of multiple linear regression, to forecast the levels of seasonal TC activity across the nine basins. This method has advantages over the current techniques which forecast basin-wide levels of TC activity using predictors whose usefulness is limited to certain sections of a basin (such as the QBO's relevance only to low-latitude TC activity). The MJO may also be useful as a seasonal predictor, even though it is an intraseasonal oscillation. For example, in the very active 2005 North Atlantic season, several MJO indices exhibited non-zero phase, indicating that it continually favored TC activity throughout the season.

In addition to the many extensions that are possible from this research, the TC boundary layer drag coefficient, and the impact of local island terrain on TC track and intensity, remain unanswered problems. These questions, and their background from the peer-reviewed literature, are presented in Chapter 1. On a personal note, after completing his ph.d. at the University of Oklahoma, the author will assume a two-year post-doctoral research appointment, under the direction of Dr. Rene Garreaud, at the University of Chile. He will participate in the 2008 UCAR-University of Chile-University of Washington cosponsored VOCALS field project to examine the climate and weather of the southeast Pacific.

To conclude succinctly, the results presented in this dissertation represent a significant and positive contribution to meteorology. Collectively, they reveal multiple characteristics of TCs in the East Pacific and North Atlantic and provide greater understanding of the complex interactions between TCs and their surrounding larger-scale environment.

Bibliography

Aberson, S. D., 1998: Five-day tropical cyclone track forecasts in the North Atlantic basin. *Wea. Forecasting*, **13**, 1005-1015.

-------, 2001: The ensemble of tropical cyclone track forecasting models in the north Atlantic basin (1976–1998). *Bull. Amer. Meteor. Soc.,* **82,** 1895-1904.

Alford, M. H., and Z. Zhao, 2007: Global patterns of low-mode internal-wave propagation. Part I: energy and energy flux. *J. Phys. Oceanogr.*, **37**, 1829–1848.

Ambaum M. H. P., B. J. Hoskins, and D. B. Stephenson, 2001: Arctic Oscillation or North Atlantic Oscillation? *J. Climate*, **14**, 3495–3507.

Amorocho, J., and J. J. DeVries, 1980: A new evaluation of the wind stress coefficient over water surfaces. *J. Geophys. Res*., **85**, 433 - 442.

Anderson, J. R., D. E. Stevens, and P. R. Julian, 1984: Temporal variations of the tropical 40-50 day oscillation. *Mon. Wea. Rev.*, **112**, 2431-2438.

Anderson, T. W., and D. A. Darling, 1952: Asymptotic theory of certain "goodness-of-fit" criteria based on stochastic processes. *Annals of Mathematical Statistics*, **23,** 193-212.

Andreas, E. L., 1998: A new sea spray generation function for wind speeds up to 32 m s^{-1}. *J. Phys. Oceanogr.*, **28**, 2175–2184.

-------, and K. A. Emanuel, 2001: Effects of sea spray on tropical cyclone intensity. *J. Atmos. Sci*., **58**, 3741-3751.

Anthes, R. A., 1972: The development of asymmetries in a three-dimensional numerical model of the tropical cyclone. *Mon. Wea. Rev*., **100**, 461-476.

-------, 1982: Tropical cyclones: their evolution, structure and effects. *Meteor. Monographs*, **19**, Amer. Meteor. Soc., 208 pp.

Arakawa, A., and W. H. Schubert. 1974: Interaction of a cumulus cloud ensemble with the large-scale environment, part I. *J. Atmos. Sci.,* **31**, 674–701.

Avila, L. A., R. J., Pasch, and J.Jiing, 2000: Atlantic tropical systems of 1996 and 1997: Years of contrasts. *Mon. Wea. Rev.*, **128**, 3695-3706.

Baldwin, M. P., L.J. Gray, T. J. Dunkerton, K. Hamilton, P. H. Haynes, W. J. Randel, J. R. Holton, M. J. Alexander, I. Hirota, T. Horinouchi, D. B. A. Jones, J. S. Kinnersley, C., 2001: The Quasi-Biennial Oscillation, *Rev. Geophys*., **39**, 179 - 229.

Bao J.-W., Wilczak J. M., Choi J. K., and Kantha L.H.., 2000: Numerical simulations of air-sea interaction under high wind conditions using a coupled model: a study of hurricane development. *Mon. Wea. Rev*., **128**, 2190–210.

Barnett, T. P., 1977: The principal time and space scales of the Pacific trade wind fields. *J. Atmos. Sci.*, **34**, 221-236.

Barnston A. G., and R. E. Livezey, 1987: Classification, seasonality, and persistence of low-frequency atmospheric circulation patterns. *Mon. Wea. Rev.*, **115**, 1083–1126.

Barrett, B. S., L. M. Leslie, and C.-S. Liou, 2004: Relationship between climatology and model track, bearing, and speed errors. Preprints, *20th Conf. on Weather Analysis and Forecasting*, Seattle, WA, Amer. Meteor. Soc., CD-ROM, 13.6.

-------, and -------, 2005: An examination of the quality of the Atlantic tropical cyclone database. Preprints, *16th Conf. on Climate Variability and Change*, San Diego, CA, Amer. Meteor. Soc., CD-ROM, P1.30.

-------, L. M. Leslie, and B. H. Fiedler, 2006: An example of the value of strong climatological signals in tropical cyclone track forecasting: Hurricane Ivan (2004). *Mon. Wea. Rev.*, **134**, 1568-1577.

-------, 2007: Characteristics of east Pacific and north Atlantic tropical cyclones. *Mon. Wea. Rev.*, in preparation.

Bell, G. D, M. S. Halpert, R. C. Schnell, R. W. Higgins, J. Lawrimore, V. E. Kousky, R. Tinker, W. Thiaw, M. Chelliah, and A. Artusa,, 2000: Climate Assessment for 1999. *Bull. Amer. Meteor. Soc*., **81**, S1-S50.

-------, and M. Chelliah, 2006: Leading tropical modes associated with interannual and multidecadal variations in seasonal North Atlantic hurricane activity. *J. Climate*, **19**, 590–612.

Bender, M. A., R. E. Tuleya, and Y. Kurihara, 1985: A numerical study of the effect of a mountain range on a landfalling tropical cyclone. *Mon. Wea. Rev.,* **113,** 567–582.

-------, -------, and -------, 1987: A numerical study of the effect of island terrain on tropical cyclones. *Mon. Wea. Rev.,* **115,** 130–155.

-------, R. J. Ross, R. E. Tuleya, and Y. Kurihara, 1993: Improvements in tropical cyclone track forecasts using the GFDL initialization system. *Mon. Wea. Re*v., **121**, 2046-2061.

-------, and I. Ginis, 2000: Real-case simulations of hurricane–ocean interaction using a high-resolution coupled model: effects on hurricane intensity. *Mon. Wea. Rev.,* **128**, 917-946.

Benedict, J. J., and D. A. Randall, 2007: Observed characteristics of the MJO relative to maximum rainfall. *J. Atmos. Sci.*, **64**, 2332-2354.

Bergeron T., 1954: The problem of tropical hurricanes. *Q. J. R. Meteor. Soc.,* **80**, 131–64.

Bessafi, M., A. Lasserre-Bigorry, C. J. Neumann, F. Pignolet-Tardan, D. Payet, and M. Lee-Ching-Ken, 2002: Statistical prediction of tropical cyclone motion: an analog-CLIPER approach. *Wea. Forecasting,* **17**, 821-831.

-------, and M.C. Wheeler, 2006: Modulation of south Indian Ocean tropical cyclones by the Madden-Julian oscillation and convectively-coupled equatorial waves. *Mon. Wea. Rev.*, **134**, 638-656.

Betts, A. K, and M. J. Miller, 1993: The Betts–Miller scheme. The representation of cumulus convection in numerical models, *Meteor. Monogr.,* **46**, Amer. Meteor. Soc., 107–121.

Biondi F., A. Gershunov, and D. R. Cayan, 2001: North Pacific decadal climate variability since 1661. *J. Climate*, **14**, 5–10.

Bister, M., and K. A. Emanuel, 1998: Dissipative heating and hurricane intensity. *Meteor. Atmos. Phys.,* **65,** 233–240.

Blackadar, A. K., 1979: High resolution models of the planetary boundary layer. *Advances in Environmental Science and Engineering*. Gordon and Breach, New York, 50-85.

Blake E. S., and W. M. Gray, 2004: Prediction of August Atlantic basin hurricane activity. *Wea. Forecasting*, **19**, 1044–1060.

Bluestein, H. B., 1992: *Synoptic-dynamic meteorology in midlatitudes: principles of kinematics and dynamics*. Oxford Univ. Press, Vol. 1.

Brand, S. and J. W. Belloch, 1973: Changes in the characteristics of typhoons crossing the Philippines. *J. Appl. Meteor.*, **12**, 104-109.

-------, and -------, 1974: Changes in the characteristics of typhoons crossing the island of Taiwan. *Mon. Wea. Rev.,* **102,** 708–713.

Braun, S. A., and W.-K. Tao, 2000: Sensitivity of high-resolution simulation of Hurricane Bob (1991) to planetary boundary layer parameterizations. *Mon. Wea. Rev.*, **128,** 3941-3961.

Brennan, J. F., 1935: Relation of May-June weather conditions in Jamaica to the Caribbean tropical disturbances of the following season. *Mon. Wea. Rev.*, **63**, 13-14.

Briegel, L. M., and W. M. Frank, 1997: Large-scale influences on tropical cyclogenesis in the western North Pacific. *Mon. Wea. Rev.*, **125**, 1397-1413.

Broccoli, A. J., T. L. Delworth, and N. C. Lau, 2001: The effect of changes in observational coverage on the association between surface temperature and the Arctic Oscillation. *J. Climate*, **14**, 2481–2485.

Brunt, A.T., 1968: Space-time relationships of cyclonic rainfall in the north-east Australian region. *Civil Engineering Transactions*, The Institution of Engineers, Australia, **CE10**.

Buckley, B. W., L. M. Leslie and M. S. Speer, 2003: The impact of observational technology on climate database quality: tropical cyclones in the Tasman Sea. *J. Climate*, **16**, 2640-2645.

Burpee, R. W., 1988: Grady Norton: hurricane forecaster and communicator extraordinaire. *Wea. and Forecasting*, **3**, 247–254.

Caplan, P., J. Derber, W. Gemmill, S.-Y. Hong, H.-L. Pan and D. Parrish, 1997: Changes to the 1995 NCEP operational medium-range forecast model analysis–forecast system. *Wea. Forecasting*, **12**, 581-594.

Cangialosi, J. P. and S.S. Chen, 2005: A numerical study of the topographic effects on the structure and rainfall in Hurricane Georges (1998). *26th Conf. on Hurr. and Trop. Meteor.*, Miami, FL, Amer. Meteor. Soc., CD-ROM, 13D.4.

Carrier, G. F., A. L. Hammond, and O. D. George, 1971: A model of the mature hurricane. *J. Fluid Mech.*, **47**, 145-170.

Chan J. C. L., J. Shi, and C. Lam, 1998: Seasonal forecasting of tropical cyclone activity over the western North Pacific and the South China Sea. *Wea. Forecasting*, **13**, 997–1004.

-------, 2005: The physics of tropical cyclone motion. *Annu. Rev. Fluid Mech.*, **37**, 99–128.

-------, and W. Zhou, 2005: PDO, ENSO and the early summer monsoon rainfall over south China. *Geophys. Res. Lett.*, **32**, L08810.

Chang, S. W., 1982: The orographic effects induced by an island mountain range on propagating tropical cyclones. *Mon. Wea. Rev*., **110**, 1255-1270.

Charney, J. and A. Eliassen, 1964: On the growth of the hurricane depression. *J. Atmos. Sci.,* **21**, 68–75.

Charnock, H., 1955: Wind stress on a water surface, *Quart. J. Roy. Meteor. Soc.,* **81**, 639-640.

Chavez F. P., J. Ryan, S. E. Lluch-Cota, and C. M. Ñiquen, 2003: From anchovies to sardines and back: Multidecadal change in the Pacific Ocean. *Science*, **299**, 217–221.

Chen, Q.-S., L.-E. Bai, and D. H. Bromwich, 1997: A harmonic-Fourier spectral limited-area model with an external wind lateral boundary condition. *Mon. Wea. Rev.,* **125**, 143-167.

Chu P.-S., and J. Wang, 1997: Tropical cyclone occurrences in the vicinity of Hawaii: Are the differences between El Niño years significant? *J. Climate*, **10**, 2683–2689.

-------, and X. Zhao, 2007: A Bayesian regression approach for predicting seasonal tropical cyclone activity over the central North Pacific. *J. Climate*, **20**, 4002–4013.

Clark J. D., and P. Chu, 2002: Interannual variation of tropical cyclone activity over the central North Pacific. *J. Meteor. Soc. Japan*, **80**, 403–418.

Côté, J., S. Gravel, A. Méthot, A. Patoine, M. Roch, and A.N. Staniforth. 1998: The operational CMC-MRB global Environmental Multiscale (GEM) model. Part 1: Design consideration and formulation. *Mon. Wea. Rev.* **126,** 1373-1395.

Cullen, M. J. P., 1993: The unified forecast/climate model. *Meteor. Mag.,* **122**, 81-122.

Davis C., and L. F. Bosart, 2002: Numerical simulations of the genesis of Hurricane Diana (1984). Part II: Sensitivity of track and intensity prediction. *Mon. Wea. Rev*., **130**, 1100-1124.

Dawe, J. T., and L. Thompson, 2007: PDO-related heat and temperature budget changes in a model of the north Pacific. *J. Climate*, **20**, 2092–2108.

Delleur, J. W., and M. L. Kavvas, 1980: Reply to Akaike's Information Criterion. *J. Appl. Meteor*., **19**, 116-117.

DeMaria, M., S. D. Aberson, K. V. Ooyama, and S. J. Lord, 1992: A nested spectral model for hurricane track forecasting. *Mon. Wea. Rev*., **120**, 1628-1643.

-------, and J. Kaplan, 1994: A statistical hurricane intensity prediction scheme (SHIPS) for the Atlantic basin. *Wea. Forecasting*, **9**, 209–220.

-------, 1996: The effect of vertical shear on tropical cyclone intensity change. *J. Atmos. Sci.*, **53**, 2076–2088.

-------, and J. Kaplan, 1999: An updated statistical hurricane intensity prediction scheme (SHIPS) for the Atlantic and eastern north Pacific basins. *Wea. Forecasting.*, **14**, 326–337.

Depperman, Rev C. E., 1947: Notes on the origin and structures of Philippine typhoons. *Bull. Amer. Meteor. Soc.*, **28**, 399–404.

Dickson R. R., and J. Namias, 1976: North American influences on the circulation and climate of the North Atlantic sector. *Mon. Wea. Rev.*, **104**, 1255–1265.

Dudhia, J., 1989: Numerical study of convection observed during the Winter Monsoon Experiment using a mesoscale two-dimensional model. *J. Atmos. Sci.,* **46**, 3077-3107.

Dunn, G. E. 1940. Cyclogenesis in the tropical Atlantic. *Bull. Amer. Meteor. Soc.*, **21**, 215–229.

-------, and B. I. Miller, 1960: *Atlantic Hurricanes*, Louisiana State Univ. Press, Baton Rouge, Louisiana, 377pp.

-------, 1971: A brief history of the United States hurricane warning service. *Muse News*, **3**, 140-143.

Dvorak, V., 1975: Tropical cyclone intensity analysis and forecasting from satellite imagery. *Mon. Wea. Rev.*, **103**, 420-430.

-------, 1984: Tropical cyclone intensity analysis using satellite data. NOAA Tech. Report NESDIS 11. Available from NOAA/NESDIS, 5200 Auth Rd., Washington DC, 20233, 47pp.

Elmore K. L., 2005: Alternatives to the chi-squared test for evaluating rank histograms from ensemble forecasts. *Wea. Forecasting*, **20**, 789–795.

Elsner J. B., and C. P. Schmertmann, 1993: Improving extended-range seasonal predictions of intense Atlantic hurricane activity. *Wea. Forecasting*, **8**, 345–351.

-------, and C. P. Schmertmann, 1994: Assessing forecast skill through cross validation. *Wea. Forecasting*, **9**, 619–624.

-------, A. A. Tsonis, and T. H. Jagger, 2006: High-frequency variability in hurricane power dissipation and its relationship to global temperature. *Bull. Amer. Meteor. Soc.*, **87**, 763–768.

-------, and T. H. Jagger, 2006: Comparison of hindcasts anticipating the 2004 Florida hurricane season. *Wea. Forecasting*, **21**, 182–192.

Emanuel, K.A., 1986: An air-sea interaction theory for tropical cyclones. Part I: Steady state maintenance. *J. Atmos. Sci*., **43**, 585-604.

-------, 1995: Sensitivity of tropical cyclones to surface exchange coefficients and a revised steady-state model incorporating eye dynamics. *J. Atmos. Sci*, **52**,3969–3976.

-------, 2003a: A similarity hypothesis for air-sea exchange at extreme wind speeds. *J. Atmos. Sci*., **60**, 1420-1428.

-------, 2003b: Tropical cyclones. *Ann. Rev. Earth Planet*, **31**, 75-104.

-------, 2004: Tropical cyclone enegertics and structure. In *Atmospheric Turbulence and Mesoscale Meteorology*, E. Fedorovich, R. Rotunno and B. Stevens, eds., Cambridge University Press, 280 pp.

-------, 2005: Increasing destructiveness of tropical cyclones over the past 30 years. *Nature*, **436**, 686-688.

-------, 2006: Climate and tropical cyclone activity: A new model downscaling approach. *J. Climate*, **19**, 4797-4802.

Evans, J. L., and R. E. Hart, 2003: Objective indicators of the life cycle evolution of extratropical transition for Atlantic tropical cyclones. *Mon. Wea. Rev.*, **131**, 909–925.

Fett, R. W., 1966: Upper level structure of the formative tropical cyclone. *Mon. Wea. Rev.*, **94**, 9-18.

Fraedrich, K., and L. M. Leslie, 1987: Combining predictive schemes in short-term forecasting. *Mon. Wea. Rev.*, **115**, 1640-1644.

-------, and B. Rückert, 1998: Metric adaption for analog forecasting. *Physica A*., **253**, 379-393.

-------, C. Raible, and F. Sielmann, 2003: Analog ensemble forecasts of tropical cyclone tracks in the Australian region. *Wea. Forecasting*, **18**, 3-11.

Frank, W. M., and G. S. Young, 2007: The interannual variability of tropical cyclones. *Mon. Wea. Rev.*, in press.

Franklin, J. L., C. J. McAdie, and M. B. Lawrence, 2003: Trends in track forecasting for tropical cyclones threatening the United States, 1970–2001. *Bull. Amer. Meteor. Soc.,* **84**, 1197-1203.

Frappier, A., T. Knutson, K.-B. Liu, and K. Emanuel, 2007: Perspective: coordinating paleoclimate research on tropical cyclones with hurricane-climate theory and modeling. *Tellus A*, **59**, 529–537.

Geerts, B. and M. Wheeler, 1998: The Madden-Julian Oscillation. Available online http://www-das.uwyo.edu/~geerts/cwx/notes/chap12/mjo.html, accessed September 17, 2007.

Gershunov, A., and T. P. Barnett, 1998: Interdecadal modulation of ENSO teleconnections. *Bull. Amer. Meteor. Soc.*, **79**, 2715–2725.

Glickman T. S., 2000: *Glossary of Meteorology*. 2d ed. Amer. Meteor. Soc., 855 pp.

Goerss, J. S., and R. Jeffries, 1994: Assimilation of synthetic tropical cyclone observations into the Navy Operational Global Atmospheric Prediction System. *Wea. Forecasting.,* **9**, 557-576.

-------, 2000: Tropical cyclone track forecasts using an ensemble of dynamical models. *Mon. Wea. Rev.,* **128**, 1187-1193.

-------, C. R. Sampson, and J. M. Gross, 2004: A history of western north Pacific tropical cyclone track forecast skill. *Wea. Forecasting*, **19**, 633-638.

Goldenberg, S. B. and L. J. Shapiro, 1996: Physical mechanisms for the association of El Niño and West African rainfall with Atlantic major hurricane activity. *J. Climate*, **9**, 1169-1187.

-------, Landsea, C. W., Mestas-Nuñez, A. M. and Gray, W. M. 2001. The recent increase in Atlantic hurricane activity: Causes and implications. *Science*, **293**, 474–479.

Goodrich, G. B., 2007: Influence of the Pacific decadal oscillation on winter precipitation and drought during years of neutral ENSO in the western United States. *Wea. Forecasting*, **22**, 116–124.

Grantz K., B. Rajagopalan, M. Clark, and E. Zagona, 2007: Seasonal shifts in the North American monsoon. *J. Climate*, **20**, 1923–1935.

Gray, B. M., 1988: Seasonal frequency variations of the 40-50 day oscillation. *Int. J. Climatol.*, **8**, 511-519.

Gray, L. J., E. F. Drysdale, T. J. Dunkerton, and B. N. Lawrence, 2001: Model studies of the interannual variability of the Northern Hemisphere stratospheric winter circulation: The role of the quasi-biennial oscillation, *Q. J. R. Meteorol. Soc.*, **127**, 1413– 1432.

Gray, W. M. 1968. Global view of the origin of tropical disturbances and storms. *Mon. Wea. Rev*. **96**, 669–700.

-------, and D. J. Shea, 1973: The hurricane's inner core region: Part II: Thermal stability and diurnal characteristics. *J. Atmos. Sci.*, **30**, 1565-1576.

-------, 1979: Tropical cyclone intensity determination through upper-tropospheric aircraft reconnaissance. *Bull. Amer. Meteor. Soc.*, **60**, 1069–1074

-------, 1984a: Atlantic seasonal hurricane frequency. Part I: El Niño and 30 mb quasi-biennial oscillation influences. *Mon. Wea. Rev*, **112**, 1649–1668.

-------, 1984b: Atlantic seasonal hurricane frequency. Part II: Forecasting its variability. *Mon. Wea. Rev.*, **112**, 1669–1683.

-------, C. W. Landsea, P. W. Mielke Jr., and K. J. Berry, 1992: Predicting Atlantic seasonal hurricane activity 6–11 months in advance. *Wea. Forecasting*, **7**, 440–455.

-------, -------, -------, and -------, 1993: Predicting Atlantic basin seasonal tropical cyclone activity by 1 August. *Wea. Forecasting*, **8**, 73–86.

-------, -------, -------, and -------, 1994: Predicting Atlantic basin seasonal tropical cyclone activity by 1 June. *Wea. Forecasting*, **9**, 103–115.

-------, -------, -------, and -------, 1998: Forecast of Atlantic seasonal hurricane activity for 1998. Department of Atmospheric Science Report, Colorado State University, Fort Collins, CO, 18 pp.

Grell, G., J. Dudhia, and D. Stauffer, 1994: A description of the Fifth-Generation Penn State/NCAR Mesoscale Model (MM5). *NCAR Technical Note*, NCAR/TN-398+STR.

Gruber A., 1974: The wavenumber–frequency spectra of satellite-measured brightness in the Tropics. *J. Atmos. Sci.*, **31**, 1675–1680.

Gutzler D. S., G. N. Kiladis, G. A. Meehl, K. M. Weickmann, and M. Wheeler, 1994: The global climate of December 1992–February 1993. Part II: Large-scale variability across the tropical western Pacific during TOGA COARE. *J. Climate*, **7**, 1606–1622.

Hall J. D., A. J. Matthews, and D. J. Karoly, 2001: The modulation of tropical cyclone activity in the Australian region by the Madden–Julian oscillation. *Mon. Wea. Rev*, **129**, 2970–2982.

Hawkins, H. F., and D. T. Rubsam, 1968: Hurricane Hilda, 1964: II. Structure and budgets of the hurricane on October 1, 1964. *Mon. Wea. Rev.*, **96**, 617-636.

-------, 1983: Hurricane Allen and island obstacles. *J. Atmos. Sci.*, **40**, 1360–1361.

Hawkins, J. D., T. F. Lee, J. Turk, C. Sampson, J. Kent, and K. Richardson, 2001: Real-time internet distribution of products for tropical cyclone reconnaissance. *Bull. Amer. Meteo. Soc*., **82**, 567-578.

Hendon, H. H., and B. Liebmann, 1990: The intraseasonal (30–50 day) oscillation of the Australian summer monsoon. *J. Atmos. Sci.*, **47**, 2909–2924.

-------, and -------, 1994: Organization of convection within the Madden–Julian oscillation. *J. Geophys. Res*, **99**, 8073–8083.

-------, 2000: Impact of air–sea coupling on the Madden–Julian oscillation in a general circulation model. *J. Atmos. Sci.*, **57**, 3939–3952.

-------, B. Liebmann, M. Newman, J. D. Glick, and J. E. Schemm, 2000: Medium-range forecast errors associated with active episodes of the Madden–Julian Oscillation. *Mon. Wea. Rev.*, **128**, 69–86.

-------, M. C. Wheeler, and C. Zhang, 2007: Seasonal dependence of the MJO–ENSO relationship. *J. Climate*, **20**, 531–543.

Herbert, P. J., and K. O. Poteat, 1975: A Satellite Classification Technique for Subtropical Cyclones. *NOAA Technical Memorandum*, **NWS SR-83**, 25 pp.

-------, 1978: Intensification criteria for tropical depressions of the western North Atlantic. *Mon. Wea. Rev.*, **106**, 831-840.

-------, 1980: The Atlantic hurricane season of 1979. *Mon. Wea. Rev.*, **108**, 973-990.

Hess, J. C. and Elsner, J. B. 1994. Historical developments leading to current forecast models of annual Atlantic hurricane activity. *Bull. Amer. Meteor. Soc.*, **75**, 1611–1621.

Heymsfield G. M., J. B. Halverson, E. Ritchie, J. Simpson, J. Molinari, and L. Tian, 2006: Structure of highly sheared Tropical Storm Chantal during CAMEX-4. *J. Atmos. Sci.*, **63**, 268–287.

Higgins, R. W., and S. D. Schubert, 1996: Simulations of persistent North Pacific circulation anomalies and interhemispheric teleconnections. *J. Atmos. Sci.,* **53,** 188–208.

-------, and K. C. Mo, 1997: Persistent North Pacific circulation anomalies and the tropical intraseasonal oscillation. *J. Climate,* **10,** 224–244.

-------, and W. Shi, 2001: Intercomparison of the principal modes of interannual and intraseasonal variability of the North American Monsoon System. *J. Climate,* **14***,* 403-417.

-------, and -------, 2006: Relationships between Gulf of California moisture surges and tropical cyclones in the Eastern Pacific basin. *J. Climate,* **19***,* 4601-4620.

-------, and D. J Gochis, 2007: Synthesis of results from the North American Monsoon Experiment (NAME) process study. *J. Climate*, **20**, 1601-1607.

Ho, C.-H., J.-H. Kim, J.-H. Jeong, H.-S. Kim, and D. Chen, 2006: Variation of tropical cyclone activity in the South Indian Ocean: El Niño–Southern Oscillation and Madden-Julian Oscillation effects. *J. Geophys. Res.*, **111**, D22101.

Hoffman, R. N., and S. M. Leidner, 2005: An introduction to the near–real–time QuikSCAT data. *Wea. Forecasting*, **20**, 476–493.

Hogan, T. and T. Rosmond, 1991: The description of the Navy Operational Global Atmospheric Prediction System's spectral forecast model. *Mon. Wea. Rev*., **119**, 1786-1815.

Holland, G., 1980: An analytic model of the wind and pressure profiles in hurricanes. *Mon. Wea. Rev*., **108**, 1212-1218.

-------, 1981: On the quality of the Australian tropical cyclone data base. *Aust. Meteorol. Mag.,* **29**, 169-181.

-------, 1983: Tropical cyclone motion: environmental interaction plus a beta effect. *J. Atmos. Sc*i., **40**, 328-342.

-------, and P. J. Webster, 2007: Heightened tropical cyclone activity in the North Atlantic: natural variability or climate trend? *Philos. Trans. R. Soc. London,* **A**.

Holton, J. R., 2004: *Introduction to dynamic meteorology*. Academic Press, 4th ed.

Hope, J. R., and C. J. Neumann, 1970: An operational technique for relating the movement of existing tropical cyclones to past tracks. *Mon. Wea. Rev*., **98**, 925-933.

-------, 1975: Atlantic hurricane season of 1974. *Mon. Wea. Rev.*, **103**, 285–293.

Horsfall, F., M. DeMaria, and J. M. Gross, 1997: Optimal use of large-scale boundary and initial fields for limited-area hurricane forecast models. Preprints, *22d Conf. on Hurricanes and Tropical Meteorology,* Fort Collins, CO, Amer. Meteor. Soc., 571–572.

Hurrell, J. W., 1995: Decadal trends in the North Atlantic Oscillation: Regional temperatures and precipitation. *Science*, **269**, 676–679.

-------, Y. Kushnir, G. Ottersen, and M. Visbeck, 2003: An overview of the North Atlantic Oscillation. *The North Atlantic Oscillation: Climatic Significance and Environmental Impact, Geophys. Monogr.,***134**, Amer. Geophys. Union, 1–35.

Inness, P.and J. M. Slingo, 2003: Simulation of the MJO in a coupled GCM. I: Comparison with observations and an atmopshere-only GCM. *J. Climate*, **16**, 345-364.

Jagger, T. H., and J. B. Elsner, 2006: Climatology models for extreme hurricane winds near the United States. *J. Climate*, **19**, 3220–3236.

Jarvinen, B. R., C. J. Neumann, and M. A. S. Davis, 1984: A tropical cyclone data tape for the north Atlantic basin, 1886-1983: contents, limitations, and uses. *NOAA Tech. Mem.,* NWS NHC-22, 28pp.

Johansson, A., 2007: Prediction skill of the NAO and PNA from daily to seasonal time scales. *J. Climate*, **20**, 1957–1975.

Jones, C., D. E. Waliser, and C. Gautier, 1998: The influence of the Madden-Julian Oscillation on ocean surface heat fluxes and sea surface temperature. *J. Climate*, **11**, 1057-1072.

-------, and B.C. Weare 1996. The role of low-level moisture convergence and ocean latent-heat fluxes in the Madden and Julian Oscillation. *J. Climate,* **9**, 3086-104.

-------, 2000: Occurrence of extreme precipitation events in California and relationships with the Madden–Julian oscillation. *J. Climate,* **13**, 3576–3587.

-------, D. E. Waliser, J.-K. E. Schemm, and K.-M. Lau, 2000: Prediction skill of the Madden and Julian oscillation in dynamical extended range forecasts. *Climate Dyn*, **16**, 273–289.

-------, and J.-K. E. Schemm, 2000: The influence of intraseasonal variations on medium-range weather forecasts over South America. *Mon. Wea. Rev.,* **128,** 486–494.

-------, L. M. V. Carvalho, R. W. Higgins, D. E. Waliser, and J. K. E. Schemm, 2004: A statistical forecast model of tropical intraseasonal convective anomalies. *J. Climate,* **17,** 2078–2095.

Jones P. D., T. Jonsson, and D. Wheeler, 1997: Extension to the North Atlantic Oscillation using early instrumental pressure observations from Gibraltar and South-West Iceland. *Int. J. Climatol.*, **17**, 1433-1450.

Jorgensen, D. P., 1984: Mesoscale and convective scale characteristics of mature hurricanes. Part I: general observations by research aircraft. *J. Atmos. Sci.*, **41,** 1268–85.

Kalnay, E., M. Kanamitsu, and W. E. Baker, 1990: Global numerical weather prediction at the National Meteorological Center. *Bull. Amer. Meteor. Soc.,* **71**, 1410-1428.

-------, and coauthors, 1996: The NCEP/NCAR 40-year reanalysis project. *Bull. Amer. Meteor. Soc*, **77**, 437–471.

Kanamitsu, M., 1989: Description of the NMC global data assimilation and forecast system. *Wea. Forecasting,* **4***,* 335-342.

Kepert, J. D., 2006: Observed Boundary Layer Wind Structure and Balance in the Hurricane Core. Part II: Hurricane Mitch. *J. Atmos. Sci.*, **63**, 2194–2211.

Kessler, W.S., M.J. McPhaden, and K.M. Weickmann, 1995: Forcing of intraseasonal Kelvin waves in the equatorial Pacific. *J. Geophys. Res.*, **100**, 10613-10631.

Khalsa, S.J.S., E J. Steiner. 1988. A TOVS dataset for study of the tropical atmosphere. *J. Appl. Meteor*., **27**, 851-862.

Kim, J.H., C. H. Ho, C. H. Sui, and S. K. Park, 2005: Dipole structure of interannual variations in summertime tropical cyclone activity over East Asia. *J. Climate*, **18**, 5344–5356.

Kim, K. Y., and Q. Wu, 1999: A comparison study of EOF techniques: analysis of nonstationary data with periodic statistics. *J. Climate*, **12**, 185–199.

Kimball, S. K., and F. C. Dougherty, 2006: The sensitivity of idealized hurricane structure and development to the distribution of vertical levels in MM5. *Mon. Wea. Rev.*, **134**, 1987–2008.

Kintanar, R. L., and L. A. Amadore, 1974: Typhoon climatology in relation to weather modification activities. WMO, No. 408. [Available from WMO Secretariat, CP 5, CH-1211, Geneva 20, Switzerland.].

Klein, W. H., 1952: Winter precipitation as related to the 700-millibar circulation. *Bull. Amer. Meteor. Soc.*, **9**, 439-453.

Kleinschmidt, E., Jr., 1951: Basics of a theory of the tropical cyclone. *Arch. Meteor. Geophys. Bioklimatol.,* **4A,** 53–72

Knaff, J. A., 1993: Evidence of a stratospheric QBO modulation of tropical convection. Department of Atmospheric Science Paper 520, Colorado State University, Fort Collins, CO, 91 pp.

-------, 1998: Predicting Summertime Caribbean Pressure in Early April. *Wea. Forecasting*, **13**, 740–752.

Kossin, J. P., and C. S. Velden, 2004: A pronounced bias in tropical cyclone minimum sea level pressure estimation based on the Dvorak Technique. *Mon. Wea. Rev.*, **132**, 165–173.

-------, K. R. Knapp, D. J. Vimont, R. J. Murnane, and B. A. Harper, 2007: A globally consistent reanalysis of hurricane variability and trends, *Geophys. Res. Lett.,* **34**, L04815.

Klotzbach, P. J., and W. M. Gray, 2003: Forecasting September Atlantic basin tropical cyclone activity. *Wea. Forecasting*, **18**, 1109–1128.

-------, and W. M. Gray, 2004: Updated 6–11 month prediction of Atlantic basin seasonal hurricane activity. *Wea. Forecasting*, **19**, 917–934.

-------, 2007: Recent developments in statistical prediction of seasonal Atlantic basin tropical cyclone activity. *Tellus A*, **59**, 511–518.

Knutson, T. R., and K. M. Weickmann, 1987: 30-60 day atmopsheric osciallations: composite life cycles of convection and circulation anomalies. *Mon. Wea.Rev.*, **115**, 1407-1436.

Krishnamurti T. N., and D. Subrahmanyam, 1982: The 30–50 day mode at 850 mb during MONEX. *J. Atmos. Sci.*, **39**, 2088–2095.

-------, D. K. Oosterhof, and A. V. Metha, 1988: Air-sea interaction on the timescale of 30-50 days. *J. Atmos. Sci.*, **45**, 1304-1322.

-------, C. M. Kishtawal, T. LaRow, D. Bachiochi, Z. Zhang, C. E. Williford, S. Gadgil, and S. Surendran, 1999: Improved skills for weather and seasonal climate forecasts from multimodel superensemble. *Science,* **285**, 1548-1550.

-------, -------, D. W. Shin, and C. E. Williford, 2000a: Multimodel superensemble forecasts for weather and seasonal climate. *J. Climate,* **13**, 4196-4216.

-------, -------, T. LaRow, D. Bachiochi, Z. Zhang, C. E. Williford, S. Gadgil, and S. Surendran, 2000b: Improving tropical precipitation forecasts from a multianalysis superensemble. *J. Climate,* **13**, 4217-4227.

-------, S. Surendran, D. W. Shin, R. J. Correa-Torres, T. S. V. Kumar, E. Williford, C. Kummerow, R. Adler, J. Simpson, R. Kakar, W. S. Olson and F. J. Turk, 2001: Real-time multianalysis–multimodel superensemble forecasts of precipitation using TRMM and SSM/I products. *Mon. Wea. Rev.,* **129**, 2861-2883.

-------, and D. R. Chakraborty, 2005: The Dynamics of Phase Locking. *J. Atmos. Sci.*, **62**, 2952–2964.

-------, S. Pattnaik, L. Stefanova, T. S. V. Vijaya Kumar, B. P. Mackey, A. J. O'Shay and R. J. Pasch., 2005: The hurricane intensity issue. *Mon. Wea. Rev.*, **133**, 1886–1912.

-------, T. S. V. V. Kumar, A. K. Mitra, W. T. Yun, L. Stefanova, B. P. Mackey, A. J. O'Shay, and W. K. Dewar, 2005: Weather and seasonal climate forecasts using the superensemble approach. *Predictability of Weather and Climate*. Cambridge University Press.

Krishnan, R., and M. Sugi, 2003: Pacific decadal oscillation and variability of the Indian summer monsoon rainfall. *Clim. Dyn.*, **21**, 233–242.

Kuhnel, I., 1989: Spatial and temporal variations in Australo-Indonesian region cloudiness. *Int. J. Climatol.*, **9**, 395-405.

Kurihara, Y., M. A. Bender, and R. T. Ross, 1993: An initialization scheme of hurricane models by vortex specification. *Mon. Wea. Rev.,* **121,** 2030-2045.

-------, -------, R. E. Tuleya, and R. J. Ross, 1995: Improvements in the GFDL hurricane prediction system. *Mon. Wea. Rev.,* **123,** 2791-2801.

-------, R. E. Tuleya, and M. A. Bender, 1998: The GFDL hurricane prediction system and its performance in the 1995 hurricane season. *Mon. Wea. Rev.,* **126,** 1306-1322.

Kutzbach, J. E., 1967: Empirical eigenvectors of sea-level pressure, surface temperature and precipitation complexes over North America. *J. Appl. Meteor.*, **6**, 791-802.

Lakshmanan, V., T. Smith, G. Stumpf, and K. Hondl, 2007: The warning decision support system–integrated information. *Wea. Forecasting*, **22**, 596–612.

Landsea, C., 1993: A climatology of intense (or major) Atlantic hurricanes. *Mon. Wea. Rev.*, **121**, 1703-1714.

-------, N. Nicholls, W. M. Gray, and L.A. Avila, 1996: Downward trends in the frequency of intense Atlantic hurricanes during the past five decades. *Geo. Res. Letters*, **23**, 1697-1700.

-------, J. L. Franklin, C. J. McAdie, J. L. Beven, J. M. Gross, B. R. Jarvinen, R. J. Pasch, E. N. Rappaport, J. P. Dunion, and P. P. Dodge, 2004: A reanalysis of hurricane Andrew's intensity. *Bull. Amer. Meteor. Soc.*, **85**, 1699–1712.

-------, 2007: Counting Atlantic tropical cyclones back to 1900, *Eos Trans. AGU,* **88**, 197-202.

Large, W. G., 1979: The turbulent fluxes of momentum and sensible heat over the open sea during moderate to strong winds. Ph.D Thesis, Institute of Oceanography and Department of Physics, University of British Columbia, pp. 180.

-------, and S. Pond, 1981: Open ocean momentum flux measurements in moderate to strong winds. *J. Phys. Oceanogr.*, **11**, 324-336.

-------, and -------, 1982: Sensible and latent heat flux measurements over the ocean. *J. Phys. Oceanogr.,* **12,** 464–482.

Larson, J., Y. Zhou, and R.W. Higgins, 2005: Characteristics of landfalling tropical cyclones in the United States and Mexico: climatology and interannual variability. *J. Climate*, **18**, 1247–1262.

Lau K.-M., and P. H. Chan, 1985: Aspects of the 40–50 day oscillation during the northern winter as inferred from outgoing longwave radiation. *Mon. Wea. Rev*, **113**, 1889–1909.

-------, and -------, 1986: The 40–50 day oscillation and the El Niño/Southern Oscillation: a new perspective. *Bull. Amer. Meteor. Soc.*, **67**, 533–534.

-------, and C.-H. Sui, 1997: Mechanisms of short-term sea surface temperature regulation: Observations during TOGA COARE. *J. Climate*, **10**, 465–472.

Lawrence, M. B., 2002: *Tropical cyclone report: Hurricane Lili 21 September-04 October*. National Hurricane Center, Miami, Florida. [Available on-line at http://www.nhc.noaa.gov/2002lili.shtml].

Lea, A. S. and Saunders, M. A. 2006. How well forecast were the 2004 and 2005 Atlantic and US hurricane seasons? *Weather*, **61**, 245–249.

Leslie, L., K. Fraedrich, and T. Glowacki, 1989: Forecasting the skill of a regional numerical weather prediction model. *Mon. Wea. Rev.*, **117**, 550–557.

-------, and -------, 1990: Reduction of tropical cyclone position errors using an optimal combination of independent forecasts. *Wea. Forecasting*, **5**, 158-161.

-------, G. J. Holland, M. Glover, and F. J. Woodcock, 1990: A climatological-persistence (CLIPER) scheme for predicting Australian region tropical cyclone tracks. *Aust. Met. Mag*., **38**, 87-92.

Li, S., W. A. Robinson, M. P. Hoerling, and K. M. Weickmann, 2007: Dynamics of the extratropical response to a tropical Atlantic SST anomaly. *J. Climate*, **20**, 560–574.

Liebmann B., H. H. Hendon, and J. D. Glick, 1994: The relationship between tropical cyclones of the western Pacific and Indian Oceans and the Madden–Julian Oscillation. *J. Meteor. Soc. Japan*, **72**, 401–411.

Lighthill, J., 1998: Fluid mechanics of tropical cyclones. *Theor. Comp. Fluid Mech*, **10**, 3-21.

Lin, Y.-L., D. B. Ensley, S. Chiao, and C.-Y. Huang, 2002: Orographic influences on rainfall and track deflection associated with the passage of a tropical cyclone. Mon. Wea. Rev., **130**, 2929-2950.

Liu, K.-B., 2007. Paleotempestology. *Encyclopedia of QuaternaryScience* (edS. Elias). Elsevier, Amsterdam, 1978–1986.

Liu, Y., D. Zhang, and M. K. Yau, 1997: A multiscale numerical study of Hurricane Andrew (1992). Part I: Explicit simulation and verification. *Mon. Wea. Rev.,* **125,** 3073–3093.

Lloyd-Hughes, B., M. A. Saunders and P. Rockett, 2004: A consolidated CLIPER model for improved August-September ENSO prediction skill, *Wea. Forecasting*, **19**, 1089-1105.

Lo, F., and H. H. Hendon, 2000: Empirical extended-range prediction of the Madden–Julian oscillation. *Mon. Wea. Rev*, **128**, 2528–2543.

Lonfat, M., A. Boissonnade, and R. Muir-Wood, 2007: Atlantic basin, U.S. and Caribbean landfall activity rates over the 2006-2010 period: an insurance industry perspective. *Tellus A*, **59**, 499–510.

Lord, S. J., 1993: Recent developments in tropical cyclone track forecasting with the NMC global analysis and forecast system. Preprints, *20th Conf. on Hurricanes and Tropical Meteorology,* San Antonio, TX, Amer. Meteor. Soc., 290-291.

Lorenz, D. J. and D. L. Hartmann, 2006: The effect of the MJO on the North American Monsoon. *J. Climate*, **19**, 333-343.

Lorenz, E. N., 1969: The predictability of a flow which possesses many scales of motion. Tellus, **21**, 289-307.

Lyons, S. W., 2004: U.S. tropical cyclone landfall variability: 1950–2002. *Wea. Forecasting*, **19**, 473–480.

Madden, R. A., and P. R. Julian, 1971: Detection of a 40–50 day oscillation in the zonal wind in the tropical Pacific. *J. Atmos. Sci.*, **28**, 702–708.

-------, and -------, 1972: Description of global-scale circulation cells in the tropics with a 40–50 day period. *J. Atmos. Sci.*, **29**, 1109–1123.

-------, and -------, 1994: Observations of the 40–50-Day tropical oscillation—a review. *Mon. Wea. Rev.*, **122**, 814–837.

Makin, V. K., 2005: A note on the drag of the sea surface at hurricane winds. *Boundary Layer Meteor.*, **115**, 169-176.

Maloney E. D., and D. L. Hartmann, 2000: Modulation of eastern North Pacific hurricanes by the Madden–Julian oscillation. *J. Climate*, **13**, 1451–1460.

-------, and J. T. Kiehl, 2002: MJO-related SST variations over the tropical eastern Pacific during Northern Hemisphere summer. *J. Climate*, **15**, 675-689.

-------, and S. K. Esbensen, 2007: Satellite and buoy observations of boreal summer intraseasonal variability in the tropical northeast Pacific. *Mon. Wea. Rev.*, **135**, 3–19.

Mandal, V., U. K. De, and B. K. Basu, 2007: Precipitation forecast verification of the Indian summer monsoon with intercomparison of three diverse regions. *Wea. Forecasting*, **22**, 428–443.

Manly, B. P. J., 1976: Exponential data transformations. *The Statistician*, **25**, 37-42.

Mann, M. E., and K. A. Emanuel, 2006: Atlantic hurricane trends linked to climate change, *Eos Trans. AGU,* **87**, 233-241.

-------, K. A. Emanuel, G. J. Holland, and P. J. Webster, 2007: Atlantic tropical cyclones revisited. *EOS*, **88**, 349-350.

Mantua, N. J., S. R. Hare, Y. Zhang, J. M. Wallace, and R. C. Francis,1997: A Pacific interdecadal climate oscillation with impacts on salmon production. *Bull. Amer. Meteor. Soc.*, **78**, 1069-1079.

-------, and -------, 2002: The Pacific Decadal Oscillation, *J. Oceanography*, **58**, 35–44.

Marks, D. G., 1992: The beta and advection model for hurricane track forecasting. *NOAA Tech. Memo*. NWS NMC-70, 89 pp.

Markus, R. M., N. F. Halbeisen, and J. F. Fuller, 1987: Air Weather Service; our heritage, 1937-1987, Military Airlift Command U.S. Air Force, Scott AFT, Illinois, 167 pp.

Marquardt, K. Sato, and M. Takahashi, 2001: The quasi-biennial oscillation, *Rev. of Geophysics*, **39**, 179-229..

Maynard, R. H., 1945: Radar and weather. *J. Meteor.*, **2**, 214-226.

McAdie, C. J., and M. B. Lawrence, 2000: Improvements to tropical cyclone track forecasting in the Atlantic basin, 1970-1998. *Bull. Amer. Meteor. Soc.,* **81**, 989-999.

McBride, J. L., 1981: Observational analysis of tropical cyclone formation. Part I: Basic description of data sets. *J. Atmos. Sci*., **38**, 1117-1131.

McGregor, S., N. J. Holbrook, and S. B. Power, 2007: Interdecadal sea surface temperature variability in the equatorial Pacific Ocean. Part I: The role of off-equatorial wind stresses and oceanic Rossby waves. *J. Climate*, **20**, 2643–2658.

McPhaden, M. J., and S. P. Hayes, 1991: On the variability of winds, sea surface temperature and surface layer heat content in the western equatorial Pacific. *J. Geophys. Res.,* **96**, 3331–3342..

Merrill, R. T., 1988: Environmental influences on hurricane intensification. *J. Atmos. Sci.*, **45**, 1678–1687.

Miller, B. I., 1965: A simple model of the hurricane inflow layer. *Weather Bureau Technical Note*, **18**, 16 pp.

Minobe, S., 2000: Spatio-temporal structure of the pentadecadal variability over the North Pacific. *Prog. Oceanogr*., **47**, 381– 408.

Mlawer, E. J., S. J. Taubman, P. D. Brown, M. J. Iacono, and S. A. Clough, 1997: Radiative transfer for inhomogeneous atmospheres: RRTM, a validated correlated-k model for the longwave. *J. Geophys. Res.*, **102**, 16663-16682.

Mo, K. C., 2000: Intraseasonal modulation of summer precipitation over North America. *Mon. Wea. Rev.,* **128,** 1490–1505.

-------, 2001: Adaptive filtering and prediction of intraseasonal oscillations. *Mon. Wea. Rev*., **129**, 802–817.

Moller, J. D., and M. T. Montgomery, 1999: Vortex Rossby-waves and hurricane intensification in a barotropic model. *J. Atmos. Sci.*, **56**, 1674 – 1687.

Montgomery, M. T., 1997: A theory for vortex Rossby-waves and its application to spiral bands and intensity changes in hurricanes. *Q. J. R. Meteorol. Soc.*, **123**, 435–465.

Mosedale T. J., D. B. Stephenson, M. Collins, and T. C. Millsu, 2006: Granger causality of coupled climate processes: Ocean feedback on the North Atlantic Oscillation. *J. Climate*, **19**, 1182–1194.

Murnane, R.J., 2004: Climate research and reinsurance. *Bull. Amer. Meteor. Soc.*, **85**, 697–707.

Nakazawa T., 1988: Tropical super cloud clusters within intraseasonal variations over the western Pacific. *J. Meteor. Soc. Japan*, **66**, 823–839.

Namias, J., 1951: The great Pacific anticyclone of winter 1949-50: a case study in the evolution of climactic anomalies. *J. Atmos. Sci.*, **8**, 251–261.

Neumann, C. J., 1972: An alternate to the HURRAN tropical cyclone forecast system. *NOAA Tech. Memo*. NWS SR-62, 22 pp.

-------, and J. R. Hope, 1972: Performance analysis of the HURRAN tropical cyclone forecast system. *Mon. Wea. Rev.,* **100**, 245-255.

-------, and M. B. Lawrence, 1975: An operational experiment in the statistical-dynamical prediction of tropical cyclone motions. *Mon. Wea. Rev.*, **109**, 522-538.

-------, and P. W. Leftwich, 1977: Statistical guidance of the prediction of eastern north Pacific tropical cyclone motion - part 1. *NOAA Tech. Memo*, NWS WR-125, 32 pp.

-------, and J. M. Pelissier, 1981a: An analysis of Atlantic tropical cyclone forecast errors, 1970-1979. *Mon. Wea. Rev*., **109**, 1248-1266.

-------, and -------, 1981b: Models for the prediction of tropical cyclone motion over the north Atlantic: an operational evaluation. *Mon. Wea. Rev*., **109**, 522-538.

-------, B. R. Jarvinen, and A. G. Pike, 1981: Tropical cyclones of the north Atlantic ocean, 1871-1981. *Historical Climatology Series 6-2*, National Climatic Data Center, Asheville, NC, 174 pp.

-------, and C. J. McAdie, 1991: A revised National Hurricane Center NHC83 model (NHC90). *NOAA Tech. Memo.* NWS NHC-44, 35 pp.

-------, 1993: Global Overview - Chapter 1. *Global guide to tropical cyclone forecasting*, **31**, World Meteorological Organization. Geneva, Switzerland.

Nicholls, N., 1988: El Nino—Southern Oscillation impact prediction. *Bull. Amer. Meteor. Soc.*, **69**, 173–176.

Olander, T. L, and C. S. Velden, 1997: Satellite-based objective estimates of tropical cyclone intensity estimates. Preprints, *22d Conf. on Hurricanes and Tropical Meteorology,* Miami, FL, Amer. Meteor. Soc., 499–500.

-------, and -------, 2007: The Advanced Dvorak Technique: continued development of an objective scheme to estimate tropical cyclone intensity using geostationary infrared satellite imagery. *Wea. Forecasting*, **22**, 287–298.

Ooyama, K. V., 1969: Numerical simulation of the life cycle of tropical cyclones**.** *J. Atmos. Sci.*. **26**, 3–40.

-------, 1982: Conceptual evolution of the theory and modeling of tropical cyclones. *J. Meteor. Soc. Japan*, **60**, 369–379.

Osborn, T. J., 2004: Simulating the winter North Atlantic Oscillation: the roles of internal variability and greenhouse gas forcing. *Clim. Dyn.*, **22**, 605-623.

-------, 2006: Recent variations in the winter North Atlantic Oscillation. *Weather*, **61**, 353-355.

Owens, B. F. and Landsea, C. W. 2003. Assessing the skill of operational Atlantic seasonal tropical cyclone forecasts. *Wea. Forecasting*, **18**, 45–54.

Paegle, J. N., L. A. Byerle, and K. C. Mo, 2000: Intraseasonal modulation of South American summer precipitation. *Mon. Wea. Rev.,* **128,** 837–850.

Palmén, E. H., 1948: On the formation and structure of tropical cyclones. *Geophysica*, Univ. of Helsinki, **3**, 26-38.

-------, and C. W. Newton, 1969: Atmospheric circulation systems: their structure and physical interpretation. Academic Press, 603 pp.

Pasch, R. J., M. B. Lawrence, L. A. Avila, J. L. Beven, J. L. Franklin and S. R. Stewart, 2004: Atlantic hurricane season of 2002. *Mon. Wea. Rev.,* **132**, 1829-1859.

Paterson, L. A., B. N. Hanstrum, N. E. Davidson, and H. C. Weber, 2005: Influence of environmental vertical wind shear on the intensity of hurricane-strength tropical cyclones in the Australian region. *Mon. Wea. Rev.*, **133**, 3644–3660.

Peng, M.S. and S.W. Chang, 2002: Numerical forecasting experiments on typhoon Herb (l996). *J. Meteor. Soc. Japan*, **80**, 1325-1338.

Pike A. C., and C. J. Neumann, 1987: The variation of track forecast difficulty among tropical cyclone basins. *Wea. Forecasting*, **2**, 237–241.

Pires, C. A., and R. A. P. Perdigão, 2007: Non-Gaussianity and asymmetry of the winter monthly precipitation estimation from the NAO. *Mon. Wea. Rev*., **135**, 430–448.

Pohl, B. and P. Camberlin, 2006: Influence of the Madden-Julian Oscillation on East African rainfall. Part I: Intraseasonal variability and regional dependency ; Part II: March-May season extremes and interannual variability. *Quart. J. Roy. Meteorol. Soc*., **132**, 2521-2560.

Pond, S., and W.G. Large, 1978: A system for remote measurements of air-sea fluxes of momentum, heat and moisture during moderate to strong winds. Ms. Rep. 32, Institute of Oceanography, University of British Columbia, 55 pp.

Powell, M. D. and P. G. Black, 1990: The relationship of hurricane reconnaissance flight-level wind measurements to winds measured by NOAA's oceanic platforms. *J. Wind Eng. Indu. Aerodynamics*, **36**, 381-392.

-------, S. H. Houston, and T. A. Reinhold, 1996: Hurricane Andrew's landfall in South Florida, Part I: standardizing measurements for documentation of surface wind fields. *Wea. Forecasting*, **11**, 329-349.

-------, and S. D. Aberson, 2001: Accuracy of United States tropical cyclone landfall forecasts in the Atlantic basin (1976-2000). *Bull. Amer. Meteor. Soc*., **82**, 2749-2768.

-------, P. J. Vickery, and T. A. Reinhold, 2003: Reduced drag coefficient for high wind speeds in tropical cyclones. *Nature*, **422**, 279-283.

Press, W. H., 1992: *Numerical recipies in C: the art of scientific computing*. Cambridge University Press, 994 pp.

Radford, A. M., 1994: Forecasting the movement of tropical cyclones at the Met. Office. *Met. Apps*., **1**, 355-363.

Ramage, C. S., 1959: Hurricane development. *J. Meteor.,* **16**, 227-237.

Rappaport, E., 1993: Preliminary report Hurricane Andrew. 28 pp. (updated March 2, 1993). Miami, Fla., National Hurricane Center.

Rasmusson E. M., and T. H. Carpenter, 1982: Variations in tropical sea surface temperature and surface wind fields associated with the Southern Oscillation/El Niño. *Mon. Wea. Rev.*, **110**, 354–384.

Reed, J. W., 1961: Circulation anomalies and tropical storms. *J. Atmos. Sci.*, **18**, 122.

Reichler, T., and J. O. Roads, 2005: Long-range predictability in the tropics. Part II: 30–60-day variability. *J. Climate*, **18**, 634–650.

Reynolds, R. W., N. A. Rayner, T. M. Smith, D. C. Stokes, and W. Wang, 2002: An improved in situ and satellite SST analysis for climate. *J. Climate*, **15**, 1609–1625.

Richman, M. B., 1981: Obliquely rotated principal components – an improved meteorological map typing technique. *J. Appl. Meteor.*, **20**, 1145-1159.

Riehl, H., 1948: On the formation of typhoons. *J. Meteor.*, **5**, 247-264.

-------, 1950: A model of hurricane formation. *J. Appl. Phys.,* **21,** 917–925.

-------, 1954: Tropical Meteorology. McGraw-Hill, 392 pp.

Rosenthal, S. L., 1978: Numerical simulation of tropical cyclone development with latent heat release by the resolvable scales I: model description and preliminary results. *J. Atmos. Sci.*, **35**, 258– 271.

Rotunno R., and K. A. Emanuel, 1987: An air-sea interaction theory for tropical cyclones. Part II. *J. Atmos. Sci.*, **44**, 542–561.

Ruane, A.C., and J.O. Roads, 2007: 6-Hour to 1-Year variance of five global precipitation sets. *Earth Interactions*, **11**, 1–29.

Sadler, J. C., 1976: A role of the tropical upper tropospheric trough in early season typhoon development. *Mon. Wea. Rev.*, **104**, 1266-1278.

Sanders, F. and R. W. Burpee, 1968: Experiments in barotropic hurricane track forecasting. *J. Appl. Meteo*r., **7**, 313-323.

Saunders, M. A. and Lea, A. S. 2005. Seasonal prediction of hurricane activity reaching the coast of the United States. *Nature* **434**, 1005–1008.

Schneider, N., and B. D. Cornuelle, 2005: The forcing of the Pacific decadal oscillation. *J. Climate*, **18**, 4355–4373.

Schwing, F.B., T. Murphree, and P. M. Green, 2002: The Northern Oscillation Index (NOI): a new climate index for the northeast Pacific. *Prog. in Oceanography*, **53**, 115-139.

Shapiro, L. J. and Goldenberg, S. B. 1998. Atlantic sea surface temperatures and tropical cyclone formation. *J. Climate*, **11**, 578–590.

Sharp R. J., M. A. Bourassa, and J. J. O'Brien, 2002: Early detection of tropical cyclones using SeaWinds-derived vorticity. *Bull. Amer. Meteor. Soc.*, **83**, 879–889.

Sheets, R. H., 1990: The National Hurricane Center: past, present and future. *Wea. Forecasting,* **5,** 185-232.

Shinoda, T., H. H. Hendon, and J. Glick, 1998: Intraseasonal variability of surface fluxes and sea surface temperature in the tropical Western Pacific and Indian Oceans. *J. Climate*, **11**, 1685–1702.

Sriver, R., and M. Huber, 2006: Low frequency variability in globally integrated tropical cyclone power dissipation, *Geophys. Res. Lett.,* **33**, L11705.

Shuman, F. G., 1989: History of numerical weather prediction at the National Meteorological Center. *Wea. Forecasting*, **4**, 286-296.

Sievers, O., K. Fraedrich, and C. C. Raible, 2000: Self-adapting analog ensemble predictions of tropical cyclone tracks. *Wea. Forecasting*, **15**, 623-629.

Simpson, R. H., 1974: The hurricane disaster potential scale. *Weatherwise,* **27**, 169, 186.

Smith, S. D., 1980: Wind stress and heat flux over the ocean in gale force winds. *J. Phys. Oceanogr.,* **10,** 709-726.

Smith, S.R., J. Brolley, J.J. O'Brien, and C.A. Tartaglione, 2007: ENSO's impact on regional U.S. hurricane activity. *J. Climate*, **20**, 1404–1414.

Smith T., and V. Lakshmanan, 2006: Utilizing Google Earth as a GIS platform for weather applications. Preprints, *22d Int. Conf. on Interactive Information Processing Systems (IIPS) for Meteorology, Oceanography, and Hydrology*, Atlanta, GA, Amer. Meteor. Soc., CD-ROM, 8.2.

Sobel, A. H., and S. J. Camargo, 2005: Influence of western North Pacific tropical cyclones on their large-scale environment. *J. Atmos. Sci.*, **62**, 3396–3407.

Sriver, R., and M. Huber, 2006: Low frequency variability in globally integrated tropical cyclone power dissipation, *Geophys. Res. Lett.,* **33**, L11705.

Stephens M. A., 1974: EDF statistics for goodness of fit and some comparisons. *J. Amer. Stat. Assoc.*, **69**, 730–737.

Stewart, S. R., 2005: *Tropical cyclone report: Hurricane Ivan 2-26 September 2004*. National Hurricane Center, Miami, Florida. [Available on-line at http://www.nhc.noaa.gov/2004ivan.shtml].

Straus, D. M., and J. Shukla, 2002: Does ENSO force the PNA? *J. Climate*, **15**, 2340–2358.

Tanabe, S., 1963: Low latitude analysis at the formative stage of typhoons in 1962. *Kishocho Kenkyu Jiho*, **15**, 405-418.

Tao, W.-K., and J. Simpson, 1993: The Goddard cumulus ensemble model. Part I: Model description. *Terr., Atmos. Oceanic Sci*., **4**, 35-72.

Tiedtke, M., W. A. Heckley, and J. Slingo, 1988: Tropical forecasting at ECMWF: The influence of physical parameterization on the mean structure of forecasts and analyses. *Quart. J. Roy. Meteor. Soc*, **114**, 639–664.

Thompson, D. W. J., and J. M. Wallace, 1998: The Arctic Oscillation signature in the wintertime geopotential height and temperature fields. *Geophys. Res. Lett*., **25,** 1297-1300.

Thompson, P. D. 1977: How to improve accuracy by combining independent forecasts. *Mon. Wea. Rev.*, **105**, 228-229.

Torrence, C., and G. P. Compo, 1998: A practical guide to wavelet analysis. *Bull. Amer. Meteor. Soc.*, **79**, 61–78.

Toth, Z., and E. Kalnay, 1993: Ensemble forecasting at NMC: The generation of perturbations. *Bull. Amer. Meteorol. Soc.*, **74**, 2317-2330.

-------, Y. Zhu, and T. Marchok, 2001: The use of ensembles to identify forecasts with small and large uncertainty. *Wea. Forecasting*, **16**, 436–477.

Trenberth, K. E., 1990: Recent observed interdecadal climate changes in the Northern Hemisphere. *Bull. Amer. Meteor. Soc.*, **71**, 988–993.

-------, 1997: The definition of El Niño. *Bull. Amer. Meteor. Soc.*, **78**, 2771–2777.

-------, and D. J. Shea, 2006: Atlantic hurricanes and natural variability in 2005, *Geophys. Res. Lett.,* **33**, L12704.

-------, and L. Smith, 2006: The vertical structure of temperature in the tropics: different flavors of El Niño. *J. Climate*, **19**, 4956–4973.

Velden, C. S., and L. M. Leslie, 1991: The basic relationship between tropical cyclone intensity and the depth of the environmental steering layer in the Australian region. *Wea. Forecasting,* **6**, 244-253.

Vitart, F. and Stockdale, T. N. 2001. Seasonal forecasting of tropical storms using coupled GCM integrations. *Mon. Wea. Rev.*, **129**, 2521–2537.

-------, 2003: Monthly forecasting system. ECMWF Tech. Memo. 424, 70 pp.

-------, S. Woolnough, M. A. Balmaseda, and A. M. Tompkins, 2007: Monthly forecast of the Madden–Julian Oscillation using a coupled GCM. *Mon. Wea. Rev.*, **135**, 2700–2715.

von Storch H., and J. Xu, 1990: Principal Oscillation Pattern analysis of the tropical 30–60 day oscillation. Part I: Definition of an index and its prediction. *Climate Dyn*, **4**, 179–190.

-------, and A. Smallegange, 1991: The phase of the 30- to 60-day oscillation and the genesis of tropical cyclones in the western Pacific. Max-Planck-Institut für Meteorologie Rep. 66, 22 pp.

Waliser D. E., C. Jones, J.-K. E. Schemm, and N. E. Graham, 1999: A statistical extended-range tropical forecast model based on the slow evolution of the Madden–Julian oscillation. *J. Climate*, **12**, 1918–1939

Walker, G. T., and E. W. Bliss, 1932: World Weather V. *Memoirs of the Royal Meteorological Society*, **4**, 53-84.

Wallace, J. M., and D. S. Gutzler, 1981: Teleconnections in the geopotential height field during the northern hemisphere winter. *Mon. Wea. Rev.*, **109**, 784–812.

-------, North Atlantic Oscillation/annular Mode: Two Paradigms - one phenomenon. *Quart. J. Roy. Meteor. Soc.*, **126**, 791-805

Walsh, J. E., and M. B. Richman, 1981: Seasonality in the associations between surface temperatures over the United States and the North Pacific Ocean. *Mon. Wea. Rev.,* **109**, 767-783.

Wang, S.-T., 1997: A meteorological analysis of Typhoon Herb of 1996. Central Weather Bureau, Unpublished manuscript.

Wang Y., J. D. Kepert, and G. Holland, 2000: On the effect of sea spray evaporation on tropical cyclone boundary-layer structure and intensity. *23rd Conf. Hurric. Trop. Meteorol.*, Dallas, TX

Weare, B. C., 1977: Empirical orthogonal analysis of Atlantic Ocean surface temperatures. *Quart. J. Roy. Meteor. Soc.*, **103**, 467-478.

-------, and Nasstrom, J.S. 1982: Examples of extended empirical orthogonal function analysis. *Mon. Wea. Rev.,* **110**, 481-485.

Weber, H. C. 2003: Hurricane track prediction using a statistical ensemble of numerical models. *Mon. Wea. Rev.,* **131**, 749-770.

Webster, P. J., G. J. Holland, J. A. Curry, and H.-R. Chang, 2005: Changes in tropical cyclone number, duration, and intensity in a warming environment. *Science*, **309**, 1844-1846.

Weickmann K. M., G. R. Lussky, and J. E. Kutzbach, 1985: Intraseasonal (30–60 day) fluctuations of outgoing longwave radiation and 250 mb streamfunction during northern winter. *Mon. Wea. Rev*, **113**, 941–961.

Weightman, R. H., 1919: The West India hurricane of September 1919 in the light of sounding observations. *Mon. Wea. Rev.*, **47**, 717-721.

Wheeler M., and K. M. Weickmann, 2001: Real-time monitoring and prediction of modes of coherent synoptic to intraseasonal tropical variability. *Mon. Wea. Rev*, **129**, 2677–2694.

-------, and H. H. Hendon, 2004: An all-season real-time multivariate MJO index: Development of an index for monitoring and prediction. *Mon. Wea. Rev.,* **132**, 1917-1932.

Weller R. A., and S. P. Anderson, 1996: Surface meteorology and air–sea fluxes in the western equatorial Pacific warm pool during the TOGA Coupled Ocean–Atmosphere Response Experiment. *J. Climate*, **9**, 1959–1990.

Wexler, H., 1947: Structure of hurricanes as determined by radar. *Ann. N.Y. Acad. Sci*., **48**, 821–844.

Whitaker, J. S., and K. M. Weickmann, 2001: Subseasonal variations of tropical convection and week-2 prediction of wintertime western North American rainfall. *J. Climate*, **14**, 3279-3288.

Wilks D. S., 1995: *Statistical Methods in the Atmospheric Sciences*. Academic Press, 467 pp.

Willoughby, H. E., J. A. Clos and M. G. Shoreibah, 1982: Concentric eye walls, secondary wind maxima, and the evolution of the hurricane vortex. *J. Atmos. Sci,* **39**, 395–411.

Wright, P. B., 1985: The Southern Oscillation: An ocean-atmosphere feedback system? *Bull. Amer. Meteor. Soc.*, **66**, 398-412.

WMO 2006. *Statement on Tropical Cyclones and Climate Change*, Available at http://www.wmo.ch/web/arep/arep-home.html.

Wu, L., S. A. Braun, J. Halverson and G. Heymsfield. 2006: A numerical study of Hurricane Erin (2001). part I: model verification and storm evolution. *J. Atmos. Sci,*, **63**, 65–86.

Xie, L., T. Yan, L. J. Pietrafesa, J. M. Morrison, and T. Karl, 2005: Climatology and interannual variability of North Atlantic hurricane tracks. *J. Climate*, **18**, 5370–5381.

Xue, Yan, R. W. Higgins, H.-K. Kim and V. Kousky, 2002: Impacts of the Madden Julian Oscillation on U.S. temperature and precipitation during ENSO-neutral and weak ENSO winters. *26th Climate Diagnostics and Prediction Workshop*, Amer. Meteor. Soc.

Yanai, M., 1964: Formation of tropical cyclones. *Rev. Geophys.*, **2,** 367-414.

Yasunari T., 1980: A quasi-stationary appearance of 30 to 40 day period in the cloudiness fluctuations during the summer monsoon over India. *J. Meteor. Soc. Japan*, **58**, 225–229.

Yeh, T.-C. and R. L. Elsberry, 1993a: Interaction of typhoons with the Taiwan orography. Part I: Upstream track deflections. *Mon.Wea. Rev.,* **121,** 3193–3212.

-------, and -------, 1993b: Interaction of typhoons with the Taiwan orography. Part II: Continuous and discontinuous tracks across the island. *Mon. Wea. Rev.,* **121,** 3213–3233.

Zehr, R. M., 2003: Environmental vertical wind shear with Hurricane Bertha (1996). *Wea. Forecasting*, **18**, 345–356.

Zhang, C., 2005: Madden-Julian Oscillation. *Rev. Geophys.*, **43**, RG2003.

Zhang, D.-L., and R. A. Anthes, 1982: A high-resolution model of the planetary boundary layer--sensitivity tests and comparison with SESAME-79 data. *J. Appl. Meteor*., **21**, 1594-1609.

Zheng, X., and C. S. Frederiksen, 2007: Statistical prediction of seasonal mean southern hemisphere 500-hPa geopotential heights. *J. Climate*, **20**, 2791–2809.

Zhou, S., and A. J. Miller, 2005: The Interaction of the Madden–Julian Oscillation and the Arctic Oscillation. *J. Climate*, **18**, 143–159.

Appendix: tables and figures

Table 1.1. Definitions, geographic regions, and abbreviations of the two basins (EPAC and NATL) and the seven sub-basins (CARIB, GOM, EEPAC, CEPAC, WEPAC, CPAC, and AMDR).

Basin	Latitude		Longitude		Text abbr.
	South	North	East	West	
East Pacific	all TCs in the best-track dataset				EPAC
North Atlantic	all TCs in the best-track dataset				NATL
Caribbean	10°N	20°N	60°W	90°W	CARIB
Gulf of Mexico	18°N	31°N	82.5°W	98°W	GOM
East East Pacific	n/a	n/a	n/a	100°W	EEPAC
Central East Pacific	n/a	n/a	100°W	115°W	CEPAC
West East Pacific	n/a	n/a	115°W	140°W	WEPAC
Central Pacific	n/a	n/a	140°W	180°W	CPAC
Atlantic Main Development Region	10°N	20°N	n/a	n/a	AMDR

Table 1.2: Criteria for HURRAN (Hope and Neumann, 1970) analog selection.

Selection Criteria	**Selection Range**
Radius of acceptance circle (distance from the existing storm)	2 ½ ° of latitude
Time of year	Current date +/- 15 days
Acceptance sector (heading)	22 ½ ° of current storm
Acceptance speed	+/- 5 kt (current storm <10 kt) +/- 50% (10 kt < current storm < 20 kt) +/- 10 kt (current storm > 20 kt)

Table 2.1: Tropical cyclone prediction methods used in this study.				
Name	**Acronym**	**Reference**	**Organization**	**Comments**
Statistical and Dynamical Hurricane Track Model	A98E	Neumann and McAdie (1991)	NOAA TPC	
NCEP Global Forecast System	AVNO	Kanamitsu (1989); Lord (1993)	NCEP	Aviation run
Beta and Advection Models	BAMS BAMM BAMD	Marks (1992); Holland (1983)	NOAA TPC	S-shallow-layer M-medium-layer D-deep-layer
Climatology and Persistence Model	CLP5	Neumann (1972)	NOAA TPC	
Canadian Meteorological Center Model	CMC	Côté et al. (1998)	CMC	
Geophysical Fluid Dynamics Laboratory Hurricane Forecast System	GFDL	Kurihara et al. (1993, 1995, 1998); Bender et al. (1993)	NOAA GFDL	
Consensus Forecast Models	CONU GUNS GUNA	Goerss (2000)	NCEP TPC	CONU: a consensus of at least two of GFDL, GFDN (U.S. Navy run of GFDL), GFS, NOGAPS, and UKMET GUNS: consensus of GFDL, UKMET, and NOGAPS GUNA: consensus of GFDL, UKMET, NOGAPS, and GFS
Limited Area Sine Transform Barotropic Model	LBAR	Chen et al. (1997); Horsfall et al. (1997)	NOAA TPC	
U.S. Navy	NOGAPS	Hogan and	Fleet Numerical	

Operational Global Atmospheric Prediction System		Rosmond (1991); Goerss and Jeffries (1994)	Meteorological and Oceanographic Center (FNMOC)	
United Kingdom Meteorological Office Model	UKMET	Cullen (1993); Heming et al. (1995)	UKMET	
TPC Official Forecast	OFCL		NOAA TPC	

Table 2.2: Hurricane Ivan trajectory errors for the thirty-five 24-h forecasts generated between 0000 UTC 4 Sept. and 1200 UTC 12 Sept. The acronyms are defined in Table 2.1.

Acronym	Heading error (degrees)	Position error (km)
A98E	**-0.4**	74
AVNO	6.2	115
BAMD	3.7	107
BAMM	1.5	83
BAMS	3.2	139
CLP5	**-0.8**	87
CMC	3.0	108
CONU	5.9	82
GFDL	4.0	86
GUNA	6.3	91
GUNS	5.8	77
LBAR	3.2	97
NOGAPS	4.3	75
UKMET	4.6	78
NHC OFCL	5.8	85

Table 2.3: p values (for $\alpha = 0.01$, two-tailed t-test) comparing model trajectory errors to zero, CLP5, or OFCL. p values less than 0.005 imply that the model errors are significantly different from zero, CLP5, or OFCL at the 99% confidence level. p values in **bold** represent cases where there is no statistically significant difference between the models' heading errors and no (zero) error, CLP5, or OFCL. The acronyms are defined in Table 1.			
Acronym	**No Error**	**CLP5**	**OFCL**
A98E	**0.718**	**0.726**	0.000
AVNO	0.000	0.000	**0.630**
BAMD	0.000	0.000	0.022
BAMM	**0.072**	**0.007**	0.000
BAMS	0.014	0.002	0.037
CLP5	**0.441**	1.000	0.000
CMC	0.000	0.000	0.001
CONU	0.000	0.000	**0.814**
GFDL	0.000	0.000	0.020
GUNA	0.000	0.000	**0.326**
GUNS	0.000	0.000	**0.966**
LBAR	0.001	0.000	**0.005**
UKMET	0.000	0.000	**0.191**
NOGAPS	0.000	0.000	**0.074**
NHC OFCL	0.000	0.000	1.000

Table 2.4: Selected examples from the 2004 tropical Atlantic season where mean 24-h statistical-climatological model position errors are less than average 24-h NWP model position errors over the life of the TC. Acronyms are defined in Table 2.1.				
Storm name	**Statistical-climatological model**	**Model position error (km)**	**NWP model**	**Model position error (km)**
Bonnie	A98E	107	AVNO	170
			GUNA	181
			LBAR	135
Danielle	A98E	165	AVNO	212
	CLP5	192	UKMET	191
Ivan	A98E	80	AVNO	104
	CLP5	94	GFDL	96
			NOGAPS	96
			GUNA	83
Jeanne	A98E	107	GFDN	115
			NOGAPS	119
			UKMET	117

Table 3.1: CSU seasonal forecasts of TC activity. Skill relative to climatology (1.00 is a perfect forecast)

	TCC	HC	IHC
December	0.05	-0.08	0.08
April	-0.13	-0.33	-0.17
June	0.57	0.46	0.42
August	0.61	0.60	0.69

Table 3.2: Mean and standard deviation of number of TCs that form per season (TCC). Coefficient of variation is mean divided by standard deviation.

Basin	Mean seasonal TCC	Standard deviation of TCC	Coefficient of Variation
Western Pacific	27.8	4.4	0.16
EPAC	15.9	4.4	0.28
NATL	12.1	5.1	0.42
CARIB	2.1	1.8	0.84
GOM	2.5	1.6	0.67
EEPAC	2.3	1.5	0.63
CEPAC	9.3	3.2	0.34
WEPAC	3.4	2.1	0.63
CPAC	1.0	1.2	1.25
AMDR	5.9	3.4	0.59

Table 3.3: Anderson-Darling test of normality for TC activity metrics.

	TCC	**HC**	**IHC**	**ACE**	**PDI**	**STCD**	**SSD**	**SMD**	**SED**
EPAC	0.32	0.54	0.41	0.50	0.62	0.39	0.35	0.28	0.41
NATL	0.80	0.97	1.77	1.37	1.86	17.31	0.75	1.26	0.92
CARIB	2.26	2.63	4.52	2.16	3.11	1.28	0.82	0.61	0.16
GOM	1.07	2.29	6.34	2.25	3.35	1.35	1.15	1.19	0.48
EEPAC	0.90	4.39	14.12	2.59	4.04	1.35	3.47	0.37	0.41
CEPAC	0.44	0.64	0.80	0.56	0.31	1.01	0.38	0.27	0.43
WEPAC	0.94	0.92	1.96	1.36	1.42	1.25	0.59	0.53	0.22
CPAC	3.16	5.26	5.89	2.16	3.31	1.40	3.34	0.34	1.37
AMDR	0.85	1.73	3.73	2.33	3.09	1.18	2.03	1.29	0.42

	TCLC	**USLC**	**USLHC**	**TCLP**	**USLP**	**USLHP**
EPAC	1.34			1.09		
NATL	0.60	1.85	2.04	0.21	1.22	0.88

Table 3.4: Anderson-Darling test of normality for climate indices.

	JFM	FMA	MAM	AMJ	MJJ	JJA	JAS	ASO	SON	OND	NDJ	DFJ
NINO1	2.22	2.19	1.88	1.84	1.87	1.94	1.97	1.68	1.04	1.24	1.71	2.14
NINO3	1.10	1.93	1.28	30.26	0.28	0.63	0.83	0.82	0.63	0.59	0.71	0.79
NINO3.4	1.19	1.04	1.03	0.74	0.54	0.67	0.69	0.54	0.48	0.56	0.79	0.97
NINO4	0.39	0.68	0.66	0.34	0.31	0.36	0.42	0.34	0.24	0.20	0.21	0.29
NATL	0.62	0.39	0.18	0.24	0.21	0.37	0.40	0.65	0.87	1.00	0.68	0.72
QBO	0.74	1.08	1.30	1.36	1.34	1.08	1.11	1.23	1.15	0.79	0.74	0.62
PDO	0.61	0.55	0.78	0.41	0.26	0.70	0.77	0.53	0.42	0.34	0.41	0.47
SOI	0.51	0.19	0.25	0.38	0.52	0.27	0.34	0.17	0.31	0.51	0.62	0.45
NOI	0.59	0.41	0.38	0.27	0.47	0.20	0.39	0.24	0.27	0.29	0.28	0.61
NAO	0.51	0.20	0.41	0.42	0.35	0.50	0.23	0.32	0.30	0.16	0.56	0.35
PNA	0.57	0.44	0.16	0.46	0.56	0.22	0.31	0.59	0.25	0.38	0.45	0.27
AO	0.46	0.78	0.42	0.26	0.33	0.41	0.46	0.21	0.29	0.61	0.32	0.15

Table 3.5: Interbasin correlation of TCC, 1970-2006

	EPAC TCC	NATL TCC	CARIB TCC	GOM TCC	EEPAC TCC	CEPAC TCC	WEPAC TCC	CPAC TCC	AMDR TCC
EPAC	1.00								
NATL	-0.24	1.00							
CARIB	-0.39	0.75	1.00						
GOM	-0.30	0.66	0.45	1.00					
EEPAC	0.16	-0.06	0.05	0.03	1.00				
CEPAC	0.71	-0.08	-0.32	-0.34	-0.20	1.00			
WEPAC	0.60	-0.16	-0.16	-0.01	-0.11	0.07	1.00		
CPAC	0.61	-0.33	-0.43	-0.24	0.01	0.22	0.39	1.00	
AMDR	-0.41	0.82	0.73	0.48	-0.19	-0.19	-0.22	-0.40	1.00

Table 4.1: Sample of the real-time MJO composite indices for the August to September 2005. Pentad averages of 200 hPa velocity potential anomalies, normalized by standard deviation, are shown for each of the 10 indices for the period 02 June to 29 November 2005. Positive (negative) values correspond to positive anomalies of 200 hPa velocity potential, and thus upper-tropospheric convergence (divergence) and enhanced (suppressed) convection.

Date	**Index 1 80°E**	**Index 2 100°E**	**Index 3 120°E**	**Index 4 140°E**	**Index 5 160°E**	**Index 6 120°W**	**Index 7 40°W**	**Index 8 10°W**	**Index 9 20°E**	**Index 10 70°E**
20050801	0.44	-0.55	-1.34	-1.83	-1.41	-0.22	0.79	1.58	1.76	0.8
20050806	1.56	0.52	-0.56	-1.66	-2.11	-1.33	-0.24	0.95	1.97	1.75
20050811	0.45	0.49	0.39	0.13	-0.28	-0.51	-0.51	-0.35	0.03	0.4
20050816	-0.02	0.43	0.72	0.84	0.51	-0.09	-0.53	-0.81	-0.76	-0.23
20050821	-0.15	0.17	0.4	0.53	0.38	0.03	-0.26	-0.48	-0.51	-0.23
20050826	-0.8	-0.57	-0.17	0.4	0.91	0.86	0.49	-0.07	-0.81	-1.00
20050831	-0.78	-0.59	-0.24	0.32	0.84	0.86	0.55	0.02	-0.71	-0.98
20050905	-1.75	-2.3	-2.17	-1.22	0.69	2.07	2.39	1.9	0.18	-1.67
20050910	-0.43	-1.7	-2.42	-2.43	-1.08	0.76	1.93	2.5	1.87	-0.01
20050915	-0.13	-1.01	-1.54	-1.65	-0.86	0.36	1.18	1.63	1.34	0.18
20050920	0.86	0.62	0.21	-0.37	-0.91	-0.9	-0.57	-0.04	0.69	0.96
20050925	0.52	0.87	1.00	0.82	0.14	-0.55	-0.91	-0.99	-0.57	0.25
20050930	-0.19	-0.23	-0.15	0.05	0.28	0.35	0.26	0.05	-0.3	-0.43

Table 4.2: Correlations of each MJO index with the other nine indices.

	Index 1 80°E	**Index 2 100°E**	**Index 3 120°E**	**Index 4 140°E**	**Index 5 160°E**	**Index 6 120°W**	**Index 7 40°W**	**Index 8 10°W**	**Index 9 20°E**	**Index 10 70°E**
Index1	1									
Index2	0.785	1								
Index3	0.392	0.877	1							
Index4	-0.12	0.52	0.87	1						
Index5	-0.76	-0.2	0.3	0.734	1					
Index6	-0.99	-0.87	-0.53	-0.04	0.651	1				
Index7	-0.69	-0.99	-0.93	-0.63	0.066	0.8	1			
Index8	-0.21	-0.77	-0.98	-0.95	-0.47	0.36	0.85	1		
Index9	0.466	-0.18	-0.63	-0.93	-0.93	-0.3	0.31	0.764	1	
Index10	0.971	0.625	0.18	-0.34	-0.89	-0.9	-0.52	0.015	0.656	1

Table 4.3. First four statistical moments of the seasonal (June-Nov) MJO indices, pre- and post-transformation (Manly 1976).

	Index1 80°E	Index2 100°E	Index3 120°E	Index4 140°E	Index5 160°E	Index6 120°W	Index7 40°W	Index8 10°W	Index9 20°E	Index10 70°E
Mean	-0.06	-0.05	-0.03	0.00	0.05	0.07	0.05	0.02	-0.05	-0.08
Stdev	0.86	0.88	0.92	0.95	0.92	0.88	0.89	0.93	0.94	0.90
Skew	0.10	0.21	0.15	0.05	0.04	-0.11	-0.20	-0.11	-0.05	0.00
Kurt	-0.35	-0.06	0.03	-0.15	-0.17	-0.33	0.00	-0.03	-0.14	-0.32
K-parameter	**-0.05**	**-0.09**	**-0.06**	**0.025**	**-0.025**	**0.05**	**0.08**	**0.04**	**0.025**	**0**
Mean_T	-0.07	-0.09	-0.06	-0.01	0.04	0.08	0.08	0.03	-0.03	-0.08
Stdev_T	0.86	0.88	0.92	0.95	0.92	0.88	0.89	0.93	0.94	0.90
Skew_T	-0.01	-0.01	-0.01	-0.02	-0.02	0.00	0.00	0.00	0.02	0.00
Kurt_T	-0.35	-0.18	-0.08	-0.17	-0.18	-0.34	-0.12	-0.11	-0.15	-0.32

Table 4.4. Expected fraction of TC activity p_0 given by MJO phase frequency per index.

Index	**Total number**	**Number ENH**	**Fraction p_0**	**Number NEU**	**Fraction p_0**	**Number SUP**	**Fraction p_0**
Index 1	1066	161	0.15	774	0.73	131	0.12
Index 2	1066	169	0.16	775	0.73	122	0.11
Index 3	1066	172	0.16	771	0.72	123	0.12
Index 4	1066	175	0.16	738	0.69	153	0.14
Index 5	1066	144	0.14	764	0.72	158	0.15
Index 6	1066	125	0.12	781	0.73	160	0.15
Index 7	1066	117	0.11	784	0.74	165	0.15
Index 8	1066	133	0.12	766	0.72	167	0.16
Index 9	1066	159	0.15	760	0.71	147	0.14
Index 10	1066	165	0.15	769	0.72	132	0.12

Table 4.5. Observed fraction of TC genesis events $\hat{p}$ for each of the 9 basins and sub-basins. Indices 1-5 are shown.

All TCs			Index 1 80°E		Index 2 100°E		Index 3 120°E		Index 4 140°E		Index 5 160°E		. . .
Basin	Storm Type	MJO Phase	Number per phase	$\hat{p}$	Number per phase	$\hat{p}$	Number per phase	$\hat{p}$	Number per phase	$\hat{p}$	Number per phase	$\hat{p}$	Total Number
EPAC	TC	ENH	45	0.09	50	0.1	48	0.1	51	0.11	69	0.14	481
		NEU	345	0.72	348	0.72	355	0.74	358	0.74	357	0.74	
		SUP	91	0.19	83	0.17	78	0.16	72	0.15	55	0.11	
	H	ENH	23	0.09	29	0.11	22	0.08	19	0.07	28	0.1	270
		NEU	205	0.76	194	0.72	198	0.73	205	0.76	211	0.78	
		SUP	42	0.16	47	0.17	50	0.19	46	0.17	31	0.11	
	IH	ENH	16	0.12	15	0.11	10	0.08	10	0.08	11	0.08	133
		NEU	97	0.73	95	0.71	101	0.76	100	0.75	106	0.8	
		SUP	20	0.15	23	0.17	22	0.17	23	0.17	16	0.12	
NATL	TC	ENH	72	0.22	69	0.21	57	0.18	47	0.14	31	0.1	325
		NEU	223	0.69	222	0.68	234	0.72	224	0.69	219	0.67	
		SUP	30	0.09	34	0.1	34	0.1	54	0.17	75	0.23	
	H	ENH	42	0.23	38	0.21	37	0.2	26	0.14	18	0.1	183
		NEU	130	0.71	131	0.72	127	0.69	128	0.7	119	0.65	
		SUP	11	0.06	14	0.08	19	0.1	29	0.16	46	0.25	
	IH	ENH	20	0.27	18	0.25	14	0.19	9	0.12	8	0.11	73
		NEU	50	0.68	50	0.68	51	0.7	55	0.75	45	0.62	
		SUP	3	0.04	5	0.07	8	0.11	9	0.12	20	0.27	
CARIB	TC	ENH	15	0.28	8	0.15	7	0.13	9	0.17	5	0.09	54
		NEU	37	0.69	36	0.67	38	0.7	35	0.65	34	0.63	
		SUP	2	0.04	10	0.19	9	0.17	10	0.19	15	0.28	
	H	ENH	9	0.29	8	0.26	8	0.26	5	0.16	2	0.06	31
		NEU	22	0.71	19	0.61	18	0.58	21	0.68	20	0.65	
		SUP	0	0	4	0.13	5	0.16	5	0.16	9	0.29	
	IH	ENH	5	0.26	5	0.26	4	0.21	1	0.05	1	0.05	19
		NEU	14	0.74	11	0.58	11	0.58	14	0.74	13	0.68	
		SUP	0	0	3	0.16	4	0.21	4	0.21	5	0.26	
GOM	TC	ENH	16	0.25	16	0.25	11	0.17	7	0.11	4	0.06	65
		NEU	43	0.66	42	0.65	46	0.71	44	0.68	44	0.68	
		SUP	6	0.09	7	0.11	8	0.12	14	0.22	17	0.26	
	H	ENH	6	0.21	6	0.21	4	0.14	2	0.07	1	0.03	29
		NEU	21	0.72	19	0.66	21	0.72	21	0.72	19	0.66	
		SUP	2	0.07	4	0.14	4	0.14	6	0.21	9	0.31	
	IH	ENH	1	0.08	3	0.23	3	0.23	2	0.15	2	0.15	13
		NEU	11	0.85	8	0.62	8	0.62	9	0.69	9	0.69	
		SUP	1	0.08	2	0.15	2	0.15	2	0.15	2	0.15	
EEPAC	TC	ENH	5	0.08	5	0.08	5	0.08	2	0.03	7	0.11	62
		NEU	45	0.73	45	0.73	42	0.68	46	0.74	48	0.77	

		SUP	12	0.19	12	0.19	15	0.24	14	0.23	7	0.11	
		ENH	0	0	2	0.17	2	0.17	0	0	0	0	
	H	NEU	10	0.83	7	0.58	6	0.5	10	0.83	12	1	12
		SUP	2	0.17	3	0.25	4	0.33	2	0.17	0	0	
		ENH	0	0	0	0	0	0	0	0	0	0	
	IH	NEU	0	0	0	0	0	0	1	1	1	1	1
		SUP	1	1	1	1	1	1	0	0	0	0	
		ENH	32	0.1	34	0.11	28	0.09	30	0.1	39	0.13	
	TC	NEU	224	0.73	224	0.73	236	0.77	237	0.77	228	0.75	306
		SUP	50	0.16	48	0.16	42	0.14	39	0.13	39	0.13	
		ENH	16	0.09	17	0.1	14	0.08	12	0.07	21	0.12	
CEPAC	H	NEU	133	0.75	128	0.72	131	0.74	136	0.76	139	0.78	178
		SUP	29	0.16	33	0.19	33	0.19	30	0.17	18	0.1	
		ENH	11	0.14	10	0.13	7	0.09	6	0.08	5	0.06	
	IH	NEU	58	0.74	56	0.72	61	0.78	63	0.81	65	0.83	78
		SUP	9	0.12	12	0.15	10	0.13	9	0.12	8	0.1	
		ENH	5	0.06	9	0.11	12	0.14	15	0.18	18	0.21	
	TC	NEU	60	0.71	62	0.74	61	0.73	59	0.7	62	0.74	84
		SUP	19	0.23	13	0.15	11	0.13	10	0.12	4	0.05	
		ENH	6	0.09	10	0.15	6	0.09	7	0.11	6	0.09	
WEPAC	H	NEU	51	0.78	48	0.74	52	0.8	52	0.8	51	0.78	65
		SUP	8	0.12	7	0.11	7	0.11	6	0.09	8	0.12	
		ENH	3	0.07	4	0.1	3	0.07	4	0.1	5	0.12	
	IH	NEU	30	0.73	29	0.71	28	0.68	27	0.66	31	0.76	41
		SUP	8	0.2	8	0.2	10	0.24	10	0.24	5	0.12	
		ENH	3	0.1	2	0.07	3	0.1	4	0.14	5	0.17	
	TC	NEU	16	0.55	17	0.59	16	0.55	16	0.55	19	0.66	29
		SUP	10	0.34	10	0.34	10	0.34	9	0.31	5	0.17	
		ENH	1	0.07	0	0	0	0	0	0	1	0.07	
CPAC	H	NEU	11	0.73	11	0.73	9	0.6	7	0.47	9	0.6	15
		SUP	3	0.2	4	0.27	6	0.4	8	0.53	5	0.33	
		ENH	2	0.15	1	0.08	0	0	0	0	1	0.08	
	IH	NEU	9	0.69	10	0.77	12	0.92	9	0.69	9	0.69	13
		SUP	2	0.15	2	0.15	1	0.08	4	0.31	3	0.23	
		ENH	44	0.28	38	0.24	24	0.15	19	0.12	13	0.08	
	TC	NEU	100	0.63	104	0.65	119	0.75	115	0.72	100	0.63	159
		SUP	15	0.09	17	0.11	16	0.1	25	0.16	46	0.29	
		ENH	22	0.29	17	0.22	14	0.18	8	0.11	3	0.04	
AMDR	H	NEU	51	0.67	52	0.68	52	0.68	53	0.7	47	0.62	76
		SUP	3	0.04	7	0.09	10	0.13	15	0.2	26	0.34	
		ENH	9	0.27	9	0.27	7	0.21	2	0.06	2	0.06	
	IH	NEU	24	0.73	22	0.67	22	0.67	26	0.79	21	0.64	33
		SUP	0	0	2	0.06	4	0.12	5	0.15	10	0.3	

Table 4.6. As in Table 4.5, but Indices 6-10 are shown.

All TCs			Index 6 120°W		Index 7 40°W		Index 8 10°W		Index 9 20°E		Index 10 70°E		
Basin	Storm Type	MJO Phase	Number per phase	$\hat{p}$	Number per phase	$\hat{p}$	Number per phase	$\hat{p}$	Number per phase	$\hat{p}$	Number per phase	$\hat{p}$	Total Number
EPAC	TC	ENH	90	0.19	72	0.15	69	0.14	58	0.12	56	0.12	481
		NEU	342	0.71	360	0.75	362	0.75	369	0.77	344	0.72	
		SUP	49	0.1	49	0.1	50	0.1	54	0.11	81	0.17	
	H	ENH	43	0.16	43	0.16	46	0.17	38	0.14	31	0.11	270
		NEU	201	0.74	201	0.74	205	0.76	209	0.77	205	0.76	
		SUP	26	0.1	26	0.1	19	0.07	23	0.09	34	0.13	
	IH	ENH	19	0.14	17	0.13	23	0.17	19	0.14	18	0.14	133
		NEU	97	0.73	103	0.77	102	0.77	105	0.79	99	0.74	
		SUP	17	0.13	13	0.1	8	0.06	9	0.07	16	0.12	
NATL	TC	ENH	23	0.07	31	0.1	39	0.12	64	0.2	73	0.22	325
		NEU	236	0.73	237	0.73	235	0.72	225	0.69	223	0.69	
		SUP	66	0.2	57	0.18	51	0.16	36	0.11	29	0.09	
	H	ENH	7	0.04	15	0.08	23	0.13	36	0.2	46	0.25	183
		NEU	136	0.74	133	0.73	128	0.7	128	0.7	126	0.69	
		SUP	40	0.22	35	0.19	32	0.17	19	0.1	11	0.06	
	IH	ENH	2	0.03	4	0.05	4	0.05	14	0.19	21	0.29	73
		NEU	50	0.68	54	0.74	57	0.78	52	0.71	48	0.66	
		SUP	21	0.29	15	0.21	12	0.16	7	0.1	4	0.05	
CARIB	TC	ENH	1	0.02	9	0.17	7	0.13	12	0.22	11	0.2	54
		NEU	42	0.78	37	0.69	39	0.72	37	0.69	40	0.74	
		SUP	11	0.2	8	0.15	8	0.15	5	0.09	3	0.06	
	H	ENH	0	0	3	0.1	4	0.13	9	0.29	9	0.29	31
		NEU	21	0.68	20	0.65	20	0.65	20	0.65	21	0.68	
		SUP	10	0.32	8	0.26	7	0.23	2	0.06	1	0.03	
	IH	ENH	0	0	1	0.05	1	0.05	5	0.26	5	0.26	19
		NEU	13	0.68	13	0.68	15	0.79	13	0.68	14	0.74	
		SUP	6	0.32	5	0.26	3	0.16	1	0.05	0	0	
GOM	TC	ENH	5	0.08	7	0.11	12	0.18	15	0.23	18	0.28	65
		NEU	47	0.72	45	0.69	43	0.66	44	0.68	43	0.66	
		SUP	13	0.2	13	0.2	10	0.15	6	0.09	4	0.06	
	H	ENH	2	0.07	4	0.14	5	0.17	7	0.24	6	0.21	29
		NEU	21	0.72	20	0.69	20	0.69	21	0.72	22	0.76	
		SUP	6	0.21	5	0.17	4	0.14	1	0.03	1	0.03	
	IH	ENH	1	0.08	1	0.08	1	0.08	2	0.15	2	0.15	13
		NEU	10	0.77	9	0.69	9	0.69	9	0.69	9	0.69	
		SUP	2	0.15	3	0.23	3	0.23	2	0.15	2	0.15	
EEPAC	TC	ENH	12	0.19	13	0.21	14	0.23	11	0.18	7	0.11	62
		NEU	43	0.69	44	0.71	44	0.71	46	0.74	45	0.73	
		SUP	7	0.11	5	0.08	4	0.06	5	0.08	10	0.16	
	H	ENH	3	0.25	3	0.25	3	0.25	1	0.08	0	0	12

		NEU	7	0.58	7	0.58	8	0.67	11	0.92	10	0.83	
		SUP	2	0.17	2	0.17	1	0.08	0	0	2	0.17	
		ENH	1	1	1	1	0	0	0	0	0	0	
	IH	NEU	0	0	0	0	1	1	1	1	0	0	1
		SUP	0	0	0	0	0	0	0	0	1	1	
CEPAC	TC	ENH	50	0.16	40	0.13	36	0.12	36	0.12	38	0.12	
		NEU	222	0.73	236	0.77	241	0.79	238	0.78	223	0.73	306
		SUP	34	0.11	30	0.1	29	0.09	32	0.1	45	0.15	
	H	ENH	30	0.17	30	0.17	29	0.16	25	0.14	22	0.12	
		NEU	132	0.74	133	0.75	137	0.77	138	0.78	132	0.74	178
		SUP	16	0.09	15	0.08	12	0.07	15	0.08	24	0.13	
	IH	ENH	9	0.12	8	0.1	9	0.12	8	0.1	13	0.17	
		NEU	58	0.74	62	0.79	64	0.82	65	0.83	57	0.73	78
		SUP	11	0.14	8	0.1	5	0.06	5	0.06	8	0.1	
WEPAC	TC	ENH	19	0.23	10	0.12	9	0.11	5	0.06	6	0.07	
		NEU	60	0.71	63	0.75	61	0.73	65	0.77	59	0.7	84
		SUP	5	0.06	11	0.13	14	0.17	14	0.17	19	0.23	
	H	ENH	8	0.12	7	0.11	7	0.11	6	0.09	8	0.12	
		NEU	50	0.77	49	0.75	52	0.8	52	0.8	50	0.77	65
		SUP	7	0.11	9	0.14	6	0.09	7	0.11	7	0.11	
	IH	ENH	8	0.2	8	0.2	10	0.24	8	0.2	3	0.07	
		NEU	29	0.71	29	0.71	28	0.68	30	0.73	32	0.78	41
		SUP	4	0.1	4	0.1	3	0.07	3	0.07	6	0.15	
CPAC	TC	ENH	9	0.31	9	0.31	10	0.34	6	0.21	5	0.17	
		NEU	17	0.59	17	0.59	16	0.55	20	0.69	17	0.59	29
		SUP	3	0.1	3	0.1	3	0.1	3	0.1	7	0.24	
	H	ENH	2	0.13	3	0.2	7	0.47	6	0.4	1	0.07	
		NEU	12	0.8	12	0.8	8	0.53	8	0.53	13	0.87	15
		SUP	1	0.07	0	0	0	0	1	0.07	1	0.07	
	IH	ENH	1	0.08	0	0	4	0.31	3	0.23	2	0.15	
		NEU	10	0.77	12	0.92	9	0.69	9	0.69	10	0.77	13
		SUP	2	0.15	1	0.08	0	0	1	0.08	1	0.08	
AMDR	TC	ENH	11	0.07	15	0.09	17	0.11	37	0.23	41	0.26	
		NEU	106	0.67	115	0.72	121	0.76	108	0.68	103	0.65	159
		SUP	42	0.26	29	0.18	21	0.13	14	0.09	15	0.09	
	H	ENH	2	0.03	6	0.08	13	0.17	21	0.28	23	0.3	
		NEU	53	0.7	56	0.74	52	0.68	51	0.67	49	0.64	76
		SUP	21	0.28	14	0.18	11	0.14	4	0.05	4	0.05	
	IH	ENH	0	0	2	0.06	2	0.06	8	0.24	9	0.27	
		NEU	23	0.7	23	0.7	26	0.79	23	0.7	24	0.73	33
		SUP	10	0.3	8	0.24	5	0.15	2	0.06	0	0	

Table 4.7. Observed fraction of landfall-genesis events $\hat{p}$ for each of the 9 basins and sub-basins. Indices 1-5 are shown.

Landfall-genesis			Index 1 80°E		Index 2 100°E		Index 3 120°E		Index 4 140°E		Index 5 160°E		. . .
Basin	Storm Type	MJO Phase	Number per phase	$\hat{p}$	Number per phase	$\hat{p}$	Number per phase	$\hat{p}$	Number per phase	$\hat{p}$	Number per phase	$\hat{p}$	Total Number
EPAC	TC	ENH	4	0.06	6	0.09	5	0.08	2	0.03	4	0.06	64
		NEU	46	0.72	40	0.62	44	0.69	51	0.8	54	0.84	
		SUP	14	0.22	18	0.28	15	0.23	11	0.17	6	0.09	
	H	ENH	2	0.04	4	0.08	4	0.08	0	0	3	0.06	48
		NEU	37	0.77	34	0.71	33	0.69	40	0.83	44	0.92	
		SUP	9	0.19	10	0.21	11	0.23	8	0.17	1	0.02	
	IH	ENH	2	0.1	2	0.1	2	0.1	0	0	1	0.05	21
		NEU	15	0.71	16	0.76	15	0.71	18	0.86	19	0.9	
		SUP	4	0.19	3	0.14	4	0.19	3	0.14	1	0.05	
NATL	TC	ENH	26	0.25	22	0.22	12	0.12	11	0.11	8	0.08	102
		NEU	69	0.68	69	0.68	77	0.75	70	0.69	67	0.66	
		SUP	7	0.07	11	0.11	13	0.13	21	0.21	27	0.26	
	H	ENH	12	0.21	12	0.21	7	0.12	5	0.09	5	0.09	57
		NEU	42	0.74	39	0.68	43	0.75	41	0.72	37	0.65	
		SUP	3	0.05	6	0.11	7	0.12	11	0.19	15	0.26	
	IH	ENH	6	0.2	6	0.2	5	0.17	3	0.1	2	0.07	30
		NEU	23	0.77	22	0.73	22	0.73	23	0.77	20	0.67	
		SUP	1	0.03	2	0.07	3	0.1	4	0.13	8	0.27	
CARIB	TC	ENH	7	0.39	3	0.17	1	0.06	2	0.11	2	0.11	18
		NEU	11	0.61	12	0.67	14	0.78	14	0.78	10	0.56	
		SUP	0	0	3	0.17	3	0.17	2	0.11	6	0.33	
	H	ENH	2	0.18	2	0.18	2	0.18	2	0.18	2	0.18	11
		NEU	9	0.82	8	0.73	9	0.82	9	0.82	7	0.64	
		SUP	0	0	1	0.09	0	0	0	0	2	0.18	
	IH	ENH	2	0.33	2	0.33	1	0.17	0	0	0	0	6
		NEU	4	0.67	3	0.5	5	0.83	5	0.83	4	0.67	
		SUP	0	0	1	0.17	0	0	1	0.17	2	0.33	
GOM	TC	ENH	11	0.23	12	0.26	8	0.17	5	0.11	4	0.09	47
		NEU	31	0.66	30	0.64	33	0.7	31	0.66	30	0.64	
		SUP	5	0.11	5	0.11	6	0.13	11	0.23	13	0.28	
	H	ENH	4	0.24	4	0.24	3	0.18	1	0.06	1	0.06	17
		NEU	11	0.65	10	0.59	11	0.65	12	0.71	11	0.65	
		SUP	2	0.12	3	0.18	3	0.18	4	0.24	5	0.29	
	IH	ENH	1	0.09	2	0.18	2	0.18	2	0.18	2	0.18	11
		NEU	9	0.82	8	0.73	8	0.73	7	0.64	7	0.64	
		SUP	1	0.09	1	0.09	1	0.09	2	0.18	2	0.18	
EEPAC	TC	ENH	1	0.05	1	0.05	1	0.05	0	0	1	0.05	

		NEU	15	0.71	13	0.62	12	0.57	16	0.76	19	0.9	21
		SUP	5	0.24	7	0.33	8	0.38	5	0.24	1	0.05	
		ENH	0	0	1	0.25	1	0.25	0	0	0	0	
	H	NEU	3	0.75	2	0.5	1	0.25	4	1	4	1	4
		SUP	1	0.25	1	0.25	2	0.5	0	0	0	0	
		ENH	0	0	0	0	0	0	0	0	0	0	
	IH	NEU	0	0	0	0	0	0	1	1	1	1	1
		SUP	1	1	1	1	1	1	0	0	0	0	
		ENH	3	0.08	5	0.12	4	0.1	2	0.05	2	0.05	
	TC	NEU	30	0.75	25	0.62	30	0.75	33	0.82	34	0.85	40
		SUP	7	0.17	10	0.25	6	0.15	5	0.12	4	0.1	
		ENH	2	0.05	3	0.07	3	0.07	0	0	2	0.05	
CEPAC	H	NEU	33	0.79	30	0.71	30	0.71	34	0.81	39	0.93	42
		SUP	7	0.17	9	0.21	9	0.21	8	0.19	1	0.02	
		ENH	2	0.11	2	0.11	2	0.11	0	0	0	0	
	IH	NEU	14	0.78	14	0.78	13	0.72	15	0.83	17	0.94	18
		SUP	2	0.11	2	0.11	3	0.17	3	0.17	1	0.06	
		ENH	0	n/a	0	n/a	0	n/a	0	n/a	0	n/a	
	TC	NEU	0	n/a	0	n/a	0	n/a	0	n/a	0	n/a	0
		SUP	0	n/a	0	n/a	0	n/a	0	n/a	0	n/a	
		ENH	0	0	0	0	0	0	0	0	0	0	
WEPAC	H	NEU	1	1	1	1	1	1	1	1	1	1	1
		SUP	0	0	0	0	0	0	0	0	0	0	
		ENH	0	0	0	0	0	0	0	0	0	0	
	IH	NEU	1	1	1	1	1	1	1	1	1	1	1
		SUP	0	0	0	0	0	0	0	0	0	0	
		ENH	0	0	0	0	0	0	0	0	1	0.33	
	TC	NEU	1	0.33	2	0.67	2	0.67	2	0.67	1	0.33	3
		SUP	2	0.67	1	0.33	1	0.33	1	0.33	1	0.33	
		ENH	0	0	0	0	0	0	0	0	1	1	
CPAC	H	NEU	0	0	1	1	1	1	1	1	0	0	1
		SUP	1	1	0	0	0	0	0	0	0	0	
		ENH	0	0	0	0	0	0	0	0	1	1	
	IH	NEU	0	0	1	1	1	1	1	1	0	0	1
		SUP	1	1	0	0	0	0	0	0	0	0	
		ENH	11	0.33	8	0.24	1	0.03	2	0.06	2	0.06	
	TC	NEU	21	0.64	20	0.61	26	0.79	25	0.76	19	0.58	33
		SUP	1	0.03	5	0.15	6	0.18	6	0.18	12	0.36	
		ENH	4	0.2	3	0.15	1	0.05	1	0.05	1	0.05	
AMDR	H	NEU	16	0.8	14	0.7	17	0.85	16	0.8	14	0.7	20
		SUP	0	0	3	0.15	2	0.1	3	0.15	5	0.25	
		ENH	3	0.27	3	0.27	2	0.18	0	0	0	0	
	IH	NEU	8	0.73	7	0.64	8	0.73	9	0.82	7	0.64	11
		SUP	0	0	1	0.09	1	0.09	2	0.18	4	0.36	

Table 4.8. As in Table 4.7, but Indices 6-10 are shown.

Landfall-genesis			Index 6 120°W		Index 7 40°W		Index 8 10°W		Index 9 20°E		Index 10 70°E		
Basin	Storm Type	MJO Phase	Number per phase	$\hat{p}$	Number per phase	$\hat{p}$	Number per phase	$\hat{p}$	Number per phase	$\hat{p}$	Number per phase	$\hat{p}$	Total Number
EPAC	TC	ENH	15	0.23	17	0.27	13	0.2	8	0.12	6	0.09	64
		NEU	44	0.69	41	0.64	47	0.73	54	0.84	47	0.73	
		SUP	5	0.08	6	0.09	4	0.06	2	0.03	11	0.17	
	H	ENH	9	0.19	11	0.23	9	0.19	5	0.1	3	0.06	48
		NEU	36	0.75	33	0.69	38	0.79	41	0.85	38	0.79	
		SUP	3	0.06	4	0.08	1	0.02	2	0.04	7	0.15	
	IH	ENH	4	0.19	4	0.19	3	0.14	1	0.05	3	0.14	21
		NEU	15	0.71	15	0.71	18	0.86	19	0.9	15	0.71	
		SUP	2	0.1	2	0.1	0	0	1	0.05	3	0.14	
NATL	TC	ENH	6	0.06	10	0.1	17	0.17	22	0.22	26	0.25	102
		NEU	74	0.73	74	0.73	73	0.72	70	0.69	69	0.68	
		SUP	22	0.22	18	0.18	12	0.12	10	0.1	7	0.07	
	H	ENH	3	0.05	6	0.11	7	0.12	11	0.19	14	0.25	57
		NEU	42	0.74	40	0.7	42	0.74	41	0.72	40	0.7	
		SUP	12	0.21	11	0.19	8	0.14	5	0.09	3	0.05	
	IH	ENH	1	0.03	2	0.07	2	0.07	5	0.17	7	0.23	30
		NEU	22	0.73	22	0.73	23	0.77	23	0.77	21	0.7	
		SUP	7	0.23	6	0.2	5	0.17	2	0.07	2	0.07	
CARIB	TC	ENH	0	0	2	0.11	3	0.17	1	0.06	5	0.28	18
		NEU	14	0.78	12	0.67	13	0.72	15	0.83	12	0.67	
		SUP	4	0.22	4	0.22	2	0.11	2	0.11	1	0.06	
	H	ENH	0	0	0	0	0	0	1	0.09	3	0.27	11
		NEU	8	0.73	8	0.73	8	0.73	8	0.73	7	0.64	
		SUP	3	0.27	3	0.27	3	0.27	2	0.18	1	0.09	
	IH	ENH	0	0	0	0	0	0	1	0.17	2	0.33	6
		NEU	4	0.67	4	0.67	5	0.83	5	0.83	4	0.67	
		SUP	2	0.33	2	0.33	1	0.17	0	0	0	0	
GOM	TC	ENH	4	0.09	5	0.11	9	0.19	11	0.23	13	0.28	47
		NEU	34	0.72	32	0.68	31	0.66	30	0.64	30	0.64	
		SUP	9	0.19	10	0.21	7	0.15	6	0.13	4	0.09	
	H	ENH	2	0.12	3	0.18	3	0.18	3	0.18	4	0.24	17
		NEU	11	0.65	10	0.59	11	0.65	13	0.76	12	0.71	
		SUP	4	0.24	4	0.24	3	0.18	1	0.06	1	0.06	
	IH	ENH	1	0.09	0	0	1	0.09	2	0.18	2	0.18	11
		NEU	8	0.73	9	0.82	7	0.64	7	0.64	7	0.64	
		SUP	2	0.18	2	0.18	3	0.27	2	0.18	2	0.18	
EEPAC	TC	ENH	5	0.24	8	0.38	7	0.33	3	0.14	2	0.1	21
		NEU	14	0.67	12	0.57	13	0.62	18	0.86	15	0.71	
		SUP	2	0.1	1	0.05	1	0.05	0	0	4	0.19	

		ENH	1	0.25	1	0.25	1	0.25	0	0	0	0	
	H	NEU	2	0.5	2	0.5	2	0.5	4	1	3	0.75	4
		SUP	1	0.25	1	0.25	1	0.25	0	0	1	0.25	
		ENH	1	1	1	1	0	0	0	0	0	0	
	IH	NEU	0	0	0	0	1	1	1	1	0	0	1
		SUP	0	0	0	0	0	0	0	0	1	1	
		ENH	8	0.2	8	0.2	4	0.1	4	0.1	3	0.08	
	TC	NEU	29	0.73	27	0.68	33	0.82	35	0.88	32	0.8	40
		SUP	3	0.08	5	0.12	3	0.08	1	0.03	5	0.12	
		ENH	7	0.17	10	0.24	8	0.19	5	0.12	3	0.07	
CEPAC	H	NEU	33	0.79	29	0.69	34	0.81	36	0.86	34	0.81	42
		SUP	2	0.05	3	0.07	0	0	1	0.02	5	0.12	
		ENH	2	0.11	3	0.17	3	0.17	1	0.06	3	0.17	
	IH	NEU	14	0.78	13	0.72	15	0.83	17	0.94	14	0.78	18
		SUP	2	0.11	2	0.11	0	0	0	0	1	0.06	
		ENH	0	n/a	0	n/a	0	n/a	0	n/a	0	n/a	
	TC	NEU	0	n/a	0	n/a	0	n/a	0	n/a	0	n/a	0
		SUP	0	n/a	0	n/a	0	n/a	0	n/a	0	n/a	
		ENH	0	0	0	0	0	0	0	0	0	0	
WEPAC	H	NEU	1	1	1	1	1	1	1	1	1	1	1
		SUP	0	0	0	0	0	0	0	0	0	0	
		ENH	0	0	0	0	0	0	0	0	0	0	
	IH	NEU	1	1	1	1	1	1	1	1	1	1	1
		SUP	0	0	0	0	0	0	0	0	0	0	
		ENH	2	0.67	1	0.33	2	0.67	1	0.33	1	0.33	
	TC	NEU	1	0.33	2	0.67	1	0.33	1	0.33	0	0	3
		SUP	0	0	0	0	0	0	1	0.33	2	0.67	
		ENH	1	1	0	0	0	0	0	0	0	0	
CPAC	H	NEU	0	0	1	1	1	1	0	0	0	0	1
		SUP	0	0	0	0	0	0	1	1	1	1	
		ENH	1	1	0	0	0	0	0	0	0	0	
	IH	NEU	0	0	1	1	1	1	0	0	0	0	1
		SUP	0	0	0	0	0	0	1	1	1	1	
		ENH	1	0.03	4	0.12	6	0.18	8	0.24	9	0.27	
	TC	NEU	23	0.7	23	0.7	25	0.76	23	0.7	22	0.67	33
		SUP	9	0.27	6	0.18	2	0.06	2	0.06	2	0.06	
		ENH	0	0	2	0.1	2	0.1	4	0.2	5	0.25	
AMDR	H	NEU	16	0.8	16	0.8	16	0.8	15	0.75	14	0.7	20
		SUP	4	0.2	2	0.1	2	0.1	1	0.05	1	0.05	
		ENH	0	0	1	0.09	1	0.09	2	0.18	3	0.27	
	IH	NEU	8	0.73	7	0.64	9	0.82	9	0.82	8	0.73	11
		SUP	3	0.27	3	0.27	1	0.09	0	0	0	0	

Table 4.9. Observed fraction of landfall-actual events $\hat{p}$ for each of the 9 basins and sub-basins. Indices 1-10 are shown.

Landfall-actual			Index 1 80°E		Index 2 100°E		Index 3 120°E		Index 4 140°E		Index 5 160°E		. . .
Basin	Storm Type	MJO Phase	Number per phase	$\hat{p}$	Number per phase	$\hat{p}$	Number per phase	$\hat{p}$	Number per phase	$\hat{p}$	Number per phase	$\hat{p}$	Total Number
NATL	TC	ENH	26	0.21	23	0.19	15	0.12	15	0.12	11	0.09	124
		NEU	92	0.74	95	0.77	95	0.77	75	0.6	77	0.62	
		SUP	6	0.05	6	0.05	14	0.11	34	0.27	36	0.29	
	H	ENH	24	0.29	21	0.25	18	0.22	7	0.08	10	0.12	83
		NEU	50	0.6	54	0.65	58	0.7	60	0.72	45	0.54	
		SUP	9	0.11	8	0.1	7	0.08	16	0.19	28	0.34	
	IH	ENH	13	0.21	14	0.23	13	0.21	7	0.11	4	0.07	61
		NEU	48	0.79	43	0.7	40	0.66	47	0.77	40	0.66	
		SUP	0	0	4	0.07	8	0.13	7	0.11	17	0.28	

Landfall-actual			Index 6 120°W		Index 7 40°W		Index 8 10°W		Index 9 20°E		Index 10 70°E		. . .
Basin	Storm Type	MJO Phase	Number per phase	$\hat{p}$	Number per phase	$\hat{p}$	Number per phase	$\hat{p}$	Number per phase	$\hat{p}$	Number per phase	$\hat{p}$	Total Number
NATL	TC	ENH	4	0.03	8	0.06	16	0.13	37	0.3	29	0.23	124
		NEU	96	0.77	100	0.81	95	0.77	76	0.61	86	0.69	
		SUP	24	0.19	16	0.13	13	0.1	11	0.09	9	0.07	
	H	ENH	8	0.1	9	0.11	10	0.12	18	0.22	25	0.3	83
		NEU	49	0.59	55	0.66	57	0.69	54	0.65	50	0.6	
		SUP	26	0.31	19	0.23	16	0.19	11	0.13	8	0.1	
	IH	ENH	1	0.02	5	0.08	9	0.15	7	0.11	13	0.21	61
		NEU	45	0.74	42	0.69	41	0.67	50	0.82	45	0.74	
		SUP	15	0.25	14	0.23	11	0.18	4	0.07	3	0.05	

Table 4.10. Relevant Z-statistics for all TC, hurricane, and intense hurricane genesis events from 1978-2006. Positive (negative) Z-statistic indicates favorable (unfavorable) modulation of TC genesis.

Basin	Storm Type	MJO Phase	Index 1 80°E	Index 2 100°E	Index 3 120°E	Index 4 140°E	Index 5 160°E	Index 6 120°W	Index 7 40°W	Index 8 10°W	Index 9 20°E	Index 10 70°E
EPAC	TC	ENH	-3.52	-3.28	-3.67	-3.44	0.54	4.76	2.8	1.24	-1.76	-2.33
		NEU	-0.43	-0.17	0.72	2.47	1.24	-1.07	0.65	1.66	2.63	-0.3
		SUP	4.43	4	3.21	0.39	-2.09	-2.96	-3.21	-3.18	-1.63	2.97
	H	ENH	-3.02	-2.3	-3.57	-4.16	-1.51	2.14	2.6	2.27	-0.39	-1.82
		NEU	1.22	-0.31	0.37	2.38	2.36	0.44	0.33	1.49	2.22	1.39
		SUP	1.63	3.08	3.59	1.26	-1.54	-2.48	-2.66	-3.9	-2.51	0.1
	IH	ENH	-0.99	-1.44	-2.7	-2.77	-1.77	0.92	0.67	1.68	-0.2	-0.62
		NEU	0.08	-0.33	0.93	1.49	2.06	-0.09	1.02	1.24	1.95	0.59
		SUP	0.97	2.12	1.81	0.97	-0.91	-0.72	-1.82	-3.06	-2.35	-0.12
NATL	TC	ENH	3.55	2.65	0.69	-0.95	-2.09	-2.61	-0.83	-0.26	2.42	3.48
		NEU	-1.61	-1.78	-0.13	-0.12	-1.71	-0.26	-0.25	0.18	-0.82	-1.42
		SUP	-1.68	-0.56	-0.61	1.16	4.19	2.67	1.03	0.01	-1.42	-1.89
	H	ENH	2.96	1.82	1.5	-0.81	-1.45	-3.32	-1.2	0.04	1.81	3.61
		NEU	-0.48	-0.34	-0.89	0.21	-1.99	0.32	-0.27	-0.58	-0.4	-0.99
		SUP	-2.59	-1.61	-0.49	0.58	3.93	2.59	1.36	0.68	-1.34	-2.62
	IH	ENH	2.93	2.06	0.71	-0.94	-0.64	-2.39	-1.5	-1.81	1.02	3.14
		NEU	-0.79	-0.81	-0.47	1.13	-1.9	-0.92	0.08	1.18	-0.01	-1.22
		SUP	-2.13	-1.23	-0.15	-0.49	3.02	3.29	1.2	0.18	-1.04	-1.79
CARIB	TC	ENH	2.6	-0.21	-0.63	0.05	-0.91	-2.26	1.34	0.11	1.51	0.99
		NEU	-0.67	-1	-0.32	-0.7	-1.42	0.75	-0.84	0.06	-0.45	0.32
		SUP	-1.92	1.63	1.18	0.87	2.68	1.1	-0.13	-0.17	-0.97	-1.52
	H	ENH	2.17	1.52	1.46	-0.04	-1.15	-2.03	-0.23	0.07	2.21	2.09
		NEU	-0.2	-1.43	-1.77	-0.18	-0.88	-0.69	-1.14	-0.91	-0.83	-0.55
		SUP	-2.08	0.26	0.8	0.28	2.23	2.69	1.59	1.06	-1.18	-1.55
	IH	ENH	1.36	1.25	0.58	-1.31	-1.05	-1.59	-0.8	-0.95	1.39	1.31
		NEU	0.11	-1.45	-1.41	0.42	-0.31	-0.48	-0.51	0.69	-0.28	0.15
		SUP	-1.63	0.59	1.3	0.83	1.41	2.02	1.31	0.01	-1.08	-1.64
GOM	TC	ENH	2.14	1.93	0.17	-1.23	-1.73	-1.01	-0.05	1.46	1.85	2.72
		NEU	-1.17	-1.46	-0.28	-0.27	-0.71	-0.17	-0.79	-1.02	-0.64	-1.08
		SUP	-0.75	-0.17	0.19	1.65	2.57	1.13	1.01	-0.06	-1.07	-1.52
	H	ENH	0.84	0.71	-0.34	-1.38	-1.58	-0.81	0.49	0.78	1.39	0.78
		NEU	-0.02	-0.87	0.01	0.37	-0.74	-0.1	-0.56	-0.35	0.13	0.45
		SUP	-0.88	0.4	0.38	0.97	2.46	0.86	0.26	-0.28	-1.62	-1.46
	IH	ENH	-0.75	0.71	0.68	-0.1	0.2	-0.45	-0.38	-0.52	0.05	-0.01
		NEU	0.97	-0.9	-0.87	0	-0.2	0.3	-0.35	-0.21	-0.16	-0.23
		SUP	-0.5	0.45	0.43	0.11	0.06	0.04	0.76	0.74	0.17	0.33
EEPAC	TC	ENH	-1.55	-1.68	-1.73	-2.8	-0.51	1.87	2.52	2.41	0.62	-0.91
		NEU	0	-0.02	-0.81	0.85	1	-0.7	-0.46	-0.16	0.5	0.08

		SUP	1.69	1.96	3.12	1.85	-0.78	-0.82	-1.61	-2	-1.31	0.9
		ENH	-1.46	0.08	0.05	-1.54	-1.37	1.43	1.55	1.31	-0.64	-1.48
	H	NEU	0.83	-1.12	-1.73	1.06	2.18	-1.17	-1.19	-0.4	1.56	0.86
		SUP	0.46	1.48	2.36	0.23	-1.45	0.16	0.11	-0.7	-1.39	0.45
		ENH	-0.42	-0.43	-0.44	-0.44	-0.4	2.74	2.85	-0.38	-0.42	-0.43
	IH	NEU	-1.63	-1.63	-1.62	0.67	0.63	-1.66	-1.67	0.63	0.63	-1.61
		SUP	2.67	2.78	2.77	-0.41	-0.42	-0.42	-0.43	-0.43	-0.4	2.66
		ENH	-2.27	-2.27	-3.32	-3.12	-0.39	2.51	1.17	-0.38	-1.55	-1.48
	TC	NEU	0.23	0.2	1.88	3.12	1.1	-0.28	1.42	2.68	2.51	0.29
		SUP	2.16	2.33	1.2	-0.8	-1.02	-1.91	-2.74	-2.98	-1.69	1.23
		ENH	-2.28	-2.3	-3	-3.48	-0.67	2.13	2.51	1.54	-0.33	-1.15
CEPAC	H	NEU	0.63	-0.24	0.38	2.07	1.9	0.27	0.35	1.52	1.84	0.6
		SUP	1.63	2.97	2.92	0.95	-1.77	-2.25	-2.6	-3.28	-2.08	0.45
		ENH	-0.25	-0.73	-1.72	-2.08	-1.83	-0.05	-0.2	-0.25	-1.16	0.29
	IH	NEU	0.35	-0.18	1.16	2.21	2.29	0.22	1.19	2	2.35	0.18
		SUP	-0.2	1.09	0.35	-0.71	-1.13	-0.22	-1.28	-2.25	-1.89	-0.57
		ENH	-2.34	-1.29	-0.46	0.36	2.12	3.1	0.27	-0.49	-2.31	-2.11
	TC	NEU	-0.24	0.23	0.06	0.2	0.44	-0.38	0.3	0.16	1.23	-0.39
		SUP	2.88	1.16	0.45	-0.64	-2.59	-2.32	-0.6	0.25	0.76	2.85
		ENH	-1.32	-0.1	-1.51	-1.23	-1.01	0.15	-0.05	-0.42	-1.29	-0.71
WEPAC	H	NEU	1.06	0.21	1.38	1.88	1.22	0.67	0.34	1.46	1.55	0.86
		SUP	0	-0.17	-0.19	-1.18	-0.57	-0.96	-0.36	-1.43	-0.71	-0.39
		ENH	-1.39	-1.07	-1.53	-1.15	-0.25	1.55	1.75	2.31	0.83	-1.44
	IH	NEU	0.08	-0.28	-0.58	-0.47	0.56	-0.37	-0.41	-0.51	0.27	0.84
		SUP	1.41	1.62	2.58	1.83	-0.47	-0.94	-1.01	-1.47	-1.2	0.44
		ENH	-0.72	-1.32	-0.85	-0.38	0.59	3.23	3.46	3.59	0.87	0.26
	TC	NEU	-2.11	-1.7	-2.06	-1.64	-0.74	-1.78	-1.82	-2	-0.28	-1.62
		SUP	3.64	3.9	3.87	2.56	0.37	-0.7	-0.76	-0.79	-0.54	1.92
		ENH	-0.91	-1.68	-1.7	-1.72	-0.78	0.19	1.12	4.01	2.73	-0.94
CPAC	H	NEU	0.06	0.05	-1.07	-1.89	-1	0.59	0.57	-1.6	-1.54	1.26
		SUP	0.91	1.85	3.45	4.31	2.02	-0.9	-1.66	-1.67	-0.8	-0.67
		ENH	0.03	-0.81	-1.58	-1.6	-0.61	-0.45	-1.27	2	0.83	-0.01
	IH	NEU	-0.27	0.34	1.61	0	-0.2	0.3	1.53	-0.21	-0.16	0.38
		SUP	0.34	0.45	-0.43	1.69	0.84	0.04	-0.78	-1.55	-0.64	-0.51
		ENH	4.43	2.78	-0.36	-1.52	-1.97	-1.88	-0.62	-0.68	2.96	3.59
	TC	NEU	-2.75	-2.06	0.71	0.85	-2.46	-1.88	-0.35	1.19	-0.94	-2.07
		SUP	-1.1	-0.3	-0.58	0.49	5.01	4.03	0.96	-0.85	-1.82	-1.13
		ENH	3.37	1.55	0.54	-1.39	-2.44	-2.46	-0.86	1.22	3.11	3.56
AMDR	H	NEU	-1.08	-0.84	-0.76	0.1	-1.9	-0.69	0.03	-0.67	-0.81	-1.49
		SUP	-2.21	-0.61	0.44	1.34	4.76	3.08	0.71	-0.29	-2.16	-1.88
		ENH	1.95	1.8	0.79	-1.61	-1.25	-2.09	-0.9	-1.12	1.5	1.87
	IH	NEU	0.02	-0.78	-0.73	1.19	-1.02	-0.46	-0.5	0.89	-0.2	0.08
		SUP	-2.15	-0.97	0.1	0.13	2.5	2.46	1.39	-0.08	-1.29	-2.16

Table 4.11: Relevant *Z*-statistics for all TC, hurricane, and intense hurricane *landfall-genesis* events from 1978-2006. Positive (negative) *Z*-statistic indicates favorable (unfavorable) modulation of TC genesis of TCs, hurricanes, and intense hurricanes that go on to make landfall.

Basin	Storm Type	MJO Phase	Index 1 80°E	Index 2 100°E	Index 3 120°E	Index 4 140°E	Index 5 160°E	Index 6 120°W	Index 7 40°W	Index 8 10°W	Index 9 20°E	Index 10 70°E
EPAC	TC	ENH	-1.98	-1.42	-1.81	-2.87	-1.7	2.91	3.99	1.9	-0.54	-1.35
		NEU	-0.13	-1.83	-0.64	1.81	2.26	-0.82	-1.72	0.28	2.31	0.23
		SUP	2.34	4.19	2.98	0.65	-1.23	-1.61	-1.35	-2.07	-2.47	1.17
	H	ENH	-2.12	-1.43	-1.47	-3.07	-1.47	1.51	2.65	1.32	-0.87	-1.77
		NEU	0.7	-0.29	-0.55	2.12	3.07	0.27	-0.75	1.13	2.16	1.09
		SUP	1.36	2.04	2.47	0.46	-2.48	-1.7	-1.37	-2.59	-1.93	0.46
	IH	ENH	-0.71	-0.79	-0.82	-2.03	-1.17	1.04	1.18	0.25	-1.31	-0.15
		NEU	-0.12	0.36	-0.09	1.64	1.91	-0.19	-0.22	1.41	1.94	-0.07
		SUP	0.94	0.41	1.08	-0.01	-1.3	-0.7	-0.75	-1.98	-1.2	0.26
NATL	TC	ENH	2.93	1.58	-1.2	-1.54	-1.67	-1.83	-0.38	1.28	1.89	2.8
		NEU	-1.12	-1.15	0.71	-0.13	-1.34	-0.16	-0.23	-0.06	-0.6	-1.01
		SUP	-1.67	-0.21	0.38	1.8	3.31	1.85	0.61	-1.08	-1.17	-1.69
	H	ENH	1.25	1.07	-0.79	-1.56	-1.05	-1.52	-0.11	-0.04	0.93	1.9
		NEU	0.18	-0.73	0.53	0.44	-1.13	0.07	-0.58	0.31	0.11	-0.33
		SUP	-1.62	-0.22	0.18	1.06	2.44	1.28	0.8	-0.34	-1.1	-1.63
	IH	ENH	0.75	0.62	0.08	-0.95	-1.1	-1.43	-0.76	-0.96	0.27	1.19
		NEU	0.5	0.08	0.12	0.88	-0.61	0.01	-0.03	0.59	0.65	-0.26
		SUP	-1.49	-0.82	-0.26	-0.16	1.83	1.28	0.68	0.15	-1.13	-0.95
CARIB	TC	ENH	2.82	0.09	-1.22	-0.61	-0.3	-1.55	0.02	0.54	-1.11	1.44
		NEU	-1.09	-0.57	0.52	0.79	-1.52	0.43	-0.66	0.03	1.13	-0.52
		SUP	-1.59	0.7	0.68	-0.39	2.21	0.86	0.79	-0.53	-0.33	-0.88
	H	ENH	0.29	0.21	0.18	0.16	0.45	-1.21	-1.16	-1.25	-0.54	1.08
		NEU	0.68	0	0.7	0.9	-0.59	-0.04	-0.06	0.06	0.11	-0.63
		SUP	-1.24	-0.25	-1.2	-1.36	0.31	1.14	1.08	1.06	0.42	-0.33
	IH	ENH	1.25	1.17	0.04	-1.09	-0.97	-0.89	-0.86	-0.92	0.12	1.21
		NEU	-0.33	-1.25	0.6	0.75	-0.27	-0.37	-0.38	0.63	0.65	-0.3
		SUP	-0.92	0.4	-0.88	0.16	1.28	1.26	1.21	0.07	-0.98	-0.92
GOM	TC	ENH	1.59	1.82	0.17	-1.07	-1	-0.69	-0.07	1.38	1.63	2.31
		NEU	-1.02	-1.37	-0.32	-0.49	-1.19	-0.14	-0.85	-0.9	-1.13	-1.27
		SUP	-0.34	-0.17	0.26	1.77	2.48	0.79	1.1	-0.15	-0.2	-0.81
	H	ENH	0.97	0.87	0.17	-1.17	-0.92	0	0.88	0.65	0.32	0.92
		NEU	-0.73	-1.28	-0.7	0.12	-0.64	-0.8	-1.38	-0.66	0.47	-0.14
		SUP	-0.07	0.8	0.79	1.08	1.69	0.98	0.92	0.22	-0.95	-0.81
	IH	ENH	-0.56	0.21	0.18	0.16	0.45	-0.27	-1.16	-0.34	0.3	0.25
		NEU	0.68	0	0.03	-0.4	-0.59	-0.04	0.62	-0.61	-0.56	-0.63
		SUP	-0.32	-0.25	-0.25	0.36	0.31	0.29	0.25	1.06	0.42	0.58
EEPAC	TC	ENH	-1.32	-1.39	-1.42	-2.03	-1.17	1.72	3.98	2.89	-0.08	-0.75
		NEU	-0.12	-1.11	-1.56	0.69	1.91	-0.68	-1.7	-1.01	1.46	-0.07

		SUP	1.61	3.15	3.81	1.24	-1.3	-0.7	-1.36	-1.37	-1.83	0.93
		ENH	-0.84	0.5	0.48	-0.89	-0.79	0.83	0.9	0.76	-0.84	-0.86
	H	NEU	0.11	-1.02	-2.12	1.33	1.26	-1.05	-1.07	-0.97	1.27	0.13
		SUP	0.77	0.85	2.41	-0.82	-0.83	0.56	0.53	0.51	-0.8	0.77
		ENH	-0.42	-0.43	-0.44	-0.44	-0.4	2.74	2.85	-0.38	-0.42	-0.43
	IH	NEU	-1.63	-1.63	-1.62	0.67	0.63	-1.66	-1.67	0.63	0.63	-1.61
		SUP	2.67	2.78	2.77	-0.41	-0.42	-0.42	-0.43	-0.43	-0.4	2.66
		ENH	-1.34	-0.58	-1.05	-1.95	-1.57	1.63	1.83	-0.47	-0.87	-1.4
	TC	NEU	0.34	-1.45	0.38	1.82	1.87	-0.11	-0.87	1.5	2.27	1.11
		SUP	1	2.69	0.69	-0.33	-0.86	-1.33	-0.52	-1.42	-2.07	0.02
		ENH	-1.87	-1.55	-1.58	-2.87	-1.66	1	2.66	1.29	-0.55	-1.49
CEPAC	H	NEU	0.87	-0.19	-0.13	1.65	3.05	0.78	-0.66	1.31	2.07	1.27
		SUP	0.86	2.03	2.01	0.87	-2.27	-1.86	-1.49	-2.79	-2.14	-0.09
		ENH	-0.47	-0.55	-0.58	-1.88	-1.68	-0.08	0.77	0.54	-1.11	0.14
	IH	NEU	0.49	0.48	-0.01	1.3	2.14	0.43	-0.13	1.08	2.17	0.53
		SUP	-0.15	-0.04	0.68	0.28	-1.11	-0.46	-0.51	-1.83	-1.7	-0.88
		ENH	n/a	n/a	n/a	n/a	n/a	n/a	n/a	n/a	n/a	n/a
	TC	NEU	n/a	n/a	n/a	n/a	n/a	n/a	n/a	n/a	n/a	n/a
		SUP	n/a	n/a	n/a	n/a	n/a	n/a	n/a	n/a	n/a	n/a
		ENH	-0.42	-0.43	-0.44	-0.44	-0.4	-0.36	-0.35	-0.38	-0.42	-0.43
WEPAC	H	NEU	0.61	0.61	0.62	0.67	0.63	0.6	0.6	0.63	0.63	0.62
		SUP	-0.37	-0.36	-0.36	-0.41	-0.42	-0.42	-0.43	-0.43	-0.4	-0.38
		ENH	-0.42	-0.43	-0.44	-0.44	-0.4	-0.36	-0.35	-0.38	-0.42	-0.43
	IH	NEU	0.61	0.61	0.62	0.67	0.63	0.6	0.6	0.63	0.63	0.62
		SUP	-0.37	-0.36	-0.36	-0.41	-0.42	-0.42	-0.43	-0.43	-0.4	-0.38
		ENH	-0.73	-0.75	-0.76	-0.77	1	2.96	1.24	2.84	0.9	0.86
	TC	NEU	-1.53	-0.23	-0.22	-0.1	-1.47	-1.56	-0.27	-1.48	-1.45	-2.79
		SUP	2.87	1.19	1.18	0.94	0.9	-0.73	-0.74	-0.75	0.98	2.85
		ENH	-0.42	-0.43	-0.44	-0.44	2.53	2.74	-0.35	-0.38	-0.42	-0.43
CPAC	H	NEU	-1.63	0.61	0.62	0.67	-1.59	-1.66	0.6	0.63	-1.58	-1.61
		SUP	2.67	-0.36	-0.36	-0.41	-0.42	-0.42	-0.43	-0.43	2.5	2.66
		ENH	-0.42	-0.43	-0.44	-0.44	2.53	2.74	-0.35	-0.38	-0.42	-0.43
	IH	NEU	-1.63	0.61	0.62	0.67	-1.59	-1.66	0.6	0.63	-1.58	-1.61
		SUP	2.67	-0.36	-0.36	-0.41	-0.42	-0.42	-0.43	-0.43	2.5	2.66
		ENH	2.92	1.32	-2.05	-1.61	-1.25	-1.55	0.21	0.99	1.5	1.87
	TC	NEU	-1.16	-1.56	0.83	0.81	-1.8	-0.46	-0.5	0.5	-0.2	-0.7
		SUP	-1.62	0.67	1.19	0.63	3.48	1.97	0.43	-1.52	-1.29	-1.1
		ENH	0.61	-0.1	-1.35	-1.38	-1.11	-1.63	-0.14	-0.34	0.64	1.18
AMDR	H	NEU	0.74	-0.27	1.27	1.04	-0.17	0.68	0.65	0.81	0.37	-0.21
		SUP	-1.67	0.5	-0.22	0.08	1.28	0.62	-0.68	-0.7	-1.14	-1
		ENH	1.13	1.04	0.18	-1.47	-1.31	-1.21	-0.2	-0.34	0.3	1.08
	IH	NEU	0.01	-0.67	0.03	0.9	-0.59	-0.04	-0.75	0.73	0.77	0.04
		SUP	-1.24	-0.25	-0.25	0.36	2.01	1.14	1.08	-0.6	-1.33	-1.25

Table 4.12. Relevant *Z*-statistics for all TC, hurricane, and intense hurricane *landfall-actual* events from 1978-2006. Positive (negative) *Z*-statistic indicates favorable (unfavorable) modulation of TC genesis of TCs, hurricanes, and intense hurricanes at their time of landfall.

Basin	Storm Type	MJO Phase	Index 1 80°E	Index 2 100°E	Index 3 120°E	Index 4 140°E	Index 5 160°E	Index 6 120°W	Index 7 40°W	Index 8 10°W	Index 9 20°E	Index 10 70°E
NATL	TC	ENH	1.82	0.82	-1.22	-1.3	-1.51	-2.94	-1.61	0.14	4.66	2.43
		NEU	0.4	0.98	1.07	-2.11	-2.37	1.05	1.79	1.18	-2.46	-0.69
		SUP	-2.53	-2.31	-0.09	4.15	4.45	1.35	-0.79	-1.59	-1.59	-1.73
	H	ENH	3.51	2.36	1.37	-1.96	-0.39	-0.59	-0.04	-0.12	1.73	3.69
		NEU	-2.53	-1.56	-0.5	0.6	-3.53	-2.93	-1.5	-0.64	-1.26	-2.42
		SUP	-0.4	-0.52	-0.89	1.28	4.85	4.16	1.87	0.91	-0.14	-0.76
	IH	ENH	1.35	1.52	1.1	-1.04	-1.59	-2.45	-0.69	0.54	-0.75	1.26
		NEU	1.06	-0.39	-1.18	1.32	-1.06	0.09	-0.83	-0.81	1.84	0.28
		SUP	-2.92	-1.2	0.39	-0.64	2.87	2.1	1.61	0.51	-1.64	-1.77

Table 4.13. Summary of MJO Index 6 modulation of TC activity as measured by TC genesis events.

TC genesis events	**Phase of MJO Index 6**		
Basin	**ENH**	**NEU**	**SUP**
EPAC	**Favorable**	none	**Unfavorable**
NATL	**Unfavorable**	none	**Favorable**
CARIB	**Unfavorable**	none	none
GOM	none	none	none
EEPAC	none	none	none
CEPAC	**Favorable**	none	none
WEPAC	**Favorable**	none	**Unfavorable**
CPAC	**Favorable**	none	none
AMDR	none	none	**Favorable**

Table 4.14. MJO Index averages for each pentad from May 31 to Nov. 26, 1978-2006. Seasonal and "peak season" (Aug. 29 to Sept. 27) averages provided in last row.

Pentad	Index 1	Index 2	Index 3	Index 4	Index 5	Index 6	Index 7	Index 8	Index 9	Index 10
0602	-0.07	0.10	0.24	0.32	0.25	0.04	-0.14	-0.29	-0.33	-0.15
0607	-0.23	-0.10	0.05	0.22	0.31	0.22	0.06	-0.13	-0.31	-0.30
0612	-0.21	-0.15	-0.06	0.08	0.21	0.21	0.13	0.01	-0.17	-0.24
0617	-0.24	-0.29	-0.26	-0.13	0.10	0.26	0.29	0.22	0.00	-0.22
0622	-0.11	-0.19	-0.22	-0.17	-0.02	0.13	0.20	0.20	0.09	-0.08
0627	0.04	0.01	-0.01	-0.03	-0.04	-0.02	0.00	0.02	0.02	0.01
0702	-0.14	-0.11	-0.06	0.03	0.13	0.14	0.10	0.02	-0.10	-0.16
0707	-0.16	-0.16	-0.11	-0.01	0.12	0.17	0.15	0.07	-0.08	-0.18
0712	-0.10	-0.07	-0.02	0.04	0.11	0.11	0.06	-0.01	-0.10	-0.13
0717	-0.05	-0.05	-0.03	0.01	0.05	0.07	0.05	0.02	-0.05	-0.08
0722	-0.12	-0.14	-0.12	-0.05	0.07	0.13	0.13	0.09	-0.03	-0.13
0727	-0.18	-0.20	-0.16	-0.04	0.12	0.20	0.19	0.11	-0.06	-0.20
0801	-0.13	-0.23	-0.25	-0.19	0.00	0.18	0.25	0.23	0.07	-0.13
0806	0.03	-0.15	-0.28	-0.33	-0.20	0.03	0.20	0.30	0.27	0.06
0811	0.02	-0.08	-0.14	-0.16	-0.10	0.02	0.10	0.15	0.12	0.02
0816	-0.10	-0.13	-0.12	-0.07	0.04	0.11	0.13	0.10	0.00	-0.10
0821	0.02	0.04	0.05	0.06	0.04	0.00	-0.03	-0.06	-0.07	-0.03
0826	-0.05	0.00	0.05	0.10	0.11	0.05	-0.01	-0.08	-0.14	-0.10
0831	0.04	0.06	0.06	0.04	0.00	-0.04	-0.06	-0.06	-0.04	0.01
0905	0.04	0.06	0.07	0.06	0.02	-0.03	-0.06	-0.08	-0.07	-0.01
0910	-0.04	-0.07	-0.07	-0.04	0.01	0.06	0.07	0.06	0.01	-0.05
0915	0.02	0.00	-0.02	-0.03	-0.03	-0.01	0.00	0.02	0.02	0.02
0920	-0.05	0.05	0.14	0.21	0.17	0.04	-0.08	-0.18	-0.22	-0.12
0925	-0.28	-0.19	-0.05	0.14	0.30	0.28	0.16	-0.02	-0.25	-0.33
0930	-0.19	-0.28	-0.28	-0.18	0.05	0.23	0.29	0.26	0.06	-0.18
1005	0.00	-0.11	-0.19	-0.22	-0.13	0.03	0.14	0.20	0.17	0.02
1010	0.10	0.12	0.12	0.07	-0.03	-0.10	-0.12	-0.10	-0.03	0.07
1015	-0.01	0.07	0.13	0.17	0.13	0.01	-0.09	-0.16	-0.19	-0.08
1020	-0.10	-0.08	-0.03	0.04	0.11	0.11	0.07	0.00	-0.10	-0.13
1025	0.06	0.09	0.10	0.08	0.01	-0.07	-0.11	-0.11	-0.06	0.03
1030	-0.08	0.05	0.16	0.23	0.20	0.05	-0.09	-0.20	-0.25	-0.14
1104	-0.19	-0.17	-0.10	0.02	0.16	0.20	0.16	0.06	-0.11	-0.21
1109	-0.02	-0.05	-0.06	-0.05	-0.01	0.04	0.06	0.06	0.02	-0.02
1114	0.10	0.12	0.11	0.07	-0.02	-0.10	-0.12	-0.11	-0.04	0.06

1119	-0.05	0.01	0.07	0.11	0.10	0.04	-0.03	-0.09	-0.14	-0.09
1124	-0.07	-0.05	-0.02	0.02	0.06	0.06	0.04	0.00	-0.05	-0.07
Season Mean	-0.07	-0.06	-0.04	0.01	0.07	0.08	0.06	0.01	-0.06	-0.09
Aug 29-Sept 27 Mean	-0.05	-0.02	0.02	0.06	0.08	0.05	0.01	-0.04	-0.09	-0.08

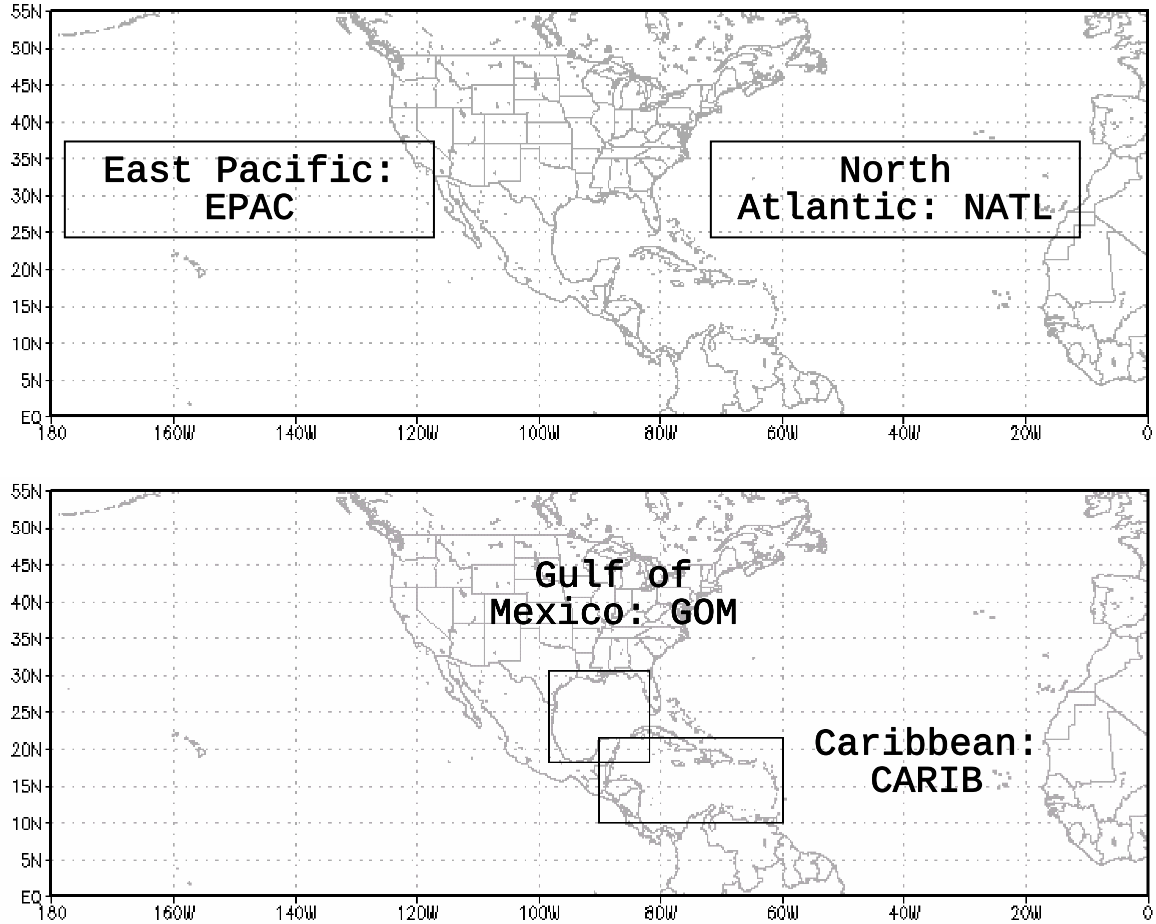

Fig. 1.1: Location of East Pacific and North Atlantic basins and Caribbean and Gulf of Mexico sub-basins.

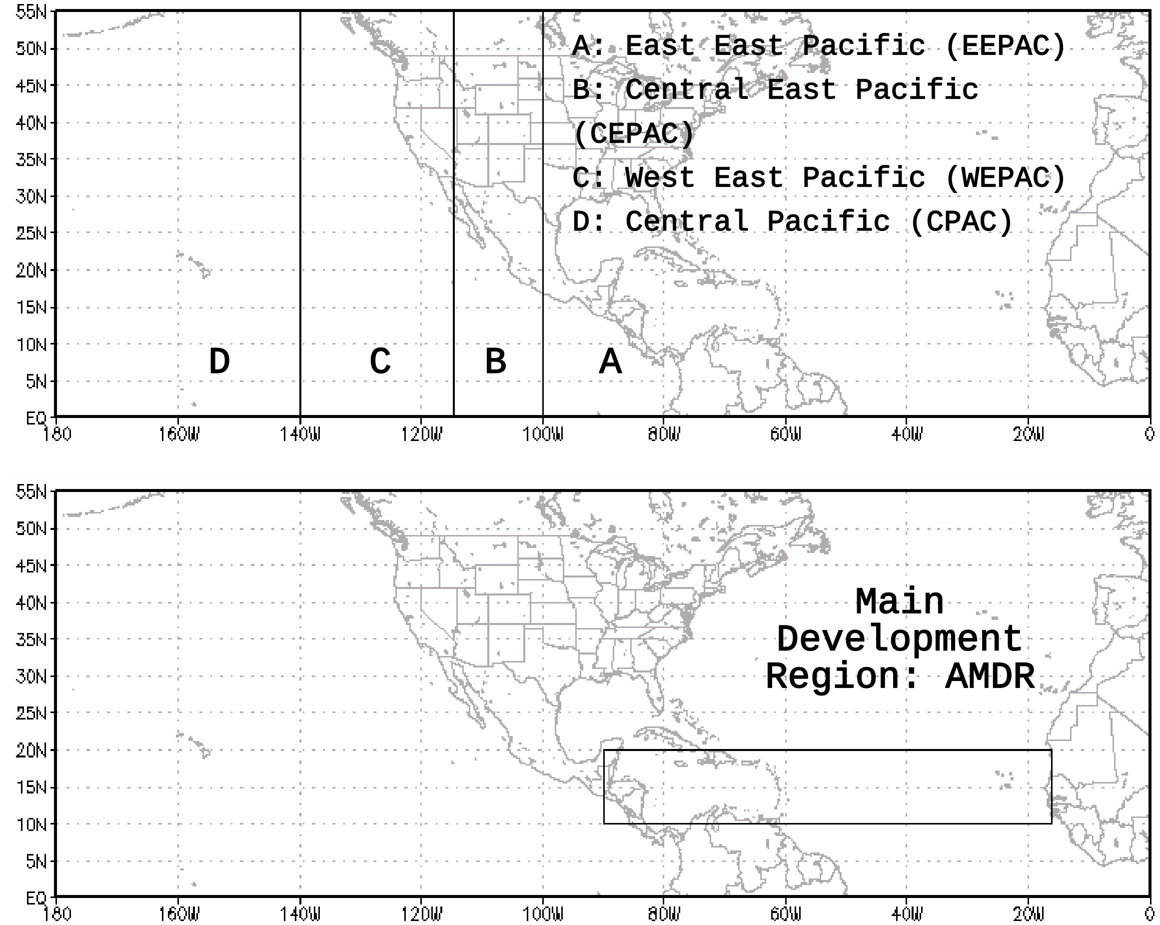

Fig. 1.2: Same as Fig. 1.1, but identifying locations of East Pacific and North Atlantic sub-basins.

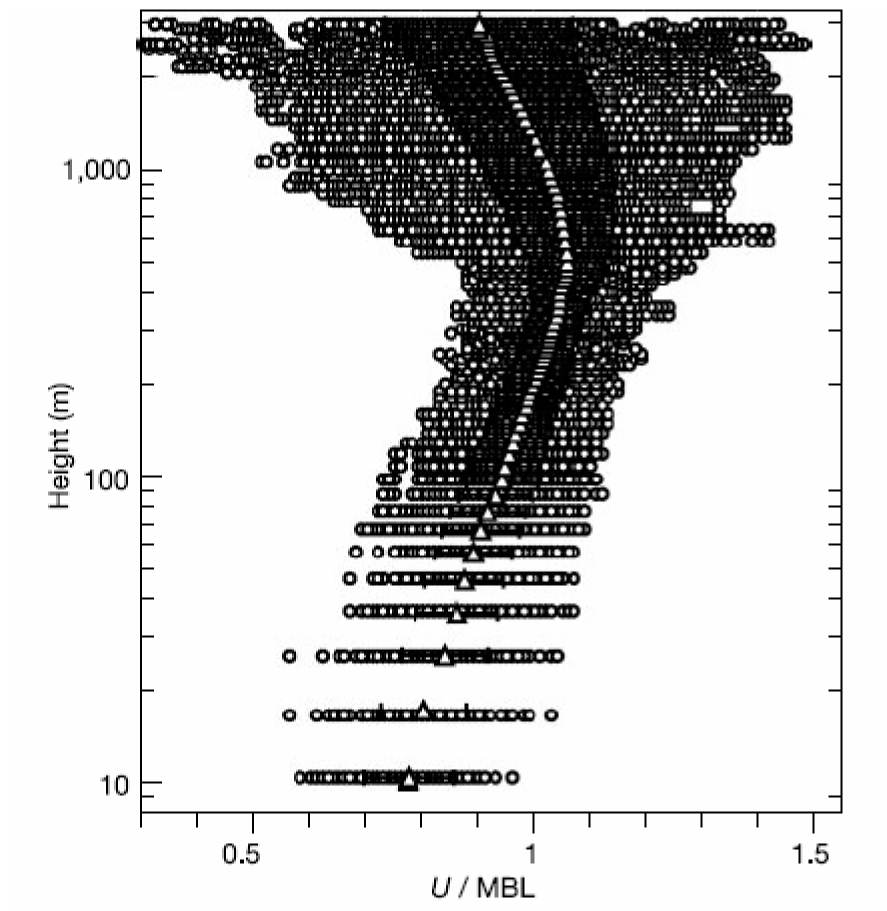

Fig. 1.3: The variation of tangential wind, *U*, with height. *U* is expressed as a ratio of the mean boundary layer (MBL) wind and follows a logarithmically-increasing profile until about 500 m, then decreases again. From Powell et al. (2003).

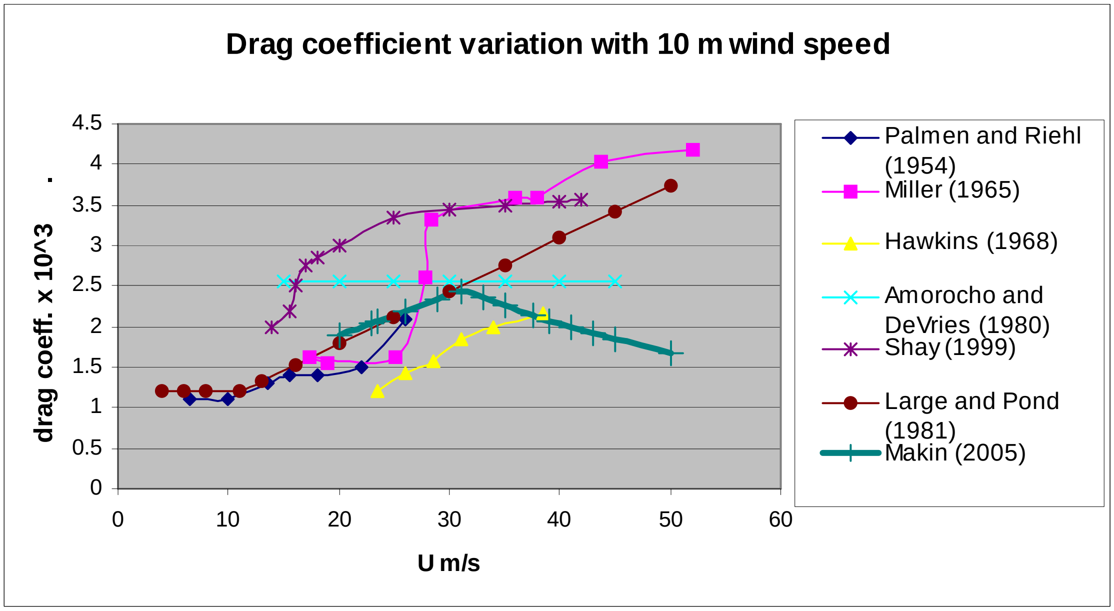

Fig. 1.4: Different parameterizations of drag coefficient as a function of ten-meter wind speed, U_{10}.

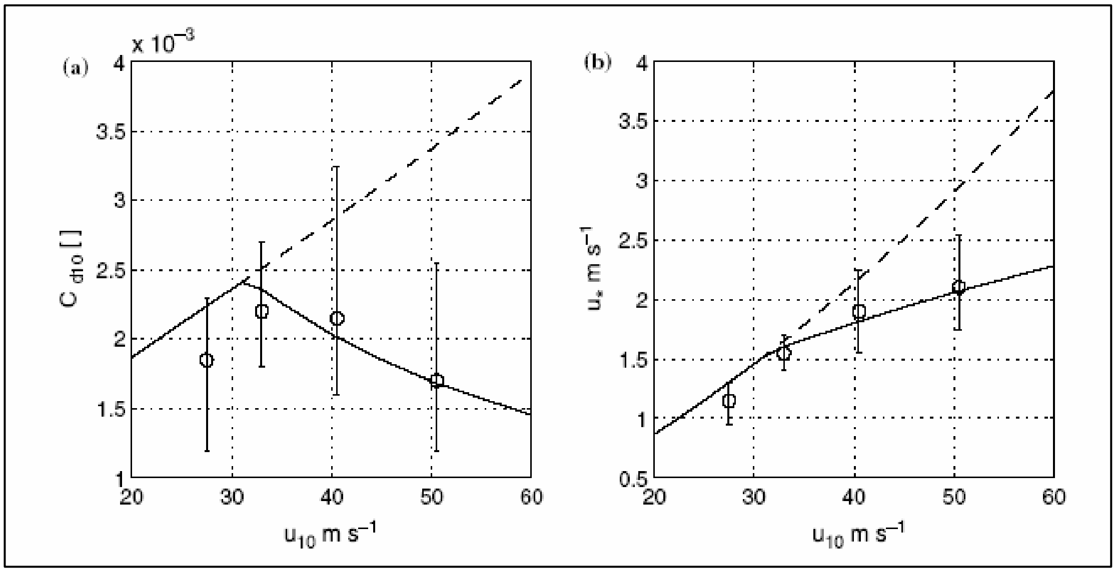

Fig. 1.5: Drag coefficient (a) and friction velocity (b) verses wind speed. Solid line fit according to the resistance law of Makin (2005), dashed line fit according to the Charnock (1955) relationship, and open circles and error bars represent observational data of Powell et al. (2003).

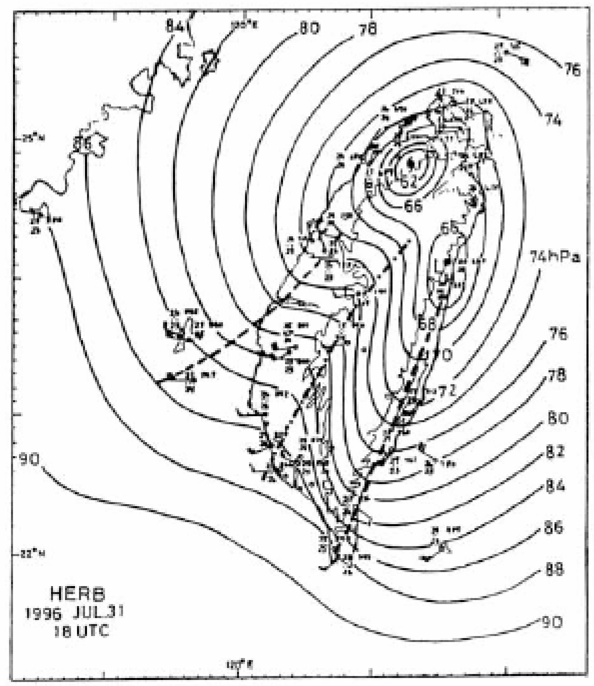

Fig. 1.6: Classic "trough-ridge-trough" sea-level pressure pattern observed in simulations of Typhoon Herb (Peng and Chang 2002).

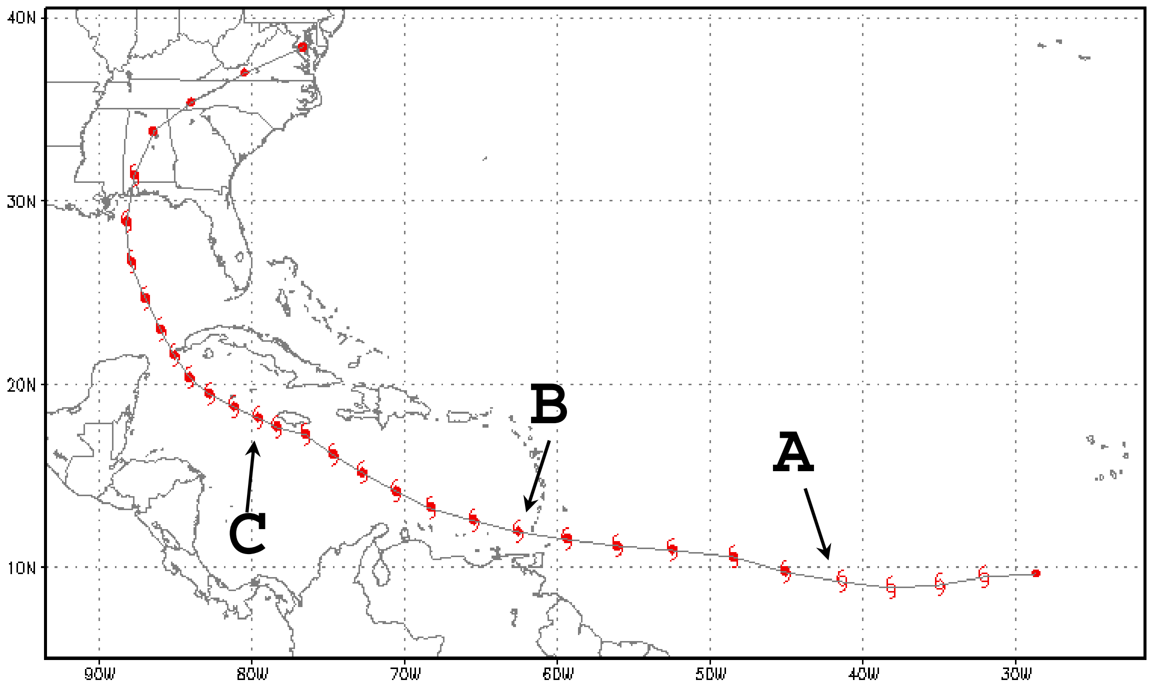

Fig. 2.1: Track of Hurricane Ivan (2004). Boxed region highlights the eight-day period from 0000 UTC 5 September to 1200 UTC 13 September when a strong climatological signal repeatedly conflicted with NWP forecasts. Letters “A”, “B”, and “C” indicate the locations of the motion climatologies depicted in Fig. 2.2.

Fig 2.2: Historical motion climatology for three locations along the track of Hurricane Ivan; locations (a)-(c) are given in lower-right corner of each panel. Number of TCs comprising relative frequency (rf) is given by n. Length of each sector corresponds to rf of a TC moving with that trajectory; rf is given by concentric circles and increases radially out from the center. Colors represent mean 24-h speeds; color legend is in upper-right corner of (a). Dark arrow represents Ivan's actual motion vector.

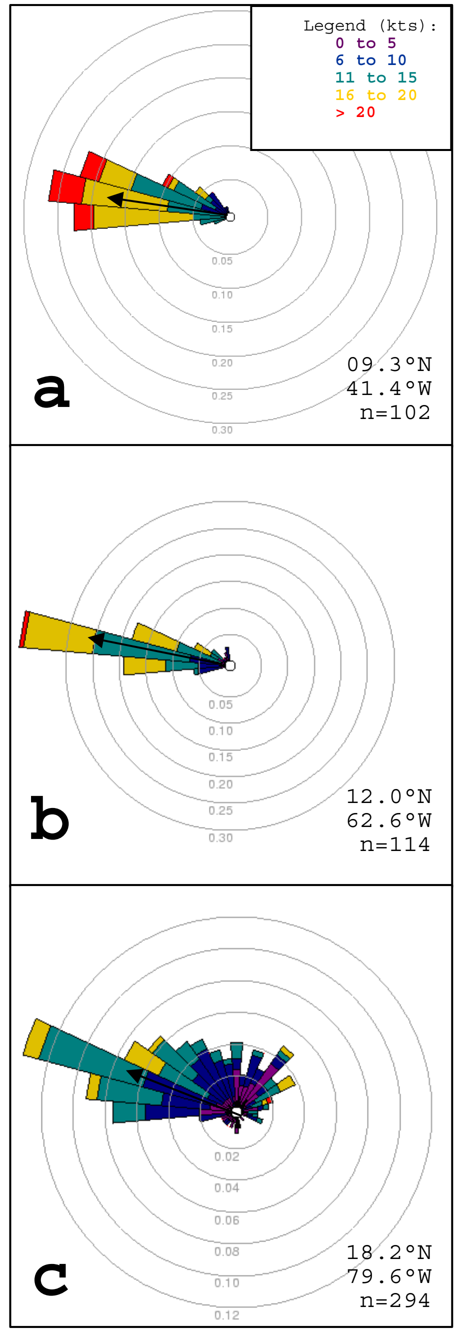

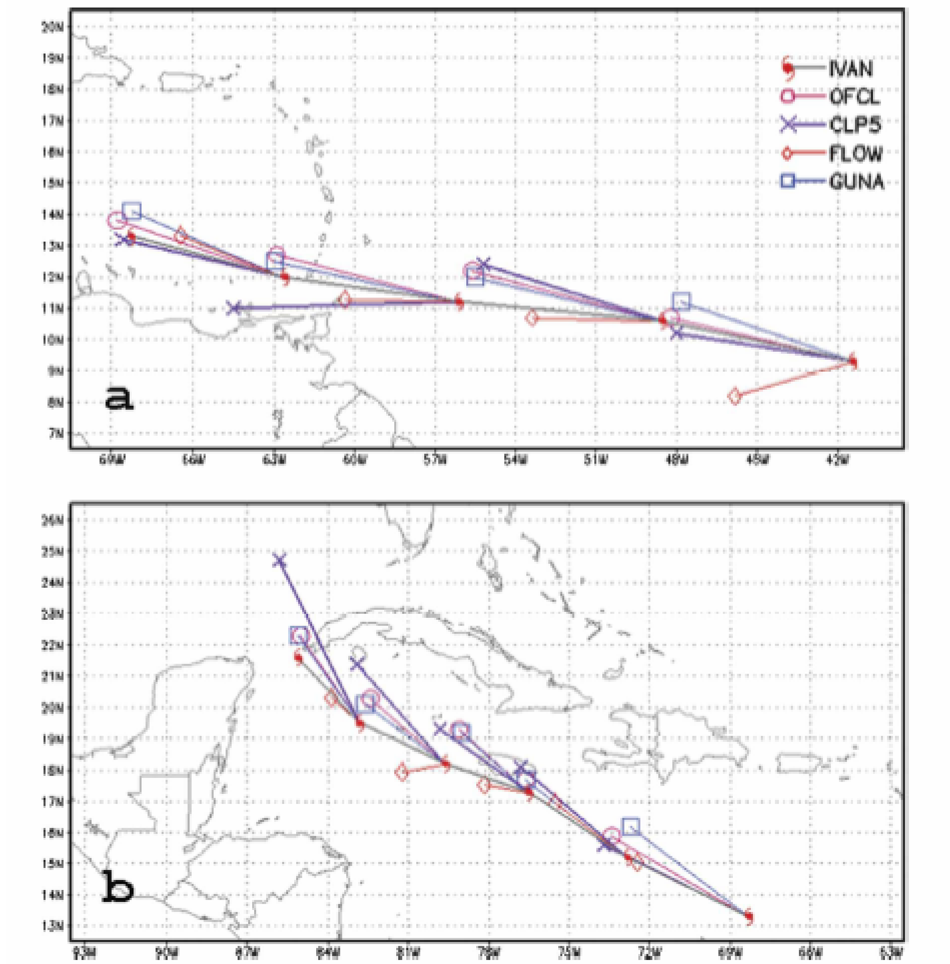

Fig. 2.3. Ivan track and model spread, and 24-h track forecasts (initialized at 0000 UTC) for OFCL (open circle), CLP5 (cross), FLOW (open diamond), and GUNA (open square) models. (a) The period from 5 to 9 September. (b) The period from 10 to 14 September. In (a), steering flow is primarily from E to W; in (b), steering flow becomes more S to N.

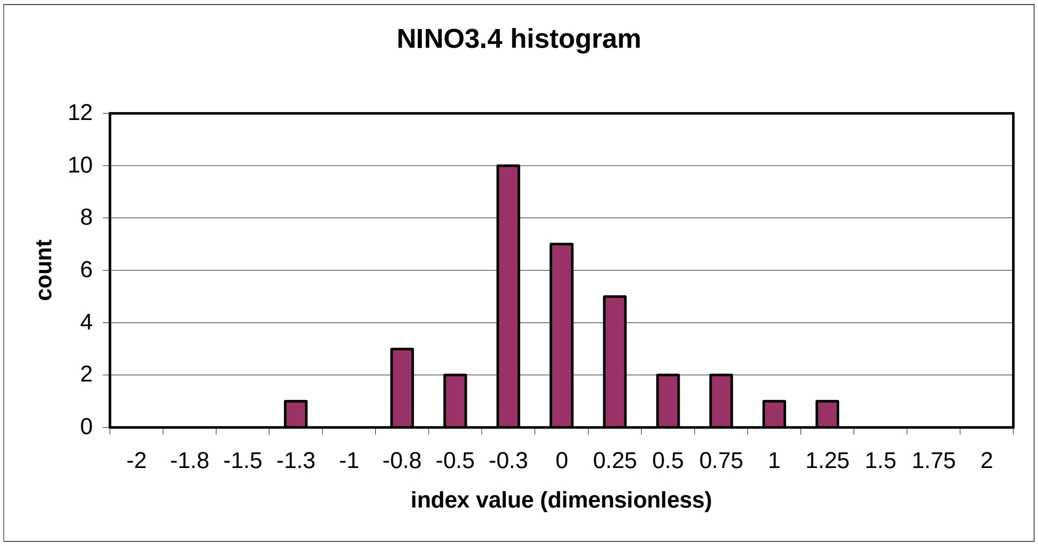

Fig 3.1: Histogram of NINO3.4 index values has a Gaussian shape.

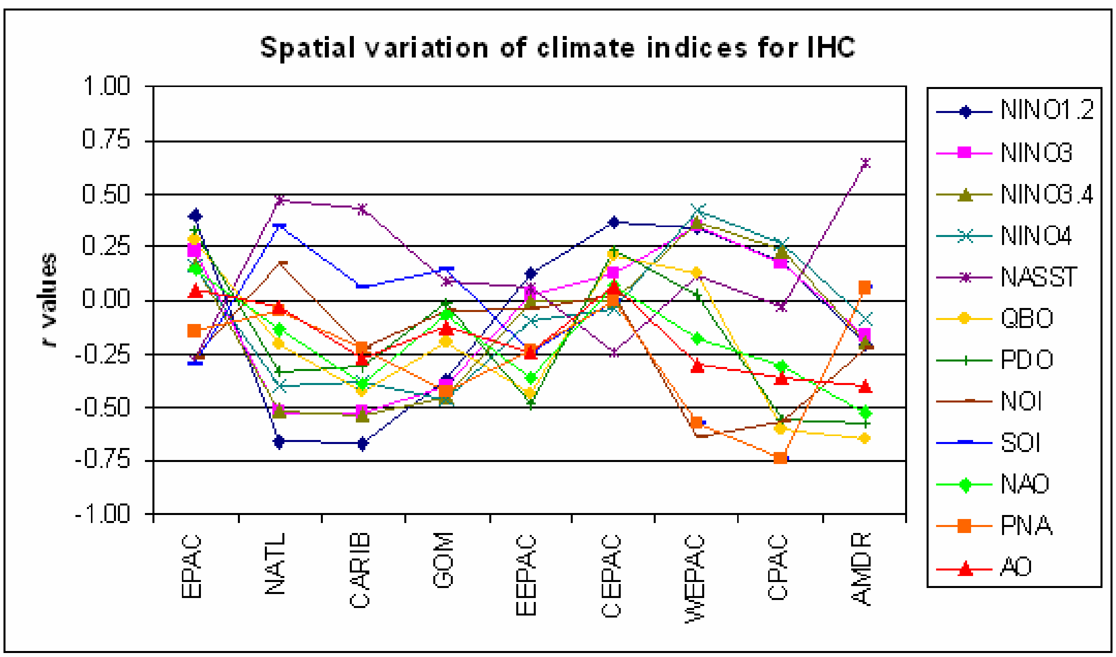

Fig. 3.2: Correlations between climate indices and IHC for each basin.

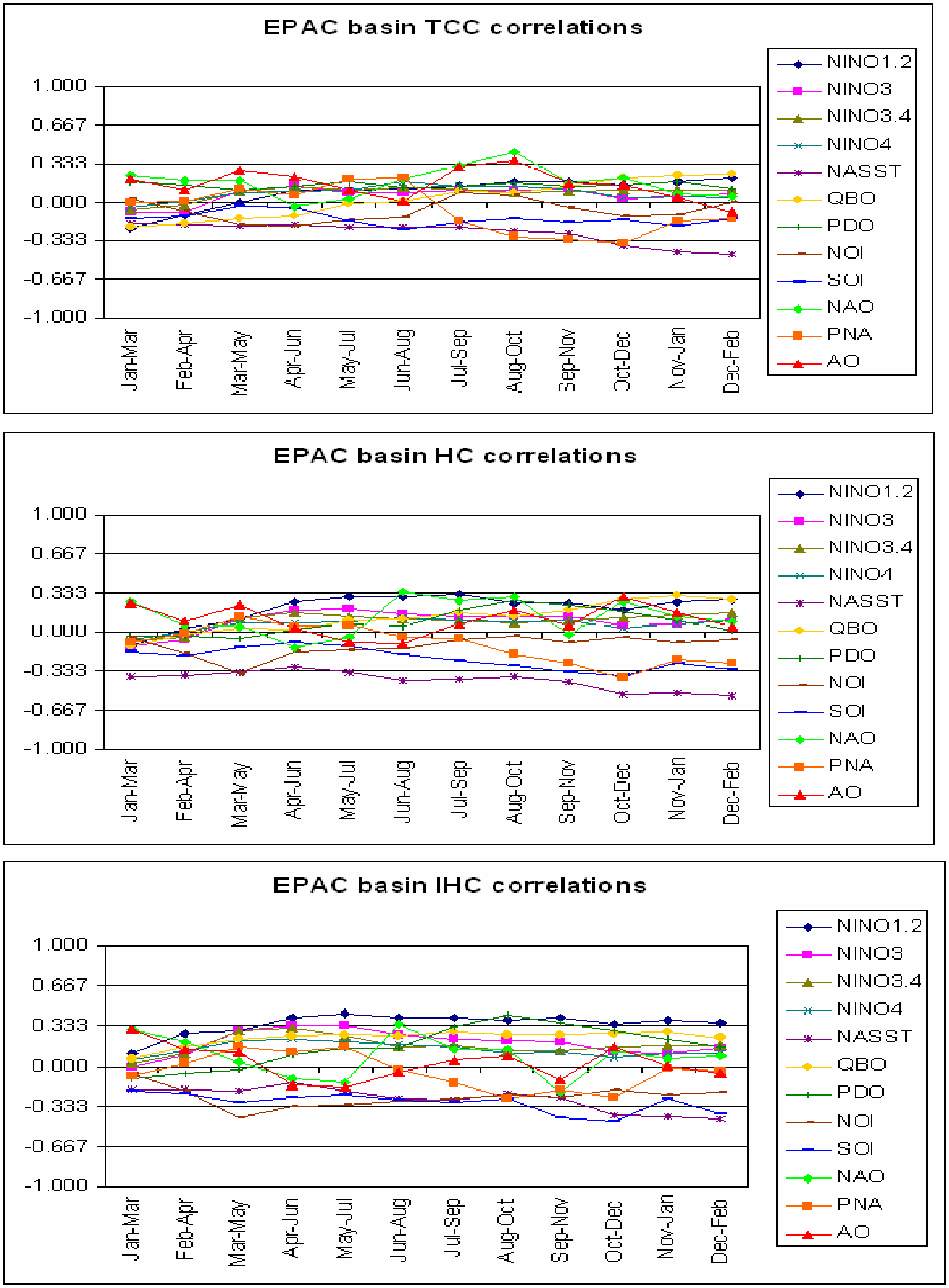

Fig. 3.3: Spearman rank correlation coefficients between climate indices NINO1.2 to AO and EPAC TC activity metrics. Statistically significant critical *r* is ± 0.329.

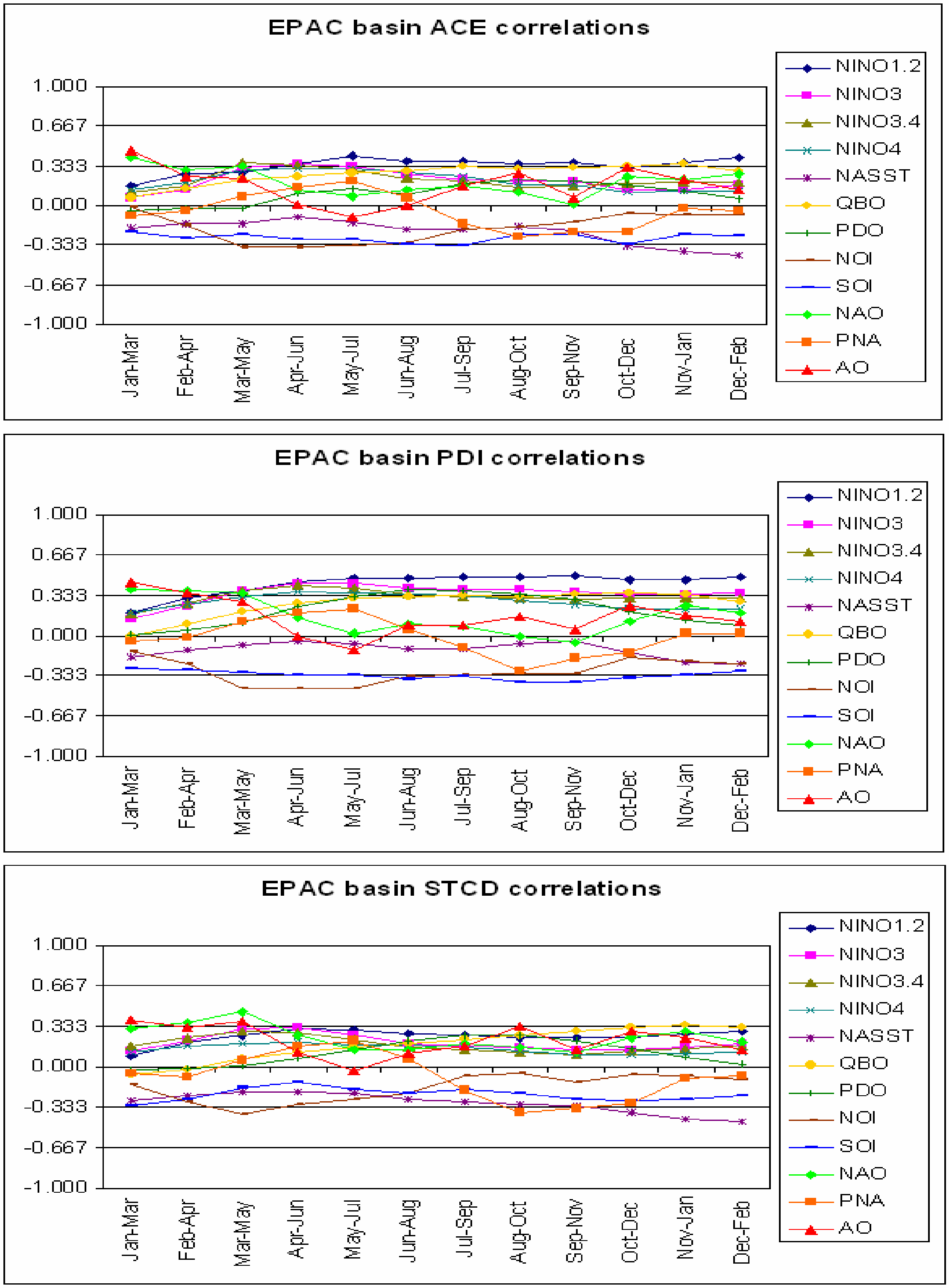

Fig. 3.4: Spearman rank correlation coefficients between climate indices NINO1.2 to AO and EPAC TC activity metrics. Statistically significant critical r is $\pm$ 0.329.

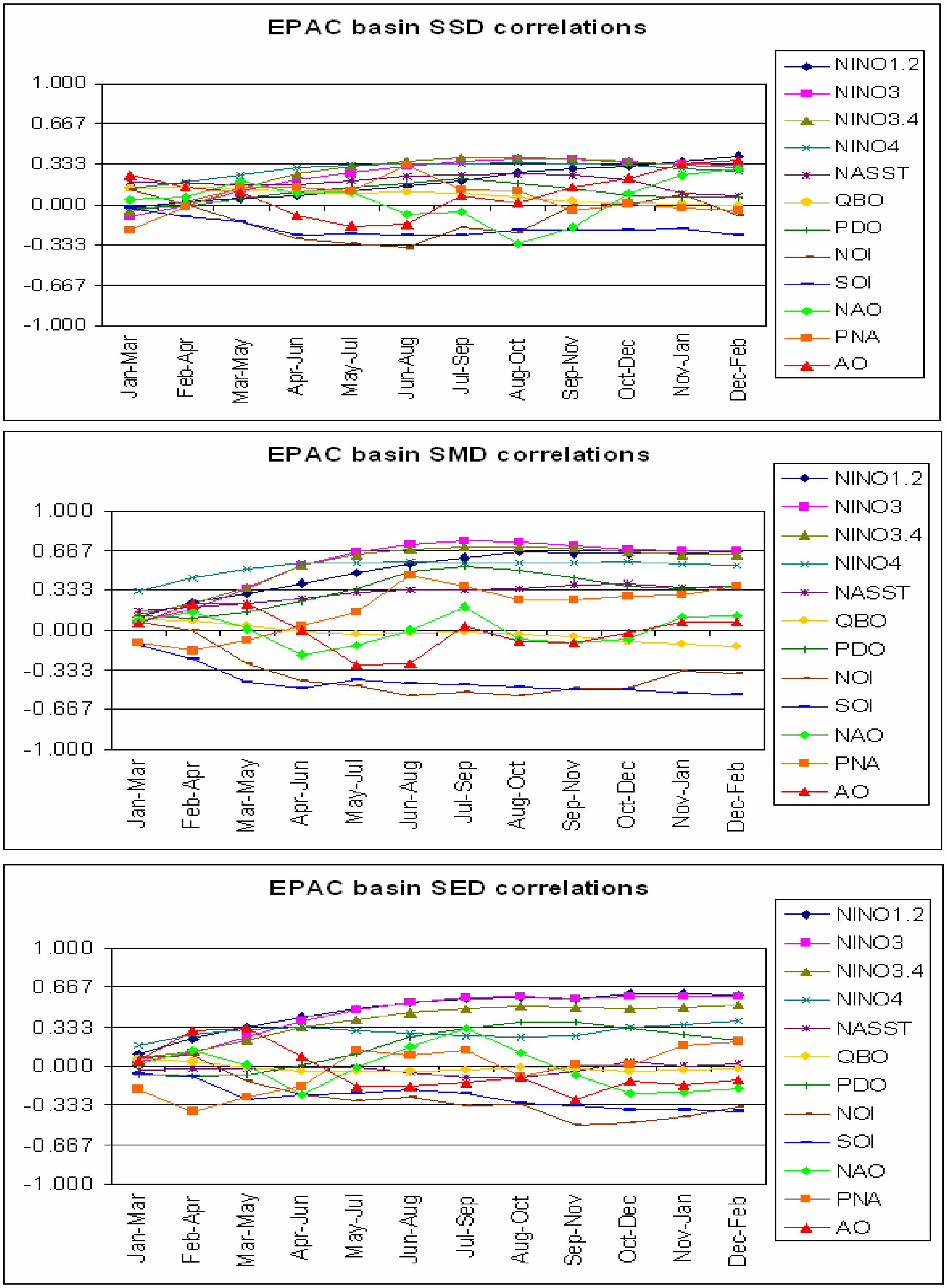

Fig. 3.5: Spearman rank correlation coefficients between climate indices NINO1.2 to AO and EPAC TC activity metrics. Statistically significant critical *r* is ± 0.329.

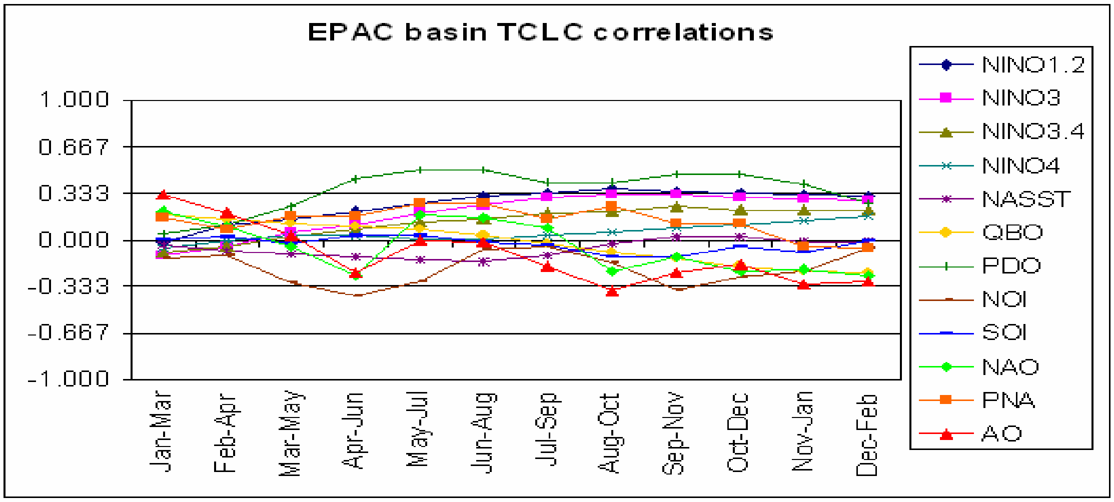

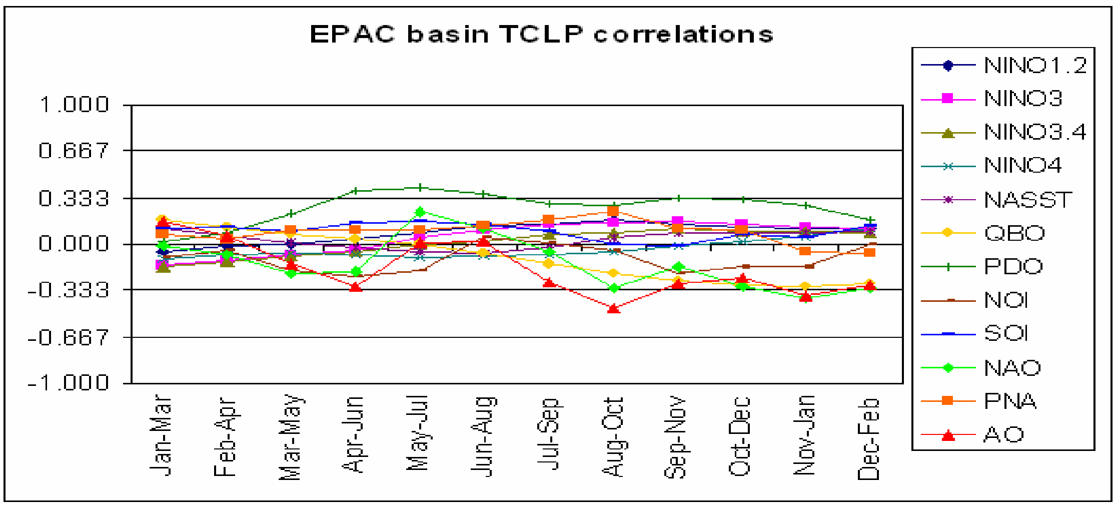

Figure 3.6: Spearman rank correlation coefficients between climate indices NINO1.2 to AO and EPAC TC activity metrics. Statistically significant critical *r* is ± 0.329.

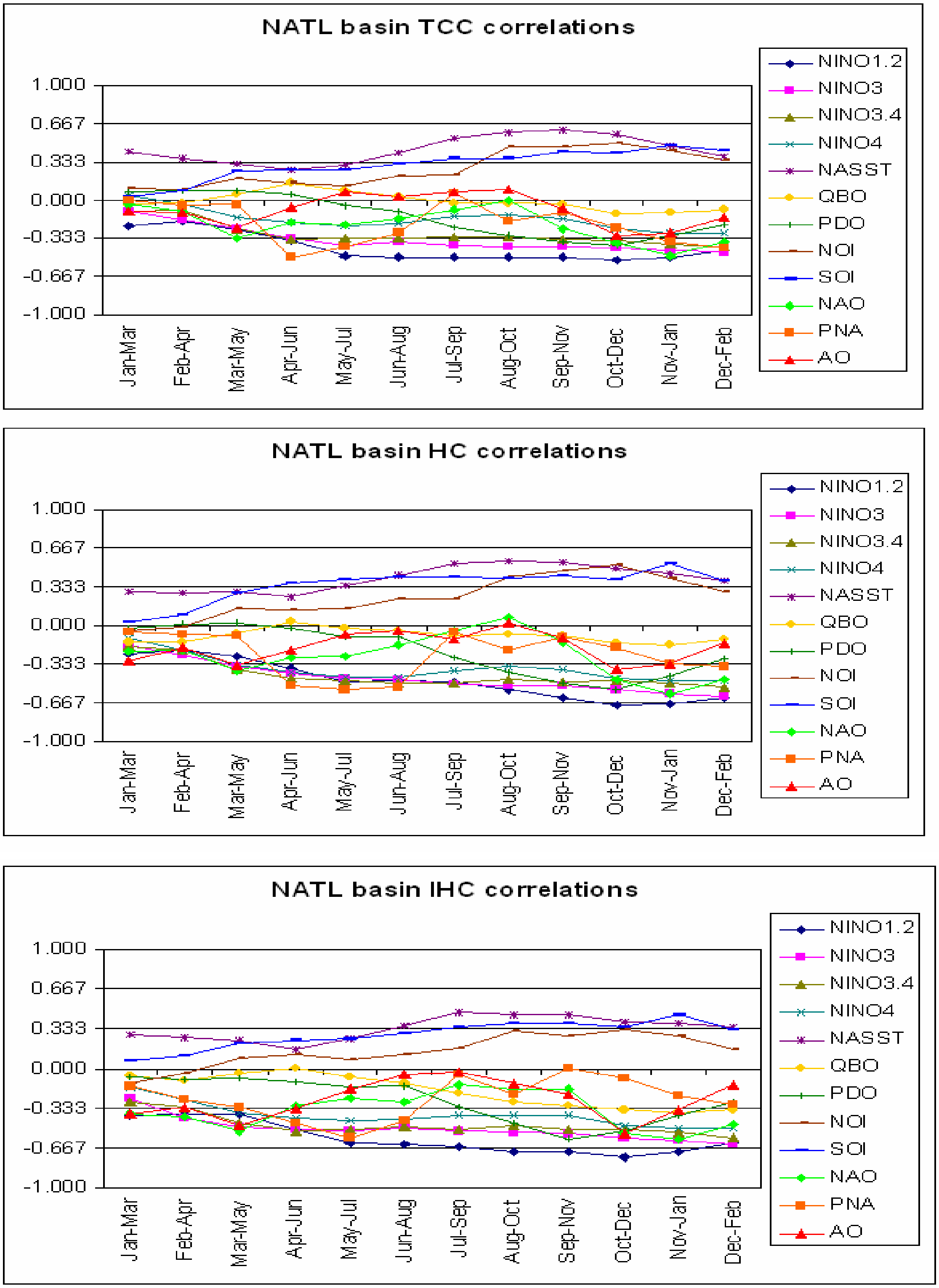

Fig. 3.7: Spearman rank correlation coefficients between climate indices NINO1.2 to AO and NATL TC activity metrics. Statistically significant critical *r* is ± 0.329.

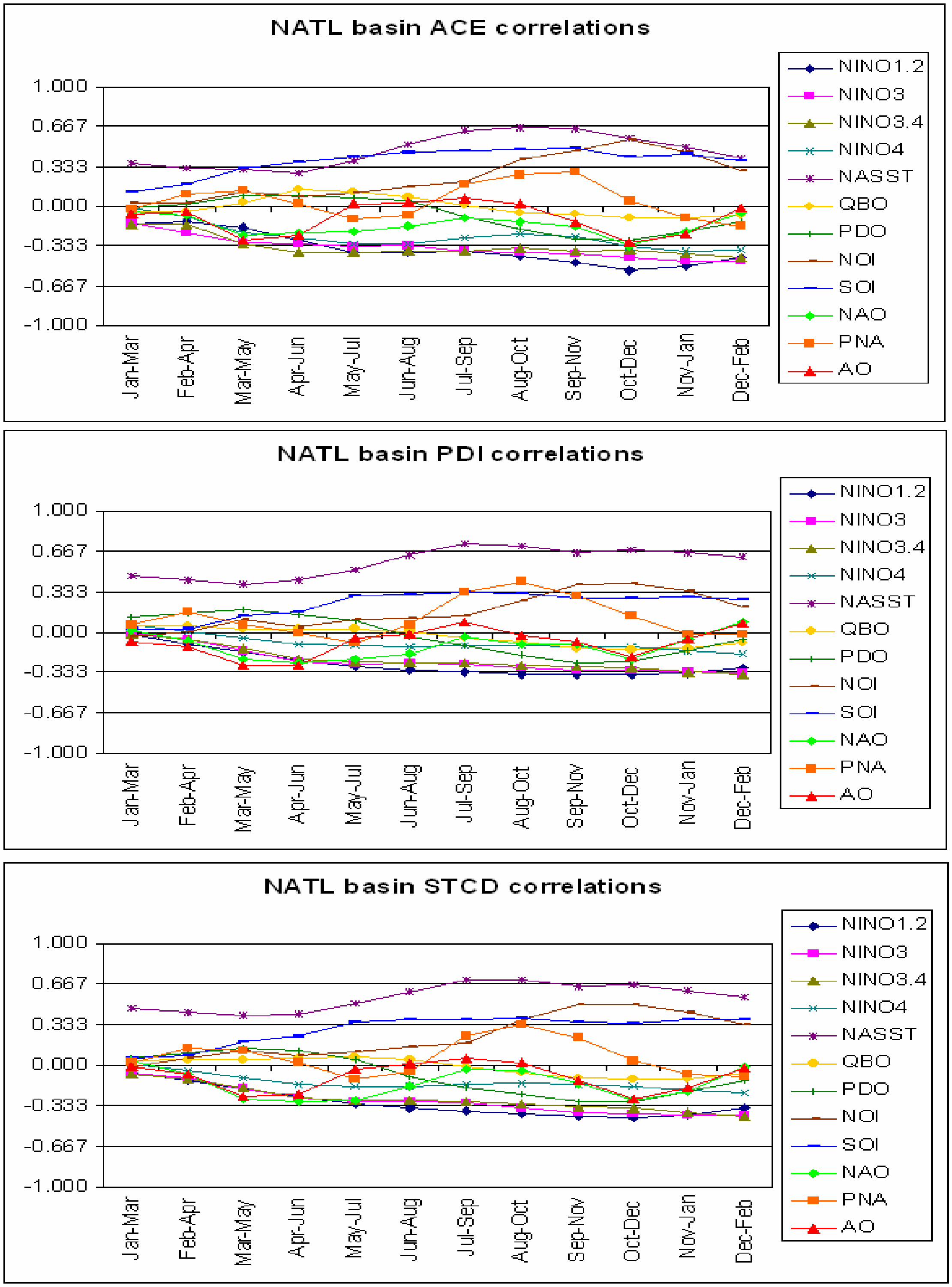

Fig. 3.8: Spearman rank correlation coefficients between climate indices NINO1.2 to AO and NATL TC activity metrics. Statistically significant critical r is $\pm$ 0.329.

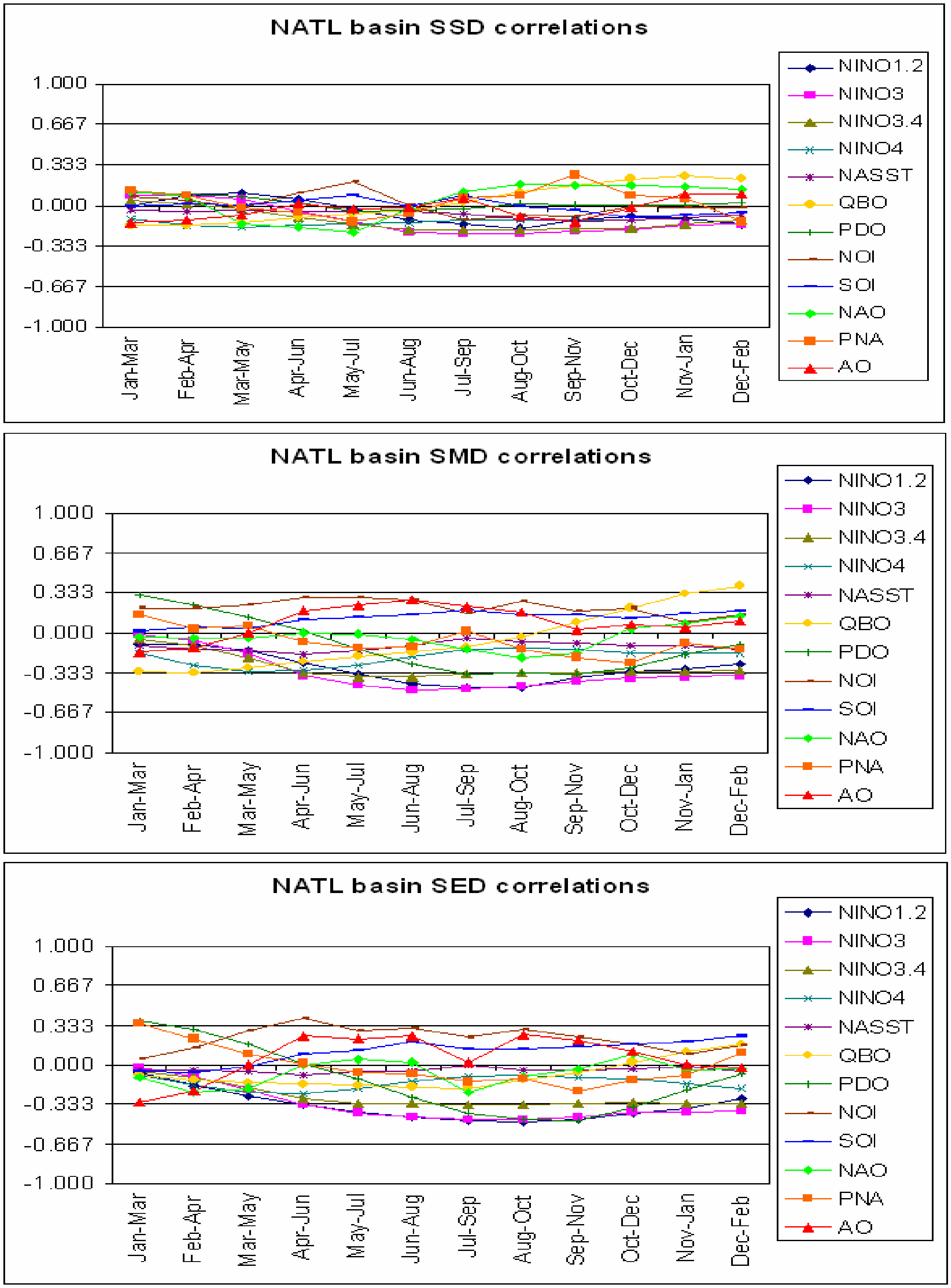

Fig. 3.9: Spearman rank correlation coefficients between climate indices NINO1.2 to AO and NATL TC activity metrics. Statistically significant critical *r* is ± 0.329.

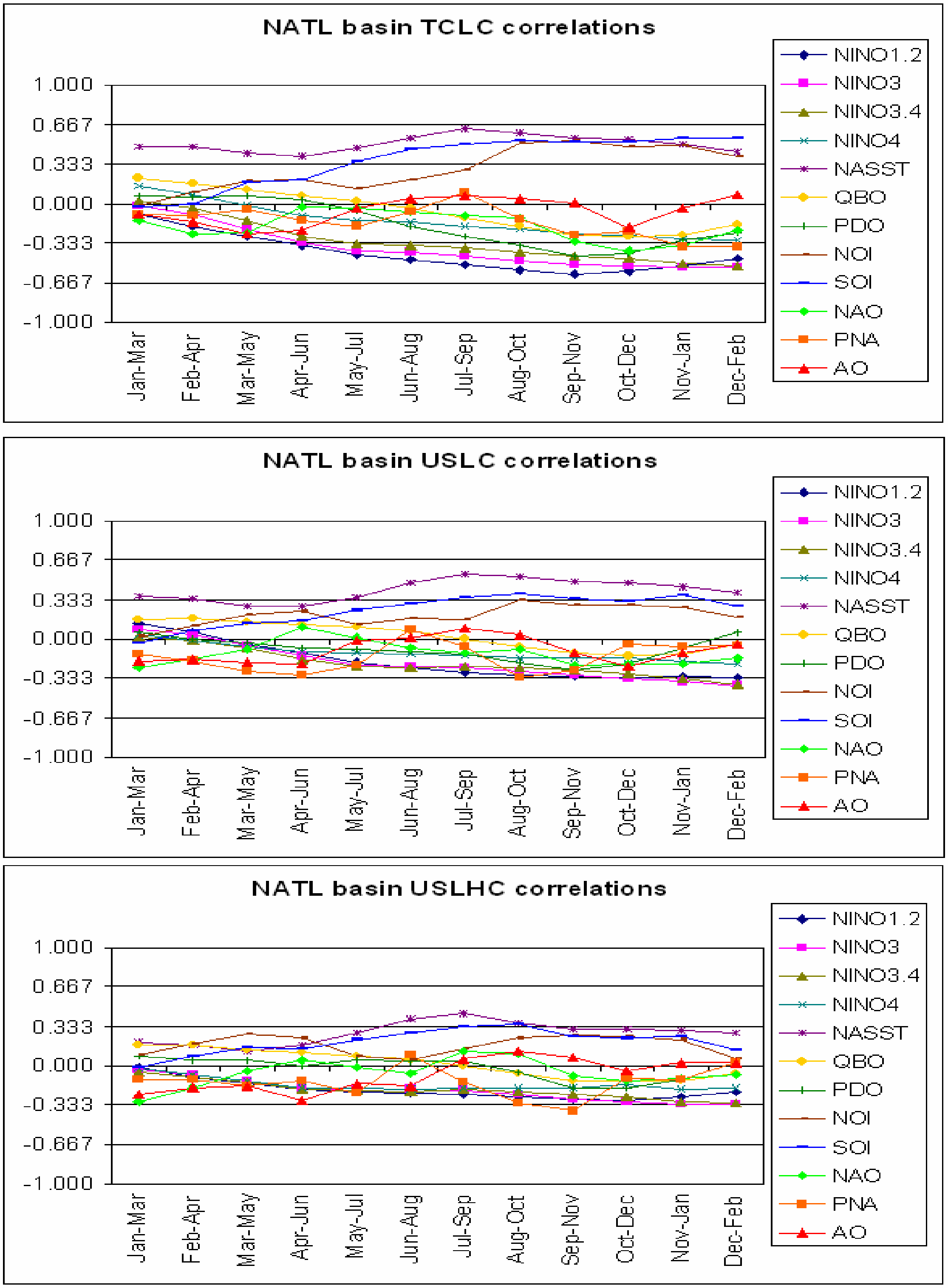

Fig. 3.10: Spearman rank correlation coefficients between climate indices NINO1.2 to AO and NATL TC activity metrics. Statistically significant critical *r* is ± 0.329.

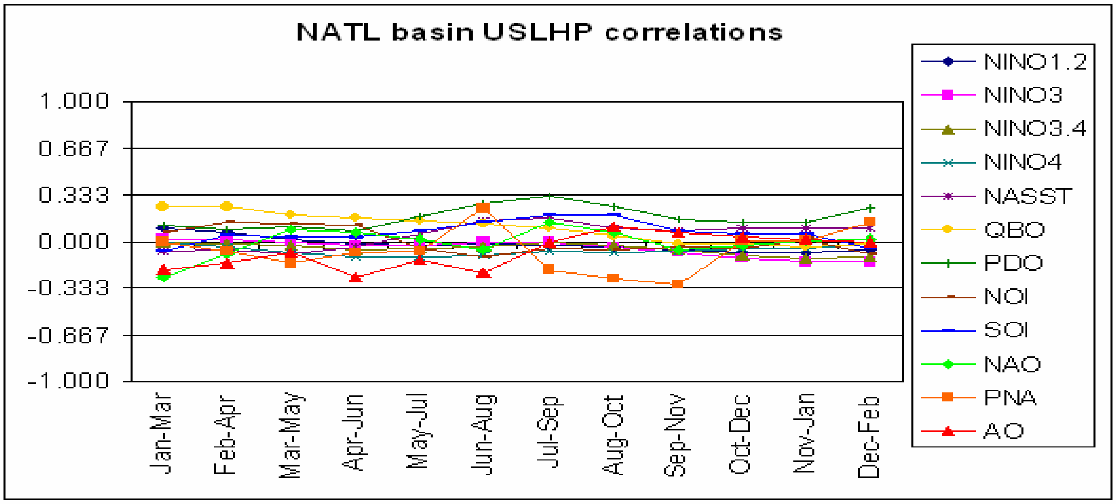

Fig. 3.11: Spearman rank correlation coefficients between climate indices NINO1.2 to AO and NATL TC activity metrics. Statistically significant critical r is $\pm$ 0.329.

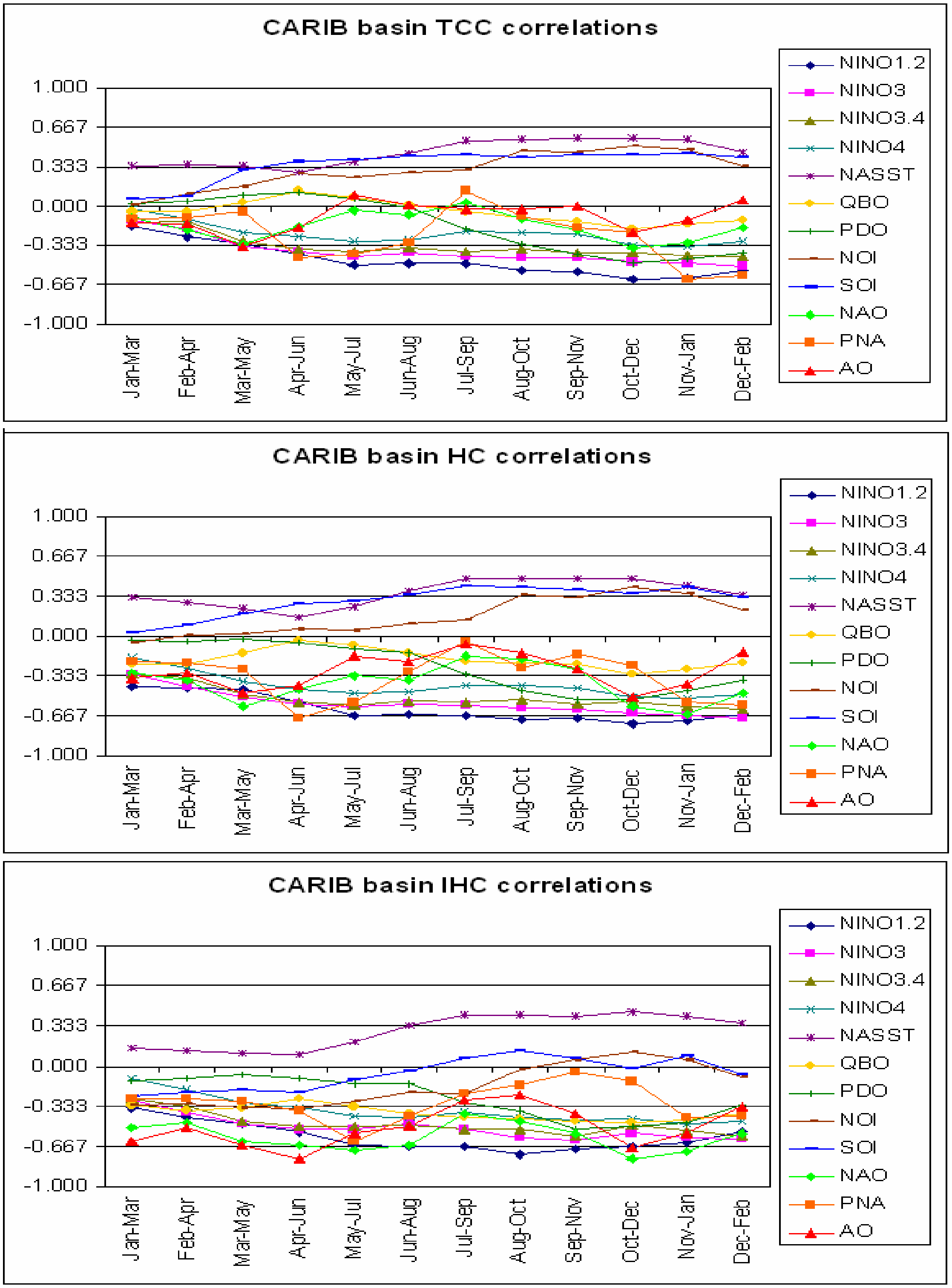

Fig. 3.12: Spearman rank correlation coefficients between climate indices NINO1.2 to AO and CARIB TC activity metrics. Statistically significant critical r is ± 0.329.

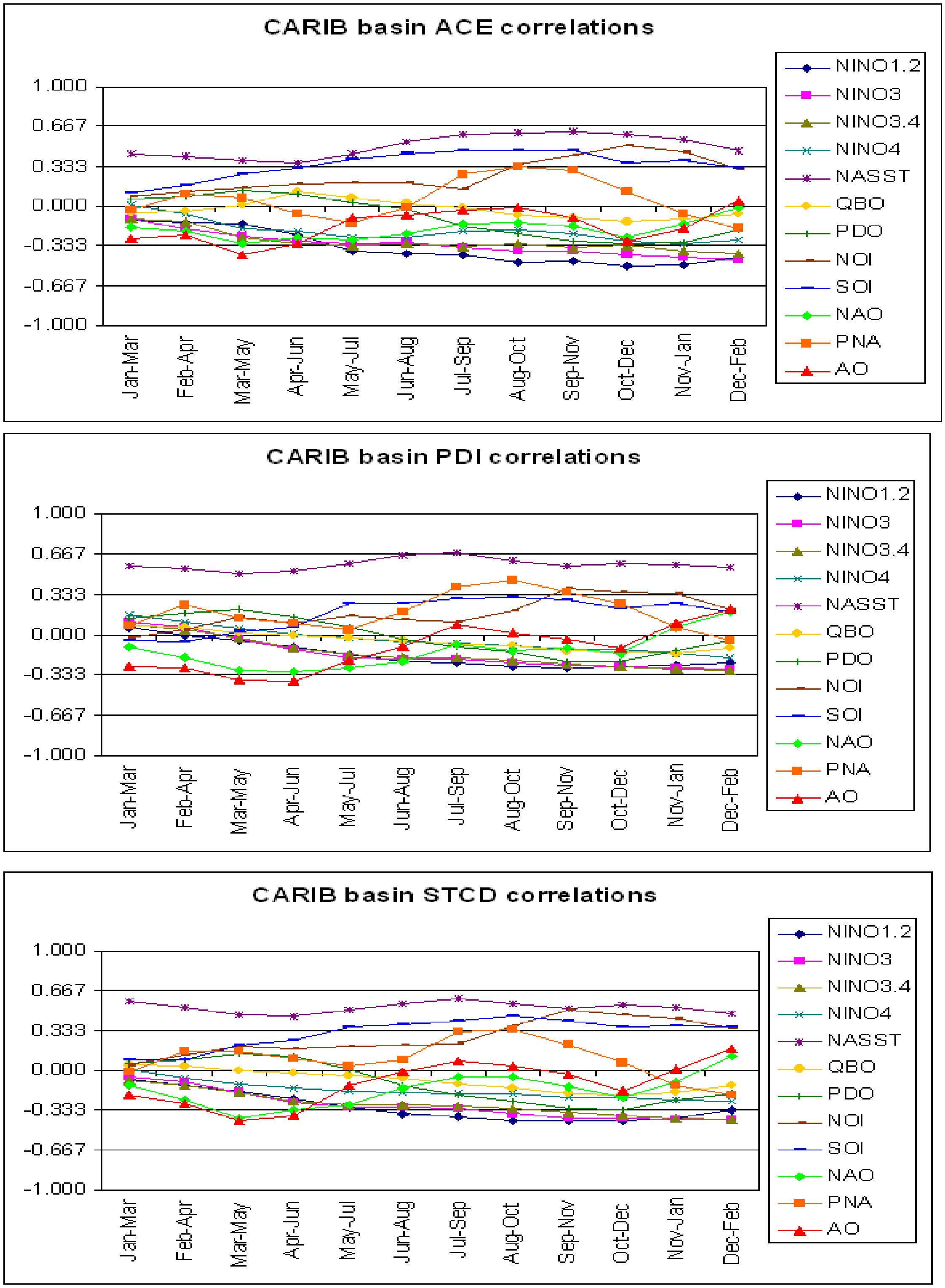

Fig. 3.13: Spearman rank correlation coefficients between climate indices NINO1.2 to AO and CARIB TC activity metrics. Statistically significant critical *r* is ± 0.329.

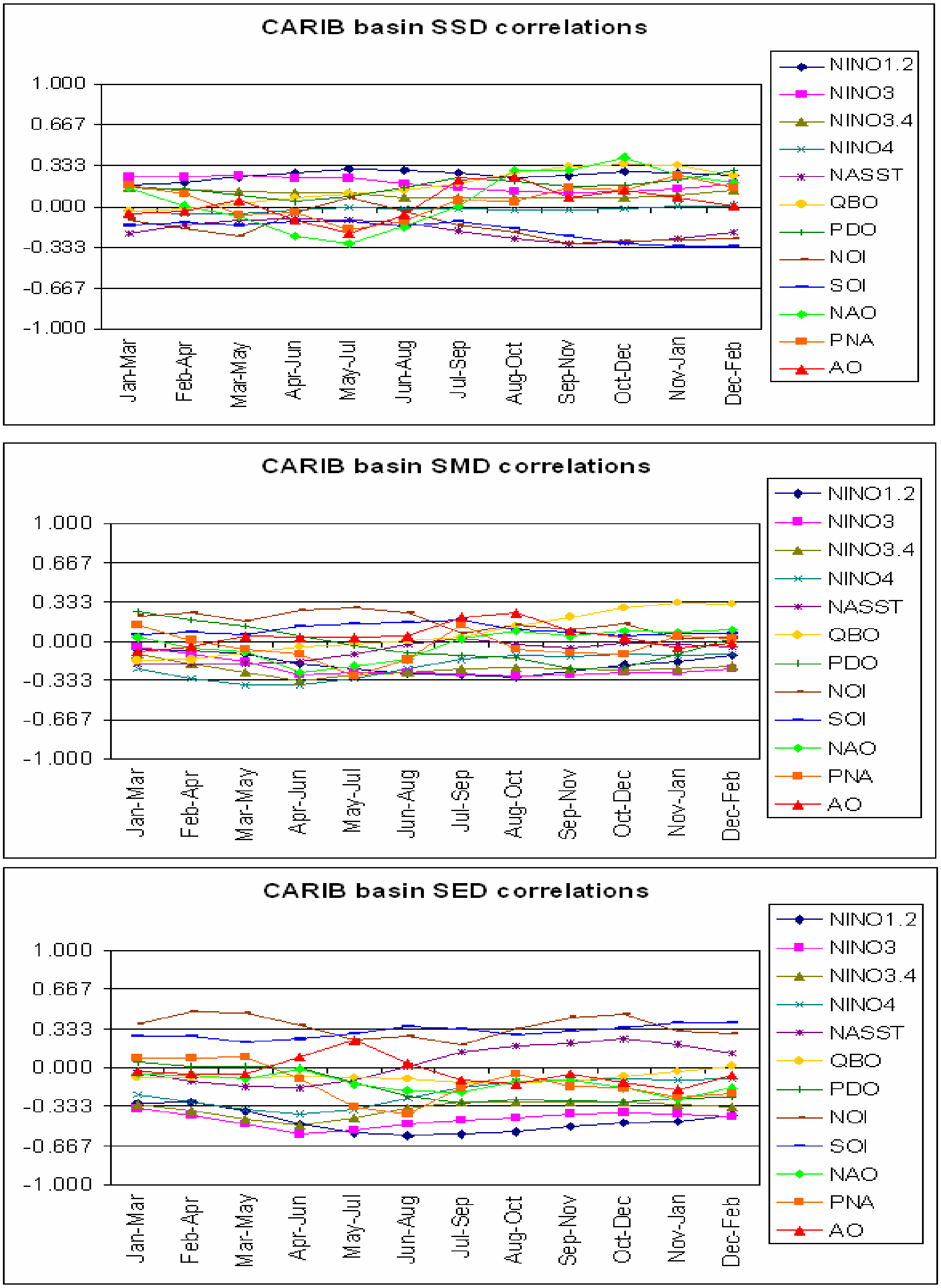

Fig. 3.14: Spearman rank correlation coefficients between climate indices NINO1.2 to AO and CARIB TC activity metrics. Statistically significant critical *r* is ± 0.329.

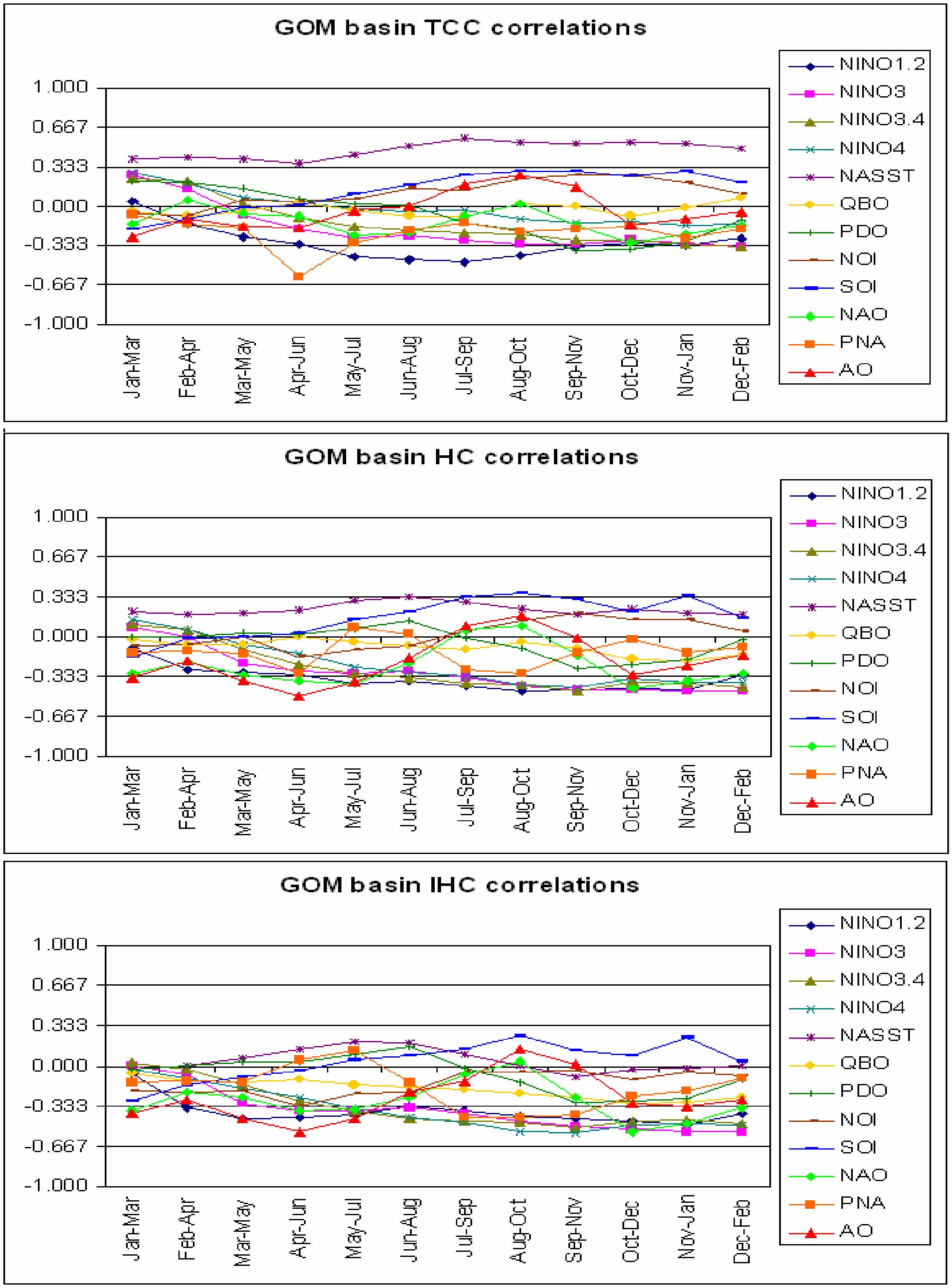

Fig. 3.15: Spearman rank correlation coefficients between climate indices NINO1.2 to AO and GOM TC activity metrics. Statistically significant critical r is $\pm$ 0.329.

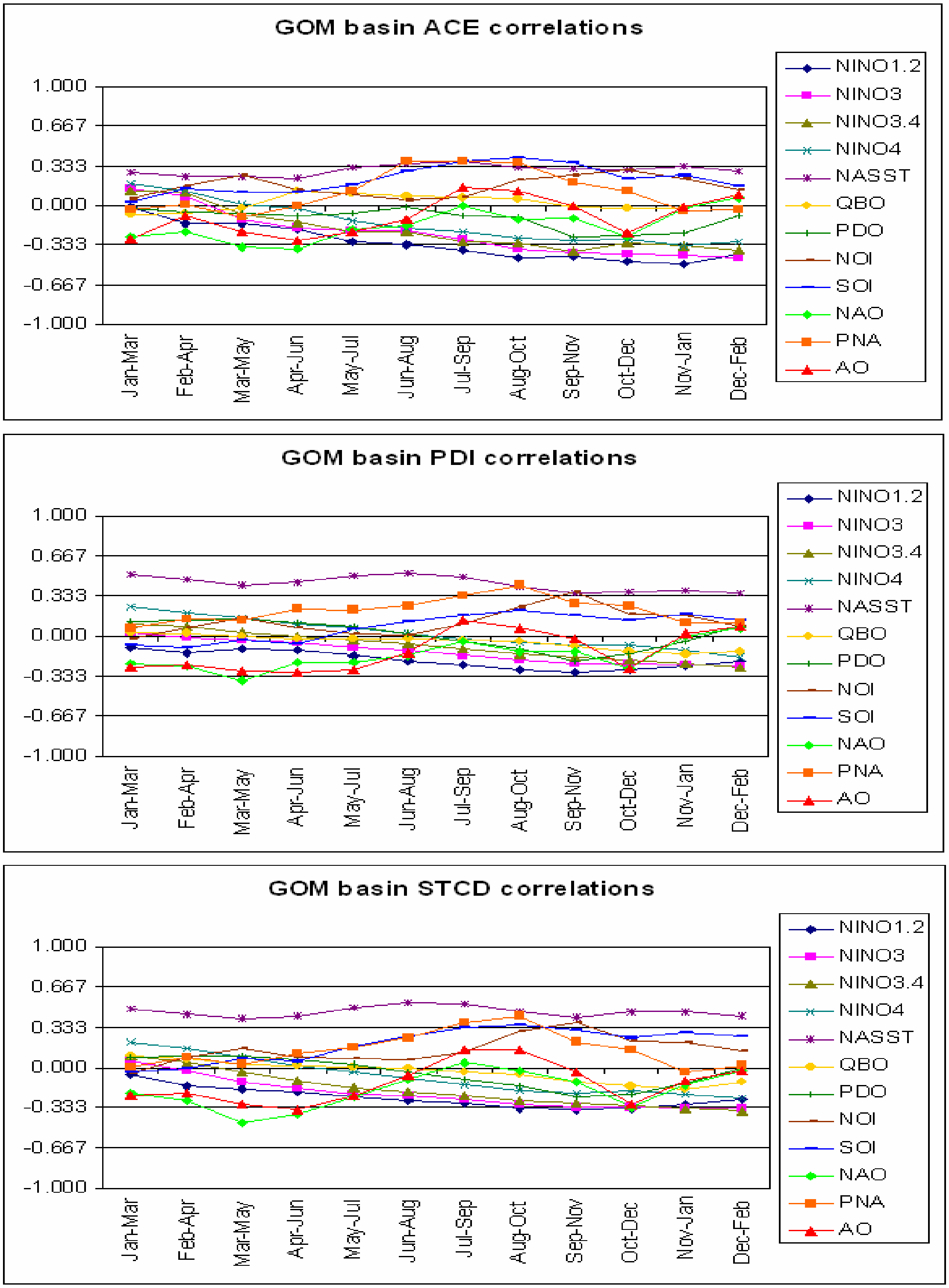

Fig. 3.16: Spearman rank correlation coefficients between climate indices NINO1.2 to AO and GOM TC activity metrics. Statistically significant critical *r* is ± 0.329.

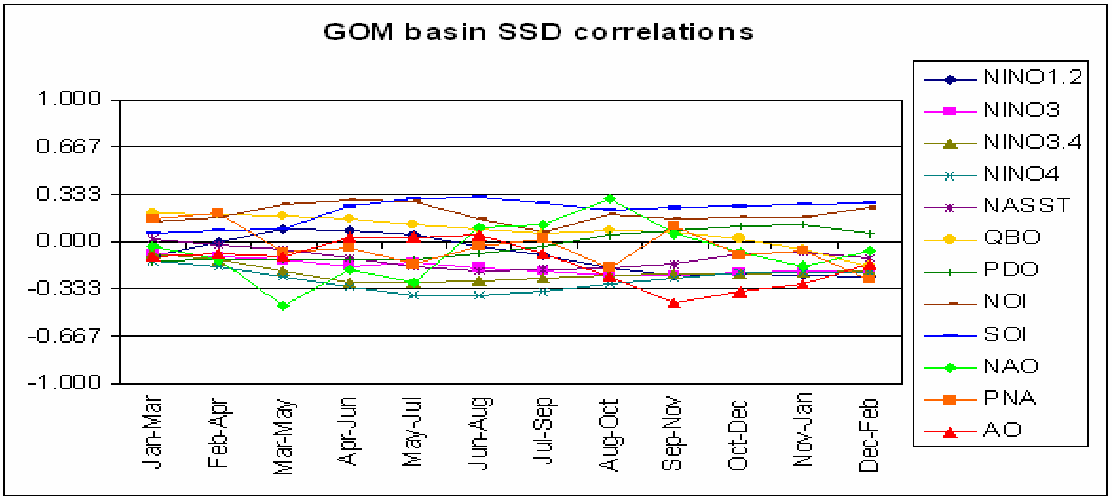

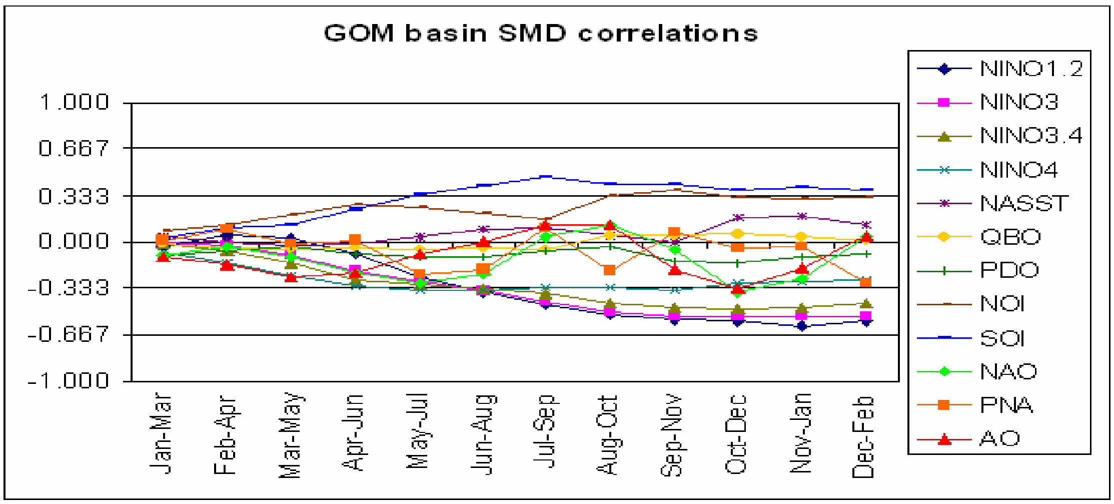

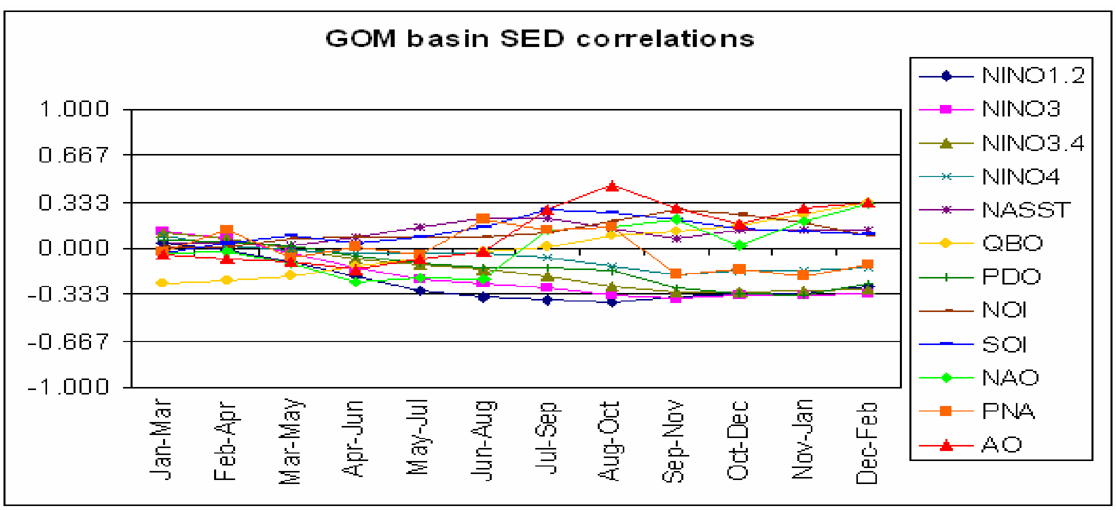

Fig. 3.17: Spearman rank correlation coefficients between climate indices NINO1.2 to AO and GOM TC activity metrics. Statistically significant critical r is $\pm$ 0.329.

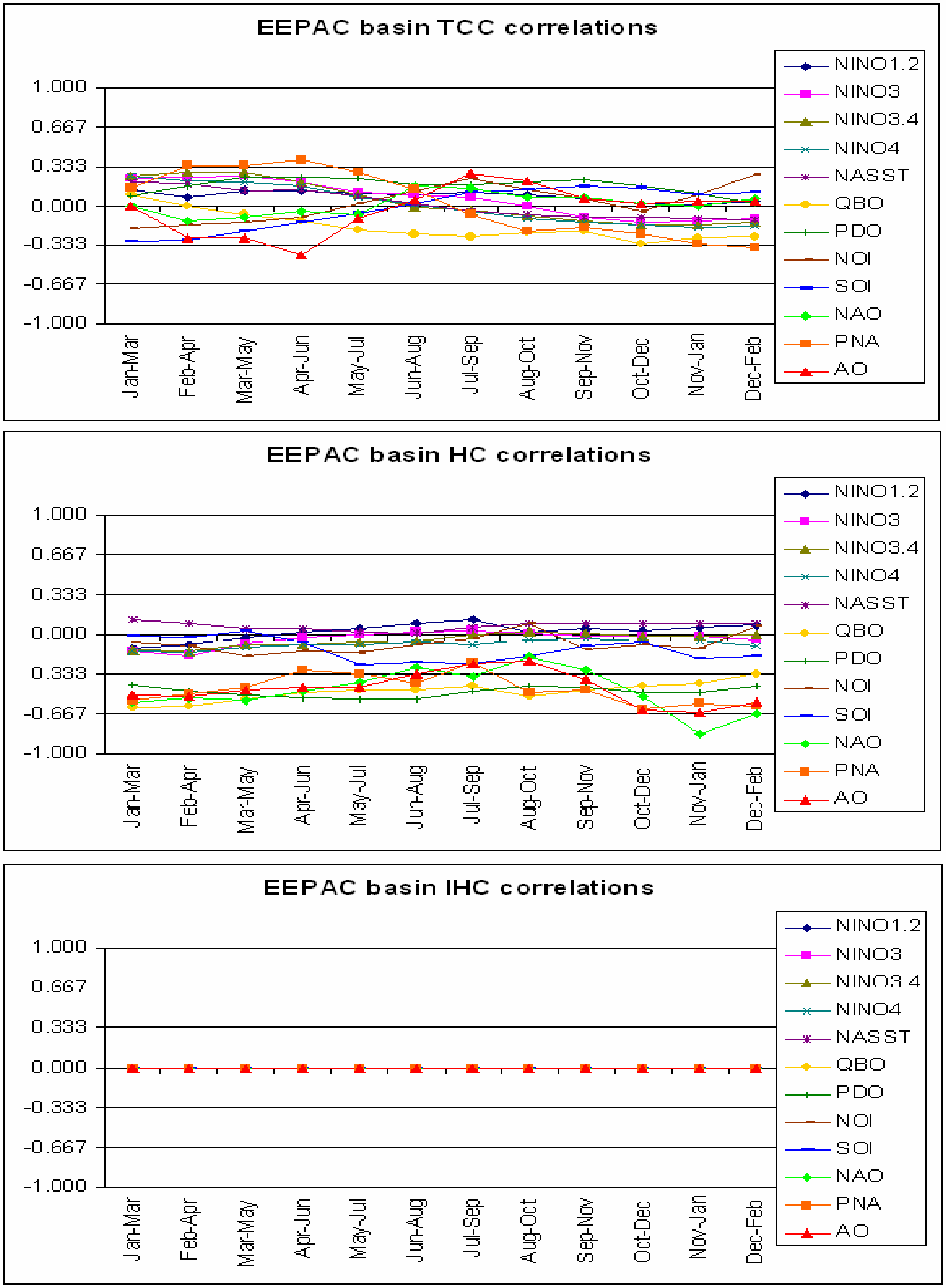

Fig. 3.18: Spearman rank correlation coefficients between climate indices NINO1.2 to AO and EEPAC TC activity metrics. Statistically significant critical r is $\pm$ 0.329.

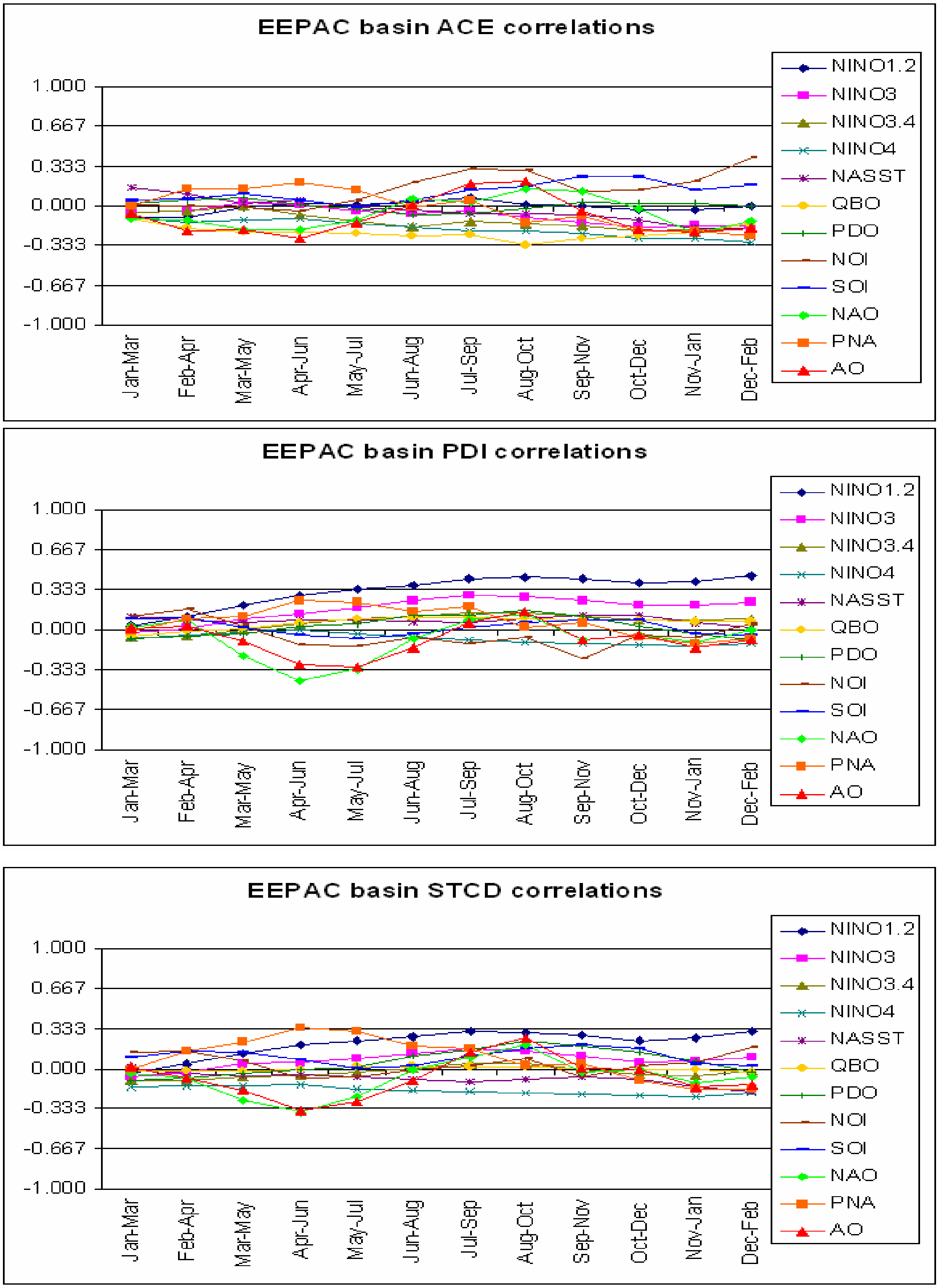

Fig. 3.19: Spearman rank correlation coefficients between climate indices NINO1.2 to AO and EEPAC TC activity metrics. Statistically significant critical *r* is ± 0.329.

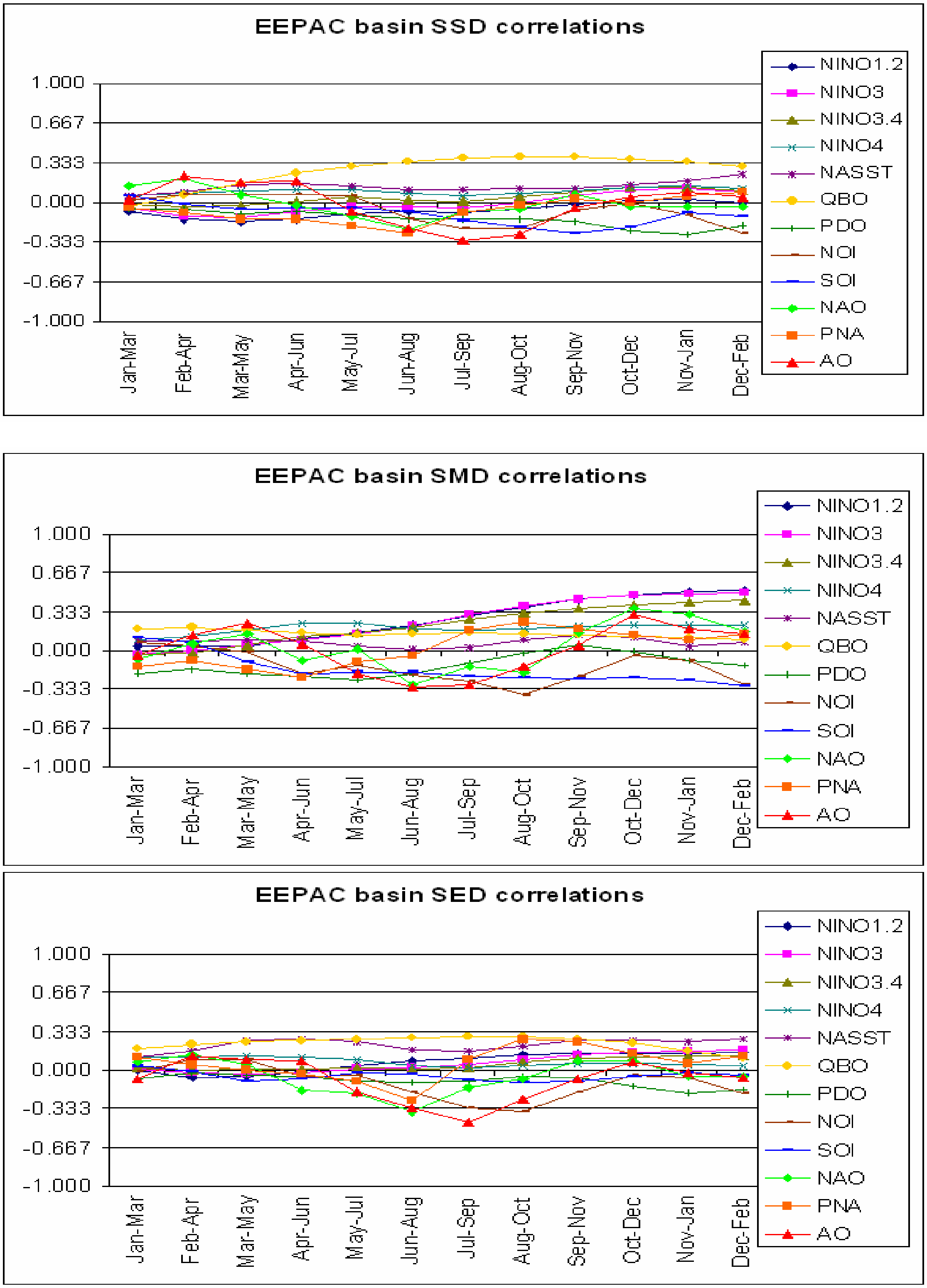

Fig. 3.20: Spearman rank correlation coefficients between climate indices NINO1.2 to AO and EEPAC TC activity metrics. Statistically significant critical *r* is ± 0.329.

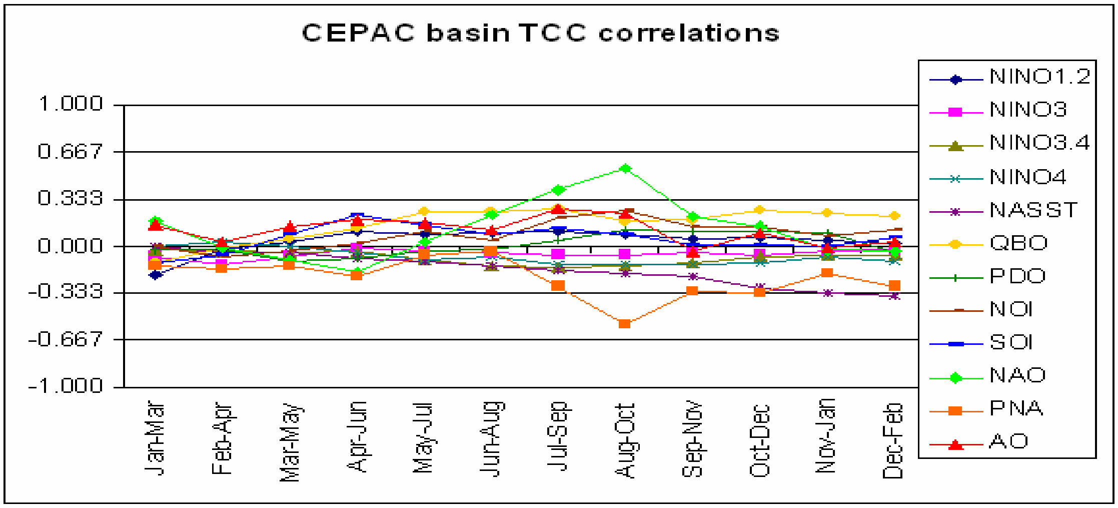

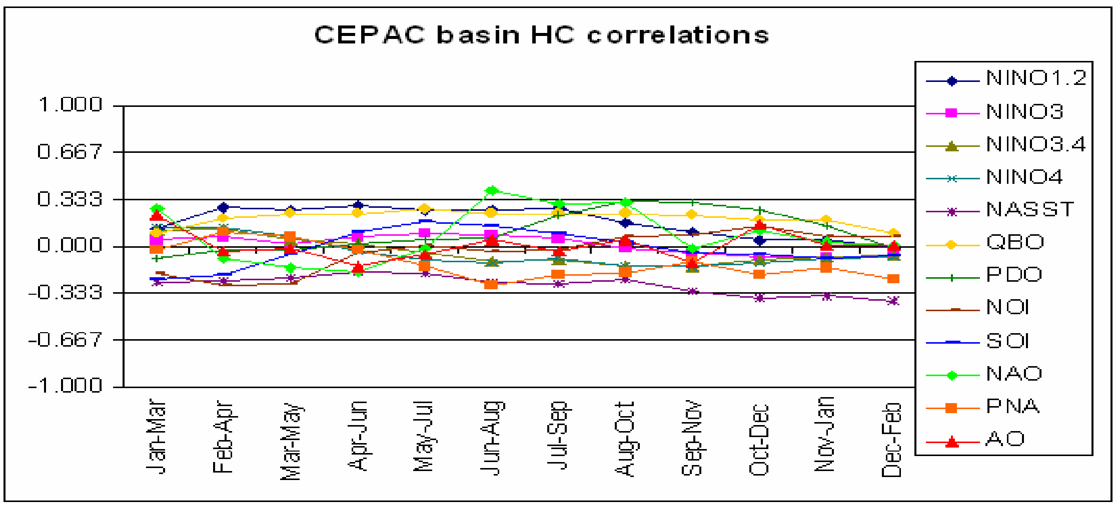

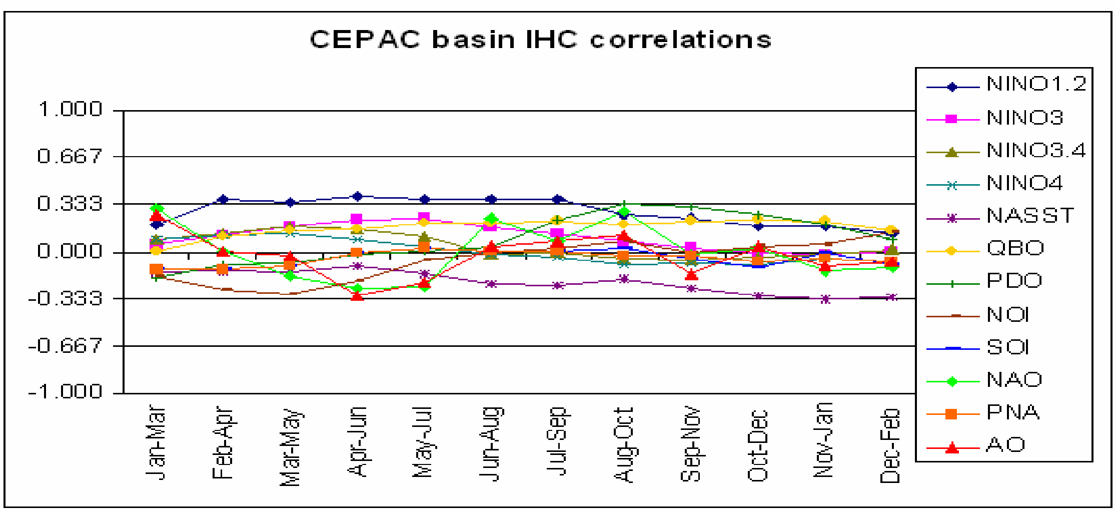

Fig. 3.21: Spearman rank correlation coefficients between climate indices NINO1.2 to AO and CEPAC TC activity metrics. Statistically significant critical r is ± 0.329.

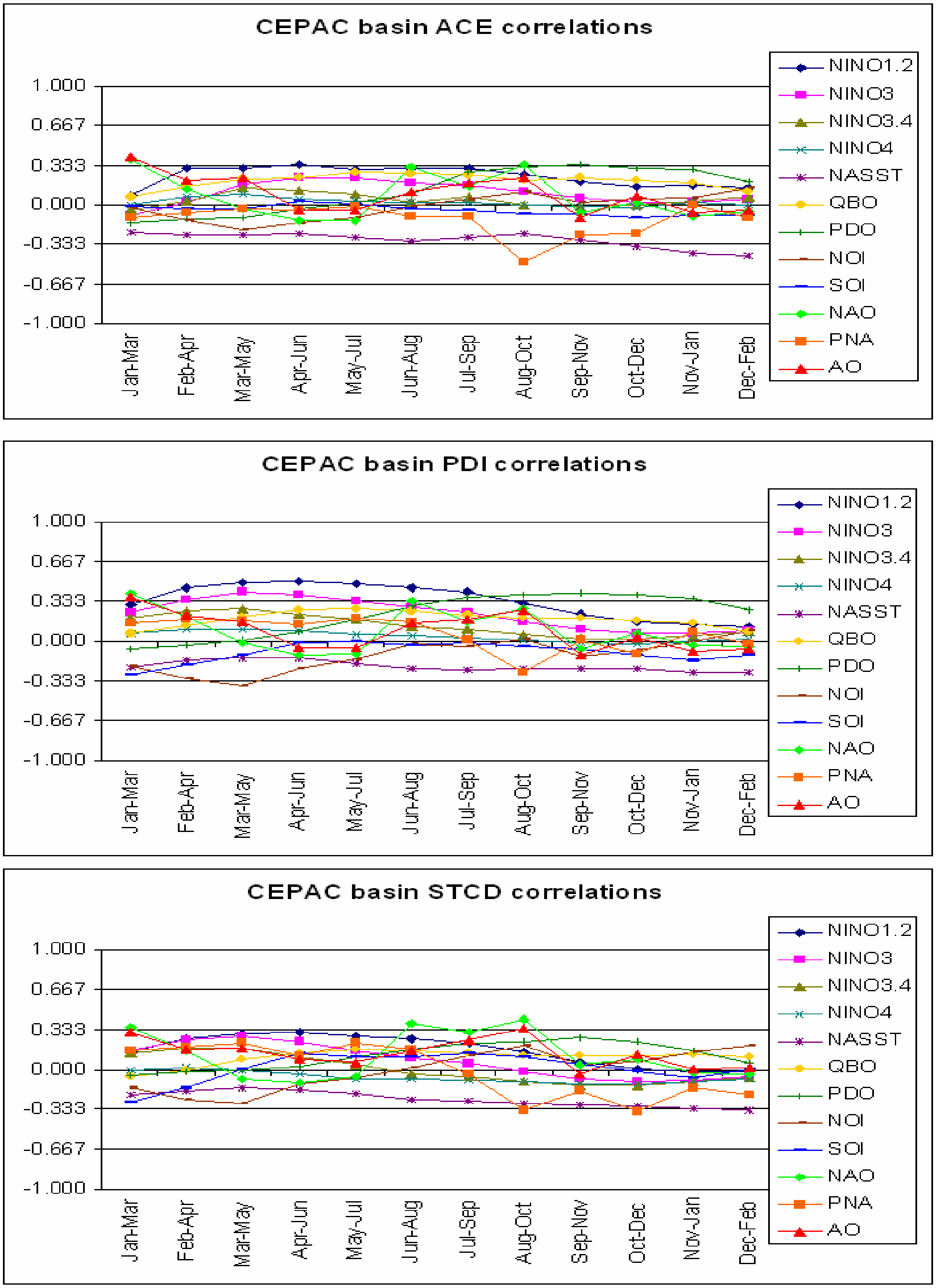

Fig. 3.22: Spearman rank correlation coefficients between climate indices NINO1.2 to AO and CEPAC TC activity metrics. Statistically significant critical r is ± 0.329.

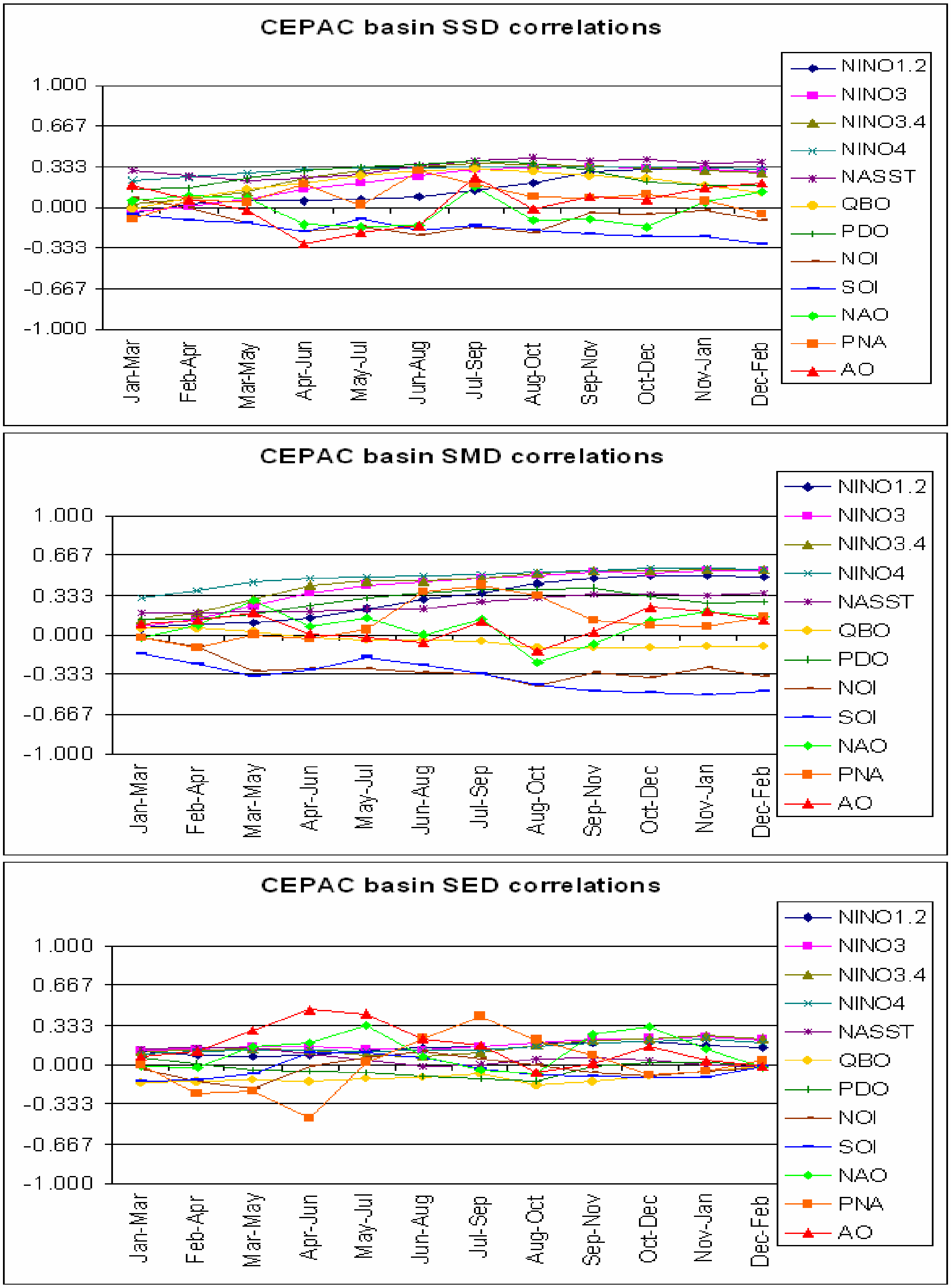

Fig. 3.23: Spearman rank correlation coefficients between climate indices NINO1.2 to AO and CEPAC TC activity metrics. Statistically significant critical r is ± 0.329.

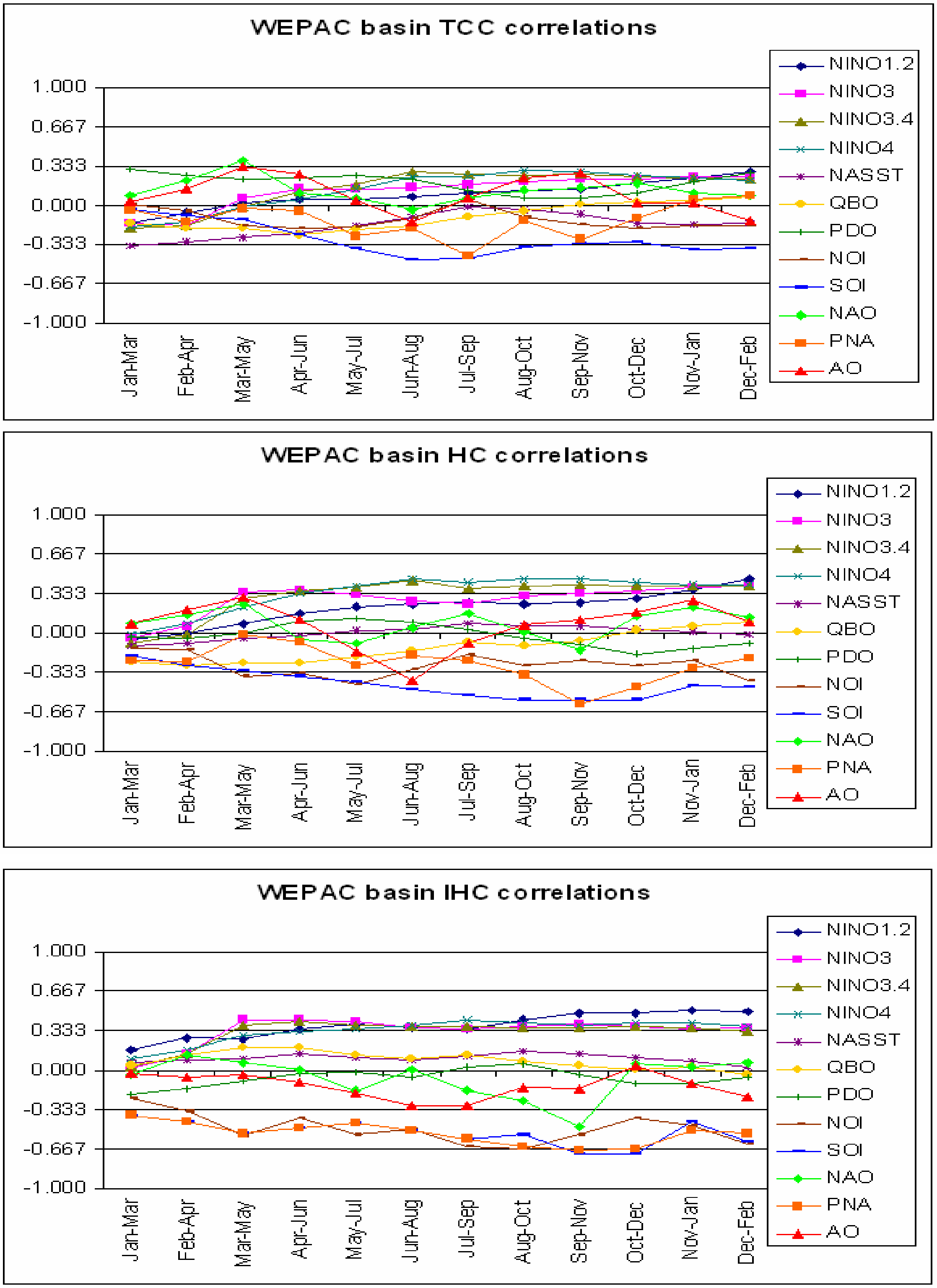

Fig. 3.24: Spearman rank correlation coefficients between climate indices NINO1.2 to AO and WEPAC TC activity metrics. Statistically significant critical *r* is ± 0.329.

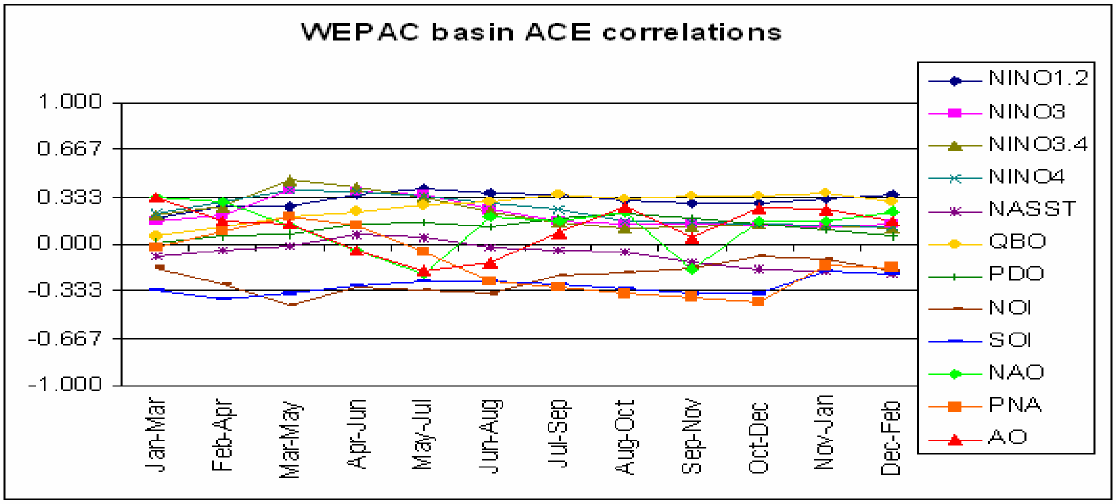

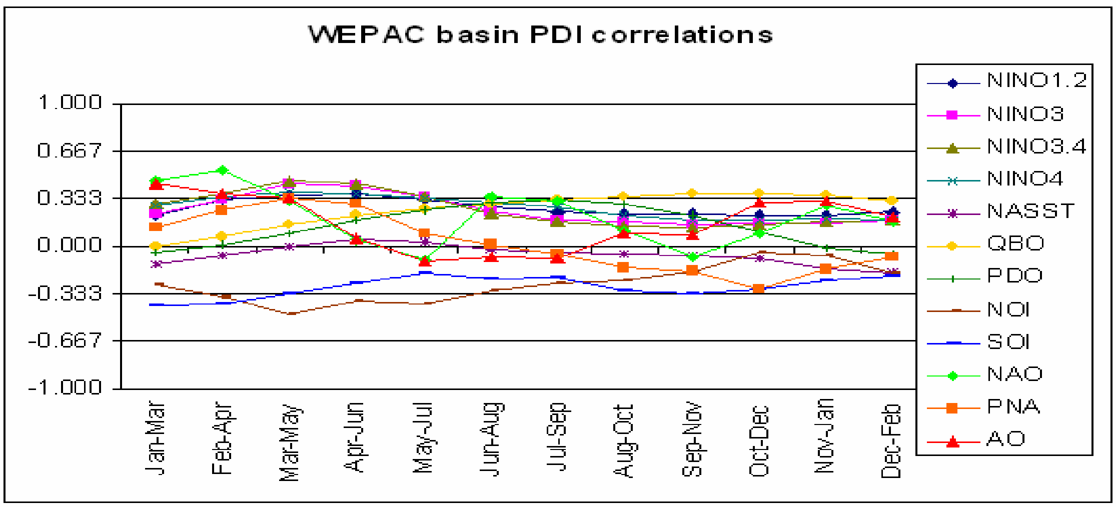

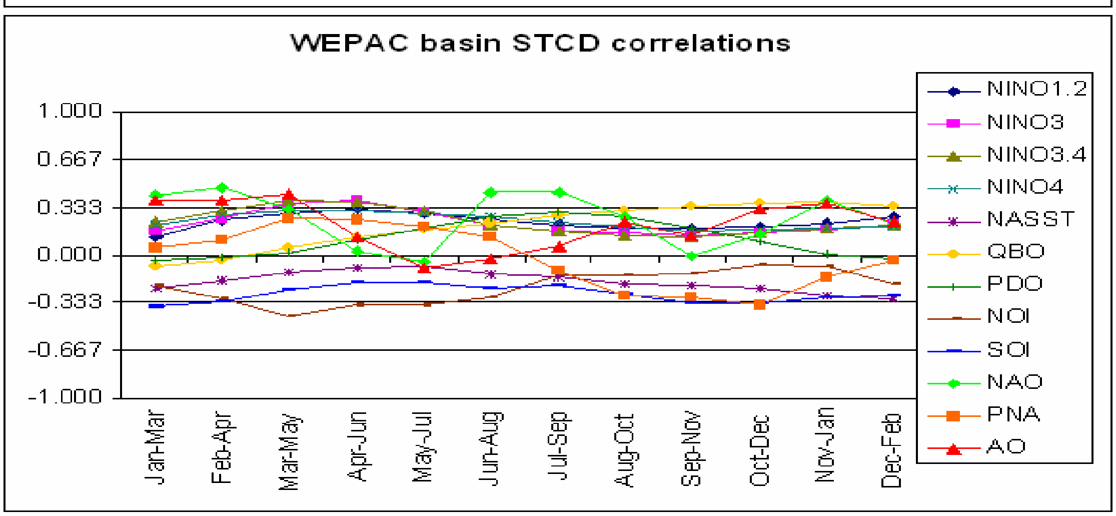

Fig. 3.25: Spearman rank correlation coefficients between climate indices NINO1.2 to AO and WEPAC TC activity metrics. Statistically significant critical *r* is ± 0.329.

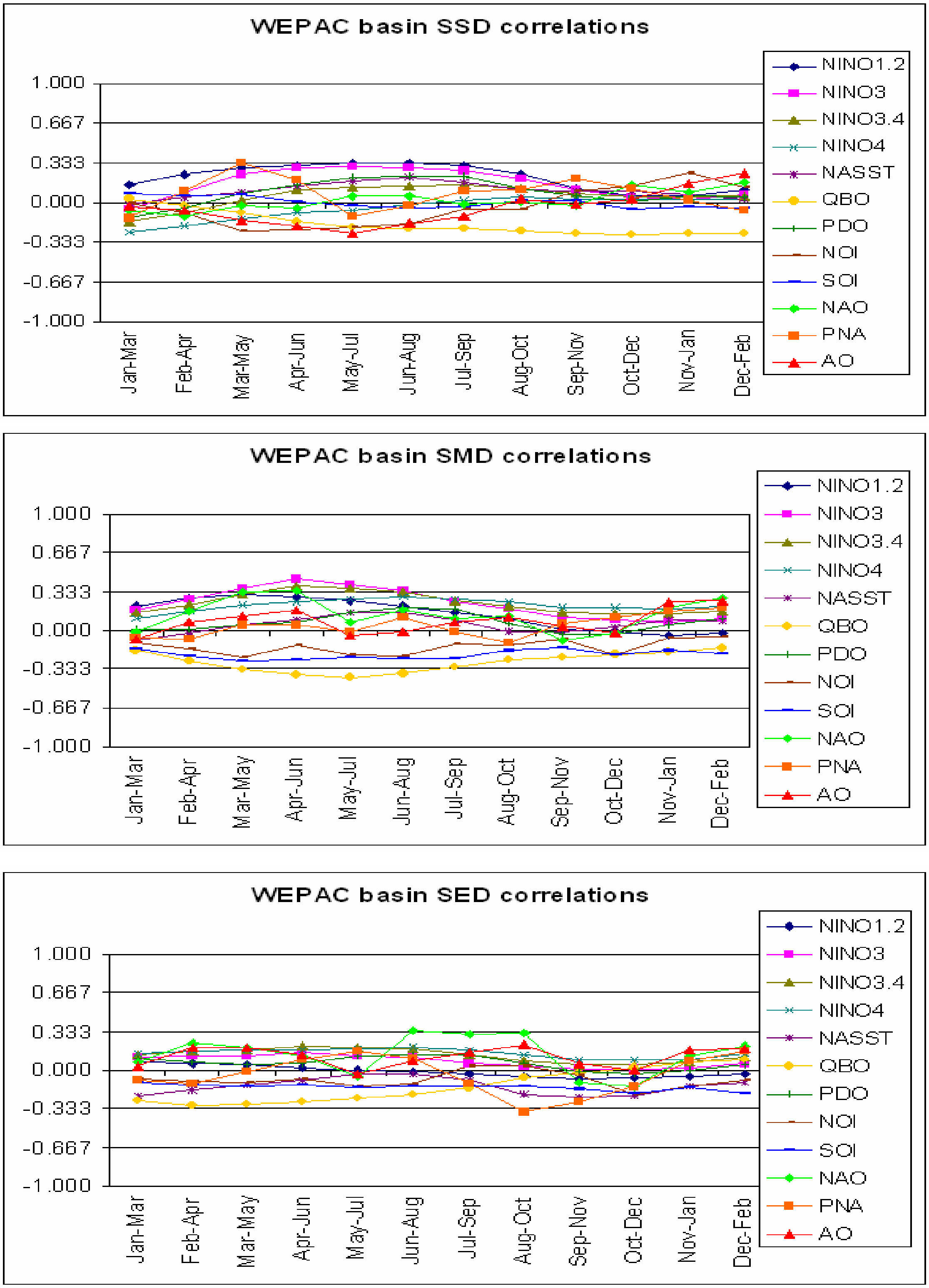

Fig. 3.26: Spearman rank correlation coefficients between climate indices NINO1.2 to AO and WEPAC TC activity metrics. Statistically significant critical *r* is ± 0.329.

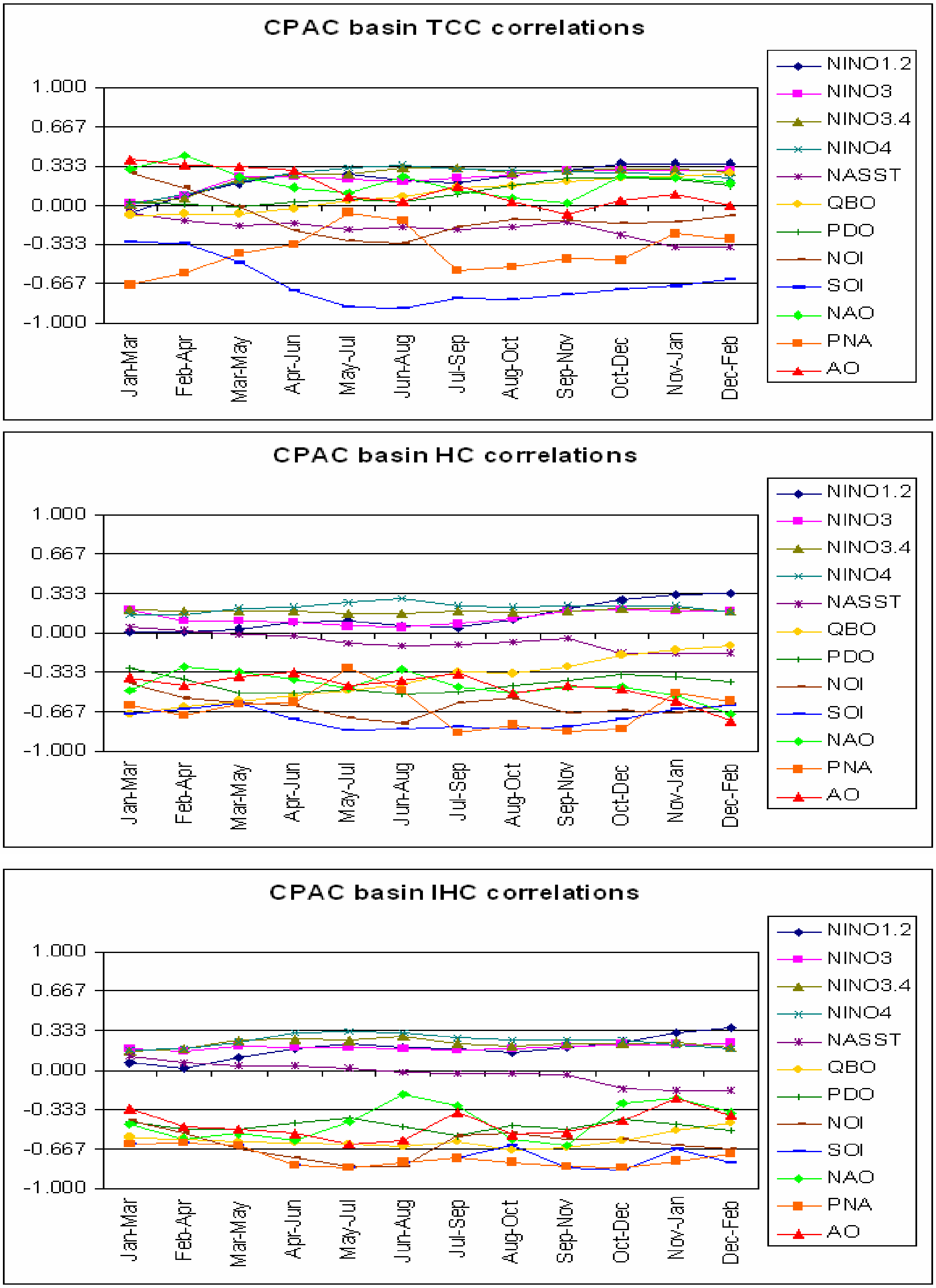

Fig. 3.27: Spearman rank correlation coefficients between climate indices NINO1.2 to AO and CPAC TC activity metrics. Statistically significant critical *r* is ± 0.329.

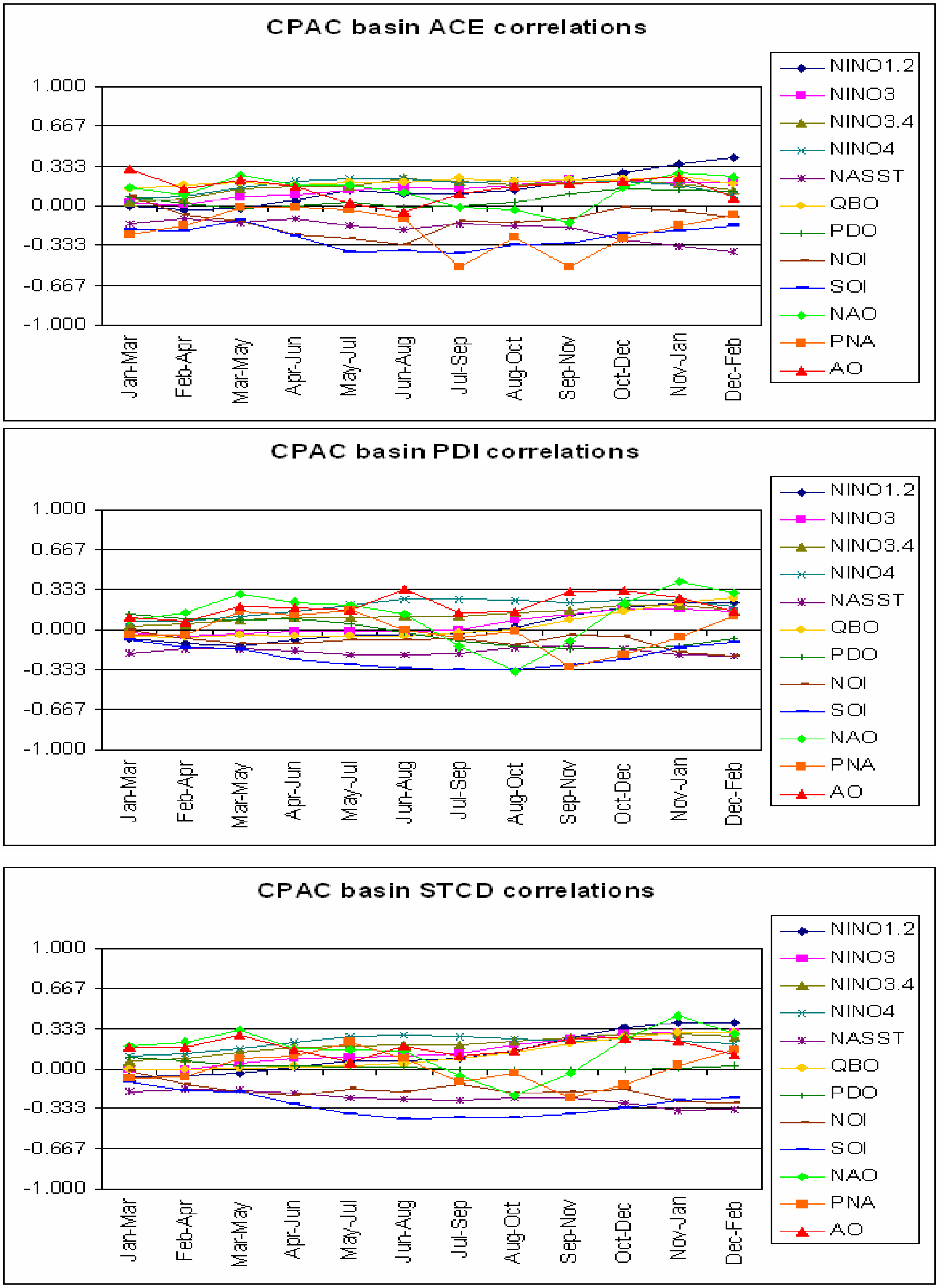

Fig. 3.28: Spearman rank correlation coefficients between climate indices NINO1.2 to AO and CPAC TC activity metrics. Statistically significant critical *r* is ± 0.329.

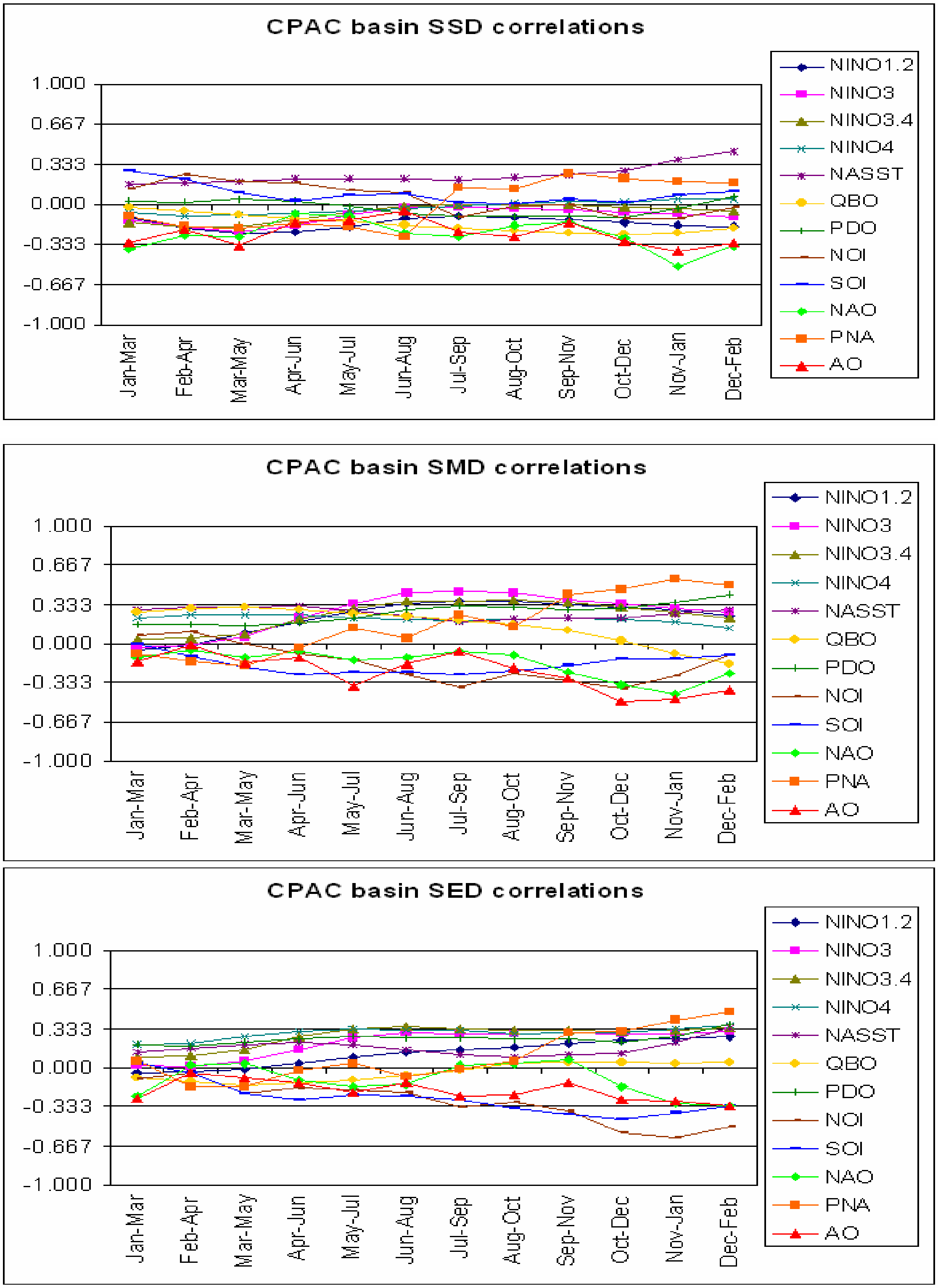

Fig. 3.29: Spearman rank correlation coefficients between climate indices NINO1.2 to AO and CPAC TC activity metrics. Statistically significant critical *r* is ± 0.329.

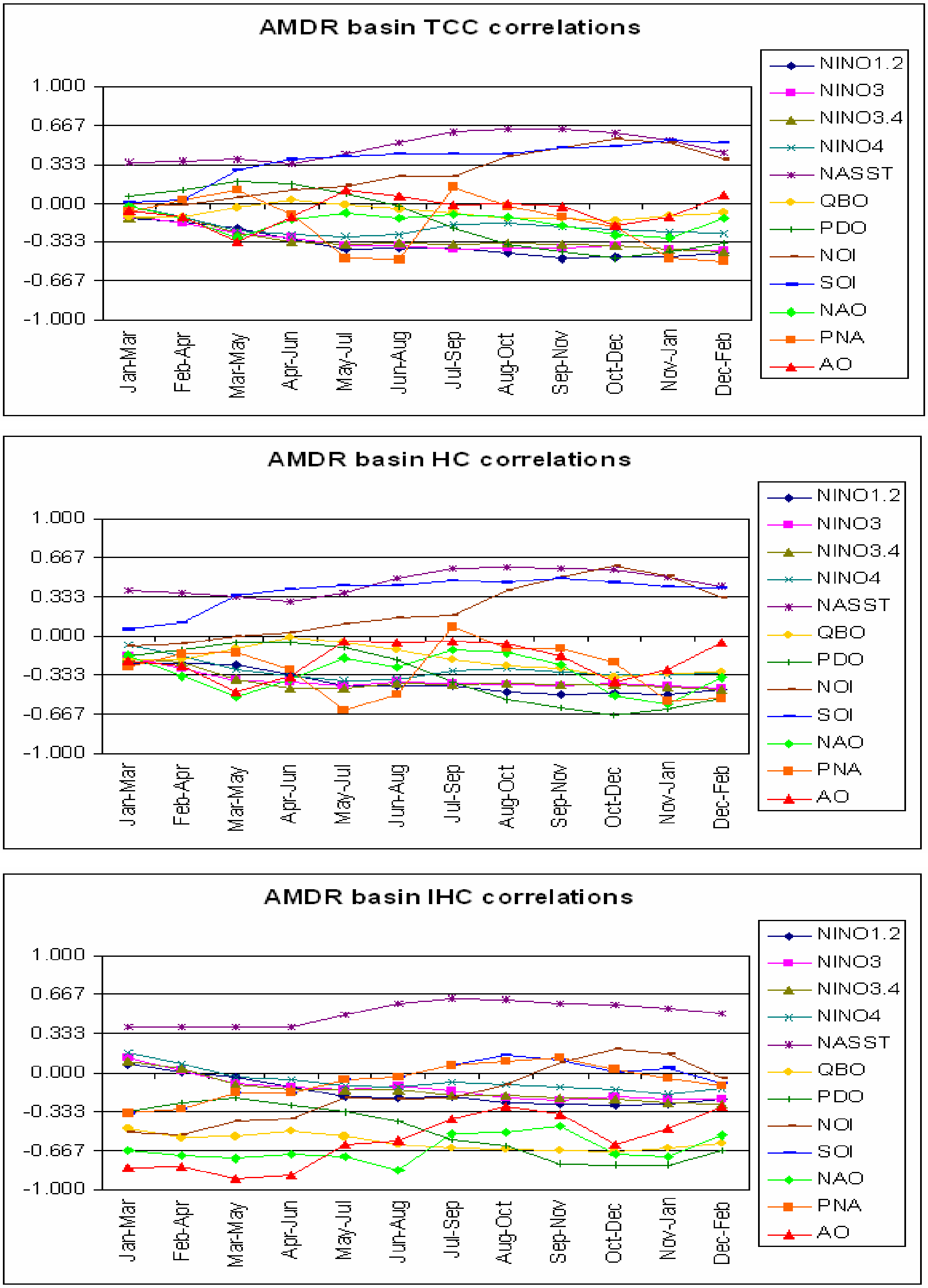

Fig. 3.30: Spearman rank correlation coefficients between climate indices NINO1.2 to AO and AMDR TC activity metrics. Statistically significant critical r is $\pm$ 0.329.

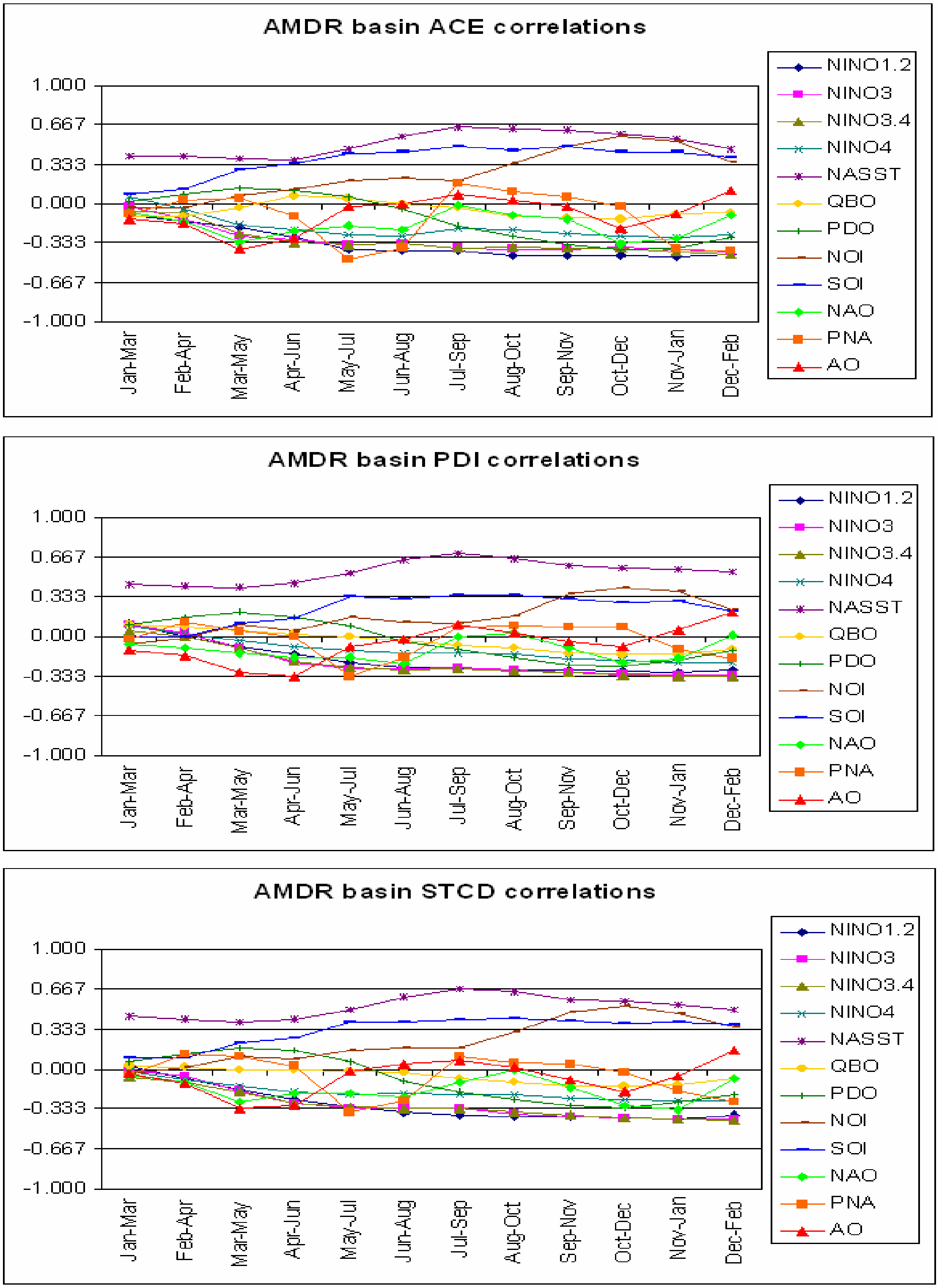

Fig. 3.31: Spearman rank correlation coefficients between climate indices NINO1.2 to AO and AMDR TC activity metrics. Statistically significant critical r is $\pm$ 0.329.

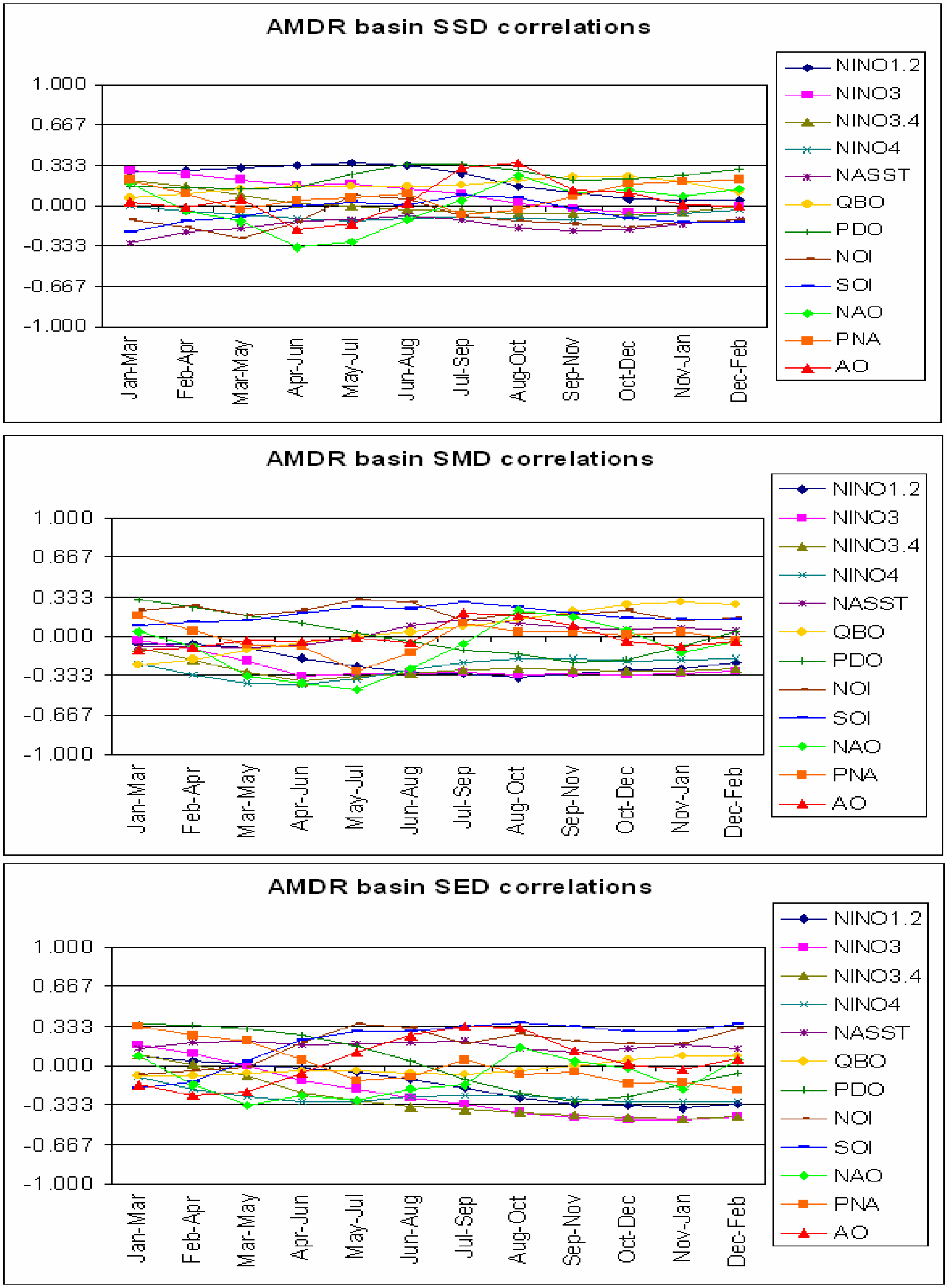

Fig. 3.32: Spearman rank correlation coefficients between climate indices NINO1.2 to AO and AMDR TC activity metrics. Statistically significant critical r is $\pm$ 0.329.

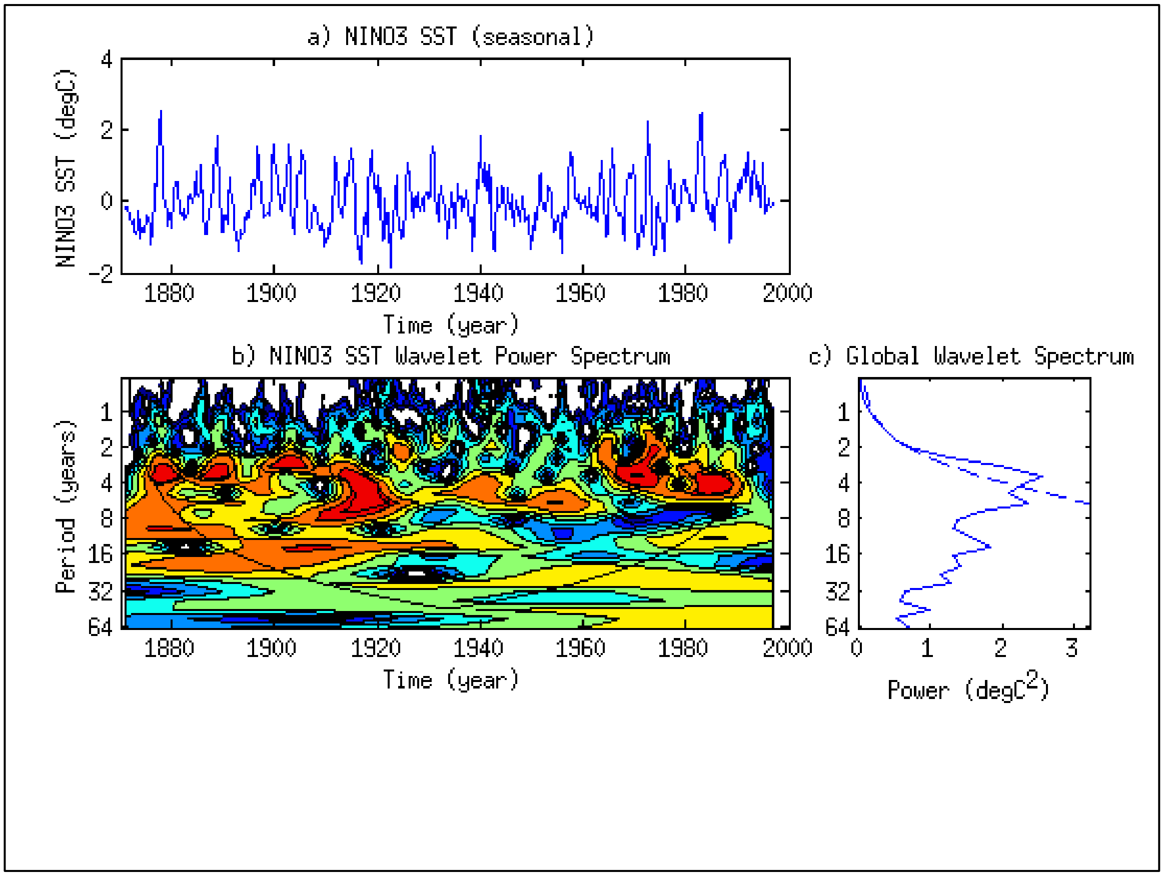

Fig. 3.33: Wavelet analysis of NINO3 SST data (a) showing peaks in the power spectrum, (b) and (c), on the timescales of the leading atmospheric modes.

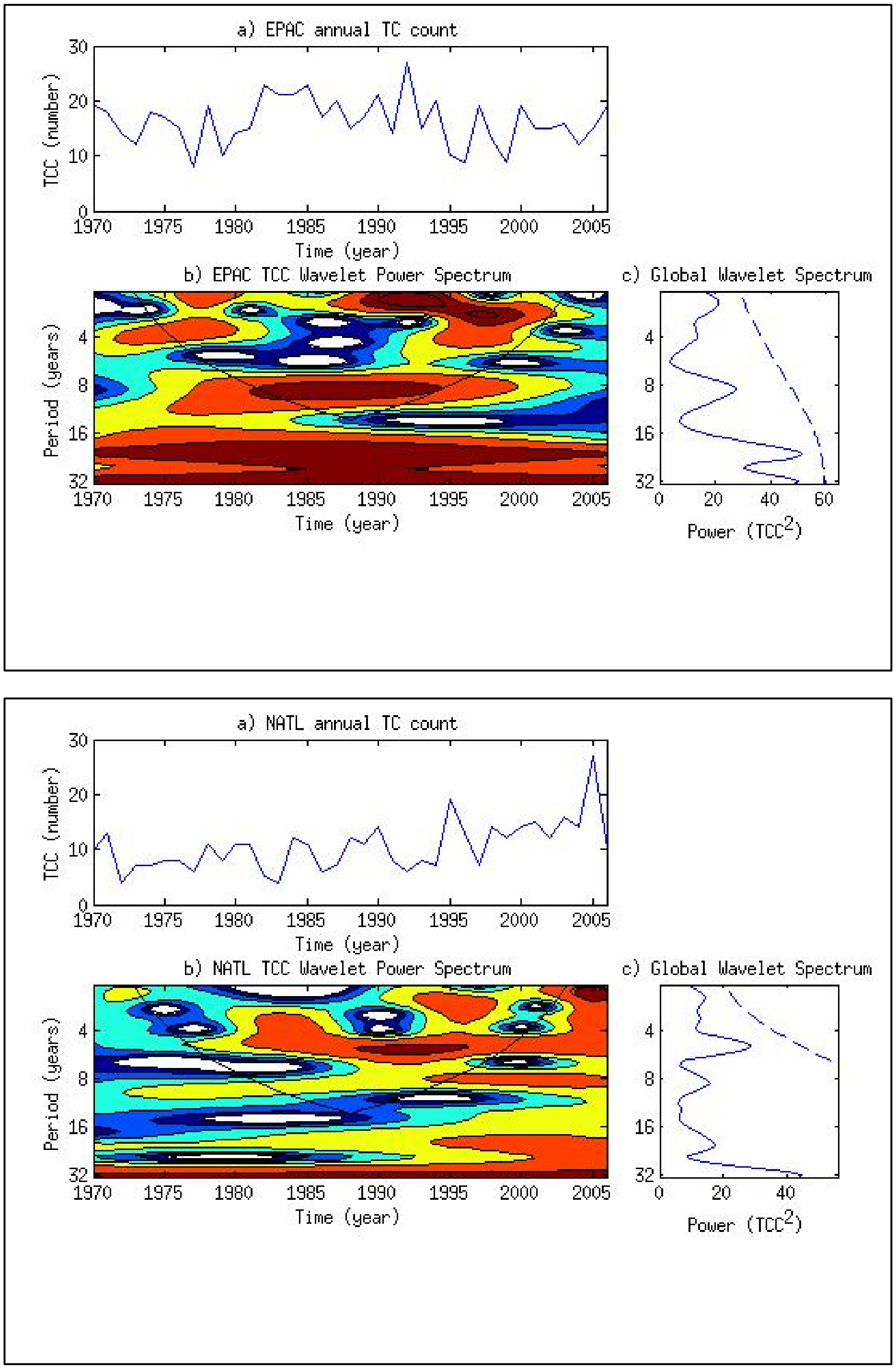

Fig. 3.34: Wavelet analysis of TCC showing peaks in the power spectrum on the timescales of the leading atmospheric modes.

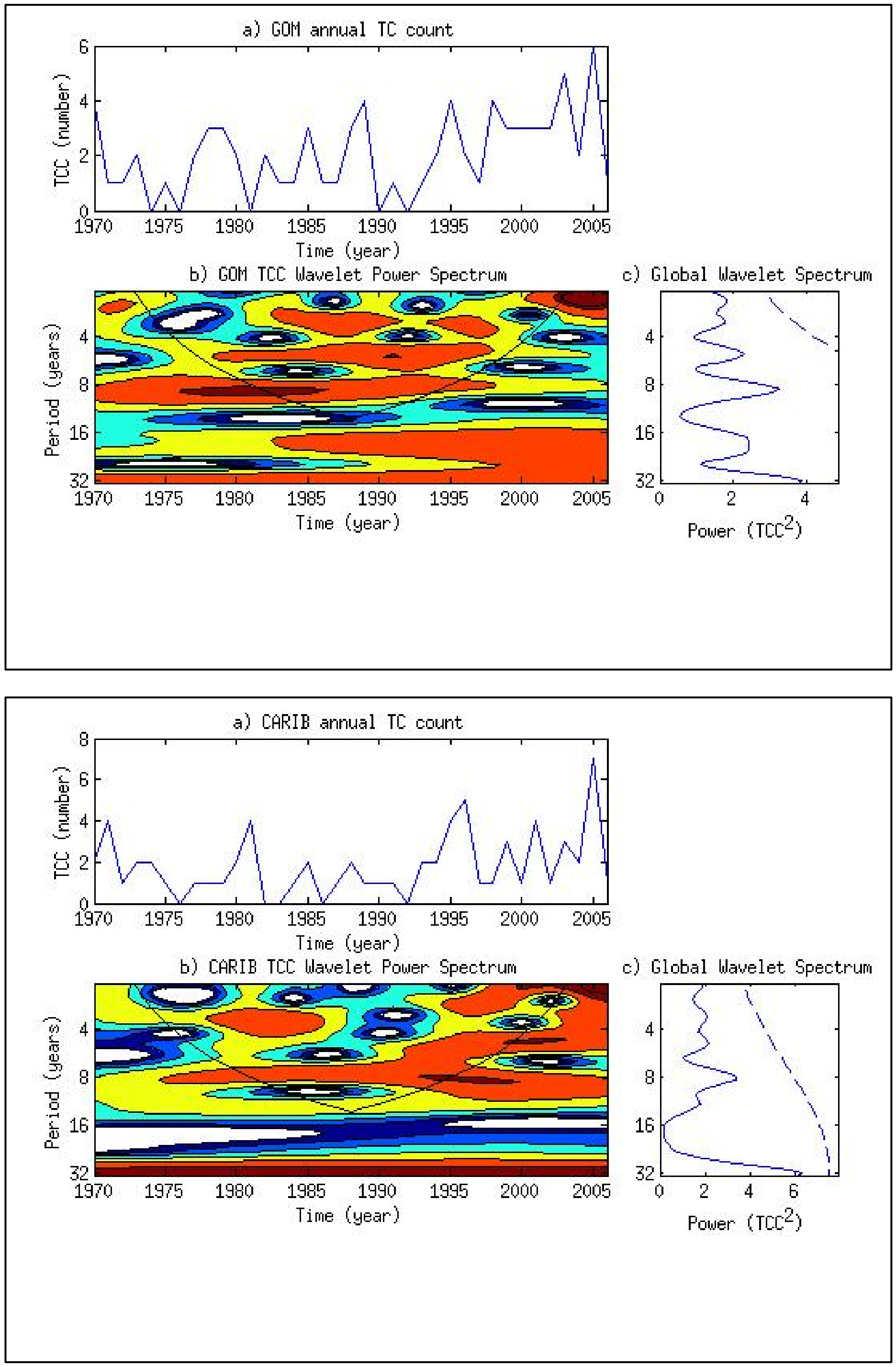

Fig. 3.35: Wavelet analysis of TCC showing peaks in the power spectrum on the timescales of the leading atmospheric modes.

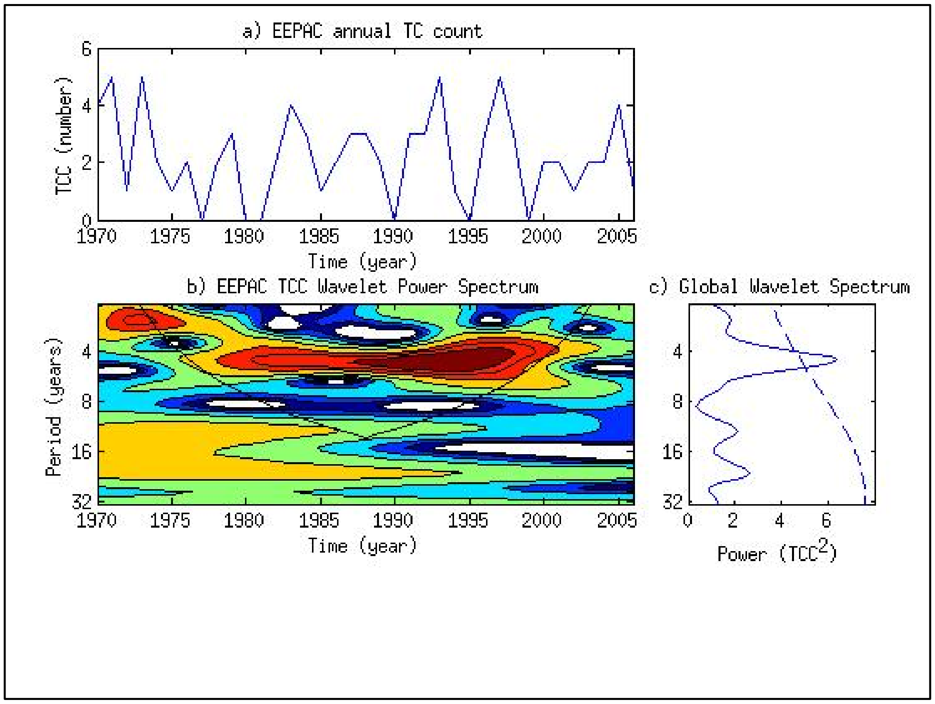

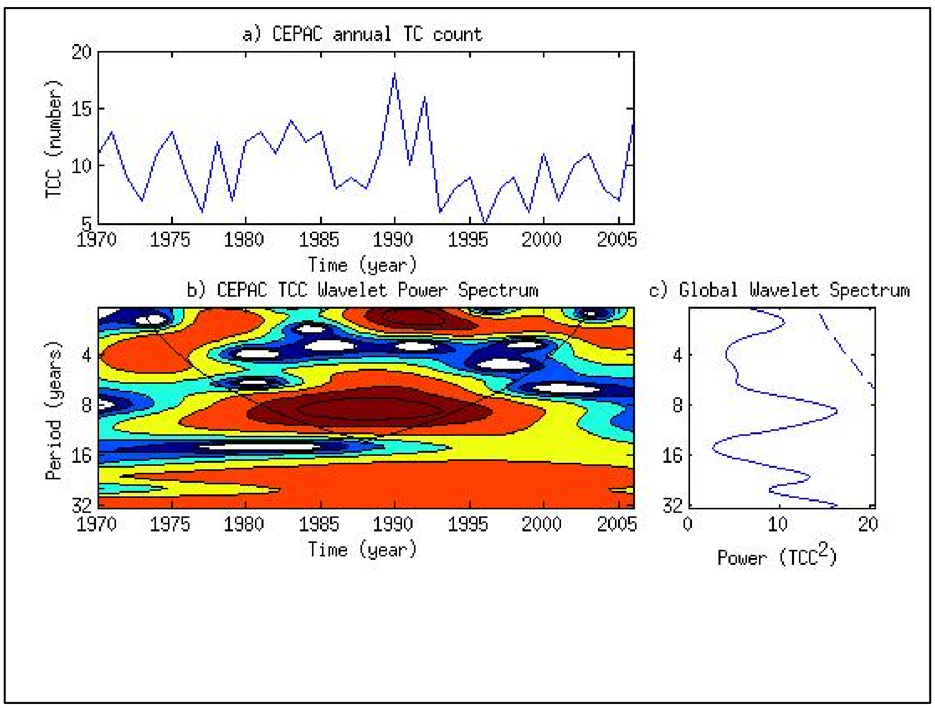

Fig. 3.36: Wavelet analysis of TCC showing peaks in the power spectrum on the timescales of the leading atmospheric modes.

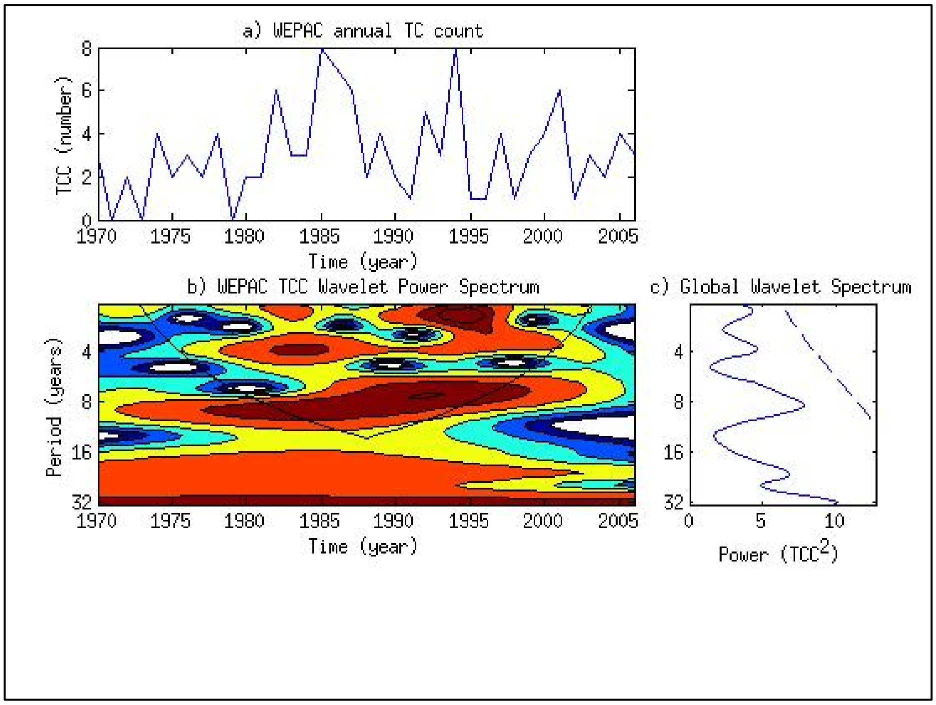

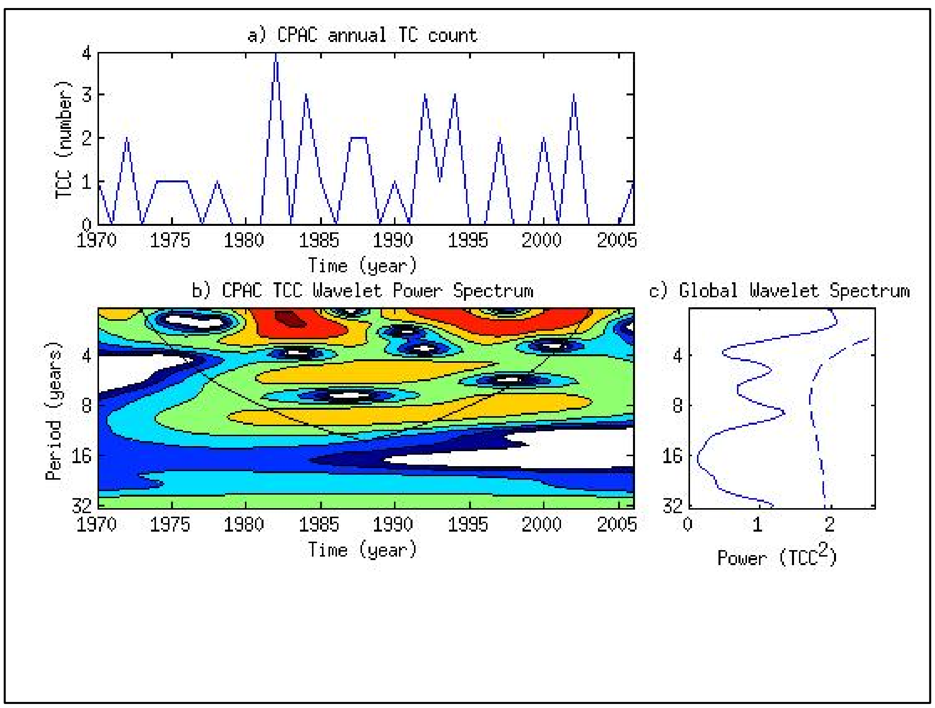

Fig. 3.37: Wavelet analysis of TCC showing peaks in the power spectrum on the timescales of the leading atmospheric modes.

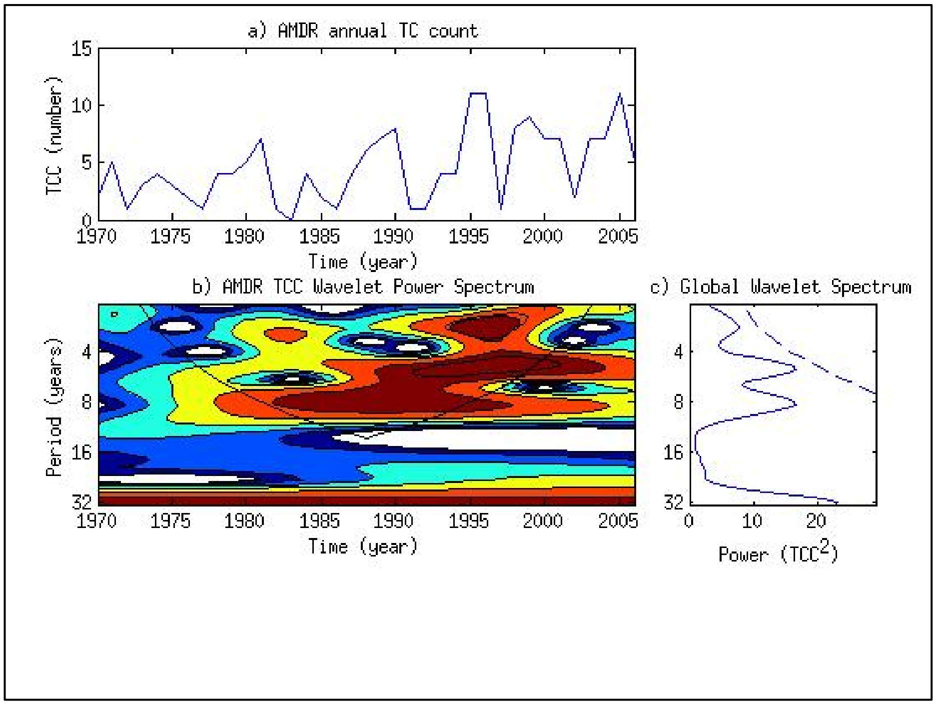

Fig. 3.38: Wavelet analysis of TCC showing peaks in the power spectrum on the timescales of the leading atmospheric modes.

Fig. 4.1 (MJ72, Figure 16): Schematic depiction of the time and space (zonal plane) variations of the disturbance associated with the 40—50-day oscillation. Dates are indicated symbolically by the letters at the left of each chart and correspond to dates associated with the oscillation in Canton's station pressure. The mean pressure disturbance is plotted at the bottom of each chart with negative anomalies shaded. The circulation cells are based on the mean zonal wind disturbance. Regions of enhanced large-scale convection are indicated schematically by the cumulus and cumulonimbus clouds. The relative tropopause height is indicated at the top of each chart.

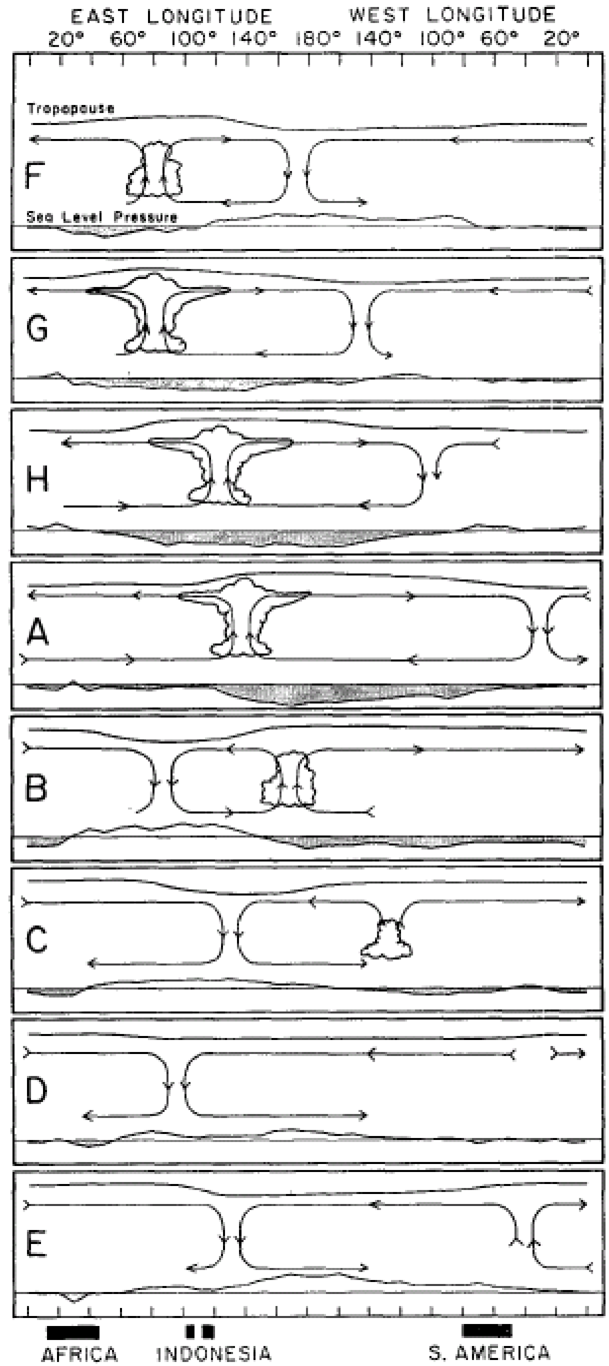

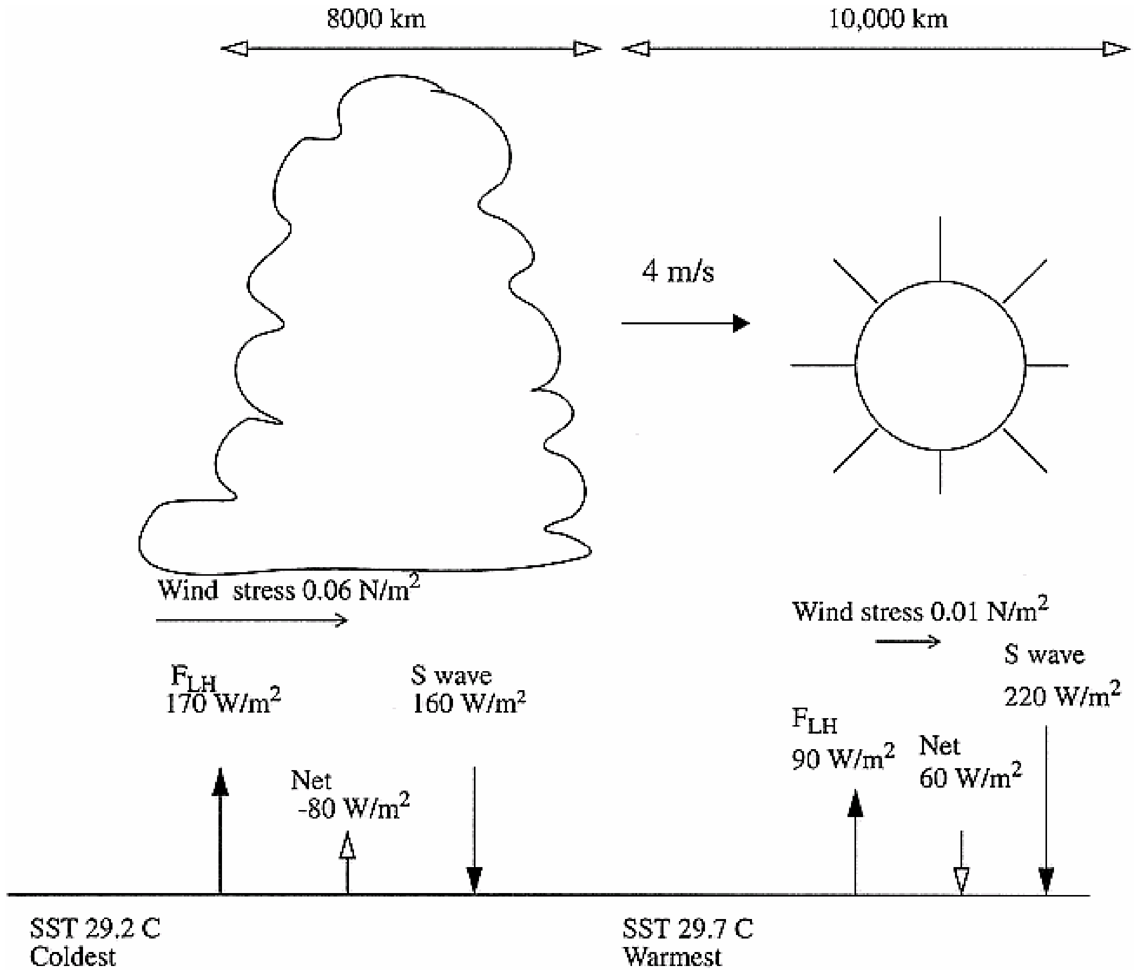

Fig. 4.2 (from Figure 14, Shinoda et al. 1998): Schematic diagram showing magnitude and phase relationship relative to the convective anomaly of the surface fluxes and SST variations produced by the canonical MJO. The asymmetric zonal scale of the cloudy-windy and suppressed-calm phases and eastward phase speed (4 m s^{-1}) of the joint atmosphere–ocean disturbance across the warm pool are indicated. Typical extrema of surface fluxes and SST over life cycle of MJO are shown for western Pacific.

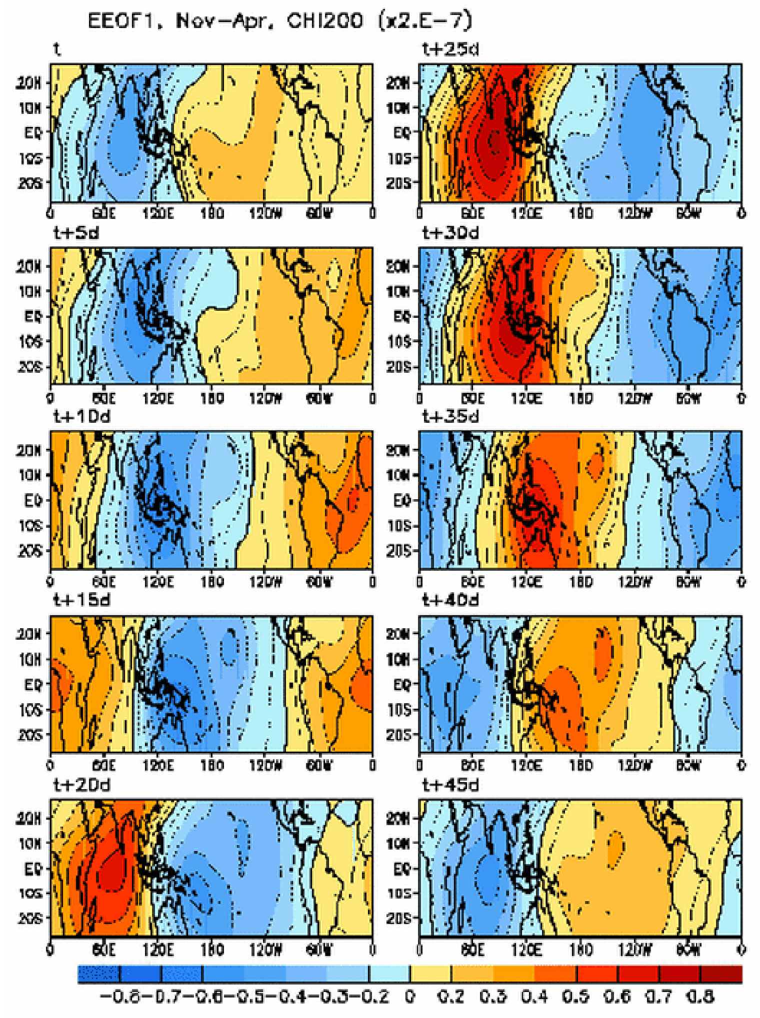

Fig. 4.3 (from Xue et al. 2002): The ten MJO patterns of the first empirical orthogonal function of 200 hPa velocity potential. Time t=0 days is in the upper-left, and time progresses every five days, to time t=20 days in lower-left, time t=25 days in upper-right, and time t=45 days in lower-right. Shading represents correlation between the empirical orthogonal function and 200 hPa velocity potential. Positive correlations (orange and red shading) correspond to suppressed convective activity; negative correlations (blue shading) correspond to enhance convective activity.

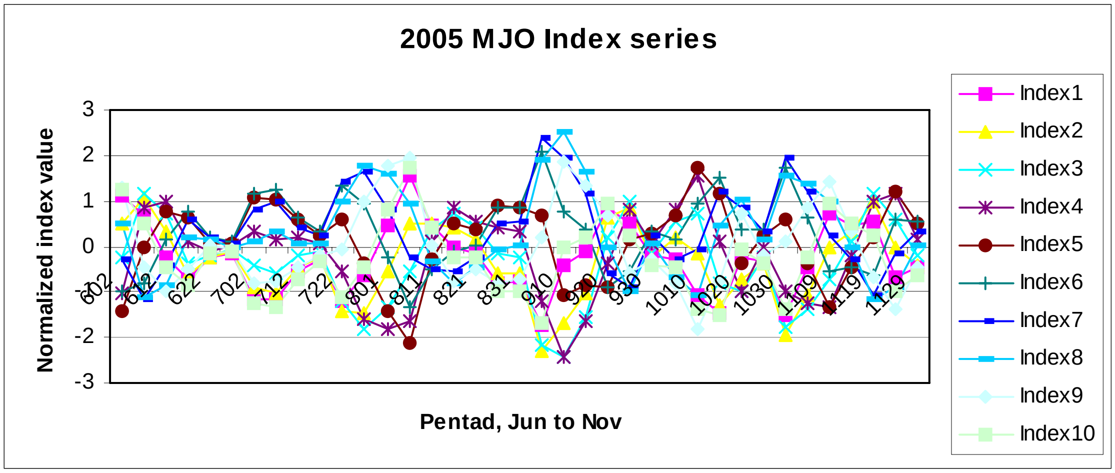

Figure 4.4: Time series of the 10 MJO Indices, with pentad data from 02 June to 29 November 2005.

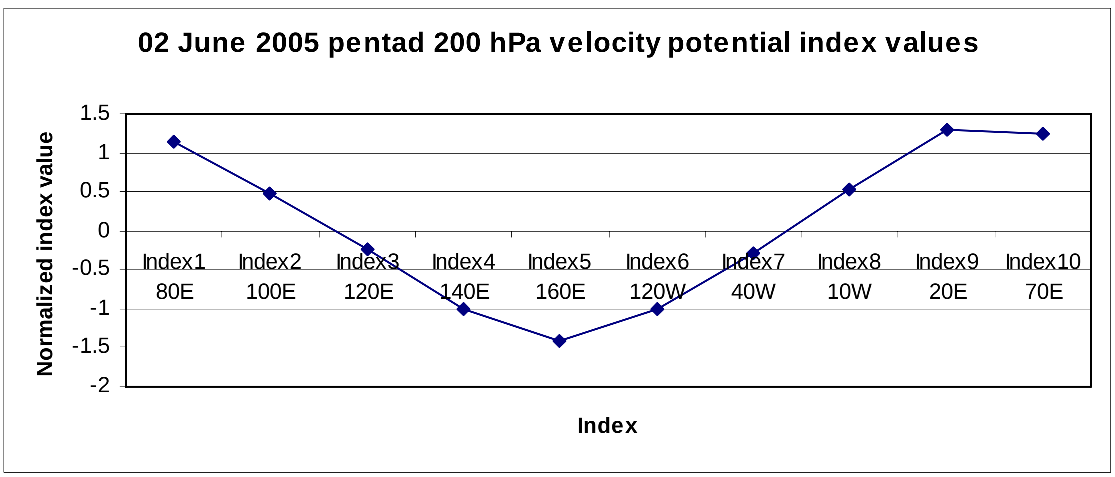

Figure 4.5: One pentad (02 June 2005) of the 10 MJO Indexes (derived from velocity potential anomalies). The zonal wavenumber one oscillation is easily noticeable.

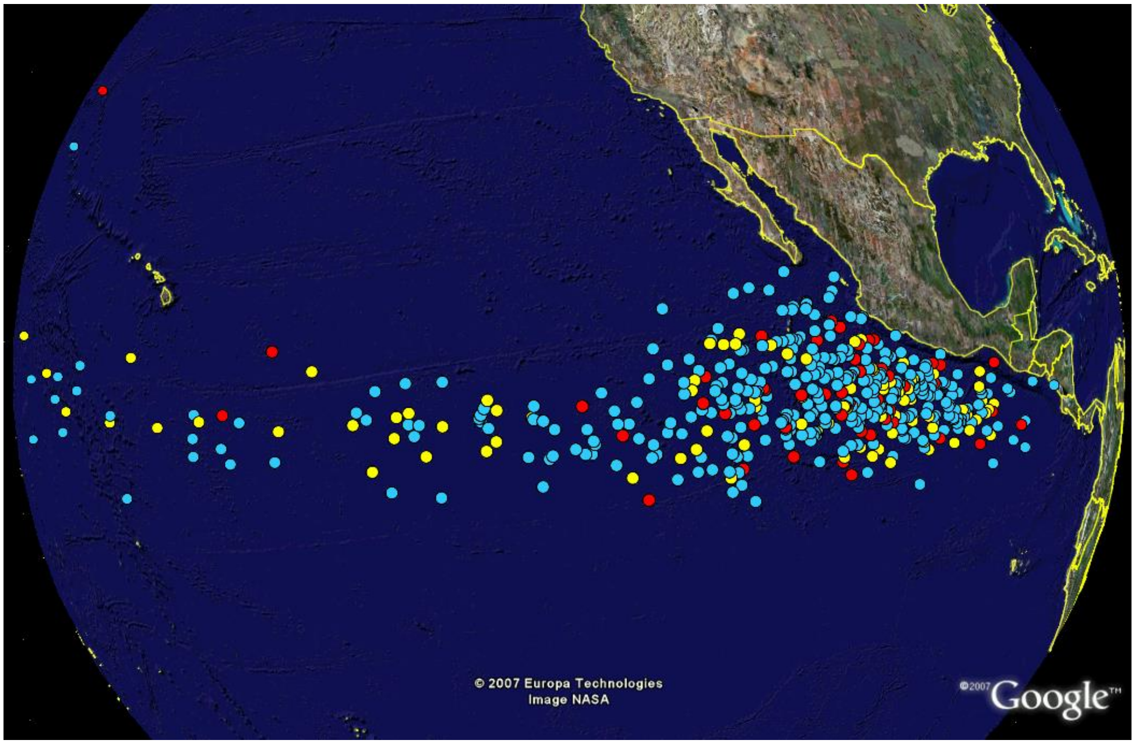

Fig. 4.6: All EPAC TC genesis points, 1978-2006, stratified by phase of MJO Index 6: yellow, cyan, and red correspond with ENH, NEU, and SUP phases, respectively.

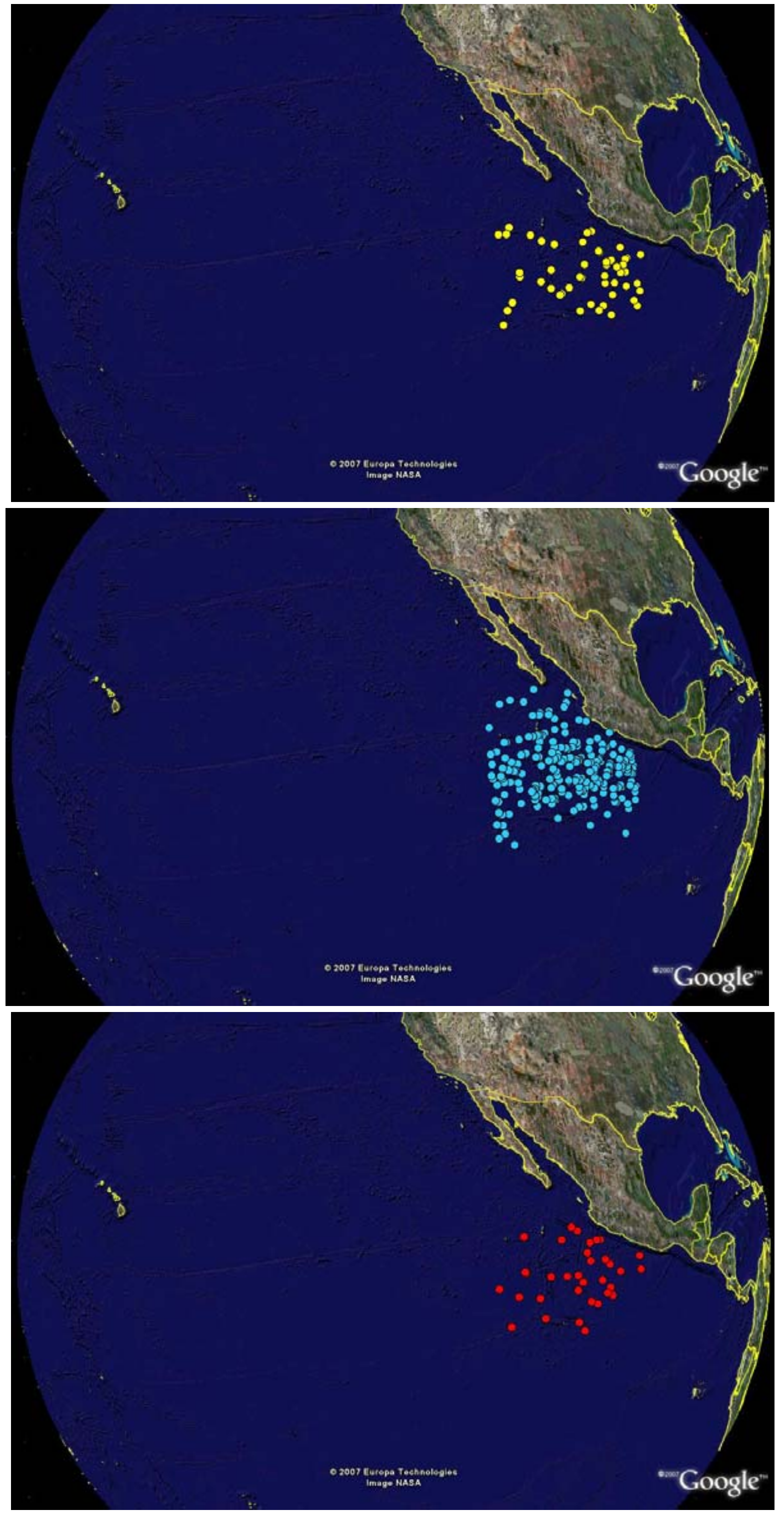

Fig. 4.7: All CEPAC TC genesis points, 1978-2006, stratified by phase of MJO Index 6: yellow, cyan, and red correspond with ENH, NEU, and SUP phases, respectively.

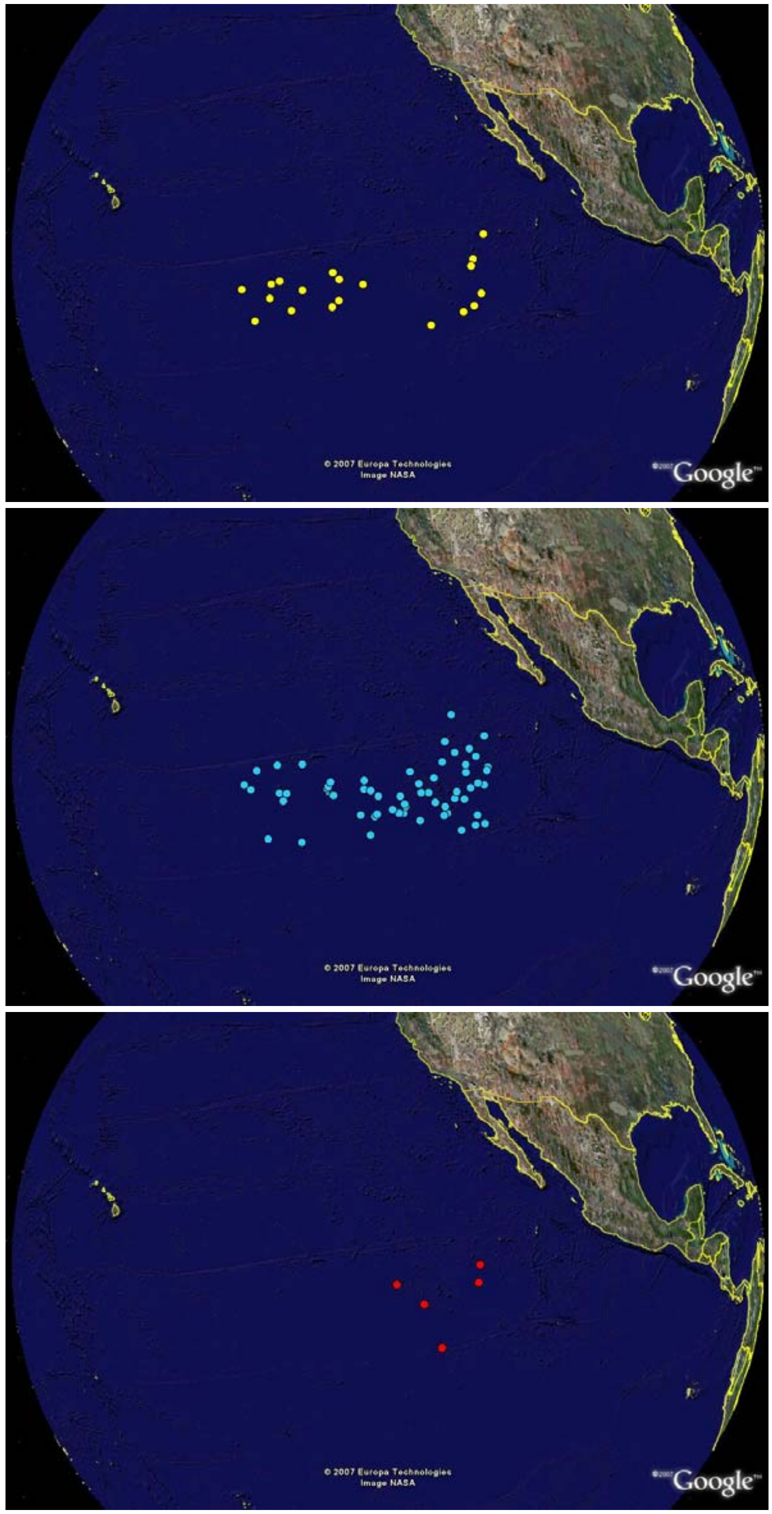

Fig. 4.8: All WEPAC TC genesis points, 1978-2006, stratified by phase of MJO Index 6: yellow, cyan, and red correspond with ENH, NEU, and SUP phases, respectively.

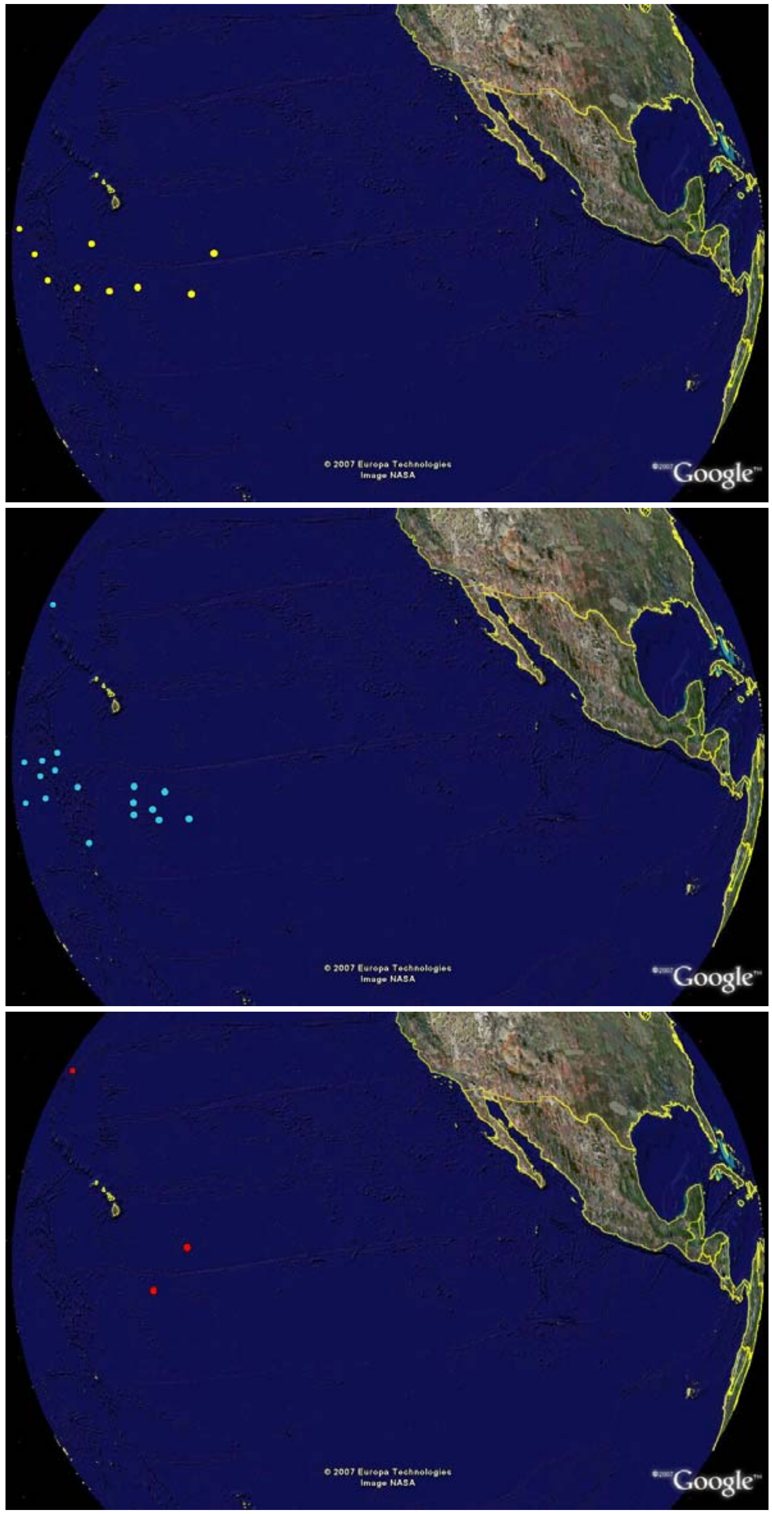

Fig. 4.9: All CPAC TC genesis points, 1978-2006, stratified by phase of MJO Index 6: yellow, cyan, and red correspond with ENH, NEU, and SUP phases, respectively.

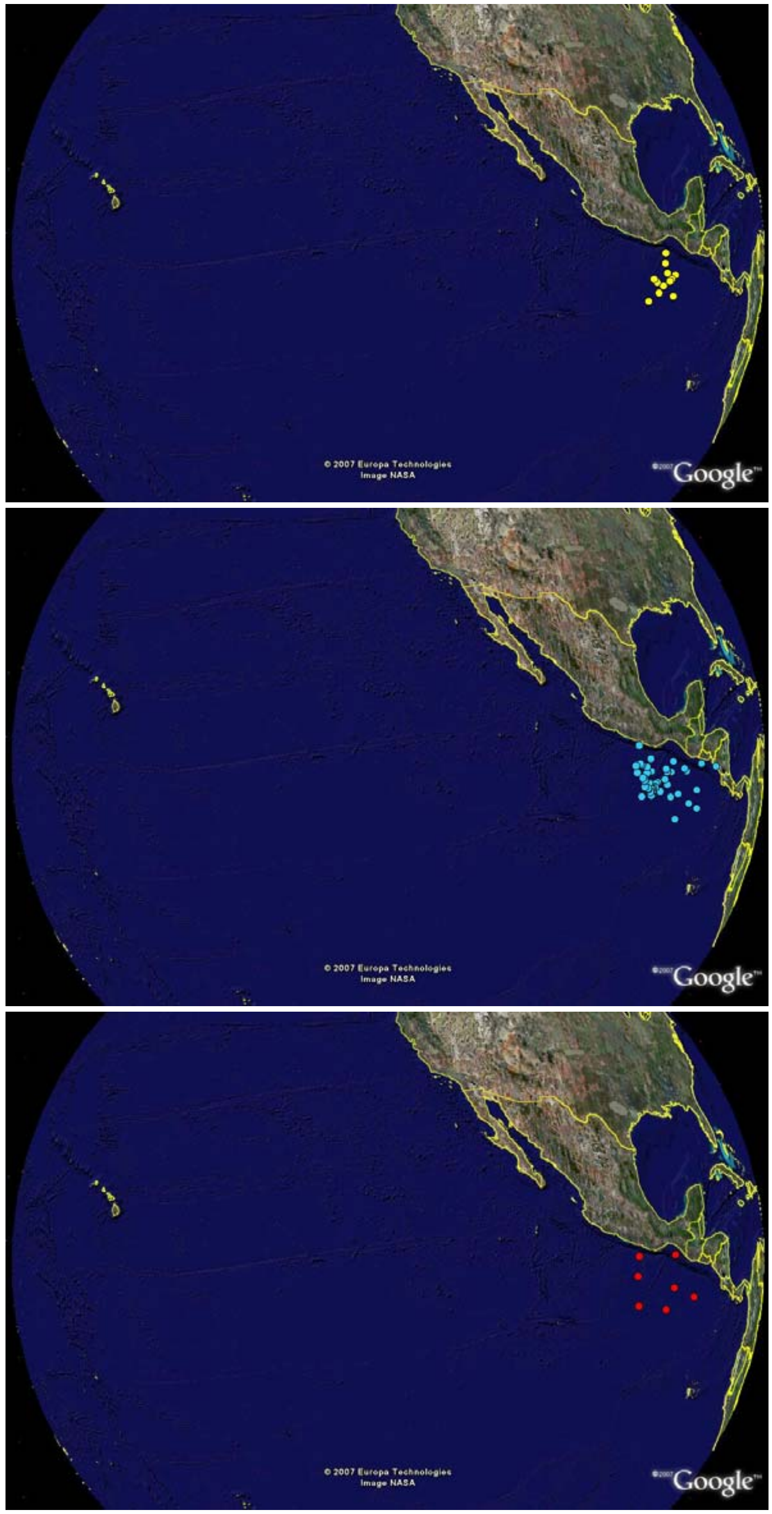

Fig. 4.10: All EEPAC TC genesis points, 1978-2006, stratified by phase of MJO Index 6: yellow, cyan, and red correspond with ENH, NEU, and SUP phases, respectively.

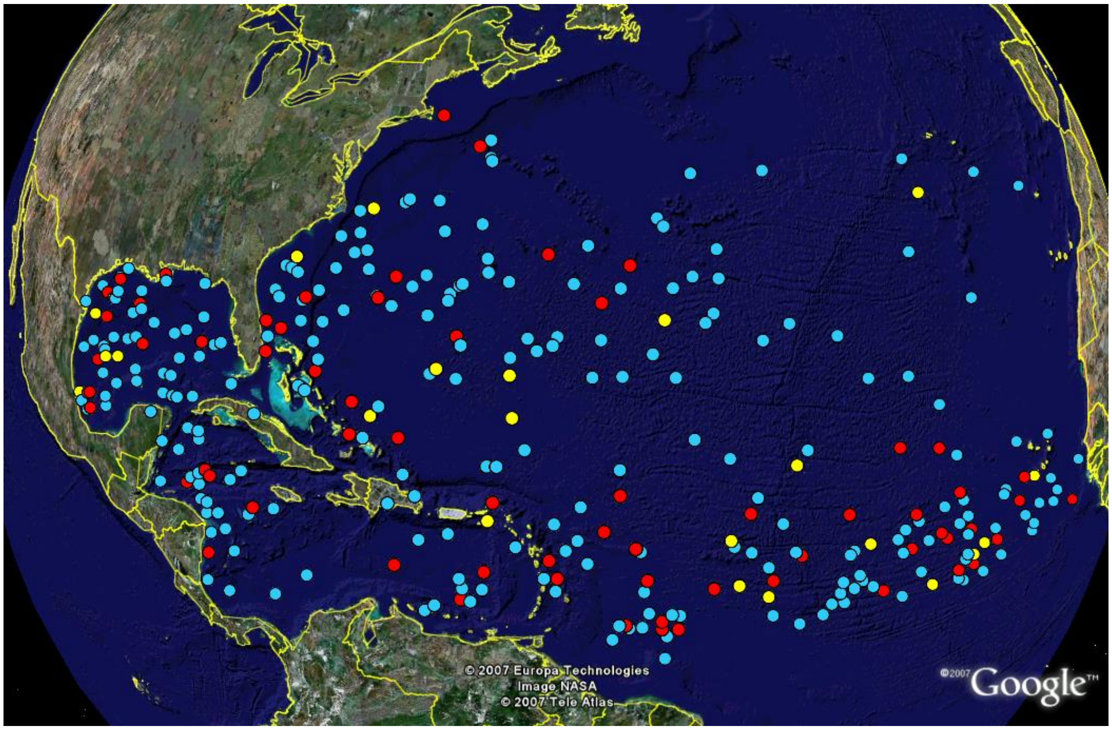

Fig. 4.11: All NATL TC genesis points, 1978-2006, stratified by phase of MJO Index 6: yellow, cyan, and red correspond with ENH, NEU, and SUP phases, respectively.

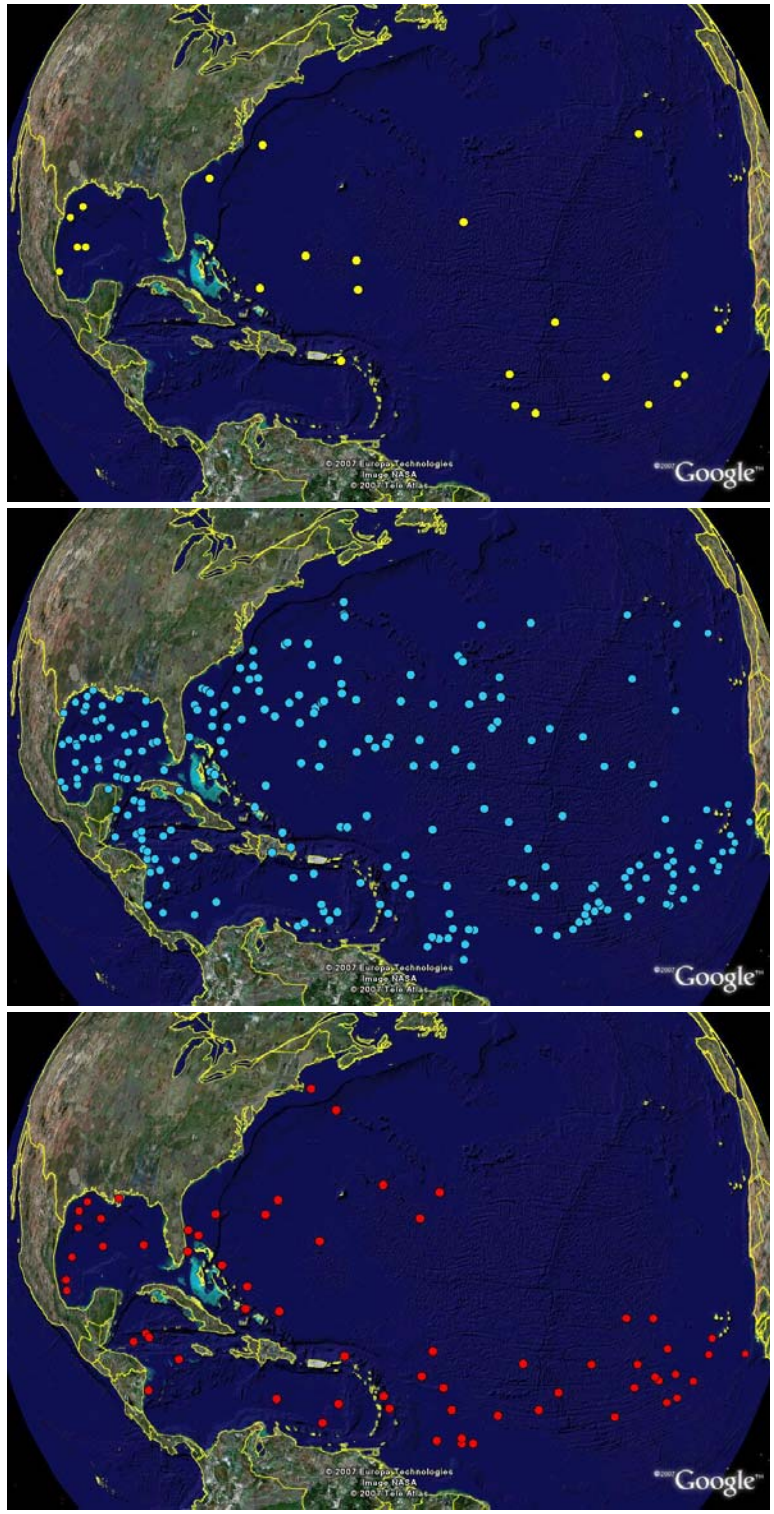

Fig. 4.12: All NATL TC genesis points, 1978-2006, stratified by phase of MJO Index 6: yellow, cyan, and red correspond with ENH, NEU, and SUP phases, respectively.

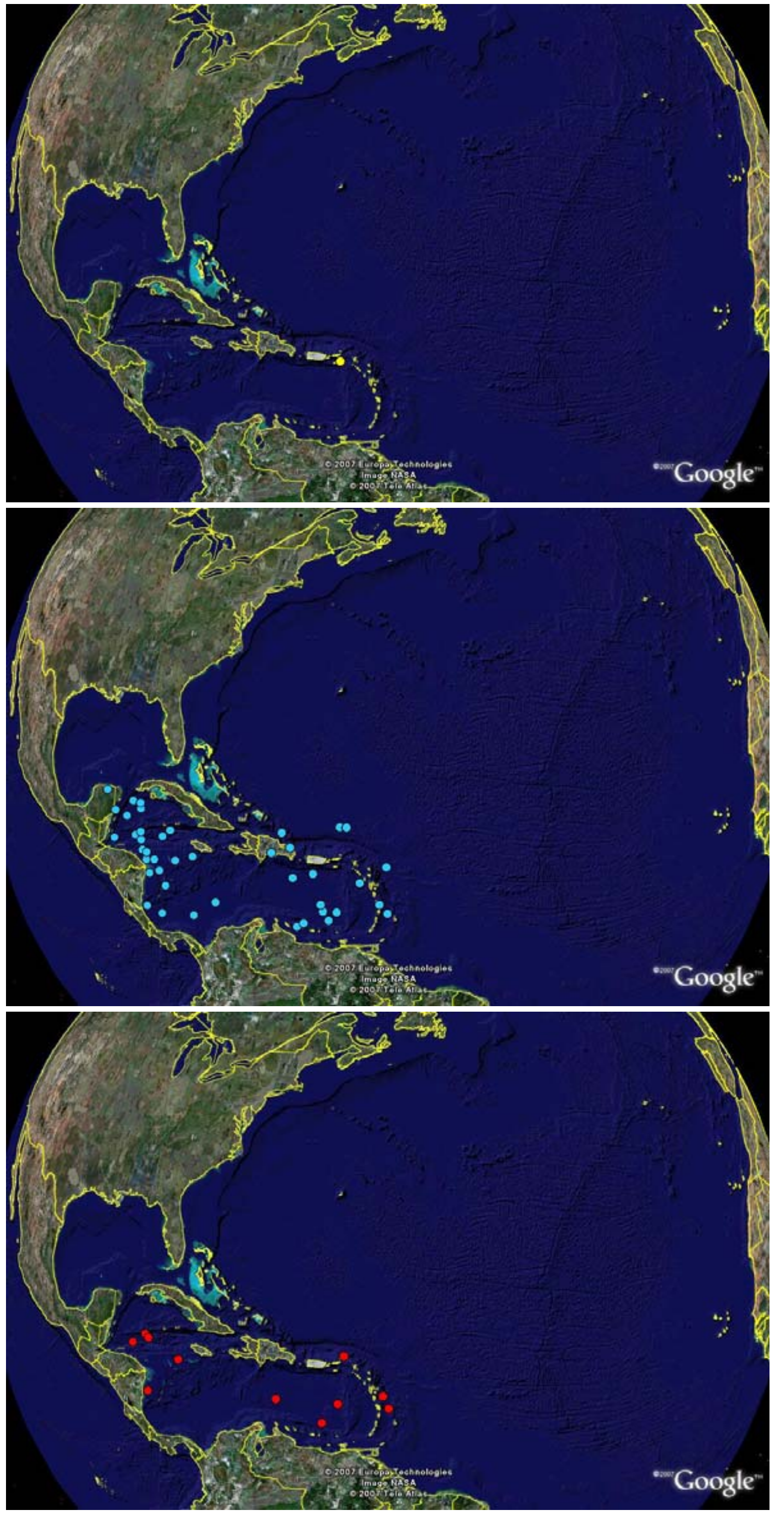

Fig. 4.13: All CARIB TC genesis points, 1978-2006, stratified by phase of MJO Index 6: yellow, cyan, and red correspond with ENH, NEU, and SUP phases, respectively.

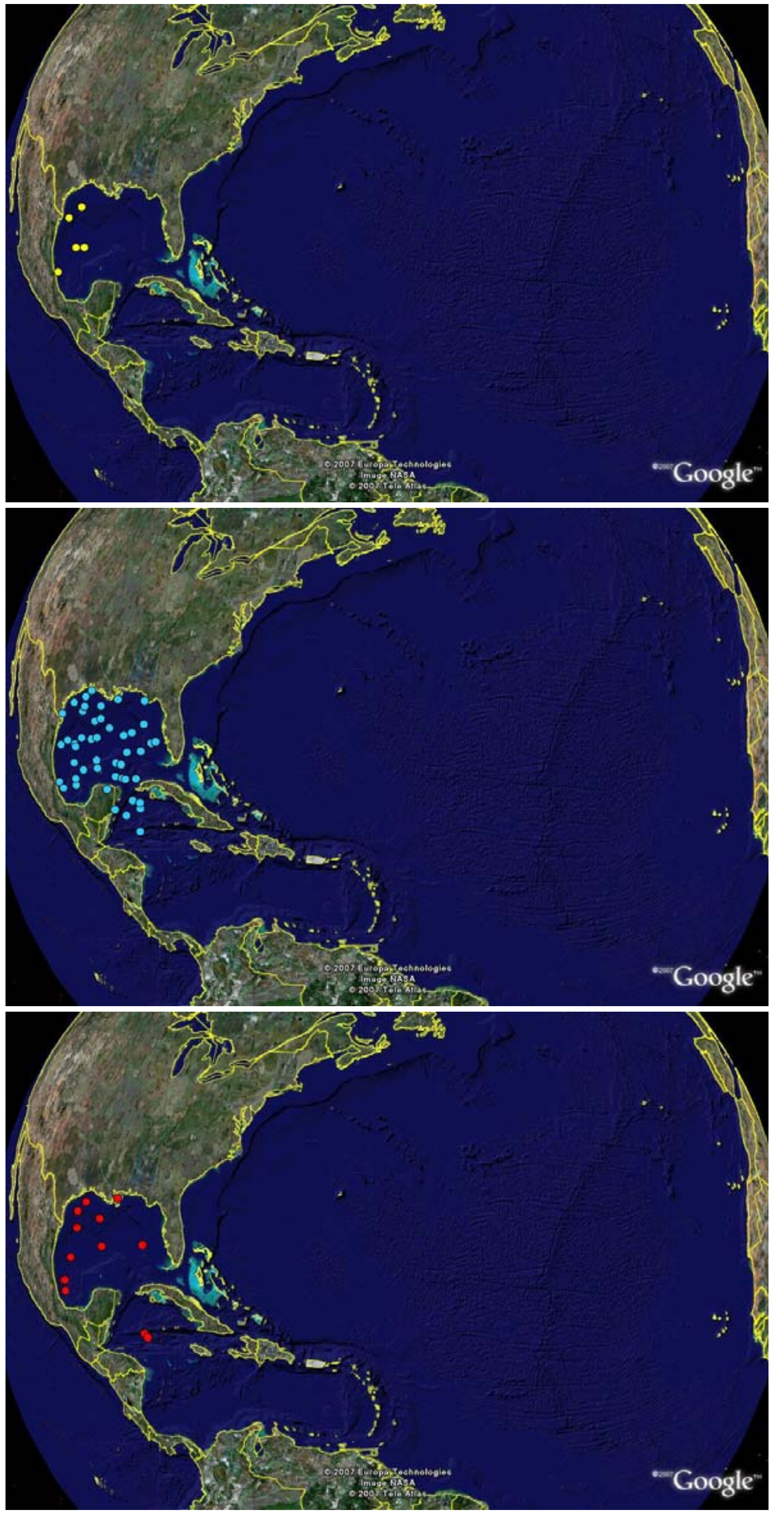

Fig. 4.14: All GOM TC genesis points, 1978-2006, stratified by phase of MJO Index 6: yellow, cyan, and red correspond with ENH, NEU, and SUP phases, respectively.

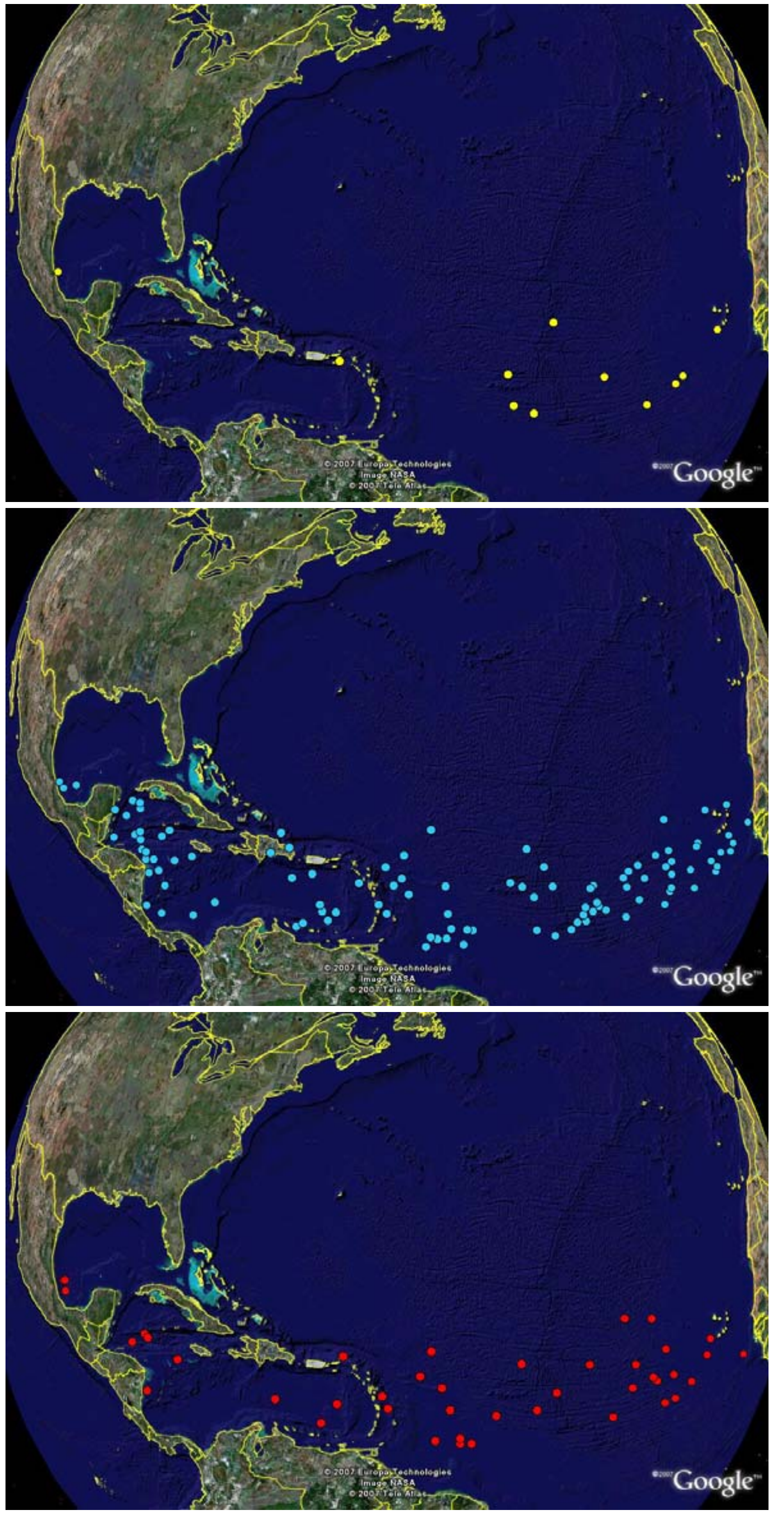

Fig. 4.15: All AMDR TC genesis points, 1978-2006, stratified by phase of MJO Index 6: yellow, cyan, and red correspond with ENH, NEU, and SUP phases, respectively.

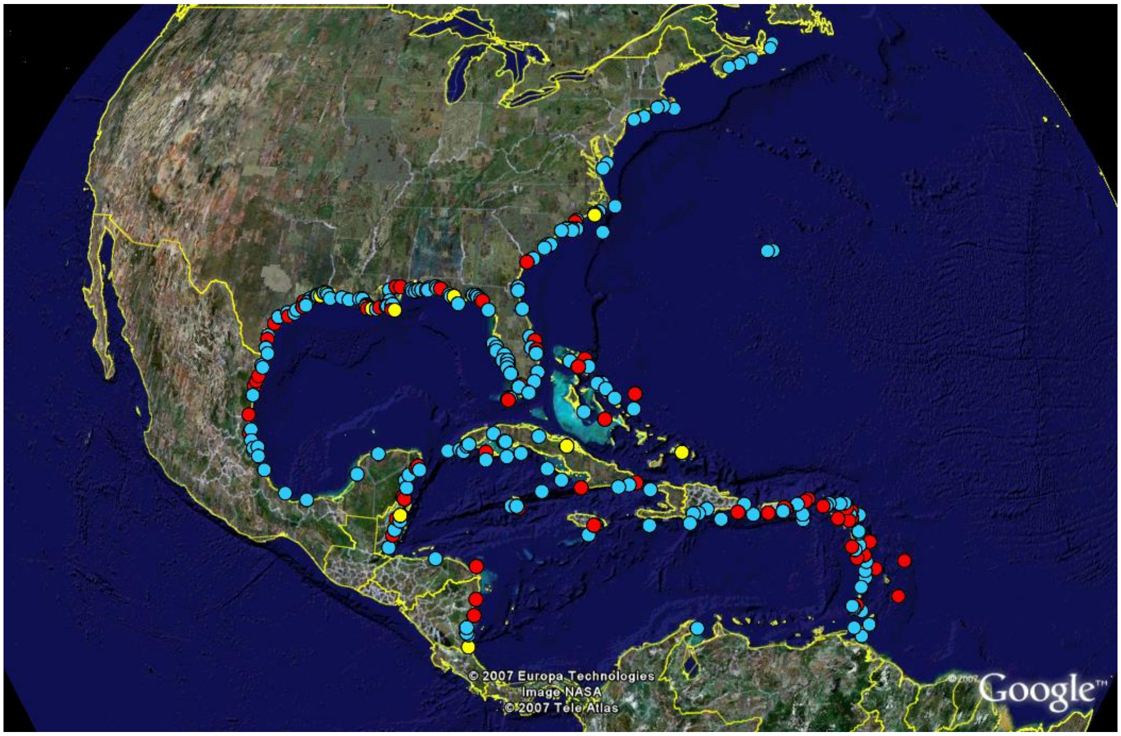

Fig. 4.16: All NATL *landfall-actual* points, from 1978-2006, stratified by phase of MJO Index 6: yellow, cyan, and red correspond with ENH, NEU, and SUP phases, respectively.

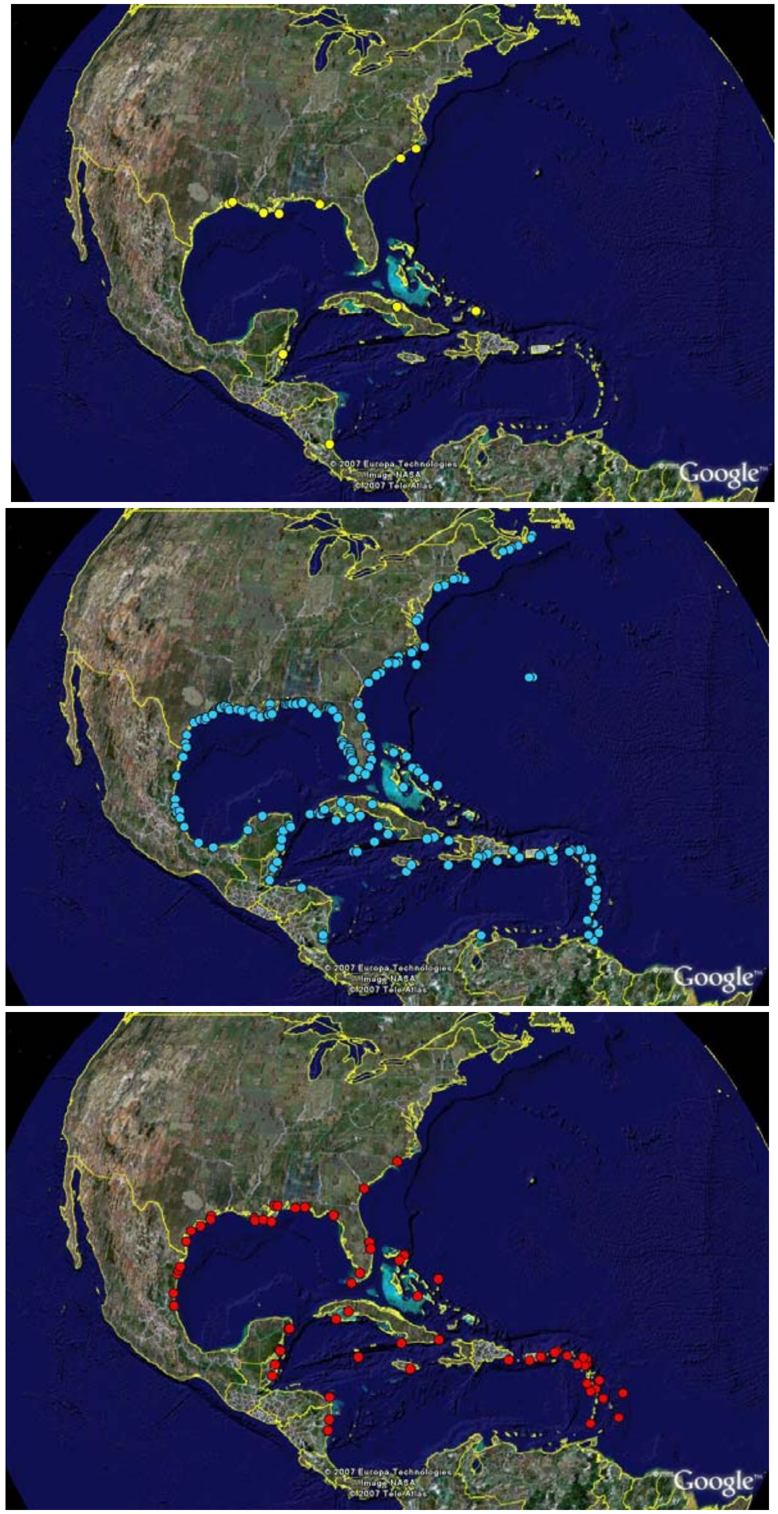

Fig. 4.17: All NATL *landfall-actual* points, from 1978-2006, stratified by phase of MJO Index 6: yellow, cyan, and red correspond with ENH, NEU, and SUP phases, respectively.

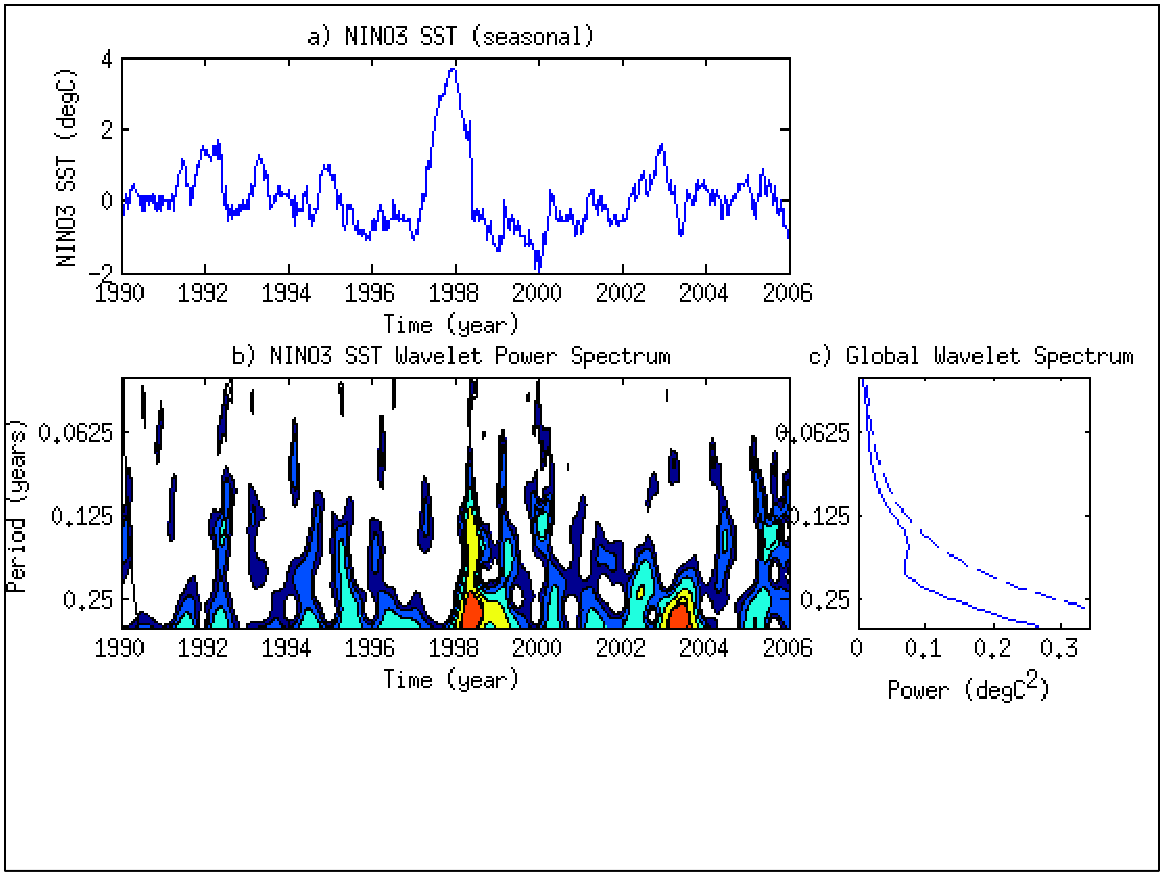

Fig. 4.18: Wavelet analysis of NINO3 SST data (a) showing peaks in the power spectrum, (b) and (c), on the timescales of the MJO.